

DISS. ETH NO. 29597

Advanced Inelastic Analysis and Design of High Strength Steel Structures with Machine-Learning-De- rived Predictive Methods

A thesis submitted to attain the degree of

DOCTOR OF SCIENCES

(Dr. sc. ETH Zurich)

presented by

ANDREAS MÜLLER

M.Sc. (TUM), Technical University of Munich

born on 20.09.1987

accepted on the recommendation of

Prof. Dr. Andreas Taras

Prof. Dr. Eleni Chatzi

Prof. Dr. Leroy Gardner

Prof. Dr. László Dunai

2023

Acknowledgements

Looking back, the last five and a half years have been a wild, life-changing, but most of all educational journey. I would especially like to thank Prof. Taras for giving me the opportunity to start my PhD at the Bundeswehr University Munich and to finish it at ETH Zurich. Your support was always of great value and kept me on track in critical moments of this work.

A big thank you goes to all my colleagues who accompanied me during this interesting time. Andrea, thank you for your dedication while working on the Hollosstab project. Without your perseverance, this work would not have been possible. The next time we will see each other will be hopefully in Sardinia. Michael, thank you for your support and your many helpful ideas, not only related to machine learning. I look forward to many more discussions, publications and refreshments. Robert, we share not only our first working days at the Bundeswehr University Munich and ETH Zurich, but also our passion for “Spitzenforschung”. Your commitment has always been a great inspiration to me. Patrick, my all-time favorite office mate, we always had our fun and many fruitful discussions. Also, thank you for trying to teach me Swiss German, even though I am a hopeless case. Vlad, your sense of humor always made the day a little better, albeit often unintentionally through flying food.

Further, this work would have not been possible to accomplish without the help of several master students. I would like to thank in particular Till Töpperwien, Alessandro Hodel, Niels Hellrigl, Oliver Allenspach and Andrea Luca Hauenstein. You guys were a huge help.

Mom and Dad, I wouldn't be here without your constant support and motivation. You both are truly amazing and have made many things possible for me. Your courage to leave everything behind and move to new places has always inspired and shaped me. I hope you can enjoy your time at Lake Constance now, at least for a while.

Finally, Manuela, I can't imagine my life without you. The last 14 years have been incredible, unfortunately I can't fit every memory into one paragraph. Starting with our time together at the university including all the ups and downs, the long nights at Harry Klein, our first (and second) apartment in Sendling (Munich) and the decision to move to Switzerland for my PhD. You are a wonderful person and a great mother to our two boys. I look forward to spending many more decades with you.

Abstract

The construction industry is a significant driver of carbon-related emissions and of climate change. In the field of structural engineering and design, this fact has led to a stricter focus on structural efficiency with respect to material choice, deployment and design utilization. For steel structures in particular, recent years have seen a push towards the use of high-strength and other high-performance steel grades, which potentially allow for significant savings in steel tonnages and thus in overall emissions and grey energy caused during the fabrication of structures and its components. However, traditional structural analysis and design methods and codes have not fully kept pace with these developments and are known to leave important margins of unexploited utilization. There is thus a need for more accurate analysis and design methods in order to fully exploit the material benefits of modern steels as a structural material.

As steel structures are typically relatively thin-walled and slender, instabilities in the elastic and plastic range play a particularly large role in the description of their their load-carrying capacity and, ultimately, of their non-linear load-deformation behaviour. Continuous advances in numerical simulation of metallic structures has opened the door to ever more precise, simulation-based design methods for steel structures. Recent research work thus focused on various aspects of the optimization and the inclusion of numerical analysis methods in the design tasks and methods for steel members and sections prone to instabilities. A project carried out by current members of the steel and composite structures research group at ETH Zurich, the RFCS-funded project Hollosstab (2016-'19), also formed the basis and defined the scope for the work carried out in this thesis: overcoming code related shortcomings in the design of *hollow sections and structures composed thereof*, made of mild and high-strength steel. However, significantly broadening the ambitions and methodological scope of Hollosstab, this thesis set out to exploit the potential of *data-driven, machine-learning techniques* in the analysis and design of steel structures of this type.

Accordingly, the present thesis is concerned with the development and establishment of a *novel, computer-aided, data-driven approach for the analysis and design of large-scale steel structures* capable of predicting the entire *non-linear deformation path*, i.e., the pre- and post-buckling range, using *beam finite elements that mimic the behaviour of advanced*

shell finite element models of closed RHS/SHS steel profiles. The approach proposed and developed in this thesis, which is referred to as DNN-DSM, uses Deep Neural Networks (DNN) to predict the *non-linear stiffness matrix terms* in a *beam element formulation* suitable for implementing within the Direct Stiffness Method (DSM). The approach is intended to allow developers of structural analysis software to combine the accuracy and precision of shell element analysis with the computational efficiency of beam element analysis, while allowing local, slenderness-dependent instability phenomena to be considered directly in the analysis.

Within the thesis, the methodology is conceptualized and developed to a degree of maturity that allowed to demonstrate its feasibility. It thereby applies a restricted scope, i.e. for individual load cases and the simpler case of hollow sections loaded in bending about a single axis. It pursues its objectives in a manner that is reflected in the thesis structure:

- i. Firstly, it reviews the traditional and advanced methods in structural steel design, and the use of machine learning in the engineering sciences, identifying their potential and shortcomings.
- ii. Subsequently, it makes use of physically validated, non-linear (GMNIA) simulations of the local buckling performance of hollow sections as key component of the data development for DNN training.
- iii. It then carries out the necessary steps to “train” DNNs for the prediction of stiffnesses and strength values in a beam finite element formulation.
- iv. It formulates the “deep neural network direct stiffness method” (DNN-DSM), by creating a bespoke simulation tool and using the programming language python.
- v. Finally, it validates the DNN-DSM method with more sophisticated benchmark shell finite element models that explicitly capture local buckling, as well as with conventional, code-based steel design and further experimental results from literature.

The thesis is wrapped up by an outlook on further steps and a widening of scope that will be needed to advance the method from the feasibility demonstration stage to industrial implementation for a wide range of steel structure applications.

Kurzfassung

Die Baubranche ist ein bedeutender Verursacher von klimaverändernden Emissionen. Im Bereich der Tragwerksplanung und des Konstruktiven Ingenieurbaus hat diese Tatsache zu einer stärkeren Konzentration auf die strukturelle Effizienz in Bezug auf die Materialauswahl sowie den Einsatz und die Ausnutzungsgrade geführt. Insbesondere bei Stahlkonstruktionen wurde in den letzten Jahren die Verwendung von hochfesten und anderen Hochleistungsstählen vorangetrieben, die erhebliche Einsparungen bei den Stahltonnagen und damit bei den Gesamtemissionen und der grauen Energie ermöglichen, die bei der Herstellung von Bauwerken und ihren Komponenten entstehen. Die herkömmlichen Methoden und Vorschriften für die Strukturanalyse und -auslegung haben jedoch mit diesen Entwicklungen nicht ganz Schritt gehalten und lassen bekanntermaßen erhebliche Nutzungsspielräume ungenutzt. Es besteht daher Bedarf an genaueren Bemessungsmethoden, um die Vorteile moderner Stähle als Bauwerkstoff voll ausschöpfen zu können.

Da Stahlkonstruktionen typischerweise relativ dünnwandig und schlank sind, spielen Instabilitäten im elastischen und plastischen Bereich eine besonders große Rolle bei der Beschreibung ihrer Tragfähigkeit und letztlich ihres nichtlinearen Last-Verformungsverhaltens. Stetige Fortschritte in der numerischen Simulation metallischer Strukturen haben die Tür zu immer präziseren, simulationsgestützten Bemessungsmethoden für Stahlkonstruktionen geöffnet. Jüngste Forschungsarbeiten konzentrierten sich daher auf verschiedene Aspekte der Optimierung und der Einbeziehung numerischer Analysemethoden in die Bemessungsaufgaben und -methoden für instabilitätsanfällige Stahlbauteile und -sektionen. Das vom RFCS finanzierte Projekt Hollosstab (2016-'19), welches von aktuellen Mitgliedern der Professur für Stahl- und Verbundbau der ETH Zürich durchgeführt wurde, bildete auch die Grundlage und definierte den Rahmen für die Arbeiten in dieser Dissertation: die Überwindung von codebezogenen Unzulänglichkeiten bei der Bemessung von Hohlprofilstrukturen. Die vorliegende Arbeit erweitert jedoch die Ziele und den methodischen Rahmen von Hollosstab erheblich, indem sie das Potenzial datengesteuerter, maschineller Lernverfahren für die Analyse und den Entwurf von Stahlkonstruktionen dieser Art auszuschöpfen versucht.

Dementsprechend befasst sich die vorliegende Arbeit mit der Entwicklung und Etablierung eines neuartigen, computergestützten, datengesteuerten Ansatzes zur Analyse und

Bemessung derartiger Strukturen, der in der Lage ist, den gesamten nichtlinearen Verformungspfad, d.h. den Vor- und Nachbeulbereich, unter Verwendung von Balken-Finite-Elementen vorherzusagen, wobei diese das Verhalten von weiterentwickelten Schalen-Finite-Elemente-Modellen von geschlossenen RHS/SHS-Stahlprofilen nachahmen. Der in dieser Arbeit vorgeschlagene und entwickelte Ansatz, der als DNN-DSM bezeichnet wird, verwendet Deep Neural Networks (DNN) zur Vorhersage der nichtlinearen Steifigkeitsmatrixterme in einer Balkenelementformulierung, die sich für die Implementierung in die direkte Steifigkeitsmethode (DSM) eignet. Der Ansatz soll Entwicklern von Baustatik-Software ermöglichen, die Genauigkeit und Präzision der Schalenelementanalyse mit der Recheneffizienz der Balkenelementanalyse zu kombinieren und gleichzeitig lokale, schlankheitsabhängige Instabilitätsphänomene direkt in der Analyse zu berücksichtigen.

Im Rahmen dieser Arbeit wurde die Methodik soweit konzipiert und entwickelt, dass ihre Durchführbarkeit nachgewiesen werden konnte. Sie gilt dabei für einen eingeschränkten Anwendungsbereich, d. h. für einzelne Lastfälle und den einfacheren Fall von Hohlprofilen, die auf Biegung um eine einzige Achse beansprucht werden. Sie verfolgt ihre Ziele auf eine Weise, die sich in der Struktur der Arbeit widerspiegelt:

- i. Zunächst wird ein Überblick über die traditionellen und fortschrittlichen Methoden der Stahlbauplanung und den Einsatz des maschinellen Lernens in den Ingenieurwissenschaften gegeben und ihr Potenzial und ihre Schwachstellen aufgezeigt.
- ii. Anschließend werden physikalisch validierte, nichtlineare (GMNIA) Simulationen des lokalen Beulverhaltens von Hohlprofilen als Schlüsselkomponente der Datenentwicklung für das DNN-Training verwendet.
- iii. Dann werden DNNs für die Vorhersage von Steifigkeits- und Festigkeitswerten in einer Balken-Finite-Elemente-Formulierung "trainiert".
- iv. Sie formuliert die "Deep Neural Network Direct Stiffness Method" (DNN-DSM), und erstellt ein hierfür ein eigenes Simulationswerkzeug mit Python.
- v. Schließlich wird die DNN-DSM-Methode mit weiteren FEM-Schalenmodellen, mit Normberechnungen und mit experimentellen Ergebnissen validiert.

Die Arbeit schließt mit einem Ausblick auf weitere Schritte und eine Erweiterung des Anwendungsbereichs, die erforderlich sind, um die Methode von der Phase der Machbarkeitsdemonstration bis zur industriellen Umsetzung für ein breites Spektrum von Stahlbauanwendungen voranzutreiben.

Connected publications

Listed below are the peer-reviewed journal articles and conference proceedings that either directly report on the same scientific studies as this thesis or from the other work related with the research topic of this thesis.

Journal publications

- Müller, A., Taras, A.: On the post-buckling rotational capacity of square hollow sections in uniform bending – An initial study of the impact of initial imperfections on deformation paths (Winner of the Bernt Johansson Outstanding Paper Award), *Steel Construction 12, No 3; 176 – 183, 2019.*
- Müller, A.; Taras, A.: Prediction of the local buckling strength and load-displacement behaviour of SHS and RHS members using Deep Neural Networks (DNN) – Introduction to the Deep Neural Network Direct Stiffness Method (DNN-DSM). *Steel Construction 15, Hollow Sections, pp. 78–90, 2022.*

Conference publications

- Müller, A., Taras, A.: Deep Neural Network Direct Stiffness Method: Initial Verification Examples, Ninth International Conference on Thin-Walled Structures, Australia, Sydney, 29 November – 1 December, 2023.
- Müller, A., Taras, A.: Deep Neural Network Direct Stiffness Method: Fundamental Steps into Beam Design, Eurosteel, Netherlands, Amsterdam, September 12-14, 2023.
- Müller, A., Taras, A.: Prediction of the local buckling behavior of structural systems using the deep neural network direct stiffness method (DNN-DSM), *Proceedings of the Annual Stability Conference, Structural Stability Research Council, North Carolina, Charlotte, April 12-14, 2023.*

- Müller, A., Taras, A., Kraus, M.: Scientific Machine and Deep Learning Investigations of the Local Buckling Behaviour of Hollow Sections, *Proceedings of the International Colloquium on Stability and Ductility of Steel Structures, Portugal, September 14-16, 2022.*
- Müller, A., Taras, A.: Prediction of the load-displacement and local buckling behavior of hollow structural sections using Deep Neural Networks (DNN), *Proceedings of the Annual Stability Conference, Structural Stability Research Council, Colorado, Denver, March 22-25, 2022.*
- Müller, A., Taras, A.: Study on the influence of measured geometric shape deviations on the deformations capacity and post-buckling behaviour of hollow sections loaded in compression and bending, *Proceedings of the Annual Stability Conference, Structural Stability Research Council, Atlanta, Georgia, April 21-24, 2020.*
- Müller, A., Töpperwien, T., Taras, A.: Imperfection evaluation methods of large scale spiral-welded tubes based on experimental tests and progressive reverse engineering procedures, *Proceedings of the 17th International Symposium on Tubular Structures (ISTS17), Singapore, December 09-12, 2019.*
- Müller, A., Taras, A.: Preliminary study on the impact of initial imperfections on the post-buckling rotation of square hollow sections in uniform bending, *Proceedings of the 14th Nordic Steel Construction Conference, Copenhagen, Denmark, September 18-20, 2019.*
- Müller, A., Taras, A.: Study on the deformation and rotation capacity of HSS hollow sections, *Proceedings of the International Colloquium on Stability and Ductility of Steel Structures, Prague, Czech Republic, September 11-13, 2019.*
- Müller, A., Hausmann, B., Taras, A.: Study on the influence of imperfections and strain hardening on the buckling strength of spiral-welded aluminium circular hollow sections, *Proceedings of the Eighth International Conference on Thin-Walled Structures, Lisbon, Portugal, July 24-27, 2018.*

Awards related to the thesis work

- 2019 - Nordic Steel Conference: Winner, Bernt Johansson Outstanding Paper Award

- 2022 –Stability and Ductility of Steel Structures Conference; Runner-up, Best Paper Award
- 2023 - AISC / SSRC Annual Stability Conference; Vinnakota Award 2023 Honorable Mention Recipient

Table of Contents

Acknowledgements.....	iii
Abstract.....	iv
Kurzfassung.....	vi
Connected publications.....	viii
Part I.....	1
1 Introduction.....	2
1.1 Starting point.....	3
1.2 Objectives.....	7
1.3 Scope.....	8
1.4 Organization.....	9
2 State of Technology.....	11
2.1 Background on the Inelastic Design of Structures.....	12
2.1.1 Introduction to plastic design.....	12
2.1.2 Rotation capacity.....	16
2.1.3 Elastic and Elastic-Plastic Plate Buckling.....	21
2.1.4 Cross-section classification.....	24
2.1.5 Design of structural systems.....	27
2.1.6 Geometric member imperfections.....	31
2.2 Categorization of Analysis Methods.....	37
2.2.1 Linear analysis.....	38
2.2.2 Linear buckling analysis (LBA).....	38
2.2.3 Materially non-linear analysis (MNA).....	39
2.2.4 Geometrically non-linear elastic analysis (GNA).....	39
2.2.5 Geometrically and materially non-linear analysis (GMNA).....	39
2.2.6 Geometrically non-linear elastic analysis with imperfections (GNIA).....	40
2.2.7 Geometrically and materially non-linear analysis with imperfections (GMNIA)	40
2.3 Direct Strength Method (DSM).....	40
2.4 Continuous Strength Method (CSM).....	43

2.4.1	Introduction and background information	43
2.4.2	Derivation of the CSM base curve.....	45
2.4.3	Non-linear material models	48
2.4.4	Determination of the relative local slenderness	55
2.4.5	Cross-section capacity based on CSM strain limits.....	56
2.5	Advanced Analysis + CSM Approach (AA+CSM)	61
2.5.1	Introduction.....	61
2.5.2	Strain averaging approach	63
2.5.3	Definition of cross-section elastic buckling stress and local buckling half-wavelength	64
2.6	Generalized Slenderness based Resistance Method (GSRM) for RHS/SHS profiles.	70
3	Research Gaps.....	76
3.1	Limitations of Traditional and Advanced Design Approaches	77
3.1.1	Cross-section classification	77
3.1.2	Non-linear material behaviour	78
3.1.3	Limitations of more advanced analysis and design methods	80
3.1.4	Role of the slenderness.....	81
3.1.5	Conclusions	86
3.2	New Approach: Machine and Deep Learning (ML/DL) in Structural Engineering...	87
3.2.1	Current trends in machine and deep learning.....	88
3.2.2	Selected application examples in the field of steel structures.....	89
3.3	Research Gaps	90
Part II	93
4	Deep Learning.....	94
4.1	Terminology – Machine Learning in a Nutshell.....	95
4.1.1	Artificial Intelligence and Machine Learning	95
4.1.2	Structured and unstructured data	96
4.1.3	Subgroups of learning algorithms.....	97
4.1.4	Overview of machine learning algorithms	98
4.2	Conceptual Introduction to Deep Neural Networks (Deep Learning).....	99

4.2.1	Brief background information	99
4.2.2	General representation of a neural network	100
4.3	Optimization Procedure in Deep Neural Networks.....	104
4.3.1	Loss functions and performance evaluation.....	104
4.3.2	Gradient descent and backpropagation.....	105
4.3.3	Influence of the amount of neurons	106
4.3.4	Feature transformation	107
5	Finite Element Models.....	109
5.1	Experimental campaign in the project HOLLOSSTAB	110
5.1.1	Full scale tests.....	111
5.1.2	Evaluation of local imperfections: Reverse engineering of specimen geometry	113
5.2	HOLLOSSTAB: Finite element modelling, validation and calibration.....	116
5.2.1	Validation against experimental tests	117
5.2.2	Calibration of GMNIA parameters.....	118
5.3	Investigations on Buckling Half-Wavelengths	120
5.3.1	Preliminary investigations on buckling lengths	122
5.3.2	Buckling lengths from experimental investigations	130
5.3.3	Conclusions and assumptions for the plastic hinge lengths from own work.....	134
5.4	Developed Finite Element Model.....	135
5.4.1	General description	135
5.4.2	Considered parameters and load cases	137
6	Data Development.....	141
6.1	Data pre-processing	142
6.1.1	Data generation workflow and used software	142
6.1.2	Data extraction	143
6.1.3	Data structure	145
6.2	Feature Engineering and Governing Results.....	147
6.2.1	Preface to presented investigations	148
6.2.2	Data set density.....	149

6.2.3	Data set splitting	155
6.2.4	Data transformation	156
6.2.5	Feature assessment	161
6.3	Hyperparameter tuning	171
6.4	Conclusions	176
Part III	179
7	DNN-DSM Methodology	180
7.1	Preface to the Direct Stiffness Method (DSM)	181
7.1.1	Introduction	181
7.1.2	Application of deformations	185
7.2	Deep Neural Network Direct Stiffness Method (DNN-DSM)	186
7.2.1	General idea	186
7.2.2	Limitations and Assumptions	186
7.2.3	Implementation for truss elements	187
7.2.4	Beam implementation	190
7.2.5	Simplified implementation of beam-column behaviour	196
7.2.6	Second order implementation	197
8	Method Evaluation	199
8.1	Verification in the elastic range	200
8.2	Cross-section verification	202
8.2.1	Cross-section capacity	203
8.2.2	Cross-section behaviour	209
8.2.3	Prediction sensitivity	215
8.3	Verification of Isolated Members	220
8.3.1	Isolated members in compression	220
8.3.2	Isolated members in compression with global second order effects	224
8.3.3	Isolated members in bending	227
8.4	Validation against Experimental Results	231
8.4.1	Stub column tests	231
8.4.2	Bending tests	240
8.5	Conclusions	257

9	Synthesis.....	260
9.1	Review of Objectives and Significance	261
9.2	Main contributions and conclusions	263
9.3	Outlook on Further Research Topics	267
	References.....	272

Part I

1

Introduction

Motivation, Scope and Limitations

Outline of the chapter:

This chapter discusses the motivation of the thesis and presents the starting point and initial ideas behind the data driven analysis and design method proposed therein. It also illustrates a set of objectives, the scope and the general organization of this thesis.

1.1 Starting point

The construction industry is one of the largest contributors to carbon dioxide (CO₂) emissions, accounting for nearly 40% of global industry-related emissions [1]. Thus, reducing CO₂ emissions in the Architecture, Engineering and Construction (AEC) industry has become a top priority throughout research and industry. In order to mitigate the impact on the environment, future tasks in the AEC industry must focus on implementing sustainable and energy-efficient practices. This involves using renewable materials, optimizing building design, promoting a circular economy (reuse) and adopting carbon-neutral fabrication technologies.

In the research field of steel and steel-based composite structures, the optimization of structural shapes and plate thicknesses, and thus the reduction of steel deployment, is a straightforward and particularly effective mechanism for a reduction of the carbon footprint and economic cost of structures. Much of the research work in the research field of steel and composite structures is dedicated to such optimization tasks. In particular, previous research work of the research group at ETH Zurich focused on various aspects of the optimization of design tasks and methods for steel members and sections prone to instabilities. As such, the overarching motivation, as well as the starting-point from the point of view of data, for the work carried out in this thesis goes back to the European research project Hollosstab. This project was carried out from 2017 to 2019 and funded by the Research Fund of Coal and Steel (RFCS) and was coordinated by the supervisor of this thesis, with its author participating in its research work.

The objective of Hollosstab was to overcome code related shortcomings in the design of standard and bespoke-shaped hollow sections made of mild and high-strength steel; e.g., conservative assumptions related to the cross-section classification with respect to their proneness to local buckling, lack of consideration of material nonlinearity for different steel grades and fabrication routes, conservative local buckling checks based on the effective width method and plate-wise classification - and thus neglect of beneficial interaction effects between mutual plates. The key result of this project was the development of the so-called “generalized slenderness-based resistance method” (GSRM), which was developed and derived as described by Toffolon in [2] for flat-faced (RHS/SHS) hollow

sections. This approach is part of the group recently-developed design methods, such as the direct strength method (DSM), the continuous strength method (CSM) or the overall interaction concept (OIC), which make use of overall slenderness formulations to formulate corresponding buckling know-down factors and thus account for local and global, as well as coupled, instabilities.

While the development of these methods has led to noticeable increases in the prediction of the strength of steel sections, and have provided a blue-print for the development of equivalent proposals and methods for arbitrary shapes of sections and materials, conservatism and scatter has not been reduced by orders of magnitude when compared to more traditional methods. Furthermore, deformation capacities and non-linear load-displacement paths are not generally part of these methods' predictions.

In order to explore some avenues for further improvements of strength predictions for high-strength steel hollow sections, in the "outlook" section of the Hollosstab-related dissertation [2], a data-driven approach using a deep neural network model (DNN) was included to predict the cross-section-dependent bearing capacity. This led to much higher prediction accuracy compared to the derived GSRM approach. These encouraging results, further worked on in [3], served as the initial starting point for the development of the approach presented in this thesis. However, the present thesis aims at taking the possibilities of DNN-based predictions of structural performance further, adding the dimensions of stiffness respectively deformation capacity to the already-promising strength predictions.

Accordingly, the present thesis is concerned with the development and establishment of *a novel, computer-aided, data-driven approach for the analysis and design of large-scale steel structures capable of predicting the entire non-linear deformation path, i.e., the pre- and post-buckling range, using beam finite elements that mimic the behaviour of advanced shell finite element models of closed RHS/SHS steel profiles.*

The technical motivation for this development comes from the following observations:

- i. Beam finite element analysis is commonly used in structural engineering for various materials, such as steel or timber, to determine the internal distribution of

forces, moments and stresses, as well as associated deformation within systems. The general implementation is based on the Direct Stiffness Method (DSM), where each element is represented through a local stiffness matrix K_{loc} , responding to external actions and imposed deformations for each component. These analyses are computationally efficient but fail to capture non-linear effects and redistributions within the structure due to plasticity, in particular local instability.

- ii. To capture the mentioned nonlinearities stemming from localized instabilities, which are very typical for thin-walled steel structural elements, over conservative assumptions are included in code provisions, such as e.g. the mentioned classification of sections in four “classes”. Alternatively, more advanced (shell-type) finite element method (FEM) models could be utilized for the entire structure, but this approach is computationally expensive and might be prone to input related errors by the engineer, always dependent on the problem related knowledge base. Moreover, it is primarily limited to research and not suitable for designing large structures due to computational inefficiencies and the complexity of modeling.

The proposed approach, hereafter referred to as DNN-DSM, uses Deep Neural Networks (DNN) techniques to predict the non-linear stiffness matrix terms in a beam element formulation suitable for implementing within the Direct Stiffness Method (DSM), further introduced in Section 7. The approach is intended to allow developers of structural analysis software to combine the accuracy and precision of shell element analysis with the computational efficiency of beam element analysis, while allowing local, slenderness-dependent instability phenomena to be considered directly in the analysis.

The basic conceptual framework of the method is illustrated, in schematic form, in Figure 1-1. The overall method derivation is basically separated in three parts:

- i. the finite element simulation and development of appropriate data sets, based on local shell-element simulations, covering for instabilities at the cross-sectional level,
- ii. the development of deep neural networks, suitable to predict the individual tangent stiffnesses,

iii. the implementation into the direct stiffness method.

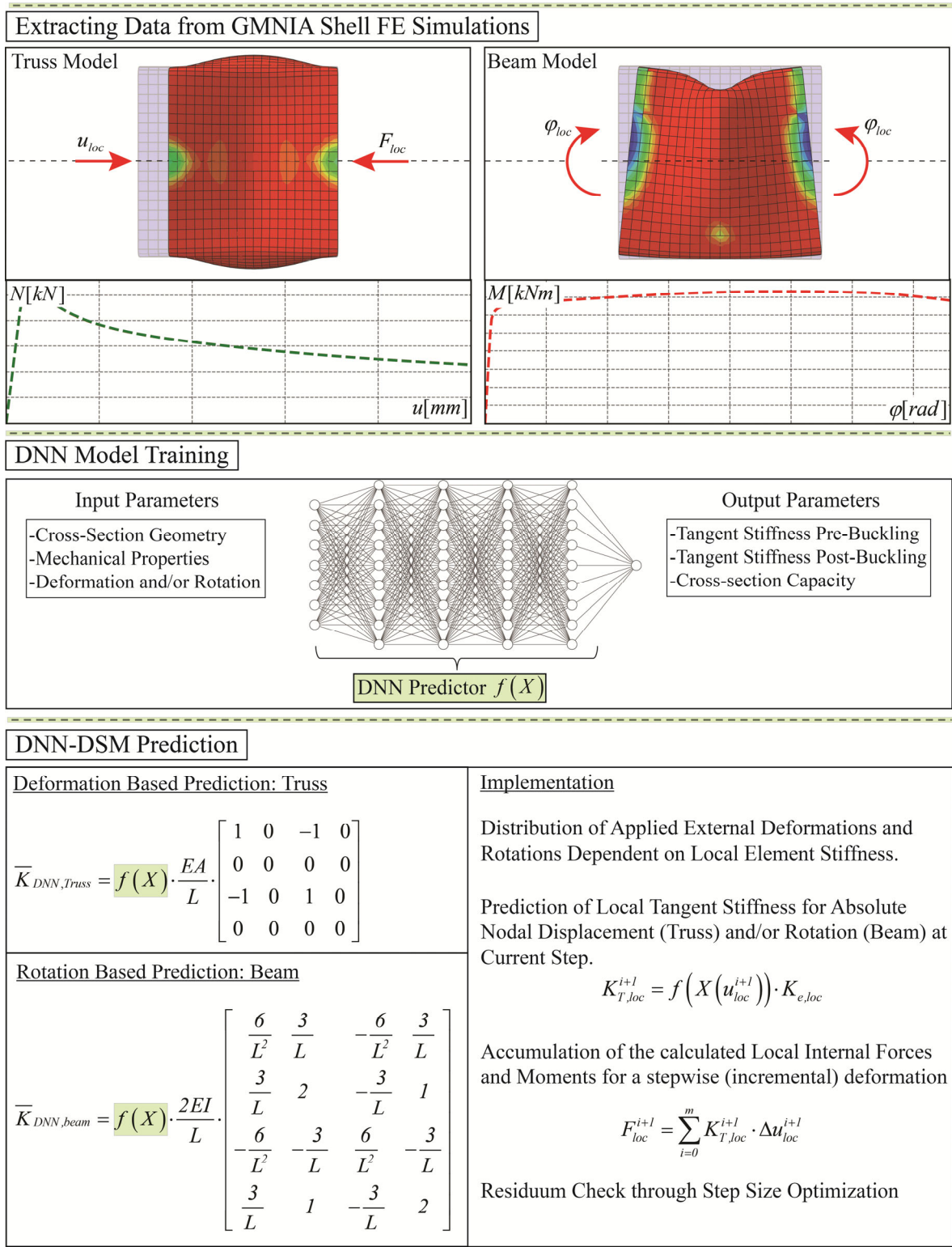


Figure 1-1: Schematic outline of the DNN-DSM approach, subdivided into three main parts

1.2 Objectives

In order to reach the overarching goal of the development and tentative, demonstrative implementation of the proposed DNN-DSM approach, a number of individual objectives will be tackled in the thesis, organized as follows:

- i. Review the traditional and advanced methods in structural steel design with the identification of shortcoming. Introduction to new design approaches and corresponding application examples based on data driven methods from machine and deep learning.
- ii. Give a brief introduction to deep learning and the design of neural networks with the aim of giving the reader a better understanding of the subject without the use of additional literature.
- iii. Starting from the finite element modelling techniques developed during the RFCS funded project Hollosstab and based on the tests carried out therein, as well as further tests in literature, verify and validate FEM models for the data development to be used in DNN training. Thereby, special attention needs to be given to effects of local buckling, plasticity, and buckling lengths.
- iv. Carry out the necessary steps for the data development and exploration of deep neural networks for the prediction of stiffnesses with a beam finite element formulation, linked to general assumptions and recommendations for feature engineering.
- v. Incorporate the “deep neural network direct stiffness method” (DNN-DSM) into the format of the direct stiffness method (DSM), thereby creating a bespoke simulation tool and using the programming language python.
- vi. Compare the results obtained using the DNN-DSM method with more sophisticated benchmark shell finite element models that explicitly capture local buckling, as well as with conventional, code-based steel design and further experimental results from literature.
- vii. Provide an outlook on the next steps in the development and generalization of the method.

1.3 Scope

Although this method is seen within a wider application range in future structural steel design, the proposed methodology is in a preliminary development stage, where different application boundaries need to be first tested and the general feasibility, strengths and weaknesses of the approach need to be assessed. Therefore, the scope of the presented thesis is bound by the following limitations:

- i. As was the case for the project Hollosstab, during which the experimental core of this thesis was elaborated, the considered structural shapes are limited to hot-rolled and cold-formed square (SHS) and rectangular (RHS) hollow sections. All profile shapes are based on European standard provisions in EN10210-2 [4] and EN10219-2 [5].
- ii. Out-of-plane global instability problems are neglected, by assuming appropriate bracing.
- iii. The data development is based on parametrized short shell finite element models to simulate local buckling only. The load cases are limited to pure compression or pure bending only.
- iv. The data development simulations are limited to steel grades S355, S460 (for cold- and hot-formed sections) and S700 (cold-formed) resp. S690 (hot-rolled). Material models are limited to a simplified bi-linear behaviour with a perfect plateau (hot-rolled and cold-formed) and advanced material models for hot-rolled [6] and cold-formed steel [7]. Three local imperfection amplitudes are used, with shapes generally based on local buckling eigenmodes.
- v. Connections are assumed as rigid in all simulations.
- vi. Rotations within beam elements are assumed equal at each end of the short members.

1.4 Organization

In the following, a summarized overview of the main content of each chapter of this thesis is given.

Chapter 2 provides a general description of state of the art topics related to inelastic design and its consideration and implementation in design methods. First, background information on classical topics from inelastic design are presented to provide a general overview on the current design implementation of code provisions. Nowadays, frequently used numerical analysis methods are further presented and briefly described. In addition, advanced inelastic analysis methods are presented, including the “direct strength method” (DSM), the “continues strain method” (CSM), the “advanced analysis continues strength method” (AA-CSM) and the “generalized slenderness based resistance method” GSRM.

Chapter 3 maps out the overall research gaps of this thesis. Therefore, topics from Chapter 2 are addressed and discussed critically, pointing out their advantages and disadvantages with respect to current trends and developments in structural engineering. Further, the idea of machine learning methods in civil engineering applications is introduced as a new data driven approach for solving otherwise computationally expensive or analytically inaccurate solutions. With this in mind, the main research gaps are formulated.

Chapter 4 presents a brief introduction to machine learning, particularly to selected topics from deep learning, which are used throughout this thesis.

Chapter 5 provides background information on the models used in the finite element simulations in this thesis. Thus, the main aspects of the Hollosstab project are presented briefly, presenting the experimental campaign and the idea behind the validation and calibration of the finite element models. Based on imperfection evaluation results from the Hollosstab project, as well as corresponding finite element models using the real geometry of the specimens, investigations on buckling half-wavelengths are performed

and compared with assumptions from the AA-CSM approach from Chapter 2. Subsequently, the developed finite element model assumptions and the parameters used for the development of the data sets are presented.

Chapter 6 forms the basis of the developed DNN models for the “DNN-DSM” approach proposed in this thesis. First, the data development, extraction and data structure are explained. A major focus is set on feature engineering, i.e., exploration, interpretation and modification of the available data to obtain better prediction results. The methods presented in this chapter are not only suited for the derived DNN-DSM approach, but are generally applicable to many problems concerning data structures and their interpretability towards analytical formulations.

Chapter 7 is dedicated to the implementation of the DNN-DSM approach. Starting with basic background information on the direct stiffness method (DSM), this chapter extends it further by incorporating the derived DNN models. The implementation of truss and beam elements is described. The corresponding modelling approaches are then presented, which are further used in the method evaluation in Chapter 8.

Chapter 8 describes the evaluation of the DNN-DSM method. The core part of the chapter is dedicated to a validation of the DNN-DSM method against existing experimental and numerical results from the literature and from the author’s own work.

Chapter 9 wraps up this thesis by providing a summary of the main steps towards the development of the presented DNN-DSM approach, followed by a set of conclusion regarding the made choices and obtained results. Shortcomings and subsequent optimizations are presented, together with a discussion of needed next steps towards a more robust and more widely-applicable approach.

2

State of Technology

Analysis and Design of Steel Structures

Outline of the chapter:

This chapter is dedicated to a thorough review of the historical development of inelastic design methods in steel structures and of how they are used in current design codes and methods, as well as to the presentation of several methods for the analysis and verification of slender steel structures that have been developed by the steel structures research community over the course of the last two decades and make use of numerical analysis at various degrees.

2.1 Background on the Inelastic Design of Structures

2.1.1 Introduction to plastic design

The possibility of considering plastic distribution of stresses along the depth of a cross-section was first proposed by Ewing [8] in 1899, but remained only a theoretical approach since no physical tests were performed to demonstrate it. During this period, structures were mainly designed limiting the stresses to the elastic limit, i.e., to the range where there is a proportional response between stress and strain according to Hooke's law. This basic conceptual design approach does not allow for any redistributions within the structure, as the maximum achievable load of the structural assembly is assumed to be equal to the load at which first yielding occurs ([9], [10]). This consideration was appropriate for a time with limited computational possibilities, considering its simplicity and inherent conservatism.

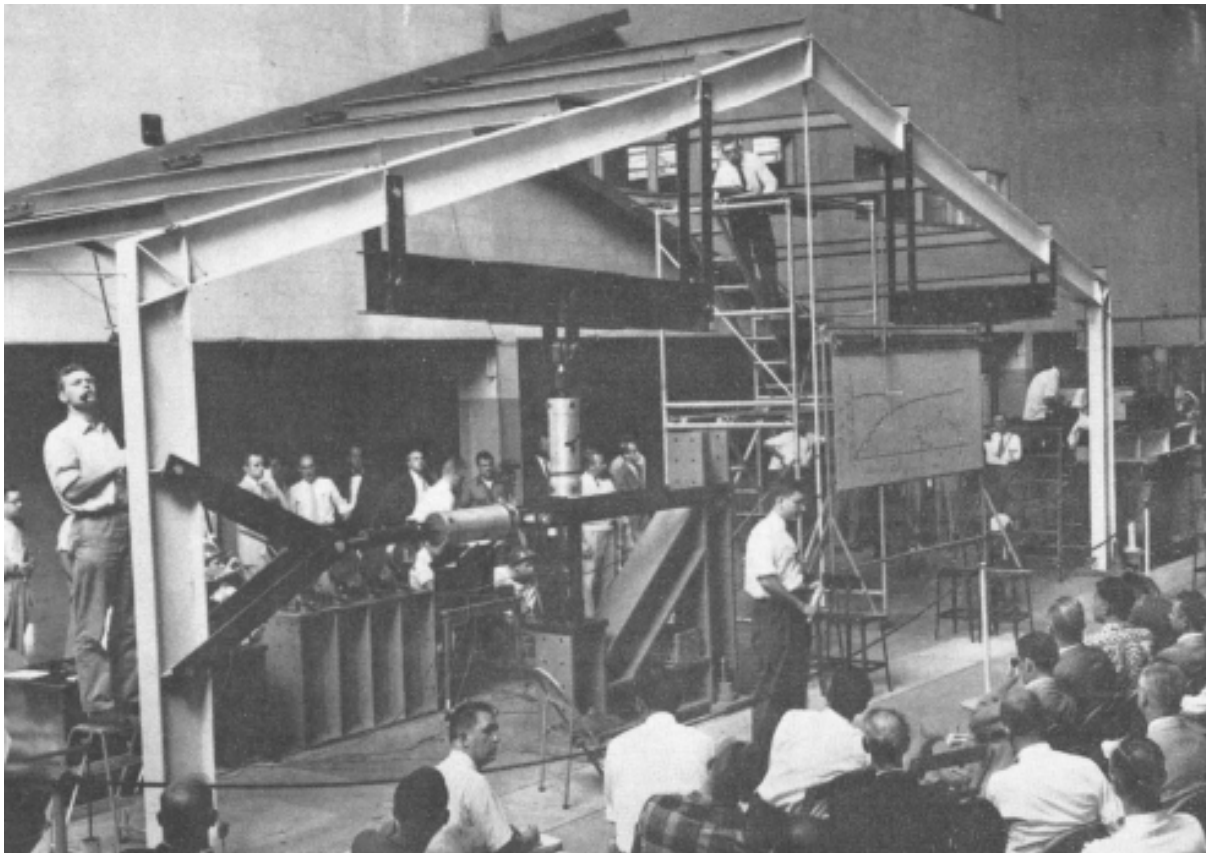


Figure 2-1: Experimental test of a gable frame at the Lehigh University around 1958 [11]

Research from the early 20th century to the late 1970s focused on exploring the advantages of plastic design, e.g. through extensive experimental campaigns, the theoretical derivation of plastic resistance for rectangular and H-shaped sections, the introduction of an elastic-perfect plastic material model, and the extension of plastic analysis to complete structures, thus recognizing the potential of plastic redistribution in statically indeterminate systems ([12]–[26]). Figure 2-1 shows an experimental test on a full-scale gable frame conducted at Lehigh University around 1958 [11]. A detailed historical overview can be found in [9], [27] and [28], to which the reader is referred for additional information.

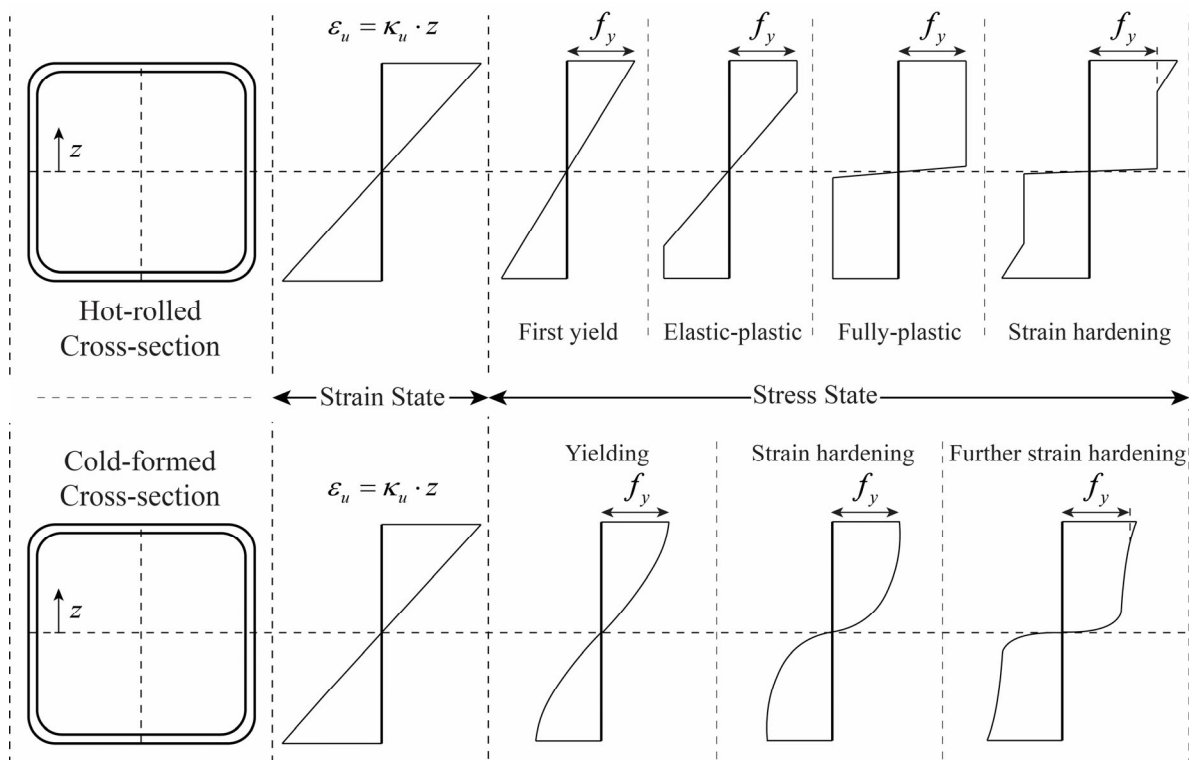


Figure 2-2: Elastic-plastic strain hardening material behaviour for a hot-rolled and cold-formed cross-section

The plastic design method allows for a far-better utilization of cross-sections and statically indeterminate systems, theoretically allowing for yielding through the entire depth of a section and at multiple points in a structure (if statically indeterminate). Figure 2-2 shows an example of the influence of a fully plastic stress distribution, as well as the additional positive effect of strain hardening, using a hot-rolled or cold-formed section

in pure bending; this explanatory illustration is inspired by one found in Wilkinson [27]. With increasing curvature, i.e. increasing maximum strain at the outermost point of the section, the stress distribution remains linear until the yield stress is reached (first yielding). This behaviour applies to hot-rolled carbon steel and was assumed to be a critical design failure criterion before the fundamentals of plastic theory were explored. While the strain continues to increase, the stress remains the same due to the pronounced yield plateau, resulting in an increased activation of the cross-section for bending resistances (“elastic-plastic” stage in the figure). At high values of curvature and strain, the elastic-plastic-strain-hardened material cross-section yields almost completely (“fully plastic”). When the entire cross-section has reached its yield point, the corresponding plastic moment is defined as M_{pl} . In addition, strain hardening may occur and the stress may exceed the yield strength (“strain hardening” in the figure).

In contrast, there is no plastic plateau in cold-formed steel and a strongly non-linear stress-strain response even at low strains $\varepsilon < 0.2\%$ (“yielding behaviour”). Immediately after yielding, strain hardening occurs and stresses in the cross-section increase beyond the plastic moment (“further strain hardening”).

When a cross section (theoretically) yields across its depth and the plastic moment M_{pl} is reached, a so-called “plastic hinge” is formed at a certain point along the beam. At this point, a large rotation (proportional to a large curvature) occurs, while the plastic moment remains theoretically constant. In the case of a statically indeterminate structure, such a scenario allows for some redistribution of moments, i.e., transfer of load due to larger deformations to parts of the structure that have not yet reached the plastic resistance. The limit up to which the “plastic hinge” can be rotated before it loses strength when compared to the plastic moment resistance is referred to in the literature as “rotational capacity” R_{cap} . Strain hardening, as well as sufficiently low proneness to local buckling and sufficient lateral stabilization, are required elements to achieve a functioning “plastic hinge”.

These fundamental considerations are behind the idea of plastic design and lead to several advantages over elastic design, such as the use of slimmer cross-sections, resulting in savings in material and thus costs, and a more economical assessment of profile-de-

pendent strength. It also allows the development of systematic failure behaviour to account for redistributions in statically indeterminate structures. Thus, failure need not occur when the plastic moment is reached at a particular point in the structure, but rather when a collapse mechanism has already formed (reaching a sufficient number of plastic hinges).

A commonly used strategy to account for maximum plastic redistributions is the virtual work method, which equates external and internal work during the stepwise formation of the collapse mechanism. This well-known analytical method, typically taught in basic structural analysis courses [29], is mostly well-suited for manual calculations, but it is not necessarily applicable to complex structures and also involves many additional assumptions in its procedure:

- i. Local and global instability problems are neglected.
- ii. The plastic hinge is reduced to one point, where the curvature is assumed to be infinite.
- iii. Strain hardening is neglected, thus, the plastic moment is not exceeded throughout the calculation process and the plastic hinge rotates without flexural resistance. Based on Neal [30] this assumption is safe sided.
- iv. The plastic resistance is not linked to a possible interaction with normal forces or concentrated stresses indicated through point loads.
- v. Second order effects are not taken into account, therefore, initial geometric imperfections (e.g. sway mode affine imperfections in frame structures) are ignored.

Nowadays, plastic design methods (e.g. plastic hinge or plastic zone analysis) are used, to some extent, in many fields of structural engineering. However, for the consideration of moment redistribution, the estimation of the cross-sectional rotational capacity is of great importance, and its accuracy may decide design safety and economy. Therefore, a short overview of the theoretical background, the influencing factors and the current design proposals is given in the following section.

2.1.2 Rotation capacity

For the application of plastic or, more generally, inelastic analysis methods, components must have a certain degree of ductility to undergo deformation after exceeding the initial yield strength in parts of the cross-section without significant loss of strength and stiffness due to material damage or, more crucially for steel sections, instabilities. The specific ductility measure used for beams and beam-columns is referred to as "rotational capacity", with the notation R , R_{dem} or R_{cap} used in the literature. The importance of the rotation capacity in design and its influence on practice was recognized in early investigations, see the preceding section. As a result, considerable efforts have been made over decades to investigate and propose influencing factors, parameters, and analytical models that describe the cross-section and load- and material-dependent inelastic rotational capacities.

Early considerations on the formation of plastic hinges were mentioned by Kazinczy [13] in 1914, who tested H-shaped beams under uniform load while they were fixed at both ends (the fixed condition was ensured by embedding the ends in concrete) and concluded that three plastic hinges were required to achieve the ultimate capacity. This was followed by studies of moment-deflection behaviour of beams under various loading conditions conducted at Lehigh University between 1940 and 1960. Driscoll Jr [31] summarized the status of rotational capacity studies in 1957. At that time, it was already known that residual stresses resulting from cooling, welding, or cold bending had an effect on the yield strength of a steel component. In addition, these factors were already known to further influence the magnitude of the plastic hinge moment, although they had little effect on a component's ability to absorb plastic rotations. Other, crucial known factors that reduce plastic hinge moment and rotational capacity include brittle fracture, local buckling, and lateral (torsional) buckling. Driscoll Jr. presented methods for calculating the rotational capacity required to form a mechanism and provided results for some specific cases of three-field continuous beams. In his 1958 dissertation, Driscoll Jr. [32] extended his method from three-field beams to the analysis of frames. The method applied to frames assumed that the length of the yield zones at each plastic hinge is zero when a structure reaches its ultimate capacity and forms a failure mechanism. These

simplifications allowed the calculation of rotational slopes and deflections in static systems using elasticity theory methods, where the plastic hinge was simply accounted for by changing the boundary conditions to allow the necessary rotational freedom.

In 1968, Galambos [33] collected the state of the art in inelastic deformability and energy absorption capacity of steel beams and steel structures with the aim of giving designers an overview of how much a steel structure can deform, but also to inform researchers in which area more work is needed. This collection contains one of the first formulas to calculate the rotation capacity of beams as a function of the slenderness constant, determined theoretically and under the condition that local and lateral buckling occur simultaneously, see Equation (2-1). It was additionally tested using experiments from [34], [35] and [36] and gave what were deemed to be good results [33].

$$R = \left(\frac{s-1}{0.7 \cdot h} \right) \cdot \left(\frac{\pi^2}{\varepsilon_y \cdot (KL/r_y)} - 1 \right) \quad (2-1)$$

where:

- $s = \sigma_u / \sigma_y$ is the ratio of the strain-hardening strain to the yield strain, also often addressed as the over-strength factor.
- $h = E_{ST} / E$ is the ratio between the elastic modulus E and the strain hardening modulus E_{st} of the used material.
- $\varepsilon_y = \sigma_y / E$ is the yield strain of the used material
- K is the effective length factor which depends on whether the adjacent span is elastic ($K = 0.54$) or yielding ($K = 0.80$); see the following Figure.

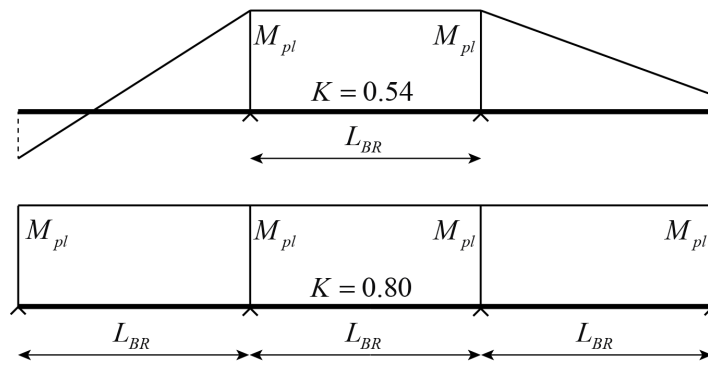


Figure 2-3: Effective length factor, Figure partially adapted from Galambos [33]

L/r_y is the unbraced slenderness ratio

r_y is the least radius of gyration of the wide-flange shape

L_{BR} is the unbraced length

In addition, Galambos [33] and Yura et al. [37] found that a rotation capacity limit $R_{cap} = 3$ is needed that covers most practical situations. In [37] and [38], a rotation capacity of was proposed after considering different systems and parameters of I-shaped profiles. A rotation capacity of $R_{cap} = 4$ was proposed by Korol and Hudoba [39] for hollow sections and adapted in [40] and [41] to determine a suitable plastic slenderness for the Australian Standard AS 4100. Continuous beams have been studied by Kuhlmann [42] and Stranghoner et al. [43], resulting in a proposed value of $R_{cap} = 2$ for I-shaped sections (also confirmed by Neal [30]) and $R_{cap} = 3$ for hollow sections, respectively. In this context, it was found that a rotation demand between 3 and 4 is suitable for most common structures and has therefore been adapted in the current standards for the derivation of slab slenderness limits.

Considerable efforts have been made to define the parameters that affect rotation capacity. Saloumi [28] has recently compiled an informative review of the quantification and sensitization factors for rotation capacity. Some of these parameters are summarized below. For additional information, the reader is referred to the original sources within the enumeration.

- i. Identification of a strength reserve after local buckling – see experimental tests in [44]
- ii. Identification of three governing parameters for the rotation capacity – flange slenderness as a key parameter, the web stiffness and the steepness of the moment gradient [42].
- iii. Investigations in [42], [43] and [45] led to the conclusion that the degree of strain hardening significantly influences the rotation capacity.
- iv. A significant influence of initial imperfections on the moment-rotation curve, the plastic hinge formation and the post-buckling behaviour in the decreasing part was observed in [46].
- v. The behaviour of RHS profiles was studied by Wilkinson [27], also using numerical (finite element) methods to suggest a new design limit. Especially the magnitude of imperfections was found to have a significant impact on the rotation capacity of stockier sections. As higher the initial imperfections were chosen, as lower the rotation capacity was.
- vi. A summary of experimental results done by different authors and provided by Kemp [47] has shown that not only the slenderness ratio for local buckling of web and flange are decisive to determine the inelastic rotation capacity, rather mostly the slenderness ratio for lateral buckling. Therefore, the available rotation capacities in the tests were set in relation with local flange and web buckling and lateral-torsional buckling.

The general representation of rotation capacity R_{cap} most commonly used today is defined by Equation (2-2). It is a measure of how far the plastic hinge can rotate before its carrying moment falls below the notational value of the plastic moment, which is determined using yield stress blocks. Thereby, φ represents the beam end sections' rotation and its limit values φ_{pl} , φ_u , $\varphi_{pl,2}$, see Figure 2-4.

$$R_{cap} = \frac{\varphi_{pl,2} - \varphi_{pl}}{\varphi_{pl}} = \frac{\varphi_{pl,2}}{\varphi_{pl}} - 1 \quad (2-2)$$

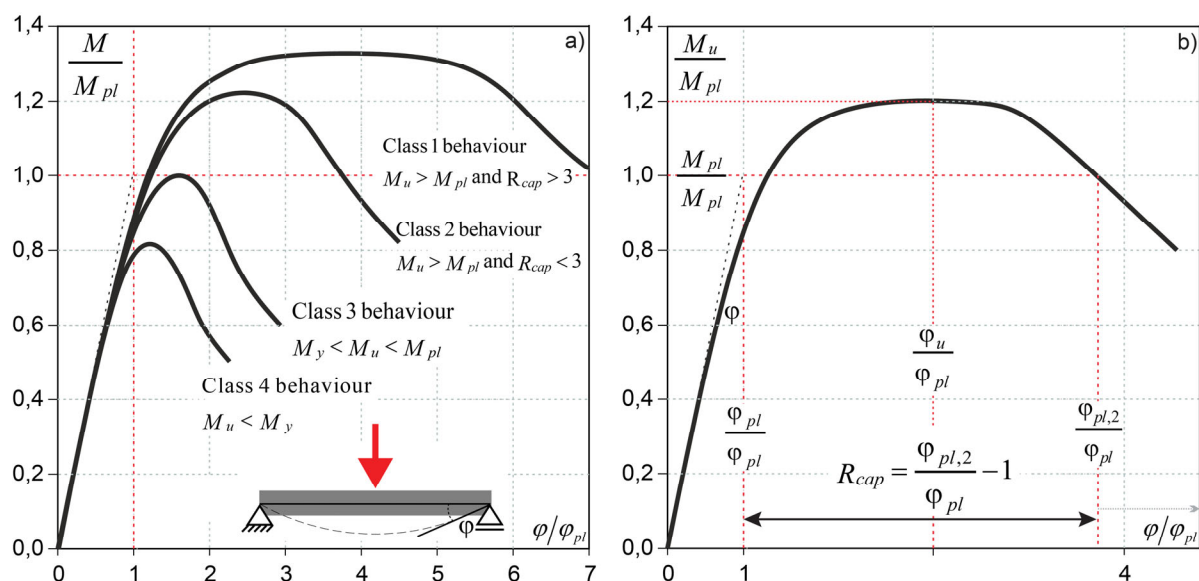


Figure 2-4: a) cross-section class dependent definition of allowable rotations according to EN 1993-1-1; b) definition of the rotation capacity

The achievable rotation is thus defined as the angle of rotation $\varphi_{pl,2}$ in a deformation-driven test or analysis where the moment falls below the theoretical value of M_{pl} . This convention is per se a simplification and demonstrates that the classic plastic analysis is necessarily only an approximation of a structure's true behaviour, with the main aim of estimating its failure load, yet without any attempt at reflecting load-deformation paths with great accuracy.

When looking at current design codes, it is noticeable that Eurocode 3 [48] and other international codes do *not explicitly* mention any limit or minimum values on rotation capacities, *but implicitly impose requirements on rotation R_{cap} as a function of cross-section classifications*. In order to account for plasticity and prevent local buckling, slenderness limits have been established for plate elements in structural members, and cross sections are considered to be composed of individual apartment plate elements. By this definition, Class 2 cross sections can achieve their plastic moment but not the rotation capacity of 3. Class 1 cross sections meet this requirement by achieving a rotation capacity greater than 3; see Figure 2-4 a). Class 3 and 4 cross-sections are limited to their elastic cross-sectional capacities or must even be considered for local buckling. Further details on the codified classification procedures are given in Section 2.1.4.

2.1.3 Elastic and Elastic-Plastic Plate Buckling

As described previously, local (plate) buckling is a key limiting and influence factor on the more global load-displacement or moment-rotation behaviour of a steel component, which is almost exclusively composed of rather thin-walled sections. Accordingly, it is important to review the historical background and state of knowledge in the field of local plate buckling of steel structures.

Early investigations on the plate buckling problem go back to the work of Bryan [49] in 1888. He derived the following differential equation for a rectangular plate subjected to uniform compression on one of the edges.

$$\frac{E \cdot t^3}{12 \cdot (1 - \nu^2)} \cdot \left(\frac{d^4 w}{dx^4} + 2 \frac{d^4 w}{dx^2 dy^2} + \frac{d^4 w}{dy^4} \right) = -\sigma_x t \frac{d^2 w}{dx^2} \quad (2-3)$$

where:

E	is the modulus of elasticity
t	is the plate thickness
ν	is the Poisson's ratio, e.g. 0.3 for steel
w	is the lateral deflection of the plate
$\sigma_x t$	is the edge compression load, as load per unit length

For hinged boundary conditions along all four edges, the solution of the differential equation from above is obtained with an approach assuming the deflection w to be represented by a trigonometric series, see Equation (2-4).

$$w = \sum_{m=1,2,3,\dots} \sum_{n=1,2,3,\dots} w_{\min} \cdot \sin\left(\frac{m\pi x}{a}\right) \cdot \sin\left(\frac{n\pi y}{a}\right) \quad (2-4)$$

Using this to solve the differential equation leads, after further steps, to the well-known solution of the elastic (critical) plate buckling stress σ_{cr} :

$$\sigma_{cr} = k_{\sigma} \cdot \frac{\pi^2 \cdot E}{12 \cdot (1 - \nu^2)} \cdot \left(\frac{t}{b}\right)^2 \quad (2-5)$$

where:

k_{σ} is the buckling coefficient for different stress distributions $\psi = \sigma_{min}/\sigma_{max}$ and boundary conditions, see Table 2-1.

Table 2-1: Buckling coefficient for different stress distributions according to [50]

	Cross-section parts supported on both sides	Cross-section parts supported on both sides
ψ	1	-1
k_{σ}	4	23.9

Current design approaches for the verification of thin-walled plates in compression make use of local buckling knockdown factors, which are formulated as functions of the relative plate slenderness. This quantity, using Eurocode 3-type notations, is given by Equation (2-6). In (2-6), the relation between this slenderness and the width-to-thickness ratio b/t is also inversed, as this will be useful in relating deformation capacities to certain slenderness values.

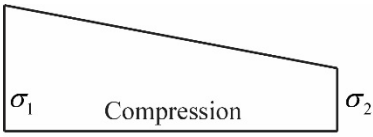
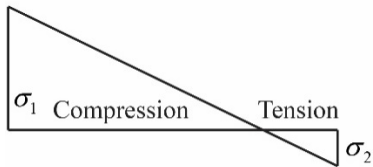
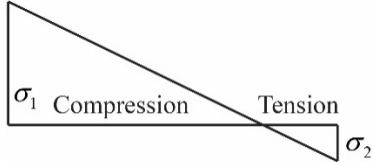
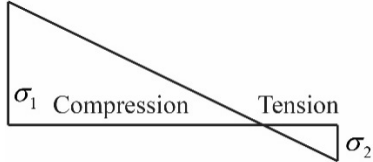
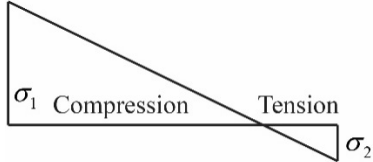
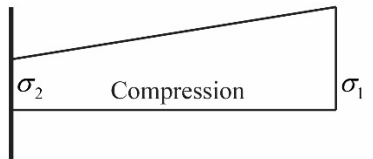
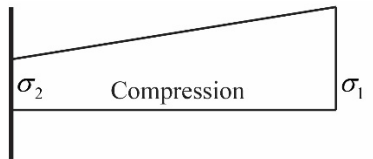
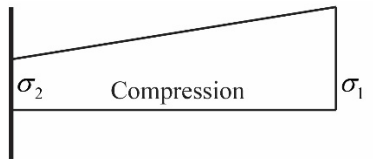
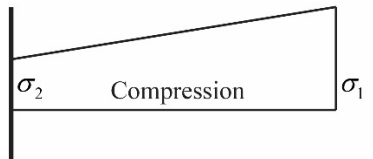
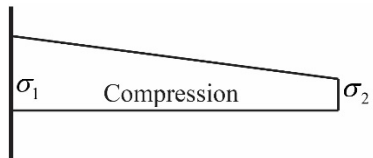
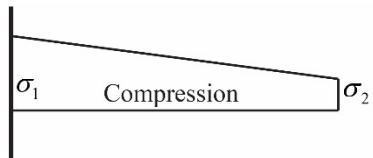
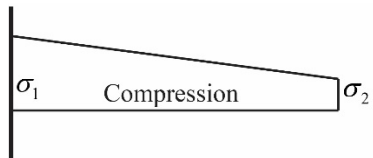
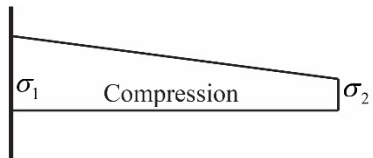
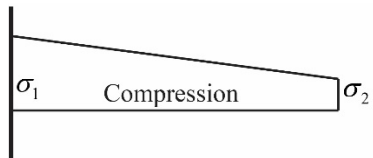
$$\bar{\lambda}_p = \sqrt{\frac{f_y}{\sigma_{cr}}} = \sqrt{\frac{12 \cdot (1 - \nu^2)}{k_{\sigma} \cdot \pi^2 \cdot E}} \cdot \frac{b}{t} \Rightarrow \frac{b}{t} = \sqrt{\frac{\pi^2 \cdot E}{12 \cdot (1 - \nu^2)}} \cdot \sqrt{\frac{1}{f_y}} \cdot \sqrt{k_{\sigma}} \cdot \bar{\lambda}_p \quad (2-6)$$

The right side of Equation (2-6) can be further simplified using the modulus of elasticity of steel with the value of $E = 210000N/mm^2$, the Poisson's ratio with $\nu = 0.3$, and a factor ε used to normalize the yield strength by its value for steel grade S235 ($\varepsilon = \sqrt{235/f_y}$) leading to:

$$\frac{b}{t} = 28.419 \cdot \sqrt{\frac{235}{f_y}} \cdot \sqrt{k_\sigma} \cdot \bar{\lambda}_p \Rightarrow \frac{b}{t} = 28.419 \cdot \varepsilon \cdot \sqrt{k_\sigma} \cdot \bar{\lambda}_p \quad (2-7)$$

This equation can be used, in conjunction with the European plate buckling curve (Winter curve) from EN 1993-1-5 [50], to determine the normative (Eurocode 3) b/t limit value for the transition between Class 3 and Class 4 sections for plates supported on both sides and loaded by pure compression ($\psi = 1 \rightarrow k_\sigma = 4.0$), leading to a value of this limit slenderness of $\bar{\lambda}_p = 0.673$.

Table 2-2: Buckling coefficients k_σ for internal and outstand plates with simply supported boundary conditions along connected edges according to EN 1993-1-5 [50]

Stress distribution	$\psi = \sigma_2/\sigma_1$	Buckling coefficient
Internal plates (SS-SS)		
	1	$k = 4$
	$1 > \psi > 0$	$k = \frac{8.2}{1.05 + \psi}$
	0	$k = 7.81$
	$0 > \psi > -1$	$k = 9.78 \cdot \psi^2 - 6.29 \cdot \psi + 7.81$
	-1	$k = 23.9$
Outstand plates (SS-free)		
	1	$k = 0.43$
	0	$k = 0.57$
	-1	$k = 0.85$
	$1 > \psi \geq -3$	$k = 0.07 \cdot \psi^2 - 0.21 \cdot \psi + 0.57$
	1	$k = 0.43$
	$1 > \psi > 0$	$k = \frac{0.578}{0.34 + \psi}$
	0	$k = 1.70$
	$0 > \psi > -1$	$k = 17.1 \cdot \psi^2 - 5 \cdot \psi + 1.7$
	-1	$k = 23.9$

Note: Compression taken as positive

This limit corresponds to the plateau length of the “Winter curve”, see Equation (2-8). The origin of this formula is based on studies by Winter [51] in the 1940s on cold-formed channel sections. In [52], a detailed background and justification of its adaptation in DIN 18800-3 is given, by checking the application of the “Winter curves” against experimental results of stiffened and unstiffened plates.

$$\rho = \frac{\bar{\lambda}_p - (0.055 \cdot (3 + \psi))}{\bar{\lambda}_p^2} \quad (2-8)$$

Using the slenderness limit and applying it to the analytical solution from Equation (2-7), a limit value for the b/t ratio can be back calculated.

$$\frac{b}{t} = 28.419 \cdot \varepsilon \cdot \sqrt{4} \cdot 0.673 = 38.25 \cdot \varepsilon \quad (2-9)$$

2.1.4 Cross-section classification

The concept of cross-sectional classification goes back mainly to [10], [53]–[55], [44], [56]–[58], [42] and is closely related to the studies that led to the development of plastic design of steel structures, presented in Section 2.1.1, and of the required rotation capacity, described in Section 2.1.2. An additional historical overview of the background of cross-section classification is given in [27], [59] as well as [28] and is thus referred to for further explanations.

The general concept of cross-section verification is one of the most crucial and deciding parameters in the design of steel members, with some practical advantages yet also many implications that affect the design’s accuracy and interpretability. It is nevertheless widely used throughout many code provisions, like the EN 1993-1-1 [48] or the AISC [60] (additional reference is made in Table 2-2 including different terminologies within capacity limits) and determines the method of verification, in particular the cross-section utilizations, associated to cross-section capacities and local buckling instabilities. Using the designation from EN 1993-1-1 [48], four cross-section classes are specified to facilitate the design process in the following, see also Table 2-3 below. The classification

of a cross-section is typically carried out upon the most slender plate element. This follows the pragmatic assumption that every structural section is split into individual plates. Thus, an SHS profile is divided into four web plates, each supported through hinges at both ends and referred to as internal elements [48]. An I-section on the other hand, is composed from a web plate, which is supported at both ends (referred to as an internal element), and two flange plates divided into two additional plates supported at one end (referred to as an external element), see Table 2-3.

Table 2-3: Subdivision in cross-section classes within different code specifications, partially adapted from Wilkinson [27]

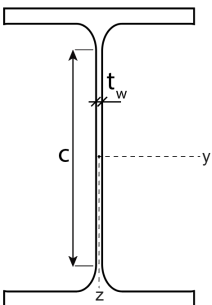
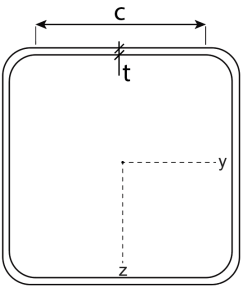
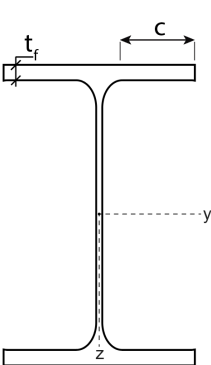
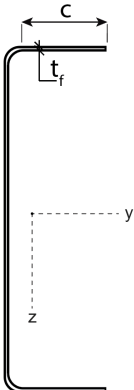
Code reference	Categorical Subdivision			
EN 1993-1-1: 2010 [61]	Class 1	Class 2	Class 3	Class 4
EN 1993-1-1:2020 [48]	Class 1	Class 2	Class 3	Class 4
AISC [60]	Compact	Non-Compact		Slender
DIN 18800 Part 1 [62]	P-P	E-P		E-E
BS 5950 [63]	Plastic	Compact	Semi-compact	Slender
CSA S16.1 [64]	Plastic or Class 1	Compact or Class 2	Non-Compact or Class 3	Slender or Class 4
AS 4100 [65]	Compact	Non-Compact		Slender

For the practically most relevant case of members in bending, the following classification definitions apply:

- i. Class 1 cross-sections can reach their plastic moment capacity M_{pl} and have sufficient rotation capacity for the safe application of plastic design methods, including methods based on plastic hinges and redistribution of internal moments in statically indeterminate structures once these notional hinges have formed (method “P-P” in Eurocode terminology). Sections categorized as Class 1 are also referred to as plastic sections.
- ii. Class 2 cross-sections can develop the full plastic moment capacity M_{pl} but fail to reach rotation capacities deemed to be required for plastic design approaches. Therefore, structures compound of Class 2 cross-sections must be analysed elastically and verified plastically (E-P), since no plastic hinge formations can be accounted for. To distinguish between Class 1 and 2 cross-sections it is therefore not only necessary to evaluate the pre-buckling range, until the point of reaching

- the maximum moment bearing capacity, but also the post-buckling behaviour, since the rotation capacity requires the knowledge of the full deformation path. Class 2 cross-section are also referred to as compact sections in [63].
- iii. The bending resistance of Class 3 cross-sections is limited to their yield moment M_{el} and cannot reach the plastic moment M_{pl} , due to local instability problems, i.e. local buckling, assumed to occur and affect the sectional stiffness and load-bearing capacity before the notional plastic moment is reached. Further used designations are semi-compact [63] or non-compact [64].
 - iv. Class 4 cross-sections cannot reach their elastic moment M_{el} due to an earlier onset of local buckling. Effective section properties need to be calculated for individual elements using the effective width method, considering all elements subjected to compression [48]. Beneficial interaction effects between mutual plates are not considered. Throughout code provision these kind of sections are also designated as slender.

Table 2-4: Cross-section class dependent c/t values according to EN 1993-1-1 [48]

	Cross-section elements supported on both edges		Cross-section elements supported on one edge	
				
Class	Pure compression	Pure bending	Pure compression	
1	$c/t \leq 28 \cdot \varepsilon$	$c/t \leq 72 \cdot \varepsilon$	$c/t \leq 9 \cdot \varepsilon$	
2	$c/t \leq 34 \cdot \varepsilon$	$c/t \leq 83 \cdot \varepsilon$	$c/t \leq 10 \cdot \varepsilon$	
3	$c/t \leq 38 \cdot \varepsilon$	$c/t \leq 121 \cdot \varepsilon$	$c/t \leq 14 \cdot \varepsilon$	

The cross-section classification in design codes is typically based on c/t limits, described through the length c of a separated plate element and its thickness t . An extract of pertinent regulations in Eurocode 3 (EN 1993-1-1: 2020 [48]) is summarized in Table 2-4. The general distinction is made between elements supported on one edge and on both

edges, loaded in pure compression, pure bending or a combined case of those and therefore presented independently.

The transition limit between class 1 and 2 is mainly based on experimental investigations and numerical simulations, since no clear differentiation can be drawn by only looking at the maximum reached bending moment, nor the maximum normal force in compression. Cross-section of both classes can reach their full plastic capacity. In addition, the rotation capacity must be examined throughout further analytical considerations and physical measurements.

The transition limit between class 2 and 3 cross-sections (reaching the elastic-plastic cross-section resistance) are based on experimental test and additional simulation results. Those are in general performed by three and four point bending tests, additional stub column tests or mono- and bi-axial eccentric compression tests [66].

The limit slenderness between class 3 to 4 cross-sections, i.e. the limit between profiles reaching the elastic capacity and those which fail to reach it due to local buckling, is determined by the theoretical consideration of the differential equation for elastic local buckling of a plate. Equation (2-3) shows the general differential equation with in plane stress σ_x for any type of edge restraints [49].

2.1.5 Design of structural systems

2.1.5.1 Analysis and verification

The design of steel structures has traditionally been a two-step process. First, a structural analysis is performed to determine the internal forces and moments within each member of the structure. Then, design checks are performed, in general consisting of (at least) cross-section checks to verify the local capacity and additional member stability checks of the most relevant members. Geometric and material nonlinearities are primarily responsible for instability and redistribution effects within a structural system. Geometrical nonlinearity is caused through the presence of second order moments and forces, indicated through the deformed state of the structure. This effect is initiated

through applied geometric local and global imperfections or first-order loading causing eccentricities of the centroid line with respect to the direction of axial loading.

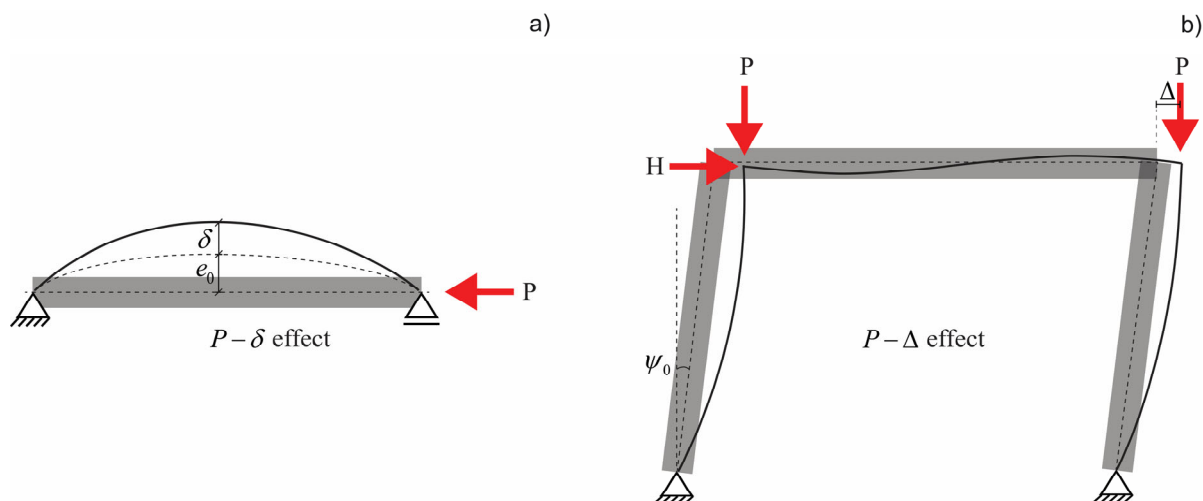


Figure 2-5: a) $P-\delta$ out-of-straightness effect on the member level; b) $P-\Delta$ out-of-plumbness effect and first order horizontal force; adapted from [67]

On the structural level, initial out-of-straightness $P-\delta$ and initial out-of-plumbness $P-\Delta$ imperfections are usually accounted for in the second order analysis. $P-\delta$ effects are related to members, where the midspan deflection e_0 is defined with respect to the perfectly straight member, see Figure 2-5 a). With ascending compression force P , the deflection e_0 increases proportionally within a linear elastic response by the value of δ . This ratio changes with respect to the used material model. $P-\Delta$ effects, on the other hand, are associated with sway deformations of the structural system, see Figure 2-5 b). An initial out-of-plumbness imperfection ψ_0 is introduced to create a horizontal deformation shift. A similar result is achieved through a first-order horizontal load H , see Figure 2-5 b). Both approaches result in a deformation Δ under increasing load P , which lead to second-order moments in the structure. In practical applications initial imperfections are either directly modelled in the analysis or, as stated above, included by adding equivalent horizontal forces to the frame structure. In some cases the directions of the applied imperfection may have a stabilizing effect on the structural behaviour. It is therefore always necessary to check the sensitivity against imperfection orientations throughout several calculations to cover also the unfavorable cases.

In Eurocode 3, the sensitivity of a structure to second-order effects is assessed using the critical load factor α_{cr} , which is defined as the ratio of the elastic critical buckling load F_{cr} and the applied design load F_{Ed} , see Equation (2-10).

$$\alpha_{cr} = \frac{F_{cr}}{F_{Ed}} \quad (2-10)$$

α_{cr} is used to assess, whether global imperfections on the member or system level need to be applied. Limit values are provided by EN 1993-1-1:2020 [48] for members prone to flexural buckling and frames affected by instability caused through sway effects, i.e. second-order $P-\Delta$ effects need to be accounted for. A limit value of $\alpha_{cr} \geq 25$ has to be fulfilled in order to ignore global instability corresponding to flexural buckling. This limit value is equivalent to the plateau value of European flexural buckling curves for members. Instability effects are either accounted for through buckling checks or cross-section checks based on second-order forces.

Frame structures need to meet the condition of $\alpha_{cr} \geq 10$ in order to be able to neglect sway effects. Based on the calculated critical load factors (on member and frame level) and the applied modelling effort EN 1993-1-1: 2020 [48] provides a flow chart describing various possibilities to assess the structural stability of frames. The presented methods are termed as $M0$ to $M5$ and EM . A description of each method is stated below.

- i. $M0$ represents a structure where member instability and sway effects are too small and no stability checks are necessary due to its construction driven boundary conditions. Flexural buckling, as well as lateral torsional buckling verifications can be neglected. The verification of the cross-section resistance may then be checked by first order internal forces and moments. This constellation can occur for tension rods and beams with rotational/lateral restraints.
- ii. $M1$ refers to first order analysis without the application of global imperfections. The only difference to method $M0$ is that lateral torsional buckling (LTB) and out of plane instability effects need to be accounted for.
- iii. $M2$ requires no application of sway mode imperfections, since the condition of $\alpha_{cr} \geq 10$ is met. Nevertheless, flexural buckling need to be accounted for due the

- condition of $\alpha_{cr,ns} < 25$. Therefore, first order analysis is applied to verify flexural buckling instability. This is the case, for example, for all non-displaceable frames or steel structures that are attached to rigid concrete cores.
- iv. *M3* requires a closer look at the determination of internal moments and forces as global sway effects ($P-\Delta$) must be considered and should rely on second-order analysis ($\alpha_{cr} \leq 10$ for elastic or $\alpha_{cr} \leq 15$ for plastic calculation). For the calculation of the in-plane buckling resistance of a single member, the buckling length $L_{k,y}$ can be taken as the system member length L between the system nodes. Out-of-plane stability checks are performed according to support conditions along the member.
 - v. *M4* requires a system calculation according to elastic second-order theory including all in-plane imperfections, i.e. $P-\Delta$ and $P-\delta$. If the corresponding out-of-straightness and out-of-plumbness imperfections are accounted for in the system calculation, no further in-plane stability checks need to be applied. Only the cross-section capacity checks at the decisive locations with internal second-order forces are to be performed. Out of plane stability verification is assessed according to *M3*.
 - vi. *M5* requires the largest modelling effort, since all in-plane and out-of-plane second order effects, including torsional effects and global sway imperfections, and all in-plane and out-of-plane local bow imperfections are considered. The verification of the buckling resistance of individual members may be omitted and is “quasi” replaced by the proof of cross-sectional resistance. The method is characterized by considerable complexity and by the need for great modelling accuracy. This can only be mastered with high-level FEM programs, so that this method is currently only used in exceptional cases in practice. However, this method can be applied with conventional computational programs to spatial bar systems in which only torsionally stiff profiles (e.g. hollow profiles) are used, so that warping torsion effects and LTB are negligible.
 - vii. An additional alternative Method *EM* “Equivalent Member Method” also known as “Effective Length Method” is implemented to the design checks as an alternative to *M2*. Although its legitimation has only a historical background, as design specifications [62] and [61] has relied on this method for many years, the limitations of this approach have been highlighted in several studies [68]–[71].

2.1.5.2 Mechanical nonlinearities

The mechanical properties of steel, hot-rolled as well as cold-formed carbon steel, make it particularly suitable for the use in plastic design approaches [7]. Hot-rolled steel is characterized through a long yield plateau, high ultimate strains, a moderate over-strength (strain hardening). Cold-formed steel, on the other hand, has no actual yield plateau and a more rounded stress-strain curve. The process of cold-working results in a material behaviour with an increased yield and ultimate strength but a reduction in the ductility. Typical stress-strain curves are shown in Figure 2-6.

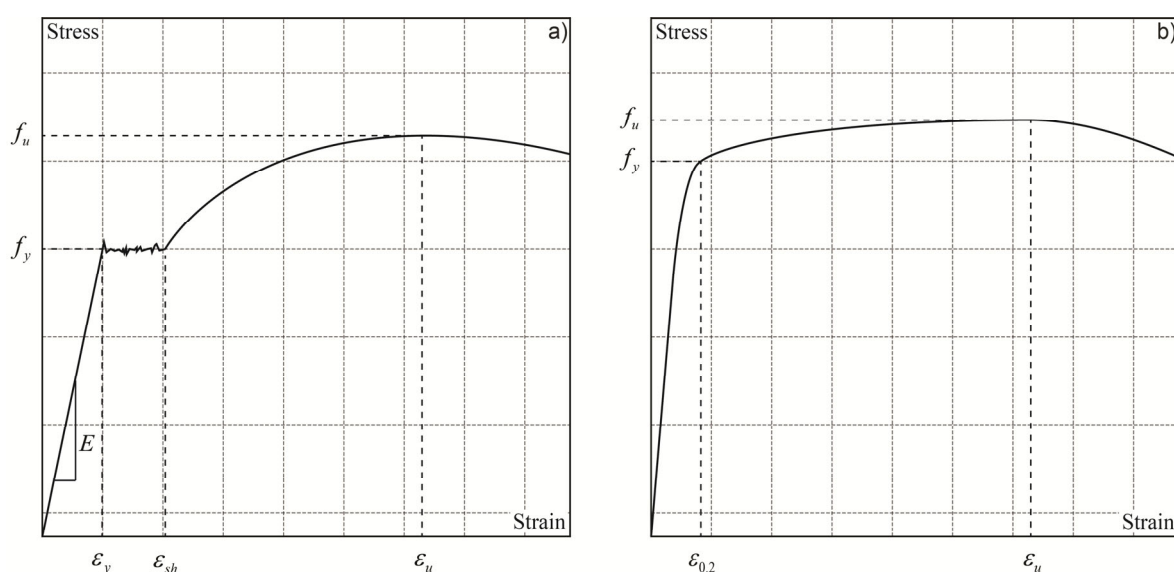


Figure 2-6: Typical stress-strain curves for a) hot-rolled steel; b) cold-formed steel

Due to a high non-linear behaviour of both, hot-rolled and cold-formed steel, internal force and moment are capable of redistribution. This is of great importance mainly in bending dominated structures, composed of compact cross-sections to ensure plastic hinge development and a sufficient rotation capacity.

2.1.6 Geometric member imperfections

One crucial part of design in specifications for steel structures is related to instability topics and the treatment and judgement of imperfections. Those appear in general as

local, global or as an inherent initial condition of residual stresses. The choice of the initial imperfection magnitude depends on different factors. Those can be summarized as follows:

- i. The type of analysis according to the considered cross-section failure linked to the cross-section class.
- ii. The type of imperfection considered for further calculations i.e. geometric imperfections only (tolerances and residual stresses) or equivalent, buckling curve dependent imperfections, specifying a bow imperfection amplitude (case of flexural buckling) to account for tolerances as well as residual stresses.
- iii. The benchmark resistance is separated through the concept of cross-section classification into an elastic or plastic calculation approach. This confinement specifies the subsequent choice of an imperfection amplitude, dependent on a cross-section-dependent imperfection factor α . This process corresponds to the global buckling concept of EN 1993-1-1:2010 [61], EN 1993-1-1:2020 [48] and prEN 1993-1-14 [72].

2.1.6.1 Local imperfections

According to EN 1993-1-5, Annex C [50] the magnitude of local imperfections for the analysis of plate buckling may be assumed with a value of $B/200$, where B is the smaller of the two corresponding dimensions of a rectangular hollow section.

$$\frac{B}{200} = \min\left(\frac{H}{200}, \frac{W}{200}\right) \quad (2-11)$$

Nevertheless, referring to the findings of Rusch and Lindner [73], as well as Toffolon and Taras [74] a determined amplitude of $e_0 = B/400$ was found to be more suitable to represent the design curve for local buckling (“Winter curve”) [50] based on results from non-linear numerical calculations.

In the following, several GMNIA calculations were performed for a centrally loaded cold-formed and hot-rolled SHS200 profile with a varying thickness and a constant length of 800 mm to ensure local buckling exclusively. LBA simulations were performed

to calculate the slenderness and the eigenshape for subsequent GMNIA simulations. Calculations were aborted as soon as the maximum of the cross-section was reached. The material model was chosen as bi-linear with a slight strain hardening slope of $E_{sh} = E/1000$. Three local imperfection amplitudes were chosen $B/200$, $B/300$ and $B/400$ for several GMNIA calculations summarized in Figure 2-7 for hot-rolled [4], as well as cold-formed [5] SHS200 profiles. The shown simulations were also published in [75], [76].

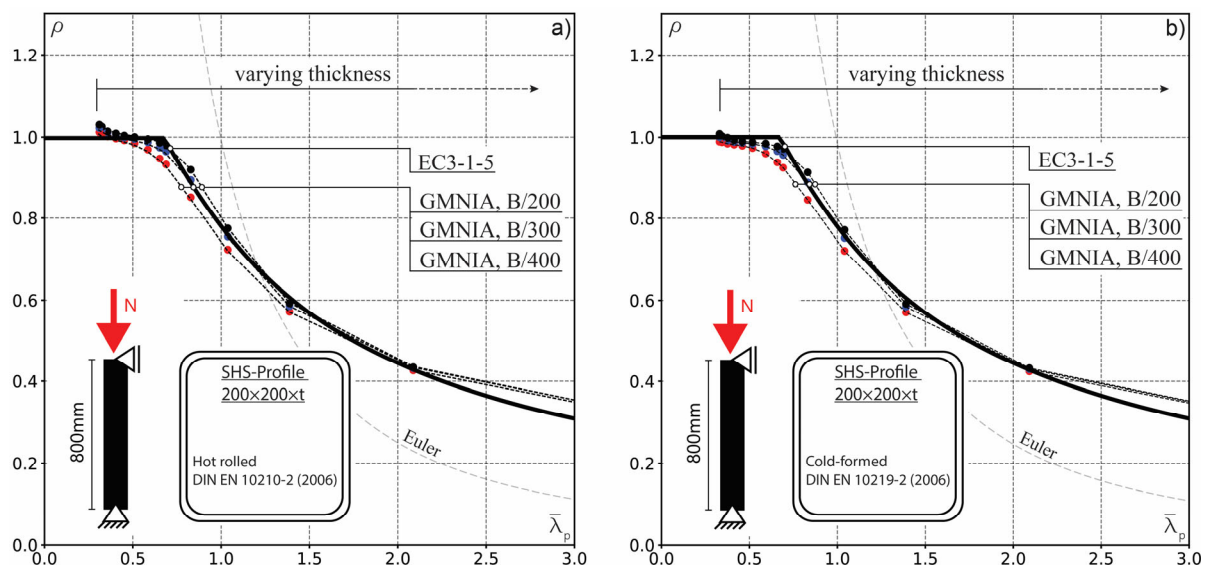


Figure 2-7: Comparison of GMNIA simulations with the resistance curve from EN 1993-1-5 [50] for an SHS200 profile; a) cold-formed; b) hot-rolled; adopted from [75]

Calculations with the local imperfection amplitude of $e_0 = B/200$ tend to lie below the Winter curve throughout the whole slenderness range. Only in the stocky region strain hardening effects start to impact the cross-section resistance. Though, results closer to the local buckling curve are obtained with imperfection amplitudes of $e_0 = B/400$, showing a better agreement and confirm the observations by [73] and [74].

2.1.6.2 Global member imperfections

According to EN 1993-1-1:2010 [61] and prEN1993-1-1:2020 [48] the equivalent bow imperfection amplitude e_0 for flexural buckling can be determined using two approaches, considering either a tabulated length-proportional value or a slenderness-based formulation based on the elastic critical buckling load from analytical considerations or numerical analysis. In both cases, those values represent equivalent imperfections based on the determination from a centrally loaded strut with an assumed initial

bow imperfection e_0 of a half sine wave. This bow imperfection is determined by introducing a moment M , calculated by second-order theory using an appropriate interaction formula; EN 1993-1-1: 2010, section 6.2.9.1, contains therefore various interaction formulae for class 1 and 2 cross-sections. This consideration leads to the general representation within the following Equation (2-12):

$$e_0 = \frac{\psi \cdot (1 - \chi \cdot \bar{\lambda}^2)}{\chi} \cdot \frac{M_{Rk}}{N_{Rk}} \quad (2-12)$$

where:

$$\bar{\lambda} = \sqrt{\frac{N_{pl}}{N_{cr}}} \quad \text{is the relative member slenderness}$$

χ is the reduction factor for flexural buckling

ψ is the interaction factor for combined bending and axial force, e.g. EN 1993-1-1:2012, Sec. 6.2.9.1 or EN 1993-1-1:2020, Sec. 8.2.9.1

M_{Rk} is the characteristic moment resistance of the critical cross-section

N_{Rk} is the characteristic axial resistance of the cross-section

The equivalent imperfection representation is normalized by the member length L in terms of a non-dimensional representation; see Equation (2-12).

$$j = \frac{e_{0,d}}{L} \quad (2-13)$$

Equation (2-12), combined with Equation (2-13), was evaluated for different interaction approaches and profiles and classified within fixed, non-dimensional limits depending on the buckling curves (a_0, a, b, c, d) and the type of cross-section verification i.e. elastic or plastic cross-section verification. These values were implemented within EN 1993-1-1:2010, Table 5.1 [61] and Table 2-5 of this work.

Table 2-5: Values of the initial imperfection amplitude $e_{0,d}/L$ for members according to EN 1993-1-1:2010

Buckling Curve	Elastic cross-section verification	Plastic cross-section verification
a_0	1/350	1/300
a	1/300	1/250
b	1/250	1/200
c	1/200	1/150
d	1/150	1/100

Since the values in Table 2-5 were exclusively derived on the basis of buckling curves used for the equivalent member method, meaning that the members are loaded by axial forces only without the combined influence of external bending moments M_y or M_z . However, as shown in [77] and [78] a combination can often lead to unfavorable values of initial equivalent imperfections. As a results of these and further investigations in [79], [80] a new formulation was developed and is introduced within the new code generation in the published version of EN 1993-1-1:2020 [48], where Table 2-5 in combination with Equation (2-13) will be replaced by Equation (2-14) in connection with Table 2-6.

$$j = \frac{e_{0,d}}{L} = \frac{\alpha \cdot \beta}{\varepsilon} \quad (2-14)$$

where:

α is the imperfection factor dependent on the flexural buckling curve

ε is the material parameter considering the steel grade

β is the reference bow imperfection

L is the member length

Table 2-6: Reference relative bow imperfection β according to EN 1993-1-1:2020 [48]

Buckling about axis	Elastic cross-section verification	Plastic cross-section verification
$y-y$	1/110	1/75
$z-z$	1/200	1/68

An additional, modified length affine formulation is implemented in the current version of EN1993-1-14: 2020 [72]:

$$e_{0,d} = \frac{\alpha \cdot L}{150} \geq \frac{L}{1000} \quad (2-15)$$

It is based on the basic formulation from Equation (2-12) with the difference that the required equivalent bow imperfection is no longer a function of ε . The influence of material yielding was captured directly in the analysis during the derivation of this expression [81]. The factor β from Equation (2-14) was additionally calibrated to a constant value of $1/150$ from 646 beam FE simulations. Note that the use of this imperfection formulation requires a modified Young's modulus of $E = 200000 \text{ N/mm}^2$. For detailed information on the derivation of Equation (2-15) the reader is referred to the work of Walport [81].

The back-calculation of slenderness-based equivalent bow imperfections, in both EN 1993-1-1:2012 and prEN1993-1-1:2020, is provided by Equation (2-16).

$$e_0 = \alpha \cdot (\bar{\lambda} - 0.2) \frac{M_{Rk}}{N_{Rk}} \quad (2-16)$$

Based on the calculations from [75], [82] a length proportional approach according to EN 1993-1-1:2010 [61] is sufficient and safe-sided when using the elastic design approach for the evaluation of imperfection amplitudes. The same can be stated for the new formulation of the imperfection amplitude (see Equation (2-14)) provided in prEN1993-1-1:2020. It should be noted that β , the reference bow imperfection (see Table 2-6), is not only dependent on the design approach (i.e. elastic or plastic cross-section verification) but also the buckling axis “y-y” or “z-z”. On the other hand, the modified

imperfection amplitude formulation from prEN 1993-1-14:2020 tend to lead to results that are rather optimistic compared to the European buckling curves for flexural buckling, although the Young's modulus was modified ($E = 200000 \text{ N/mm}^2$) throughout the FE simulations.

When using the slenderness affine imperfection amplitudes according to EN 1993-1-1:2010 and prEN 1993-1-1:2020, it is recommended to use the plastic resistance. This approach requires that the magnitude of the relative slenderness is determined beforehand. Additionally, the calculating of an imperfection amplitude for buckling around “y-y” or “z-z” axis must consider the axis-related section modulus $W_{pl,y}$ or $W_{pl,z}$.

2.2 Categorization of Analysis Methods

Table 2-7: Methods of analysis for steel structures

Analysis Type	Geometric Behaviour	Imperfections	Material Behaviour
Linear Analysis (LBA)	linear	No	linear
Linear Buckling Analysis (LBA)	linear	No	linear
Materially non-linear Analysis (MNA)	linear	No	non-linear
Geometrically non-linear Analysis (GNA)	non-linear	No	linear
Geometrically Materially non-linear Analysis (GMNA)	non-linear	No	non-linear
Geometrically non-linear Analysis with Imperfections (GNIA)	non-linear	Yes	linear
Geometrically and Materially non-linear Analysis with Imperfections (GMNIA)	non-linear	Yes	non-linear

As described in Section 2.1.5 and 2.1.6, the structural response of steel structures failing by local, global or interactive buckling is influenced mainly by two non-linear effects, driven by the material behaviour and geometric nonlinearity due to large strains and displacements. Particularly when employing numerical methods for the design of steel structures, it is important to make appropriate distinctions between the employed analysis methods, in order to have clarity on whether the above effects are taken into account, and to what extent. Accordingly, with the introduction of the Eurocodes, a com-

mon terminology has emerged for the distinction of these methods. The following summarizes presents the available methods of analysis according to EN 1993-1-6 [83] and Vayas et al. [84], which are subsequently described in a concise manner.

2.2.1 Linear analysis

The linear analysis (LA) corresponds to the term of first-order elastic analysis and is potentially the simplest type of structural analysis. The assumed material behaviour is linear elastic, hence no actual information on deformation, structural stability or plastic redistribution is obtained. Since displacement and strains are assumed to be small, the analysis is performed based on the initial, undeformed geometry of the structure. In practical applications, linear analysis is explicitly use for the verification of serviceability limit states, where small deformation are expected and reasonable. Effects of stability and plasticity need to be covered by further design checks.

2.2.2 Linear buckling analysis (LBA)

Under the assumption of small displacements, elastic material behaviour and no imperfection, this method provides buckling eigenvalues, buckling mode shapes and buckling loads. With a linear buckling analysis, the influence of geometric effects on the structural behaviour may be investigated and the provided, deformed structural shapes can be used as geometrical imperfections. The buckling load for the i^{th} buckling mode is determined from:

$$F_{cr,i} = \alpha_{cr,i} \cdot F_{Ed} \quad (2-17)$$

Buckling eigenvalues are found such that $\alpha_{cr,i} < \alpha_{cr,i+1}$. The buckling length coefficient of a column for the relevant buckling mode is calculated with:

$$\beta = \frac{1}{2} \cdot \sqrt{\frac{\pi^2 EI}{(\beta L)^2}} \quad (2-18)$$

by combining the formula before and the Euler's Formula to:

$$N_{crit,j} = \frac{\pi^2 EI}{L_{cr}^2} = \frac{\pi^2 EI}{(\beta L)^2} \quad (2-19)$$

Where $\alpha_{cr,i}$ is the eigenvalue of the relevant buckling mode, L is the length of the system and L_{cr} is the buckling length.

2.2.3 Materially non-linear analysis (MNA)

This analysis approach is known as 1st order plastic analysis. If geometric effects and imperfections are ignored, the method can be used for design. The analysis is performed on the basis of the initial, undeformed geometry but the effects of non-elastic irreversible strains must be taken into account, since displacements are small and strains large. The analysis procedure is differentiated in rigid plastic analysis, plastic hinge analysis and plastic zone analysis. The collapse load is found directly by applying the theory of plasticity with static and kinematic theorem.

2.2.4 Geometrically non-linear elastic analysis (GNA)

The GNA is used to investigate the stability of frame structures up to the buckling load under moderate displacement and limited rotation for elastic material behaviour. Also known as elastic analysis according to second-order theory when applied to frame structures with small displacements, the equilibrium is defined in the deformed state. The kinetic relation for the curvature is then typically linear or non-linear – in the latter case, the literature also speaks of 3rd order or large-displacement theory, which may be appropriate to investigate the structural response deep into the post-buckling region of plated or shell structures.

2.2.5 Geometrically and materially non-linear analysis (GMNA)

The GNMA is a combination of the MNA and GNA, also called 2nd order plastic analysis when linear, small-displacement kinematics are considered. It might be rigid plastic, plastic hinge or plastic zone analysis for framed structures. Both, geometric and material

non-linear behaviour are considered. The method provides directly ultimate limit loads for a structure or structural elements.

2.2.6 Geometrically non-linear elastic analysis with imperfections (GNIA)

The GNIA is equivalent to a GNA method that additionally takes into account initial imperfections. Usually, the analysis is made with equivalent geometrical imperfections in which the influence of structural imperfections is accounted for in the geometrical imperfections. The shape and value of imperfections are provided by the Codes and may follow the fundamental buckling mode with an appropriate scale. Since imperfections and geometric effects are already implemented, design is basically made on the cross-section level.

2.2.7 Geometrically and materially non-linear analysis with imperfections (GMNIA)

This method is appropriate for analysis and design, helping to find the true limit load. Furthermore, all relevant non-linear effects and imperfections are considered. This analysis approach will be used extensively throughout the remainder of the thesis and its application will thus be explained in more detail in appropriate chapters.

2.3 Direct Strength Method (DSM)

In the following sections, various methods of analysis and design of instability-governed slender steel structures are presented, which go beyond the previously described, codified design methods and account for instabilities by making use of more advanced concepts, be it in terms of analysis using FEM for the determination of buckling modes or slenderness values, or more complex non-linear material models.

The first such method to be described is the Direct Strength Method (DSM). The development of the DSM is based on the research presented in [85]–[87] by B.W. Schafer's group at John Hopkins University. The method focuses mainly on slender open sections and members, i.e. channel sections and Z-shaped sections made of cold-formed steel. It

departs from the traditional assumption, as used e.g. throughout the Eurocodes, that the classification of a section should be performed on the basis of individual plate slenderness values and does not rely on the effective width method; it rather provides a "direct" calculation of strength as function of overall, cross-section level slenderness values. The DSM defines strength curves (also referred to as base curves) for the total load-bearing capacity of the profile for global (G) (flexural or lateral torsional buckling), distortional (D) and local (L) buckling as follows, with the various coefficients χ_i representing buckling knockdown factors, with respect to first-yield resistances, for global (G), distortional (D) and local (L) buckling.

$$\chi_G = 0.658 \bar{\lambda}_G^{-2} \text{ for } \bar{\lambda}_G \leq 1.5; \quad \chi_G = \frac{0.877}{\bar{\lambda}_G^2} \text{ for } \bar{\lambda}_G > 1.5 \quad (2-20)$$

$$\chi_D = 1 \text{ for } \bar{\lambda}_D \leq 0.561; \quad \chi_D = \left(1 - \frac{0.25}{\bar{\lambda}_D^{1.2}}\right) \cdot \frac{1}{\bar{\lambda}_D^{1.2}} \text{ for } \bar{\lambda}_D > 0.561 \quad (2-21)$$

$$\chi_L = 1 \text{ for } \bar{\lambda}_L \leq 0.776; \quad \chi_L = \left(1 - \frac{0.15}{\bar{\lambda}_L^{0.8}}\right) \cdot \frac{1}{\bar{\lambda}_L^{0.8}} \text{ for } \bar{\lambda}_L > 0.776 \quad (2-22)$$

The formulations from Equation (2-20)-(2-22) thus require the calculation of three slenderness values according to the above strength curves:

- i. Local buckling (L): significant distortion of the cross-section, including only rotations without translation at the corners of the cross-section/member.
- ii. Distortional buckling (D): significant of the cross-section, including rotation and translation.
- iii. Global buckling (G): significant translation (flexure) and/or rotation (torsion) of the entire cross-section. Modes for columns: flexural, torsional, and torsional-flexural; for beams: lateral-torsional.

The usual way to do this in the context of DSM is to use computational tools such as the CUFSM (Constrained and Unconstrained Finite Strip Method) [88], [89] or GBTUL (Generalised Beam Theory of the University of Lisbon) [90] to calculate the elastic critical buckling stresses for these modes, accounting for the stiffness distribution within the

section. Such tools allow for an explicit decomposition of the half-wavelength dependent eigenmodes from LBA simulations, resulting in so-called "signature curves" or "master curves", as follows:

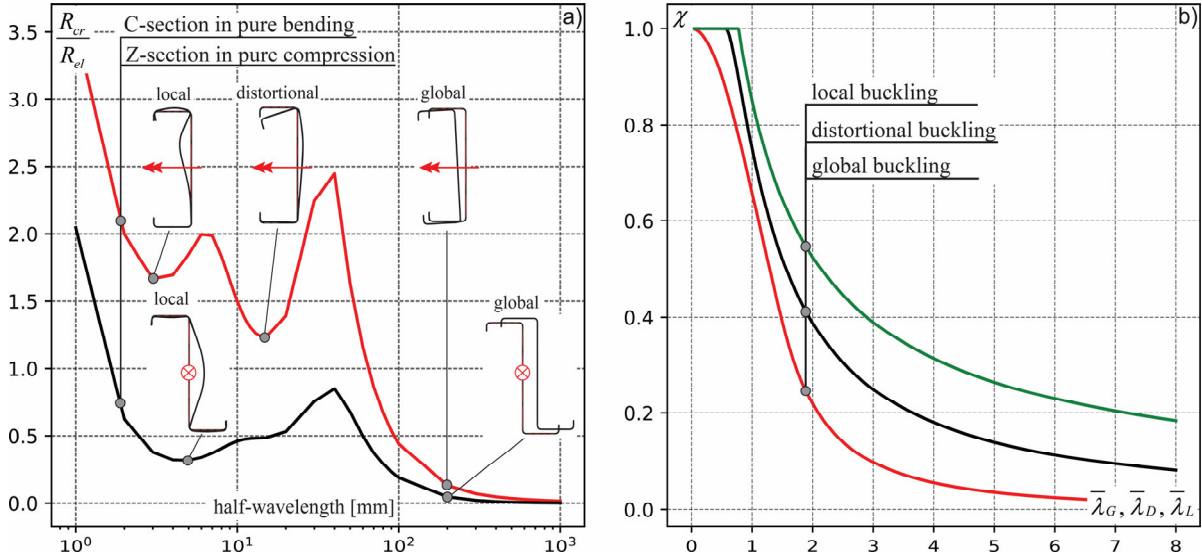


Figure 2-8: a) signature curve of a C-shaped and Z-shaped cross-section in pure bending and pure compression, respectively; b) strength curves for global, distortional and local buckling

Figure 2-8 a) shows numerical results obtained with the CUFSM software. The results of these calculations are the signature curves for individual load cases. Here, pure bending is applied to a C-shaped cross-section and pure compression to a Z-shaped cross-section. The x-axis represents each half-wavelength of the corresponding numerical model. The y-axis represents the critical buckling load normalized to the elastic section resistance, giving a load factor. Each point on the signature curve defines a slenderness associated with a corresponding buckling failure mode at the low points of the curve. The slenderness is then associated with the strength curves from Figure 2-8 b) and Equations (2-20) to (2-22). The relative slenderness is defined as:

$$\bar{\lambda}_{dsm,N} = \sqrt{\frac{A \cdot f_y}{N_{cr}}} \quad (2-23)$$

$$\bar{\lambda}_{dsm,M_y} = \sqrt{\frac{W_{el,y} \cdot f_y}{M_{cr,y}}} \quad (2-24)$$

The DSM strength curves are generally unable to distinguish between cross-sections or support conditions and therefore provide three individual curves, see Figure 2-9. These curves are based on experimental studies of column tests with cold-formed steel, including failure in local, distortional and global flexural or flexural-torsional buckling [91], [92], [85]. Figure 2-9 a) compares 267 column tests with the DSM strength curves for local and distortional buckling. Figure 2-9 b) additionally shows the experimental results for beams from 569 test results from [93], [94], [85], [95].

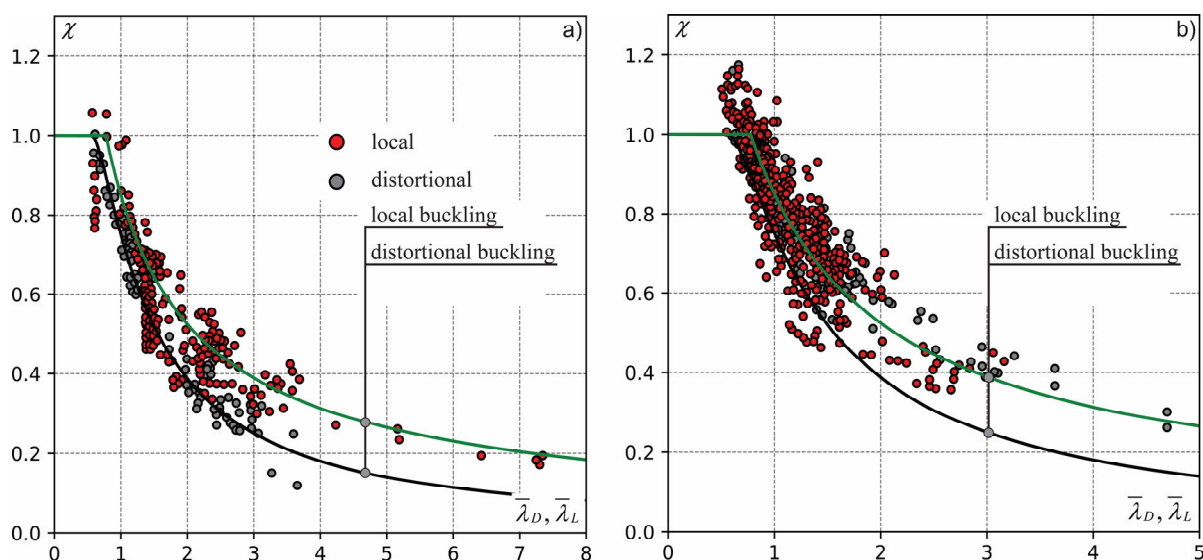


Figure 2-9: a) Comparison of DSM strength curves with test results for columns; b) comparison of DSM strength curves for beams

2.4 Continuous Strength Method (CSM)

2.4.1 Introduction and background information

The development of the continuous strength method (CSM) was motivated by several shortcomings associated to traditional methods used in hot-rolled steel design when applied to structural stainless steel. These are in general the use of a simplified material model i.e. an elastic, perfectly plastic material behaviour coupled to the concept of cross-section classification, leading to oversimplifications and inaccuracies in the prediction of the cross-section capacity. While these simplifications lead to tolerable over conservatism in the design of hot-rolled carbon steel [61], their effect is less appropriate in the context of structural stainless steel [96]. This is mainly explained by the differences

within their material models. On one hand, hot-rolled, normal-strength (up to S460) carbon steel has a linear elastic behaviour until the point of reaching the yield strength f_y , followed by a distinct yielding plateau and a strain hardening range until reaching the maximum strength f_u . Stainless steel, on the other hand, features a more rounded stress-strain curve without a pronounced yielding point, as well as a higher strain hardening range and ultimate – to – yield strength ratio ($R_m/R_{p0,2}$). This makes the concept of cross-section classification less suited for stainless steel profiles, leading to overly conservative results, especially in the range of stocky sections [97]. This well-known fact was confirmed during the extensive experimental studies carried out during the development of the CSM method. Those results are presented within the following Figure 2-10 (initially published in [98]), drawing the attention on the mentioned class-section inherent problematic.

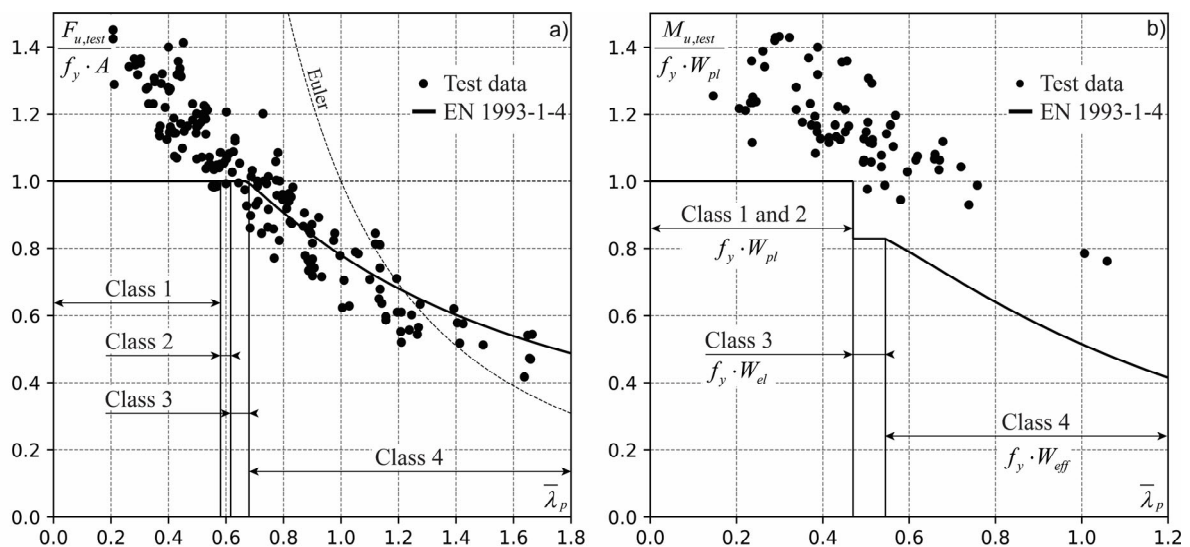


Figure 2-10: a) Comparison of 81 stub column test results with EN 1993-1-4; b) Comparison of 65 beam test results with EN 1993-1-4; diagrams partially adopted from [98]

Therefore, the goal of the CSM method is to overcome the mentioned shortcoming by using two fundamental features:

- i. A more realistic material models that takes into account strain hardening.
- ii. A so called “base curve”, which eliminates the concept of cross-section classification through a continuous local slenderness representation linked to the profile dependent deformation capacity.

It was initially introduced by Gardner in [96] and is based on several preliminary investigations conducted at the Imperial College London [99]–[105], as well as further developments over the years [98], [106]–[112] resulting in a mature design method. It has been successfully implemented in the AICS Design Guide 27 for Structural Stainless Steel [113] and in the SCI design manual for structural stainless steel [114]. The latest, topic related publications by Fieber [67] and Walport [81] deal with the development of a framework, where geometrically and materially non-linear analysis with imperfection (GMNIA) are performed using beam finite elements and CSM derived strain limits to mimic the local buckling effects.

2.4.2 Derivation of the CSM base curve

At the core of the CSM method lies the so-called “base curve”. It is defined as the cross-section deformation (or normalized strain) capacity $\varepsilon_{csm}/\varepsilon_y$ as a function the non-dimensional relative local slenderness λ_p . The peak compressive strain ε_{csm} is the notional strain at the point of reaching the peak load prior to failure. The yield strain ε_y is defined as the yield stress $f_y = \sigma_{0.2\%}$ divided by the Young’s modulus E . The base curve is a purely experimental based and calibrated curve, taking implicitly into account geometric imperfections as well as residual stresses (a similarity could be drawn to the flexural buckling curves from EN 1993-1-1 or the Winter curve from EN 1993-1-5 for local buckling). The experimental evaluation in the case of stocky stub column tests ($\lambda_p \leq 0.68$) was done according to Equation (2-25) and Figure 2-11 a) top. The measured end deformation δ_u was divided by the initial length L of the specimen and then normalized by its yield strain ε_y .

$$\frac{\varepsilon_{csm}}{\varepsilon_y} = \frac{\varepsilon_u}{\varepsilon_y} = \frac{\delta_u/L}{\varepsilon_y} \quad \text{for} \quad F_{u,test} \geq f_y \cdot A \quad \text{and} \quad \bar{\lambda}_p \leq 0.68 \quad (2-25)$$

Equation (2-26) and Figure 2-11 a) bottom explain the case of bending, again for stocky cross-sections and the local slenderness limit of $\lambda_p \leq 0.68$. The measured curvature κ_u , at the point of reaching $M_{u,test}$ was normalized by the elastic curvature defined as $\kappa_y = M_{el}/EI$.

$$\frac{\varepsilon_{csm}}{\varepsilon_y} = \frac{\varepsilon_u}{\varepsilon_y} = \frac{\kappa_u}{\kappa_y} \quad \text{for } M_{u,test} \geq f_y \cdot W_{el} \quad \text{and} \quad \bar{\lambda}_p \leq 0.68 \quad (2-26)$$

Slender sections that fail before reaching their yield strength f_y need to be considered in a modified manner within the calibration of the base curve, deviating from Equation (2-25) and (2-26). It was found [115], [109] that it is more suited to use Equation (2-27) and (2-28), by taking into account the observed cross-section capacity for compression $F_{u,test} = f_{u,test} \cdot A$ and bending $M_{u,test} = f_{u,test} \cdot W_{el}$, respectively. In summary, the problem can be reduced to two effects linked to slender cross-section, i.e. the early loss of stiffness and therefore bigger deformations due to elastic buckling [67].

$$\frac{\varepsilon_{csm}}{\varepsilon_y} = \frac{\varepsilon_{u,e}}{\varepsilon_y} = \frac{F_{u,test}}{f_y \cdot A} \quad \text{for } F_{u,test} < f_y \cdot A \quad (2-27)$$

$$\frac{\varepsilon_{csm}}{\varepsilon_y} = \frac{\varepsilon_{u,e}}{\varepsilon_y} = \frac{M_{u,test}}{f_y \cdot W_{el}} \quad \text{for } M_{u,test} < f_y \cdot W_{el} \quad (2-28)$$

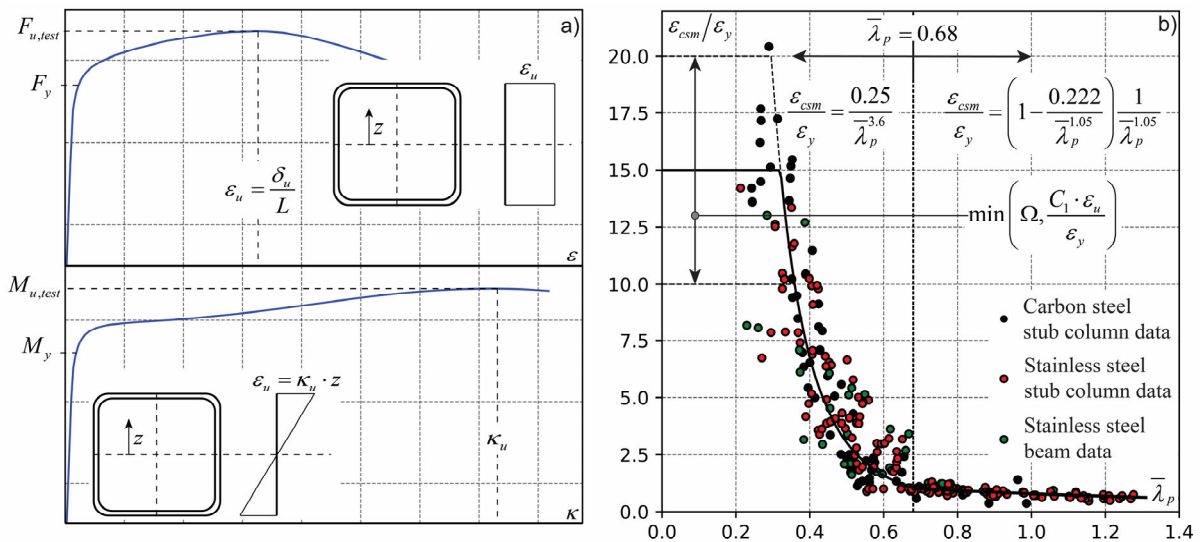


Figure 2-11: Background information on the derivation of the base curve a) evaluation of strains from experimental investigations; b) calibration of the CSM base curve with a continuous relation between the cross-section dependent local slenderness and the normalized deformation capacity based on experimental results from ([101], [116]–[128]).

The calibrated CSM base curve is divided into two main parts, i.e. separating the stocky ($\lambda_p \leq 0.68$) from the slender cross-sections ($\lambda_p > 0.68$), see Figure 2-11 b). The strain ratio $\varepsilon_{csm}/\varepsilon_y$ for stocky cross-section is described by Equation (2-29), while for slender cross-sections, prone to local buckling instability, the strain ratio is given by Equation (2-30). It should be noted at this point, that one single base curve was derived for different stainless steel grades (and later: other steel grades) and load cases, i.e. compression and bending.

$$\frac{\varepsilon_{csm}}{\varepsilon_y} = \frac{0.25}{\bar{\lambda}_p^{3.6}} \quad \text{but} \leq \min\left(\Omega, \frac{C_1 \cdot \varepsilon_u}{\varepsilon_y}\right) \quad \text{for} \quad \bar{\lambda}_p \leq 0.68 \quad (2-29)$$

$$\frac{\varepsilon_{csm}}{\varepsilon_y} = \left(1 - \frac{0.222}{\bar{\lambda}_p^{1.05}}\right) \frac{1}{\bar{\lambda}_p^{1.05}} \quad \text{for} \quad \bar{\lambda}_p > 0.68 \quad (2-30)$$

where:

$$\bar{\lambda}_p = \sqrt{\frac{f_y}{\sigma_{cr}}}$$

is the relative cross-section dependent local slenderness ranging between the CSM boundaries of $0 \leq \bar{\lambda}_p \leq 1.4$.

Ω is the first upper limit for the cross-section deformation capacity. It is a project specific design parameter that defines the maximum level of acceptable plastic deformation within a cross-section. A default value of $\Omega = 15$ is recommended to prevent excessive deformations and fulfil the code based ductility requirements of EN 1993-1-1 [48].

$$\frac{C_1 \cdot \varepsilon_u}{\varepsilon_y}$$

is the second upper limit for the cross-section deformation capacity. It is used to prevent over-predictions of the material strength when using the simplified resistance functions [129], [130] for the quad-linear material model [6].

2.4.3 Non-linear material models

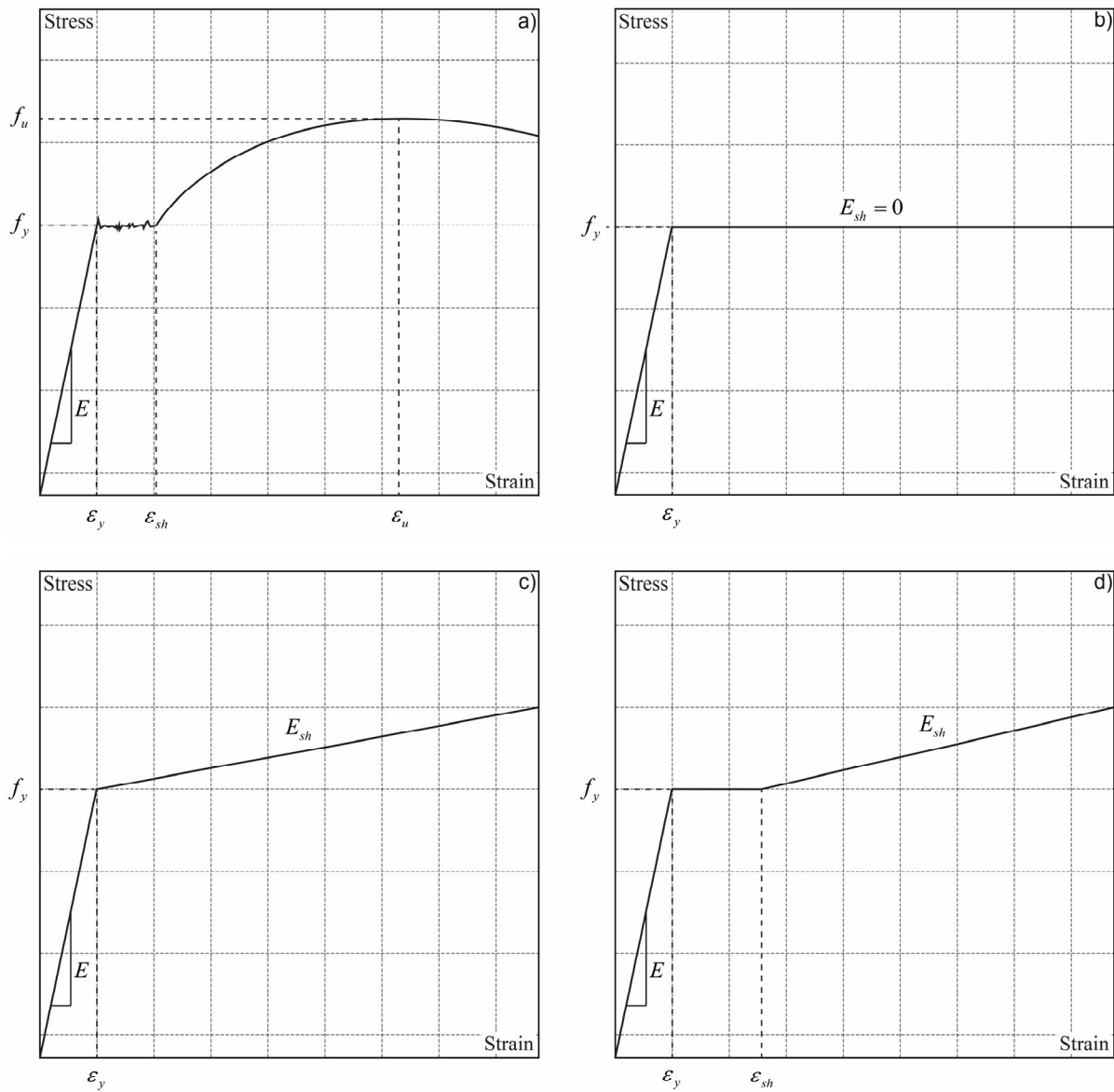


Figure 2-12: a) typical engineering stress-strain curve for hot-rolled steel; b) elastic, perfectly plastic model; c) elastic, linear hardening model; d) tri-linear model

In addition to the base curves, which define the limiting (compressive) strain as a function of a cross-sectional slenderness, the CSM relies on notional stress-strain curves to calculate the internal stress distribution at the state of limit straining, and from this calculate the resulting internal forces at failure at this stage. The following non-linear material models for carbon steel, stainless or cold-formed steel were proposed by Yun and Gardner [6], [7] and are briefly described within this section. Their implementation is motivated and linked to the development of the CSM approach, yet - apart from the CSM

framework itself - the material models presented can be of great interest in the context of non-linear FE modelling approaches such as GMNIA (geometrically materially non-linear analysis with imperfections, as these models already demonstrated their suitability for design-oriented simulations during the development of the CSM. In the following, material models for hot-rolled carbon steel and cold-formed steel are presented, which have also been incorporated into own investigations in this work.

2.4.3.1 Hot-rolled carbon steel

A typical stress-strain curve for hot-rolled carbon steel is approximately described by three regions, exemplary shown in Figure 2-12. The elastic range, where the slope is linear and defined by the Young's modulus (e.g. $E = 210000\text{N/mm}^2$ according to EN 1993-1-1 [48]), limited by the yield stress f_y and the strain ε_y . The elastic range is followed by a region of plastic yielding (constant stress) until the point of reaching the strain hardening strain ε_{sh} , where strain hardening is initiated. From this point, the stress increases non-linear at a reducing rate up to the ultimate tensile stress f_u and the corresponding tensile strain ε_u .

Figure 2-12 shows additional simplified models that have been proposed to represent the material behaviour of hot-rolled steel. Those are approximated by sectional linear regions and grouped as follows:

- i. Elastic, perfectly plastic, see Figure 2-12 b). This model forms the basis of the current design methods in EN 1993-1-1 [48].
- ii. Elastic, linear hardening model, see Figure 2-12 c). Offering the simplest consideration of strain hardening, where E_{sh} is the strain hardening modulus. It is included in EN 1993-1-5 [131] and formed the basis for the derivation of the CSM for different structural metallic elements (structural carbon steel [96], [108], [116], aluminium [132], [133], stainless-steel [98], [100]).
- iii. Tri-linear model, considering the yield plateau and strain hardening, see Figure 2-12 d).

The calibrated analytical formulations for hot-rolled carbon steel are based on over 500 experimental stress-strain curves from 34 individual sources collected by Yun and Gardner (s Table 1 in [6]) and go beyond the limited and partially complex formulations of proposed stress-strain curves [134]–[136] (find also additional information in [137], [138]). Figure 2-13 shows the two derived material models, i.e. a quad-linear material model linked to the capacity formulations of the CSM and a bilinear plus non-linear hardening material model for scientific use.

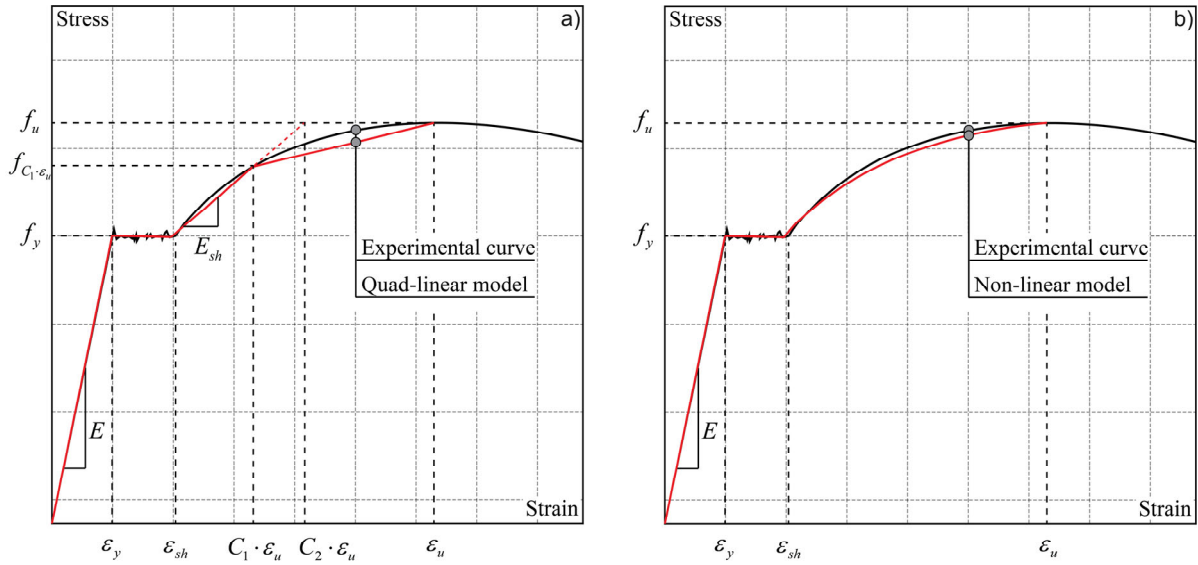


Figure 2-13: a) Proposed quad-linear material model; b) proposed bilinear plus non-linear hardening model, application partially adopted from [6]

The stress-strain curve of the quad-linear material model is characterized by three commonly available parameters (mostly available to engineers in material standards), such as the modulus of elasticity E , the yield stress f_y and the ultimate stress f_u .

$$f_{(\varepsilon)} = \begin{cases} E \cdot \varepsilon & \text{for } \varepsilon \leq \varepsilon_y \\ f_y & \text{for } \varepsilon_y < \varepsilon \leq \varepsilon_{sh} \\ f_y + E_{sh}(\varepsilon - \varepsilon_{sh}) & \text{for } \varepsilon_{sh} < \varepsilon \leq C_1 \cdot \varepsilon_u \\ f_{C_1 \cdot \varepsilon_u} + \frac{f_u - f_{C_1 \cdot \varepsilon_u}}{\varepsilon_u - C_1 \cdot \varepsilon_u}(\varepsilon - C_1 \cdot \varepsilon_u) & \text{for } C_1 \cdot \varepsilon_u < \varepsilon \leq \varepsilon_u \end{cases} \quad (2-31)$$

where:

- E_{sh} is the strain hardening modulus defined by Equation (2-32)
- ε_{sh} is the strain hardening strain defined by Equation (2-33). The boundaries $0.0015 \leq \varepsilon_{sh} \leq 0.03$ are valid for hot-rolled steel
- ε_u is the ultimate strain defined by Equation (2-34)
- $f_{C_1 \cdot \varepsilon_u}$ is the stress corresponding to the intersection of the third and fourth segments, see Figure 2-13 a)
- C_1, C_2 are the experimentally calibrated parameters defined through ε_{sh} and ε_u , see Equation (2-35) and (2-36)

$$E_{sh} = \frac{f_u - f_y}{C_2 \cdot \varepsilon_u - \varepsilon_{sh}} \quad (2-32)$$

$$\varepsilon_{sh} = 0.1 \cdot \frac{f_y}{f_u} - 0.055 \quad \text{but } 0.0015 \leq \varepsilon_{sh} \leq 0.03 \quad (2-33)$$

$$\varepsilon_u = 0.6 \cdot \left(1 - \frac{f_y}{f_u} \right) \quad \text{but } \varepsilon_u \geq 0.06 \quad (2-34)$$

$$C_1 = \frac{\varepsilon_{sh} + 0.25 \cdot (\varepsilon_u - \varepsilon_{sh})}{\varepsilon_u} \quad (2-35)$$

$$C_2 = \frac{\varepsilon_{sh} + 0.4 \cdot (\varepsilon_u - \varepsilon_{sh})}{\varepsilon_u} \quad (2-36)$$

The bilinear plus non-linear hardening material model is defined by Equation (2-37). It captures the non-linear rounded strain hardening response and therefore suitable for advanced numerical simulations.

$$f_{(\varepsilon)} = \begin{cases} E \cdot \varepsilon & \text{for } \varepsilon \leq \varepsilon_y \\ f_y & \text{for } \varepsilon_y \leq \varepsilon \leq \varepsilon_{sh} \\ f_y + (f_u - f_y) \cdot \left[\frac{K_1 \cdot \left(\frac{\varepsilon - \varepsilon_{sh}}{\varepsilon_u - \varepsilon_{sh}} \right) + K_2 \cdot \left(\frac{\varepsilon - \varepsilon_{sh}}{\varepsilon_u - \varepsilon_{sh}} \right)}{\left[1 + K_3 \left(\frac{\varepsilon - \varepsilon_{sh}}{\varepsilon_u - \varepsilon_{sh}} \right)^{K_4} \right]^{\frac{1}{K_4}}} \right] & \text{for } \varepsilon_{sh} \leq \varepsilon \leq \varepsilon_u \end{cases} \quad (2-37)$$

where:

K_{1-4} are the calibrated material coefficient based on tensile coupon tests
 $(K_1=0.4, K_2=2, K_3=400, K_4=5)$

2.4.3.2 Cold-formed steel

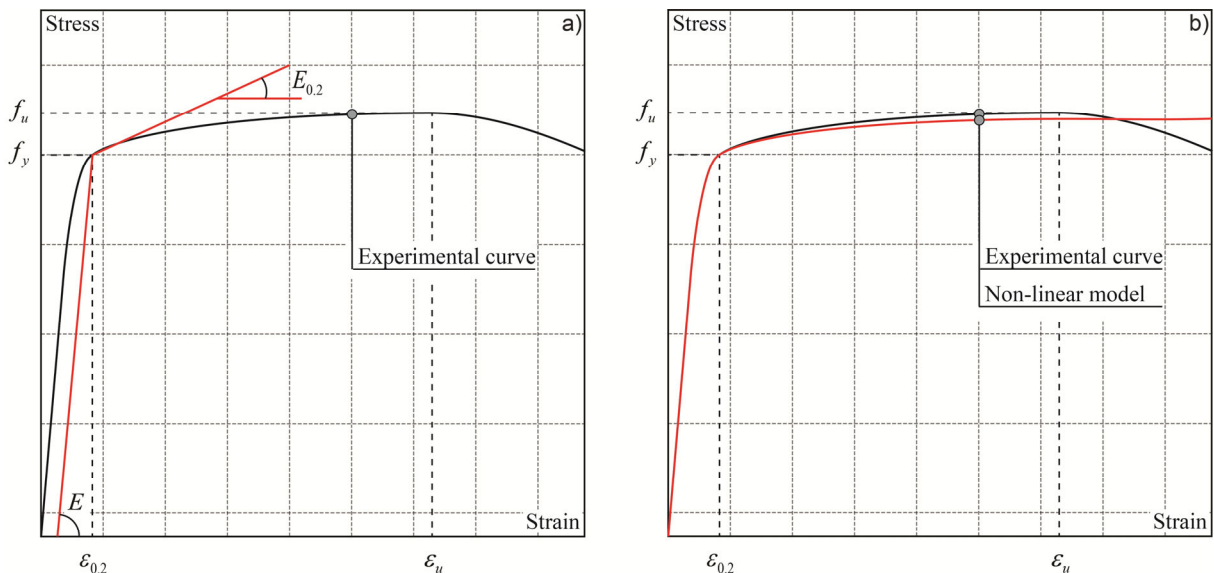


Figure 2-14: Typical stress-strain curve representation of cold-formed steel a) main material model parameters; b) representative comparison between stress-strain curves obtained experimentally and through the proposed two-stage Ramberg-Osgood material model

Cold-formed steel has, compared to hot-rolled steel, a different stress-strain response resulting in a much more rounded curve, with no sharp definition of the yield stress. Further, cold-work results in an increased yield and ultimate strength, yet, a reduced ductility. Due to the varying level of cold-work along the cross-section circumference, i.e. low plastic deformation on the cross-section faces and high plastic deformations in the corners, a non-uniformity of material properties is more common. In general, cold-formed steel, stainless steel or aluminium are often represented by the expression proposed by Ramberg and Osgood [139], which were later modified by Hill, follows by a number of studies on the material modelling of stainless steel ([140]–[142]).

Based on data from 700 experimental stress strain curves collected from literature a two-stage Ramberg and Osgood model was proposed by Yun and Gardner [7], to exploit the non-linear behaviour and strain hardening range for advanced numerical simulations. The proposed material model builds up on investigations on stainless steel by Mirambell and Real [143]. Comparable models for stainless steel were also proposed by Rasmussen [140] and Gardner and Nethercot [101], yet, were found to be partially unsuited for the adoption to the less ductile stress-strain properties of cold-formed steel.

The two-stage Ramberg-Osgood model is summarized in Equation (2-38) below.

$$\varepsilon_{(f)} = \begin{cases} \frac{f}{E} + 0.002 \cdot \left(\frac{f}{f_y} \right)^n & \text{for } f \leq f_y \\ \frac{f - f_y}{E_{0.2}} + \left(\varepsilon_u - \varepsilon_{0.2} - \frac{f_u - f_y}{E_{0.2}} \right) \cdot \left(\frac{f - f_y}{f_u - f_y} \right)^m + \varepsilon_{0.2} & \text{for } f_y \leq f \leq f_u \end{cases} \quad (2-38)$$

where:

n is the first strain hardening exponent defined by Equation (2-39) according to [142].

m is the second strain hardening exponent defined by Equation (2-40) or calculated according to [144]. The latter requires the knowledge of the measured 1% proof stress.

$E_{0.2}$ is the tangent modulus of the stress-strain curve at the yield strength (0.2% proof stress) defined by Equation (2-41).

$$n = \frac{\ln(4)}{\ln(f_y/\sigma_{0.05})} \quad (2-39)$$

$$m = 1 + 3.3 \frac{f_y}{f_u} \quad (2-40)$$

$$E_{0.2} = \frac{E}{1 + 0.002 \cdot n \cdot \frac{E}{f_y}} \quad (2-41)$$

The strain ε_u may be determined from Equation (2-42). The corresponding ultimate tensile strength f_u may be obtained from the expression in Equation (2-43).

$$\varepsilon_u = 0.6 \cdot \left(1 - \frac{f_y}{f_u}\right) \quad (2-42)$$

$$\frac{f_u}{f_y} = 1 + \left(\frac{130}{f_y}\right)^{1.4} \quad (2-43)$$

Further, strength enhancements in corner regions are modelled according to the proposals made by Rossi et al [145]. Those will be not further taken into account in the framework of this thesis.

2.4.4 Determination of the relative local slenderness

The relative slenderness $\bar{\lambda}_p$ is a dimensionless parameter, which can be derived depending on the local cross-section or the global member geometry, always connected to a normalized reduction factor capturing instability phenomena. Yet, different methods exist to calculate the local cross-section dependent slenderness $\bar{\lambda}_p$. Their level of accuracy, taking into account the full cross-section or only separated elements, can thereby differ significantly from each other. The most accurate technique requires the use of numerical methods i.e. finite element models which explicitly represent the whole cross-section geometry to account for interactive effects between connected plate elements. This approach is usually performed by using commercially available finite element software like ABAQUS [146], which in terms is more frequently used within research applications than the civil engineering practice (although, a change is clearly visible for slender structures requiring pronounced knowledge of local instabilities and instability effects). Therefore, free software applications such as the Constrained and Unconstrained Finite Strip Method “CUFSM” ([88], [89]) (provided by the John Hopkins Whiting School of Engineering, originally developed by Ben Shafer in 1997: <https://www.ce.jhu.edu/cufsm/>, see Section 2.3: Direct Strength Method) or the Generalized Beam Theory “GBT” ([90], [147]) (provided by the Instituto Superior Técnico, University of Lisbon, Portugal: <http://www.civil.ist.utl.pt/gbt/>) provide a practical and contemporary way to account for the whole cross-section bifurcation stresses. In addition, analytical formulations were derived by Seif and Schafer [148], [149] to account for full cross-section plate interaction. A modified buckling coefficient k was developed for standard steel profiles subjected to pure compression and pure bending, exclusively. In practice, this restriction is not well suited since combined load cases are the general norm. Therefore, as a progression in the framework of the CSM method Fieber [67], [150], [151] developed practical closed-form expressions. Those enable the prediction of the local buckling stresses for full cross-sections subjected to compression, bending and combined loading. Eurocode 3, Part 1-5 [131] provides the well-known formulations for the critical buckling load of isolated plates supported at both ends and one end, respectively. According to [152] the Eurocode 3 approach is considered to be conservative, leading to higher slenderness values calculated from separated plated elements. The most slender element is considered to be the leading element in the determination of the cross-section capacity.

In the described cases and throughout literature the relative local slenderness is formulated as follows:

$$\bar{\lambda}_p = \sqrt{\frac{f_y}{\sigma_{cr}}} \quad (2-44)$$

2.4.5 Cross-section capacity based on CSM strain limits

2.4.5.1 Compression Resistance

The design value for the cross-section resistance in the case of pure compression is calculated by using Equation (2-45).

$$N_{csm,Rd} = \frac{A \cdot f_{csm}}{\gamma_{M0}} \quad (2-45)$$

where:

- A is the cross section area
- f_{csm} is the CSM limiting stress
- γ_{M0} is the partial safety factor according to EN 1993-1-1

The reached stress f_{csm} is based on the slenderness dependent CSM strain limit $\varepsilon_{csm}/\varepsilon_y$, calculated from Equation (2-29) and (2-30) and implemented into (2-46).

$$f_{csm} = f_y + E_{sh} \cdot \varepsilon_y \cdot \left(\frac{\varepsilon_{csm}}{\varepsilon_y} - 1 \right) \quad (2-46)$$

The beneficial effects of strain hardening (assuming the quad linear material model from Section 2.4.3) for sections with a limiting strain $\varepsilon_{csm} > \varepsilon_{sh}$ are therefore accounted, while exceeding the EN 1993-1-1 design resistance $N_{c,Rd} = A \cdot f_y$ [48].

2.4.5.2 Bending resistance

The bending resistance for slender cross-sections made from carbon steel can be directly computed using Equation (2-47). It is the product of the CSM limiting stress f_{csm} and the elastic section modulus W_{el} .

$$M_{csm,Rd} = \frac{f_{csm} \cdot W_{el}}{\gamma_{M0}} = \frac{\varepsilon_{csm}}{\varepsilon_y} \cdot \frac{f_{csm} \cdot W_{el}}{\gamma_{M0}} \quad \text{for } \varepsilon_{csm} \leq \varepsilon_y \quad (2-47)$$

For CSM strains between ε_y (strain when reaching the yield strength) and ε_{sh} (strain indicating the end of the yield plateau and thus the beginning of strain hardening). Equation (2-48) and (2-49) can directly be used to calculate the elastic-plastic resistance of a hot-rolled I-section subjected to pure bending around the major and minor axis, respectively. Those equations were derived on the basic assumptions that plane sections remain plane and normal to the neutral axis in bending; further, that the cross-section shape does not change significantly before the strain at the extreme outer-fibre ε_{csm} is reached [129]. Assuming a strain ration of $\varepsilon_{csm}/\varepsilon_y$, the bending capacity is calculated equal to the elastic moment M_{el} . With an increase of the strain ration, i.e. the use of stockier cross-sections, the bending capacity M_{csm} asymptotically approaching the plastic moment M_{pl} . As soon as the strain ration of $\varepsilon_{sh}/\varepsilon_y$ is reached, beneficial effects of strain-hardening, arising from the CSM material models for hot-rolled or cold-formed carbon steel, can be exploited.

$$M_{y,csm,Rd} = \frac{W_{pl,y} \cdot f_y}{\gamma_{M0}} \left[1 - \left(1 - \frac{W_{el,y}}{W_{pl,y}} \right) / \left(\frac{\varepsilon_{csm}}{\varepsilon_y} \right)^\alpha \right], \quad \text{for } \varepsilon_y < \varepsilon_{csm} \leq \varepsilon_{sh} \quad (2-48)$$

$$M_{z,csm,Rd} = \frac{W_{pl,z} \cdot f_y}{\gamma_{M0}} \left[1 - \left(1 - \frac{W_{el,z}}{W_{pl,z}} \right) / \left(\frac{\varepsilon_{csm}}{\varepsilon_y} \right)^\alpha \right], \quad \text{for } \varepsilon_y < \varepsilon_{csm} \leq \varepsilon_{sh} \quad (2-49)$$

where:

W_{pl}	is the plastic section modulus
W_{el}	is the elastic section modulus
y, z	refer to major and minor axis, respectively
α	is a dimensionless coefficient that depends on the type of cross-section and axis of bending (see Table 2-8)

For even stockier cross-sections the CSM strain ε_{csm} exceeds the yield plateau limit value ε_{sh} , entering the strain hardening regime in the outer fibres of the profile. The calculated moment resistance achieves the point of $M_{csm} > M_{pl}$. The bending capacity of a cross-section can be described by Equation (2-48), (2-49) and (2-50). The full derivation of the resistance functions for I-sections and SHS/RHS can be found in [129], [152], [153].

$$M_{csm} = f_y \cdot W_{pl} - f_y \cdot W_w + W_w^* (f_{csm} - f_y) \quad (2-50)$$

$$W_w = (W_{pl} - W_{el}) \left/ \left(\frac{\varepsilon_{csm}}{\varepsilon_y} \right)^\alpha \right. \quad (2-51)$$

$$W_{w,y}^* = \int_{A_{y^*}} g(y) y dA_{y^*} \quad (2-52)$$

where:

W_w	is the portion of the elastic-plastic stress block that is missing from the theoretical plastic section modulus
W_w^*	is the additional section modulus associated with the reached strain hardening range

$g(y)$ is the function which represents the triangular stress distribution normalized by $(f_{csm} - f_y)$

For more complex material models, such as the quad-linear material model, the derived explicit functions to calculate the bending resistance start to get impractical quickly. Therefore, simplified in expression were derived in [129] for a practice oriented design. Based on a regression analysis of the geometric properties of available I-sections, as well as RHS/SHS sections a simpler expression of W_W^* was proposed as follows:

$$W_W^* = W_{pl} \cdot \left(\frac{\varepsilon_{csm} - \varepsilon_{sh}}{\varepsilon_y} \right) \cdot \beta \quad (2-53)$$

where:

β is a dimensionless coefficient, presented as a function of the type of cross-section and axis of bending (see Table 2-8)

This leads to the simplified expressions for the bending resistance M_{csm} around the major and minor axis, as shown in Equation (2-54) and (2-55).

$$M_{y,csm,Rd} = \frac{W_{pl,y} \cdot f_y}{\gamma_{M0}} \left[1 - \left(1 - \frac{W_{el,y}}{W_{pl,y}} \right) / \left(\frac{\varepsilon_{csm}}{\varepsilon_y} \right)^\alpha + \beta \left(\frac{\varepsilon_{csm} - \varepsilon_{sh}}{\varepsilon_y} \right)^2 \cdot \frac{E_{sh}}{E} \right] \quad (2-54)$$

for $\varepsilon_{csm} > \varepsilon_{sh}$

$$M_{z,csm,Rd} = \frac{W_{pl,z} \cdot f_y}{\gamma_{M0}} \left[1 - \left(1 - \frac{W_{el,z}}{W_{pl,z}} \right) / \left(\frac{\varepsilon_{csm}}{\varepsilon_y} \right)^\alpha + \beta \left(\frac{\varepsilon_{csm} - \varepsilon_{sh}}{\varepsilon_y} \right)^2 \cdot \frac{E_{sh}}{E} \right] \quad (2-55)$$

for $\varepsilon_{csm} > \varepsilon_{sh}$

Table 2-8: CSM coefficients α and β used in the bending resistance functions, adapted from [129]

	α		β	
	Axis of bending		Axis of bending	
	Major	Minor	Major	Minor
I-section	2	1.2	0.1	0.05
SHS/RHS	2	2	0.1	0.1

2.4.5.3 Combined Load Case Resistance

The case of combined loading was investigated by Liew and Gardner [108]. The derived expressions for the combined load case of compression and bending about the major and minor axis, respectively, as well as the case for biaxial bending with compression is given by Equation (2-56), (2-57) and (2-58).

$$M_{Ed,y} \leq M_{R,csm,y} = M_{csm,y} \cdot \left[1 - \left(\frac{N_{Ed}}{N_{csm}} \right)^{a_y} \right]^{1/b_y} \quad (2-56)$$

$$M_{Ed,z} \leq M_{R,csm,z} = M_{csm,z} \cdot \left[1 - \left(\frac{N_{Ed}}{N_{csm}} \right)^{a_z} \right]^{1/b_z} \quad (2-57)$$

$$\left(\frac{M_{Ed,y}}{M_{R,csm,y}} \right)^{\alpha_{csm}} + \left(\frac{M_{Ed,z}}{M_{R,csm,z}} \right)^{\beta_{csm}} \leq 1 \quad (2-58)$$

The values for the powers a_y , b_y , a_z , b_z , α_{csm} , β_{csm} are defined in Table 2-9. The tabulated powers were determined through a non-linear least squares fitting procedure and are based on the ration of the cross-section web area to gross area $a = A_w/A$ and the ratio of the plastic section moduli for buckling around the major and minor axis $W_r = W_{pl,y}/W_{pl,z}$.

Table 2-9: CSM resistance coefficients for combined load cases, adapted from [108]

	$3 \leq \frac{\varepsilon_{csm}}{\varepsilon_y} < 5$	$5 \leq \frac{\varepsilon_{csm}}{\varepsilon_y} \leq 15$	$5 \leq \frac{\varepsilon_{csm}}{\varepsilon_y} \leq 15$
	I-sections		Box sections
a_y		$a+1.2$	
b_y		0.8	
a_z	2	$8a+1.2$	$a+1.2$
b_z	1	$0.8-0.5a$	0.8
α_{csm}	$2-1.5n \geq 1$	$2-0.15W_r-5n^{1.5} \geq 1.3$	$1.75-W_r(2n^2-0.15) \leq 1.7+W_r$
β_{csm}	$0.8+5n^{2.2} \leq 4$	$0.8+(15-W_r)n^{2.2} \leq 8$	$1.6+(3.5-1.5W_r)n^2 \leq 3.7-W_r$

It was shown that the methodology within the framework of the CSM design can be extended to cross-sections subjected to combined loading. Based on the concept of a rotated planar strain surface, interaction curves were developed to enable a practical application. Those were shown to be in good agreement with first numerical results [108] and further parametric studies [112], where CSM capacity predictions for hot-rolled sections were compared to results from numerical investigations as well as current predictions from EN 1993-1-1 [61].

2.5 Advanced Analysis + CSM Approach (AA+CSM)

2.5.1 Introduction

In the more recent past, the CSM was further developed by Fieber [67] during his PhD Thesis “Structural Steel Design using Advanced Analysis with Strain Limits” investigating members and frames made from hot-rolled steel and closed (RHS/SHS) as well as open cross-sections (I-shaped). This work was additionally published in several journal publications in [154]–[156]. Recent evaluations and expansions of this same concept to stainless steel were made in the PhD thesis of Walport [81] “Design of Steel and Stainless Steel Structures by Advanced Inelastic Analysis”. The proposed advanced analysis with strain limits addresses members and frame structures, using FE-beam GMNIA simula-

tions to predict the strain- and slenderness-based profile dependent load bearing capacity. This method is further termed as AA+CSM, as an acronym for advanced analysis with continuous strength method based strain limits.

The developed procedure is generally motivated by the same shortcomings that lead to the establishment of the direct strength method (DSM) from Section 2.3 or the continuous strength method (CSM) from Section 2.4, which are present traditional code based design approaches, i.e. EN 1993-1-1 [48] and AISC 360-16 [60]. Yet, it goes beyond the CSM approach, expanding it to global structures by the incorporation of beam finite element analysis to advanced problems including local buckling phenomena. In its general motivation and in some aspects of its implementation, this concept is connected to the work in the present thesis; most noticeably, the work in this thesis and the AA+CSM approach both attempt to include local buckling phenomena in a standard (6 D.O.F.) beam element formulation.

In the AA+CSM design method proposed by Fieber [67], strain limits from the CSM base curve (see Section 2.4.2) are obtained beforehand with a corresponding calculated slenderness value and applied to represent the effects of local buckling within beam finite element calculations. This approach enables the design of members with various profiles and any cross-sectional class using beam finite elements for advanced analysis purposes. This bypasses the need for shell based FE simulations, which indeed are able to capture local instability effects due to an explicit modelling of the whole cross-section, yet are not very practical and error prone, requiring a more detailed problem knowledge.

In the context of the CSM, the cross-section capacity is based on determined strain limits, which are directly linked to the cross-section and load case dependent slenderness, by integrating the stress distribution over the depth of the profile, see therefore Section 2.4.5. In combination with the standardized material models from Section 2.4.3, the CSM directly controls the spread of plasticity through the depth of a cross-section. This enables the consideration of positive effects from strain-hardening and eliminates the effective section property calculation (effective width method from EN 1993-1-5 [131]) for class 4 section in the design work-flow. Further, global member instability effects, i.e. Th. 2. Ord. effects indicated through sway modes in frame structures, are directly captured in the beam FE analysis through explicit modelling. The advanced analysis simulations

were performed in the commercial finite element software Abaqus [146]. The used Abaqus beam elements are denoted as B31OS and B31 for open and closed cross-sections, respectively, taking into account shear deformation, i.e. Timoshenko beam elements.

The following sections summarize the main topics that form the progressive character of this method according to [67]. Among them are topics such as the strain averaging approach, advanced analytical formulation for the determination of the elastic buckling stresses for whole cross-sections and the determination of local buckling half-wavelengths derived from numerical simulations using the finite strip method (CUFSM)[88]. In sum results from 2328 cross-sections were obtained, including European and American SHS/RHS, I-, C-, T- and L-shaped structural steel profiles. Note that only the results for SHS/RHS and I-shaped profiles were used to develop the analytical formulations for the local buckling half-wavelengths [67].

2.5.2 Strain averaging approach

The standard CSM base curve was calibrated against experimental results on cross-sections subjected to pure compression and uniform bending, i.e. from stub column tests and four point bending tests, respectively. Those load cases represent uniform strain distributions along the length of the member. In practice, combined load situation are the usual cases, where a strain gradient along the member length enhances the local stability of cross-sections. As shown e.g. by Kuhlmann [42], moment gradients have in general a beneficial effect on the plastic hinge formation and thus the rotation capacity. To account for the beneficial effect of local moment gradients, the CSM strain limit is averaged over a characteristic length $L_{b,cs}$, further described as the full cross-section half-wavelength (s. Section 2.5.3.2), rather than simply to a peak strain at the maximum moment along the member length. A similar approach was stated by Lay and Galambos throughout [157], [158]. There, the formation of plastic hinges for Class 1 cross-sections was investigated, resulting the observation that inelastic buckling occurs when the compression flange has yielded along the length of the inelastic local buckling half-wavelength (in the case of uniform bending).

The strain averaging approach is applied as follows. The investigated member is discretized in n element (beam elements). The element size should be smaller or at least equal to $L_{b,cs}$ (estimated buckling half-wavelength). After discretization and load application the system is calculated stepwise. The region with the highest bending moment M_{max} indicates the formation of a plastic hinge and consequently the location of the strain averaging length. The stepwise calculated strains – assuming first order beam finite elements with a single integration point at the centre of the element – are averaged over the number of elements ($\varepsilon_{Ed,Lb}$) within the buckling half-wavelength $L_{b,cs}$. The member capacity is then calculated from the condition $\varepsilon_{Ed,Lb} \leq \varepsilon_{csm}$ and Equation (2-59).

$$\frac{\varepsilon_{Ed,Lb}}{\varepsilon_{csm}} \leq 1.0 \quad (2-59)$$

$$\varepsilon_{Ed,Lb} = \frac{1}{n} \sum_{i=1}^n \varepsilon_i \quad \text{and} \quad n \geq 1$$

2.5.3 Definition of cross-section elastic buckling stress and local buckling half-wavelength

The conceptual background for the calculation of the cross-section level elastic buckling stresses and local buckling half-wavelengths is derived from the consideration of plates with simply-supported and fixed boundary conditions. Assuming this leads to a lower and upper bound of elastic buckling stresses from individual plates of a cross-section; where the lower bound is provided by the minimum buckling stress of the flange or the web of a cross-section with simply-supported boundary conditions, i.e. $\sigma_{cr,f}^{SS}$ or $\sigma_{cr,w}^{SS}$, as well as the upper bound provided by the minimum buckling stress of the flange or the web with fixed boundary conditions, i.e. $\sigma_{cr,f}^F$ or $\sigma_{cr,w}^F$. The level of element interaction depend in general on constituent plate proportions, calibrated to analytical expressions derived from simulations. The full cross-section dependent elastic critical buckling stress is $\sigma_{cr,cs}$ is expressed in the general formulation given by Equation (2-60).

$$\sigma_{cr,cs} = \sigma_{cr,p}^{SS} + \zeta (\sigma_{cr,p}^F - \sigma_{cr,p}^{SS}) \quad \text{where} \quad 0 \leq \zeta \leq 1 \quad (2-60)$$

The same conceptual principle was applied to the calculation of the buckling half-wavelength $L_{b,cs}$, assuming that the full half-wavelength lies between the half-wavelengths of isolated plates with simply supported $L_{b,p}^{SS}$ and fixed $L_{b,p}^F$ boundary conditions along adjoined edges, see Equation (2-61).

$$L_{b,cs} = L_{b,p}^{SS} - \zeta (L_{b,p}^{SS} - L_{b,p}^F) \quad \text{where } 0 \leq \zeta \leq 1 \quad (2-61)$$

2.5.3.1 Determination of local buckling stresses

In the following, expression for the determination of the local buckling elastic stresses $\sigma_{cr,cs}$ are briefly presented for SHS and RHS profiles. A detailed presentation on a wider set of profiles as well as the derivation of the analytical formulations is based on investigations from Fieber [67]. Those investigations were additionally published in condensed representation throughout journal publications in [150], [151].

$$\sigma_{cr,p}^{SS} = \min(\beta_f \cdot \sigma_{cr,f}^{SS}, \beta_w \cdot \sigma_{cr,w}^{SS}) \quad (2-62)$$

$$\sigma_{cr,p}^F = \min(\beta_f \cdot \sigma_{cr,f}^F, \beta_w \cdot \sigma_{cr,w}^F) \quad (2-63)$$

where:

β_f, β_w are steering parameter to recognise buckling affected cross-section parts, in each case, defined as ratios of the maximum applied compressive stresses $\sigma_{max,cs}$, described by Equation (2-64) and (2-65) subjected to the following condition:

Condition: if $\beta_f > 1$ then $\beta_w = 1$ or if $\beta_w > 1$ then $\beta_f = 1$

Additionally, the maximum applied stress $\sigma_{max,cs}$ is defined through Equation (2-66) as the maximum compressive stress in the flange $\sigma_{max,ff}$ or the web $\sigma_{max,w}$.

$$\beta_f = \frac{\sigma_{\max,cs}}{\sigma_{\max,f}} \quad (2-64)$$

$$\beta_w = \frac{\sigma_{\max,cs}}{\sigma_{\max,w}} \quad (2-65)$$

The consideration from Equation (2-64) and (2-65) can be simplified to be equal to 1, since in the most common load situation (compression and/or major axis bending) for I-shaped sections and in all load combinations for SHS/RHS the compressive stresses along the centerline of flange and web plates is equal $\sigma_{\max,w} = \sigma_{\max,f}$.

$$\sigma_{\max,cs} = \max(\sigma_{\max,w}, \sigma_{\max,f}) \quad (2-66)$$

Table 2-10: Interaction coefficient ζ for square (SHS) and rectangular (RHS) hollow sections, adopted from Fieber [67]

Load case	Flange critical ($\phi < 1$)	Web critical ($\phi \geq 1$)
	$\zeta = \frac{t_w}{t_f} (0.24 - a_f \phi)^{0.6}$	$\zeta = \frac{t_f}{t_w} \left(0.53 - \frac{a_w}{\phi} \right)$
Compression and major axis bending	$a_f = 0.24 - \left[0.1 \cdot \left(\frac{t_f}{t_w} \right)^2 \cdot \left(\frac{h}{b} - 1 \right) \right]^{0.6}$ <i>but</i> $a_f \leq 0.24$	$a_w = 0.63 - 0.1 \cdot \frac{h}{b}$ <i>but</i> $a_w \leq 0.53$
Compression and minor axis bending	N/A	$\zeta = \frac{t_f}{t_w} \left(0.53 - \frac{a_w}{\phi} \right)$ $a_w = 0.63 - 0.1 \cdot \frac{h}{b}$ <i>but</i> $a_w \leq 0.53$

The functions for the interaction coefficient ζ are determined by Equation (2-67), developed on results from finite strip analysis, where the full cross-section elastic local buckling stress $\sigma_{cr,cs}$ was obtained for a wider range of cross-sections. The functions for ζ are summarized in Table 2-10.

$$\zeta = \frac{\sigma_{cr,cs} - \sigma_{cr,p}^{SS}}{\sigma_{cr,p}^F - \sigma_{cr,p}^{SS}} \quad \text{but} \quad 0 \leq \zeta \leq 1 \quad (2-67)$$

Note that for hot-rolled SHS/RHS with $t_f = t_w$ and welded SHS/RHS with $t_f \geq t_w$, the flange is never critical under compression and minor axis bending.

Table 2-11 introduces the factor ϕ , which defines the relative susceptibility of flange and web to local buckling at the simply-supported lower bound. It is described as follows through Equation (2-68), yet, as explained before, can be simplified to Equation (2-69) for common load cases, i.e. $\beta_f = \beta_w = 1$.

$$\phi = \frac{\beta_f \cdot \sigma_{cr,f}^{SS}}{\beta_w \cdot \sigma_{cr,w}^{SS}} = \left(\frac{\sigma_{cr,f}^{SS}}{\sigma_{cr,w}^{SS}} \right) \cdot \left(\frac{\sigma_{\max,w}}{\sigma_{\max,f}} \right) \quad (2-68)$$

$$\phi = \frac{\sigma_{cr,f}^{SS}}{\sigma_{cr,w}^{SS}} \quad \text{if} \quad \sigma_{\max,f} = \sigma_{\max,w} \quad (2-69)$$

2.5.3.2 Determination of local buckling half-wavelengths

An analytical approach by Fieber [67] to calculate the local buckling half-wavelength was calibrated against finite strip calculations with the software CUFSM ([88], [89]). The concept requires the knowledge of the buckling half-wavelength of the isolated cross-section plates with simply-supported and fixed boundary conditions. The local buckling half-wavelength can be defined from Equation (2-70):


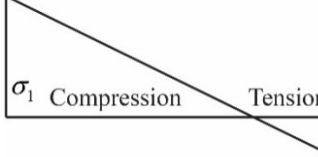
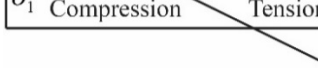
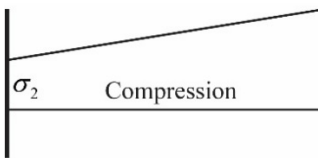
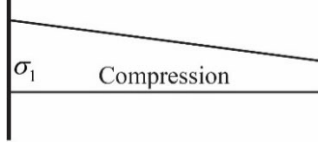
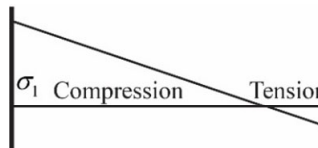
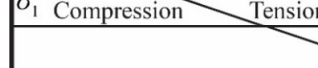
$$L_{b,p} = k_{Lb} \cdot b_p \quad (2-70)$$

where:

k_{Lb} is a coefficient to account for the boundary condition and applied stress distribution. Within the advanced CSM framework this factor is analogous to k_σ from Table 2-2, used to predict the local buckling stress $\sigma_{cr,p}$ of a plate, see additionally EN 1993-1-5 [50].

b_p is the width of an isolated plate

Table 2-11: Buckling half-wavelength coefficient k_{Lb} for internal and outstand plates with simply-supported and fixed edge conditions, adopted from Fieber [67]

Stress distribution	$\psi = \sigma_2/\sigma_1$	Simply-supported edges	Fixed edges
Internal plates (SS-SS)			
	$1 \geq \psi \geq 0.25$	$k_{Lb} = 1$	$k_{Lb} = 0.66$
	$0.25 > \psi \geq -1$	$k_{Lb} = 1 - 0.21(\psi - 0.25)^2$	$k_{Lb} = 0.66 - 0.12(\psi - 0.25)^2$
	-1	$k_{Lb} = 0.67$	$k_{Lb} = 0.47$
Outstand plates (SS-SS)			
	$1 \geq \psi \geq -1$	$k_{Lb} = \text{member length}$	$k_{Lb} = 1.65$
	$1 \geq \psi \geq 0$	$k_{Lb} = \text{member length}$	$k_{Lb} = 1.65$
	$0 > \psi \geq -1$	$k_{Lb} = \frac{0.818}{0.221 - \psi}$	$k_{Lb} = \frac{0.68}{0.41 - \psi}$
	-1	$k_{Lb} = 0.67$	$k_{Lb} = 0.48$
	$-1 > \psi \geq -3$	$k_{Lb} = 0.06\psi^2 + 0.39\psi + 1$	$k_{Lb} = 0.04\psi^2 + 0.29\psi + 0.73$

Note: Compression taken as positive

A summary of the calibrated expressions for the half-wavelength coefficient k_{Lb} is presented in Table 2-11. The basis those expression was formed by a series of finite strip analysis performed on rectangular plates with different boundary and loading conditions. A detailed explanation on the calibration process is presented further in [67].

Using Equation (2-70) in combination with the half-wavelength coefficients k_{Lb} from Table 2-11 leads to the half-wavelengths of the isolated web ($L_{b,w}^{SS}$ and $L_{b,w}^F$) and flange ($L_{b,f}^{SS}$ and $L_{b,f}^F$) with simply supported and fixed boundary conditions. Along with this information, as well as the load case dependent value for η from Table 2-12 and the factor ϕ from Equation (2-68) or (2-69), the lower and upper bound for the half-wavelength of the full cross-section ($L_{b,p}^{SS}$ and $L_{b,p}^F$) can be determined as follows:

$$L_{b,p}^{SS} = L_{b,w}^{SS}\eta + L_{b,f}^{SS}(1-\eta) \quad (2-71)$$

$$L_{b,p}^F = L_{b,w}^F\eta + L_{b,f}^F(1-\eta) \quad (2-72)$$

Subsequently, the calculation of the interaction factor ζ (see Table 2-10), provides the evaluation of the full half-wavelength $L_{b,cs}$ using Equation (2-61).

Table 2-12: Expression for the transition function η for SHS/RHS and I-shaped profiles subjected to compression and major or minor axis bending, adopted from Fieber [67]

Profile	Load case	
	$N + M_y$	$N + M_z$
SHS/RHS	$\eta = 1 - \frac{1}{\phi^3 + 1}$	
I-section	$\eta = 1 - \frac{1}{(\phi - 0.5)^3 + 1} \geq 0$	$\eta = 1 - \frac{1}{(\phi - 0.5a_1)^3 + 1} \geq 0$ where $a_1 = 2 \cdot \psi_f - 1 \geq -0.6$

2.6 Generalized Slenderness based Resistance Method (GSRM) for RHS/SHS profiles

The Generalised Slenderness based Resistance Method (GSRM) is yet another method developed over the course of the last few years to address the shortcomings of traditional design rules. It is closely related to the work carried out in the context of this thesis for two reasons: on one hand, it was developed by this thesis's supervisor and other international research partners in the context of RFCS (Research Fund for Coal and Steel) funded project HOLLOSTTAB, which stands for "Overall-Slenderness Based Direct Design for Strength and Stability of Innovative Hollow Sections". On the other hand, the project dealt with the design of high-strength or otherwise custom-made steel hollow sections, and is thus thematically directly connected with this thesis; its experimental campaign and its FEM model development and validation form the core basis and starting point for this thesis work, see Chapter 1.

Thus, the GSRM is a method which focuses on the development of design rules, similarly to other proposed methods such as the direct strength method (DSM, see Section 2.3), continuous strength method (CSM, see Section 2.4) and the overall interaction method (OIC [159], [160], also denoted as the overall concept throughout literature. The description of the method when applied to *square and rectangular hollow sections*, i.e. the same type of sections considered in this thesis, is mainly based on investigations documented in the PhD thesis of Toffolon [2] on RHS/SHS profiles.

Similarly to the DSM and CSM, the GSR-method makes use of an overall definition of the slenderness $\bar{\lambda}$ on the cross-sectional, as well as the member level and a corresponding reduction factor χ . It is generalized to account for combined load situations and takes advantage of interactive effects between mutual parts/plates of closed RHS/SHS cross-sections. In the method the local stability case ($\bar{\lambda}_L, \chi_L$) and the global stability case ($\bar{\lambda}_G, \chi_G$) are treated separately. All resistances are defined as load amplification factors and thus termed R . The generalized slenderness and the ultimate resistance are defined in Equation (2-73) and (2-74), respectively. The buckling coefficient χ is a function of the slenderness $\bar{\lambda}$, dependent on the definition of the reference resistance R_{ref} .

$$\bar{\lambda} = \sqrt{\frac{R_{ref}}{R_{cr}}} \quad (2-73)$$

$$R_b = \chi \cdot R_{ref} \quad (2-74)$$

Three definitions for R_{ref} were investigated along the conduction of the Hollosstab project [161]:

- i. R_{el} : Load amplification factor to reach the yield strength at an outer fiber of the cross-section
- ii. R_{pl} : Load amplification factor to reach the plastic resistance of the cross-section (yielding at all fibres, no strain-hardening) [162]
- iii. R_{lin-pl} : Load amplification factor to reach the resistance surface given by the plane

interaction surface
$$\frac{N_{Ed}}{N_{pl}} + \frac{M_{y,Ed}}{M_{y,pl}} + \frac{M_{z,Ed}}{M_{z,pl}} = 1$$

Of these, the definition based on R_{el} was finally demonstrated to be most advantageous, which is justified considering that the majority of gains in the design approach were achieved in the slender range of sections (class 3 and class 4).

The general idea of the GSRM approach to calculate the cross-sectional member resistance is described through Figure 2-15 a) and b). The proposed design workflow requires two steps of resistance evaluations, i.e. consideration of the cross-section resistance and the member resistance. Similarly to EN 1993-1-5 [131] and EN 1993-1-1 [48], the GSRM introduces these steps using the Winter and Ayrton-Perry formulation, respectively. The steps for the determination of the resistance $R_{b,L}$ on a cross-sectional level may be applied in combination with Figure 2-15 a) as follows.

- i. Calculation of the cross-section resistance R_{ref} in the n - m plane, according to the load combination and the applied resistance definition, see Figure 2-15 b). In this representation Ω is the applied load amplitude and φ the angle in the n - m plane.
- ii. Calculation of the critical local buckling load $R_{cr,L}$ with the same load combination. The values for $R_{cr,L}$ may be obtained from simply supported members with a very short length through available analytical formulations or numerical simulations.

Therefore, free software tool like CUFSM [88] and GBT [90] or commercially available software like ABAQUS [146] can be used.

- iii. Calculation of the local slenderness using Equation (2-73).
- iv. Calculation of the reduced cross-section resistance $R_{b,L}$, see Equation (2-74), using derived formulations for the resistance curve from Equation (2-80) to (2-82). The final design value is obtained by $\Omega \cdot R_{b,L}$ according to Figure 2-15 b).

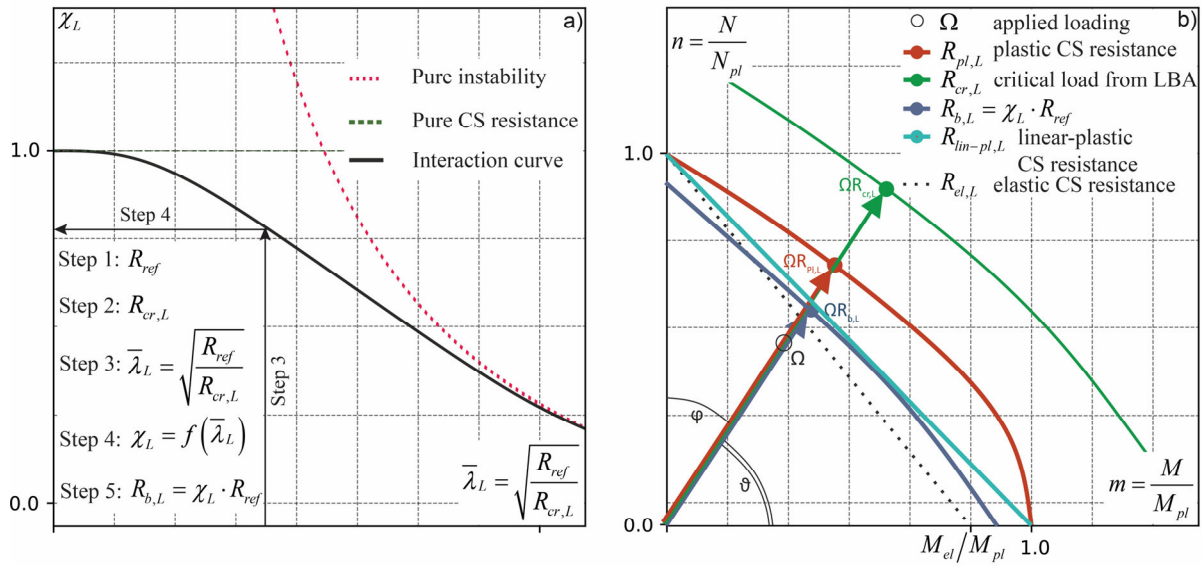


Figure 2-15: a) Design steps of the GSRM; b) n-m interaction curves for different resistance formulations, adopted from [2]

The formulation of the local buckling reduction factor χ_L is proposed as follows for two possible ranges, i.e. an elastic and plastic range, separated by a calculated load distribution dependent slenderness value (see Equation (2-75)). This procedure is similar to EN 1993-1-5 [131] where the local buckling curve (Winter curve) is separated into two parts.

$$\bar{\lambda}_L = \sqrt{\frac{R_{ref}}{R_{cr,L}}} \tag{2-75}$$

$$\bar{\lambda}_0 = 0.5 + \sqrt{0.25 - A} \tag{2-76}$$

$$A = (0.2 + 0.02 \cdot \psi_2) \cdot \frac{(1 + \psi_1)}{2} \quad \text{for hot – finished sections} \quad (2-77)$$

$$A = (0.225 + 0.025 \cdot \psi_2) \cdot \frac{(1 + \psi_1)}{2} \quad \text{for cold – formed sections}$$

$$\psi_1 = \max \left(\frac{\frac{N}{A} + \frac{M}{W_y} - \frac{M}{W_z}}{\frac{N}{A} + \frac{M}{W_y} + \frac{M}{W_z}}; \frac{\frac{N}{A} - \frac{M}{W_y} + \frac{M}{W_z}}{\frac{N}{A} + \frac{M}{W_y} + \frac{M}{W_z}} \right) \quad (2-78)$$

$$\psi_2 = \min \left(\frac{\frac{N}{A} + \frac{M}{W_y} - \frac{M}{W_z}}{\frac{N}{A} + \frac{M}{W_y} + \frac{M}{W_z}}; \frac{\frac{N}{A} - \frac{M}{W_y} + \frac{M}{W_z}}{\frac{N}{A} + \frac{M}{W_y} + \frac{M}{W_z}} \right) \quad (2-79)$$

where:

A is a calibration factor depending on the fabrication process of hot-rolling or cold-forming, see Equation (2-77).

ψ_1, ψ_2 is the maximum and the minimum factor for the stress distribution according to Equation (2-78) and (2-79), respectively.

For the elastic range $\bar{\lambda}_L > \bar{\lambda}_0$, the buckling reduction factor χ_L is proposed as follows:

$$\chi_L = \left(1 - \frac{A}{\bar{\lambda}_L^{B_2}} \right) \cdot \frac{1}{\bar{\lambda}_L^{B_2}} \quad \text{for } \bar{\lambda}_L > \bar{\lambda}_0 \quad (2-80)$$

An additional separation is made for hot-rolled and cold-formed sections in the plastic range $\bar{\lambda}_L < \bar{\lambda}_0$. The buckling reduction factor χ_L is then calculated by Equation (2-81) and (2-82). This condition is based on the different strain hardening potential according to the fabrication procedure and the corresponding steel grade. This difference is made through the factor α_{pl} , calculated by Equation (2-83).

$$\chi_L = 1 + (\alpha_{pl} - 1) \cdot \frac{\bar{\lambda}_0 - \bar{\lambda}_L}{\bar{\lambda}_0 - 0.3} \leq \min(\alpha_{pl}; 1.5) \text{ for } \bar{\lambda}_L < \bar{\lambda}_0 \text{ and hot-rolled sections} \quad (2-81)$$

$$\chi_L = 1 + (\alpha_{pl} - 1) \cdot \frac{\bar{\lambda}_0 - \bar{\lambda}_L}{\bar{\lambda}_0 - 0.25} \leq \min(\alpha_{pl}; 1.5) \text{ for } \bar{\lambda}_L < \bar{\lambda}_0 \text{ and cold-formed sections} \quad (2-82)$$

$$\alpha_{pl} = \frac{R_{pl}}{R_{el}} \quad (2-83)$$

The above equations cover the design of the cross-section at the local level. In addition, the method is also able to capture the global (member) buckling phenomenon, which in the case of standard hollow sections is generally governed by a flexural buckling mode.

- i. Calculation of the global critical elastic buckling load factor $R_{cr,G}$. For SHS/RHS profiles it is the flexural buckling load factor and uniform compression.
- ii. Calculation of the global member slenderness $\bar{\lambda}_G$, according to Equation (2-84).
- iii. Calculation of the resistance reduction factor χ_G using appropriate existing EC3 column strength curve. Equation (2-85) provides the resistance factor $R_{b,G}$.

$$\bar{\lambda}_G = \sqrt{\frac{R_{b,L}}{R_{cr,G}}} \quad (2-84)$$

$$R_{b,G} = \chi_G \cdot \chi_L \cdot R_{ref} \quad (2-85)$$

For the specific set of sections and material grades considered in Hollosstab, the GSRM was proven to lead to far more accurate, yet mechanically consistent and explicable design results. Some demonstrations of the improved accuracy when compared to Eurocode 3 regulations are shown through the following figures, taken from [2]. Figure 2-16 a) shows the results obtained with the GSRM approach for biaxial bending and cold-

formed and hot-rolled hollow sections. The predictions are normalized with the numerical results from GMNIA simulations, considered as the ground truth. The x-axis represents the local relative slenderness. The comparison with Eurocode 3 cross-section resistance predictions is made in Figure 2-16 b), plotted in the same manner as before. It is noticeable that the prediction scatter for class 4 cross-sections strongly decreases when using the GSRM, leading to results which are still save sided but more economic compared with EC3 predictions. This conclusion can be further applied to rest of the cross-section classes, since in almost all cases the GSRM design value is lower than the GMNIA results.

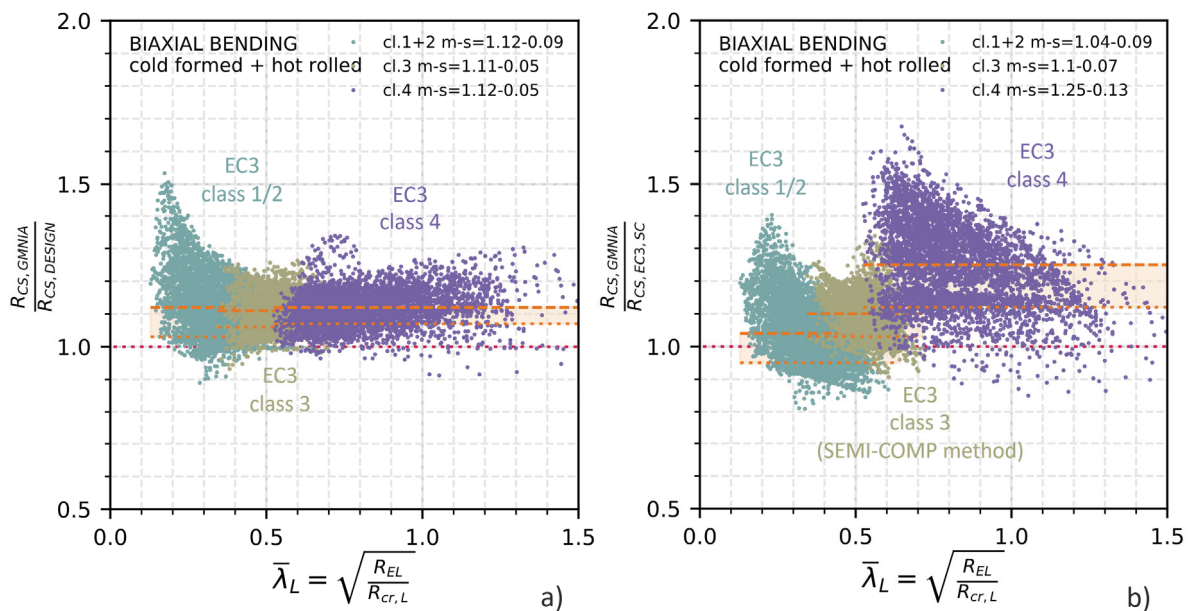


Figure 2-16: Comparison of GSRM with EC3 code provisions [48]

3

Research Gaps

Identification and Discussion

Outline of the chapter:

This chapter is subdivided in three parts:

- i. The first part summarizes the finding of the previous two chapters, in particular the introductory statement of the thesis motivation in Chapter 1 and the detailed description of the state of technology in the field of the design of steel members against instabilities in Chapter 2, and expands on the shortcomings of present design methods by means of demonstrations and calculations.
- ii. The second part describes the proposed, alternative approach, named “DNN-DSM”, and motivates its use and the potential expected from its development and application. This forms the working hypothesis of the thesis, which was tackled in subsequent parts.
- iii. Finally, the third part of this chapter formulates a series of Research Gaps, i.e. more basic scientific and engineering questions that needed to be tackled in the process of implementing the proposed new methodology.

3.1 Limitations of Traditional and Advanced Design Approaches

3.1.1 Cross-section classification

The concept of cross-section classification presented in Section 2.1.4 has a major influence on the common view on and procedures for structural design and verification of steel structures, starting with the choice of the used steel sections and extending to the assumed overall structural behaviour. Due to its inherent simplicity and the inherently “artificial” and “clear-cut” division into 4 classes, the actual load bearing capacity is often underestimated in slender ranges, for materials with pronounced strain-hardening capacities, and for structures that may require only limited plastic deformations to achieve significant redistribution effects. An accurate description of shortcomings is summarized and described by Wilkinson [27], Nseir [59], Soulumi [28] and many more throughout literature. In the following some of the shortcomings connected to the classification system are summarized:

- iv. The mutual interaction between individual plates of the cross-section is typically neglected. This leads (particularly in bending-dominated cases) to an unwarranted, high slenderness estimation and therefore an unfavorable classification. Furthermore, local strength checks are based on the most stressed plate of the cross-section. The positive effect of a local stress gradient from bending in adjacent plates is neglected although experiments [42], [163]–[166] show higher capacities due to this effect.
- v. The unrealistic, “sudden” resistance drop between class 2 (M_{pl}) and class 3 (M_{el}) cross-sections due to a “hard” geometric limit without transitions. Such a discontinuity has no physical background and arises only for reasons of a simplified capacity representation. This regulation remains in the revised version of EN 1993-1-1:2022 for general-shaped sections. For doubly-symmetric sections, Lechner [167] and Kettler [66] proposed a method developed in the RFCS project SEMI-COMP which reduces this discrepancy, by introducing a linear transition between Class 2 and Class 3 capacities; this method is introduced in the 2022 version of EN 1993-1-1 in a separate Annex B.

- vi. The fabrication process, i.e. hot-rolled or cold-formed, and therefore the strong difference in the material behaviour is not taken into account. Only the geometrical aspect in the corner regions differs in the definition of the plate width due to different radii (hot-rolled with $b-3t$ and cold-formed with $b-5t$).
- vii. Depending on the load case combination, individual plates of a cross-section can be assigned to different classes. In addition, parts classified as Class 4 undergo an iterative calculation process where the effective width method is used [131].

3.1.2 Non-linear material behaviour

The cross-section classification system is additionally bound by several simplifications, inconsistencies and shortcomings. One of the biggest simplification within this method is based on the assumption of a simple, bilinear material behaviour in the determination of plastic capacities. While this simplification is justified for hand calculations, it is clear that it is not able to accurately reflect the behaviour of various steel grades at higher levels of straining, and in particular is not accurate in light of the increased use of highly non-linear material such as aluminum, stainless steel or high strength steel. In these cases, the framework of cross-section classification will not generally be very accurate, underestimating the full material potential.

In the following, as a means to demonstrate the above statements, two simulation sets and their results are presented within Figure 3-1. The simulations serve to underline the crucial influence between simplified and more refined material models for hot-rolled carbon steel, especially in the range of stocky cross-sections. The profile considered herein was a hot-rolled SHS300 section, of varying wall thickness. The material properties for the simulations in Figure 3-1 a) were chosen according to Eurocode 3, in order to fulfill the requirements for plastic design: $f_u/f_y \geq 1.1$, $\varepsilon_f \geq 15\%$, $\varepsilon_u/\varepsilon_y \geq 15$, $\varepsilon_y = f_y/E$, where ε_f is the percentage strain after failure across the fracture surface, ε_u is the strain at the ultimate tensile strength f_u and ε_y is the strain at yield tensile strength f_y . Figure 3-1 b) shows the simulated results for the same profile (hot-rolled SHS 300) using a quad linear material model, originally derived by Yun and Gardner [6] and adopted for the new Eurocode generation within prEN1993-1-14: Design by finite element analysis. The steel grade S355 was used in these simulations. Both diagrams and axes make used

of normalized variables. The x-axis shows the rotation normalized by the plastic rotation φ/φ_{pl} . The y-axis describes the reached moment at every simulation step, normalized by the plastic profile dependent moment M/M_{pl} . The chosen colors represent the four cross-section classes into which the profiles would have been classified, i.e. red = class 4, yellow = class 3, green = class 2 and blue = class 1. The material model does only have a minor influence on class 4 and class 3 cross-section. Its influence is more pronounced within class 2 and class 1 sections, attributed as stocky. It can directly be seen that profiles originally classified as class 2, using the bi-linear material model (Figure 3-1 a)), could be classified as class 1, using a quad-linear material model (Figure 3-1 b)). By taking strain hardening to a higher extent into account, compared to current Eurocode provisions, the actual material behaviour is exploited much better leading to more economical approaches. The simulations shown in Figure 3-1 are based on shell finite element models for SHS cross-sections. It has to be remarked that the beneficial interaction between individual faces of the cross-section is taken into account in this consideration, thus avoiding the unfavorable assumption of individual plates. The figure demonstrates the fact that material models and plate slenderness have a significant influence on achievable rotations and strength values, something classification is only partially and inaccurately able to capture.

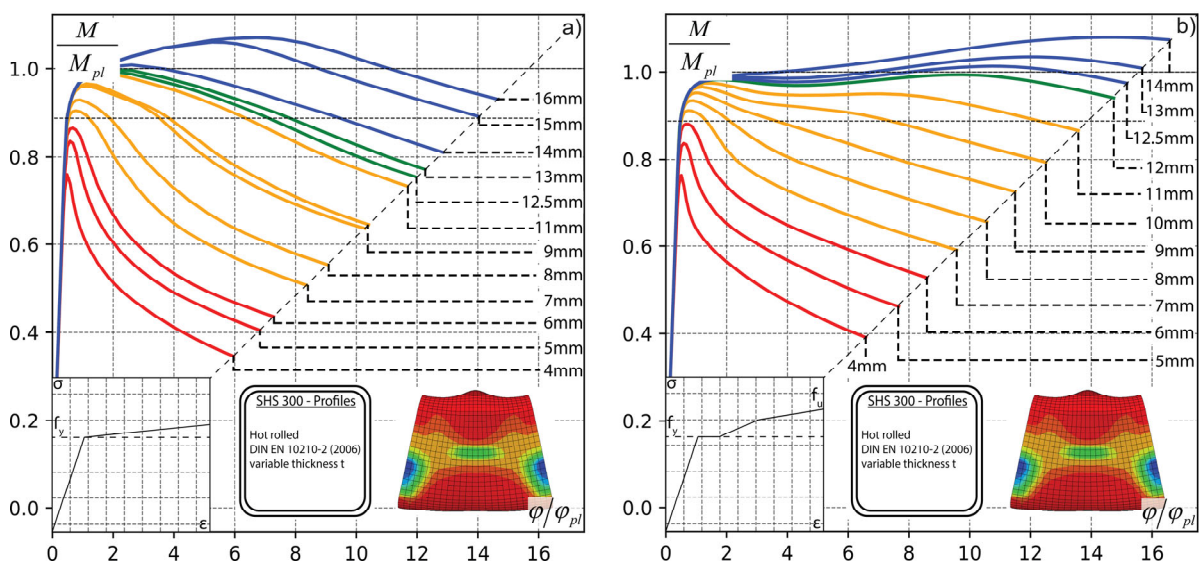


Figure 3-1: Non-linear shell FE Abaqus simulations and their results using different material models for hot-rolled steel, a) bilinear material model based on [131]; b) quad-linear material model based on [6]

3.1.3 Limitations of more advanced analysis and design methods

The presented, advanced design approaches, i.e. the DSM, CSM and GSRM have the main motivation to overcome code inherent disadvantages. The main advantage of all those methods is overcoming the need to determine cross-section classes. Those strictly set boundaries are replaced through a continuous definition of buckling strength as function of (cross-sectional, overall) slenderness. The local cross-section slenderness is a result of a previously performed elastic buckling analysis, which can be achieved by means of computer software. Freely available tools such as CUFSM or GBT are named and referred to in Section 2.4.4. Additional, commercially available software such as Abaqus provided also the option to perform LBA calculations. The major advantage is that the entire cross-section is now considered as a whole and not just approximated through individual cross-section plates as before. The main focus is therefore shifted towards the modelling approach of the cross-section and the correct determination of the elastic buckling load rather than the determination of effective widths. The role of the local slenderness is therefore discussed in Section 3.1.4.

The resistance of a cross-section, on the other hand, is a generalized function using the calculated local slenderness. The DSM uses different strength curves, comparable to the idea of the flexural buckling curve from EN 1993-1-1:2020 [48], to assess the need for local, distortional or lateral torsional buckling, see Section 2.3. It has additionally the advantage to be used as an optimization tool for cold-formed cross-sections, since one of the outputs are so called “signature-curves” which allow to assess different instability cases (local, distortional or later torsional buckling) dependent on the used profile and the buckling half-wavelength.

The CSM uses a strain based definition, dependent on a continuous slenderness definition, to determine cross-sectional deformation limits, which are used within resistance formulations and a corresponding material law. The workflow of the CSM method enables to account for strain hardening to an extent traditional approaches are not capable of. The determination of slenderness based strains allow to account for an accurate, material law dependent determination of the resistances in cold-formed and hot-rolled structural sections within a practice oriented and applicable manner. In addition, the

derived material models by Yun and Gardner ([6], [7]) are well suited within more advanced geometrically materially non-linear finite element simulations, explicitly accounting for instability effects. The GSRM approach is especially favorable in slender regions, leading to less conservative results compared to EN 1993-1-5 [50]. Its formulation is mostly based on the Winter curve for local buckling, incorporated in EN 1993-1-5, taking into account the whole stress distribution of the cross-section.

In spite of clear advantages of those methods when compared to traditional approaches, new problems are introduced with their formulation, inherent to the new workflow. A list of disadvantages related to DSM and CSM was listed by Nseir [59]. Among them, the use of a continuous slenderness leads to possible new sources of inaccuracy in their calculation. In addition, the use of a unique definition of cross-sectional slenderness as the square root of the ratio of the yielding load vs. the critical buckling load, irrespective of precise loading case, does not necessarily lend itself to an increased accuracy of the final definition of the buckling knockdown factors χ , as these will depend on such factors as the stress distribution. This is something that e.g. the DSM and the GSRM needed to tackle through the definition of a series of χ -curves.

The most important drawback of the mentioned methods (DSM, CSM, GSRM and OIC) is however given by the lack of system-level redistributions; the methods are generally focused on strength, not on deformations. Among the described methods, only the AA-CSM-approach is focused on system-level analysis; its main limitation may be given by the complexity of its application and interpretability, as several analysis steps are required before the system analysis can be assumed to be validated, including local buckling analyses of all sections, determination of buckling wavelengths, calculation of limiting strains. In addition, the method is generally also not suitable for inelastic system analysis, and is most closely comparable to an augmented, improved elastic-plastic (E-P) system analysis.

3.1.4 Role of the slenderness

The role of the slenderness, and therefore the modelling approach for its determination, is explained exemplary through an open I-shaped cross-section. Different model choices are shown in Figure 3-2. Similar investigations were performed as part of an industrial

project. FE model approaches and further references on model verification shall be taken from [82] and [168]. The general discussion of the importance of the slenderness is made here by looking at the CSM approach, presented in Section 2.4.

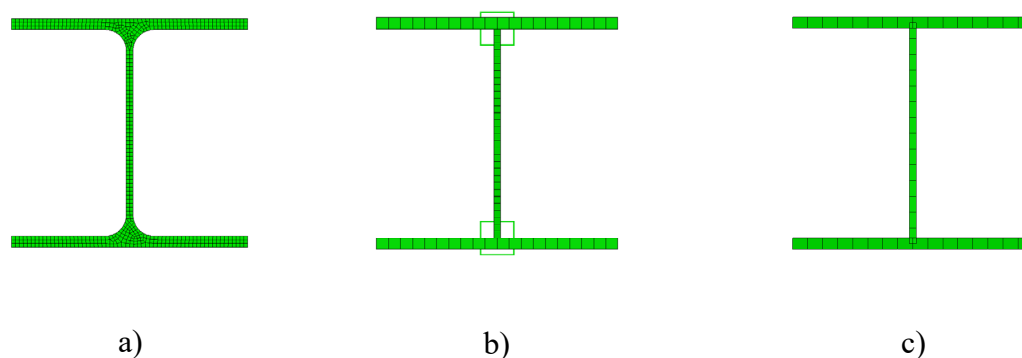


Figure 3-2: Common model approaches for I- and H-shaped profiles a) Solid-model; b) Shell-beam-model; c) Shell-model; published in [82]

Three common models for I- and H-shaped profiles are summarized in Figure 3-2, including a) solid-model; b) shell-beam model; c) shell-model. Solid models (see Figure 3-2 a)) can lead to a realistic geometry approximation, including the influence of the fillets between the web and the flanges. Nevertheless, requiring the implementation of the whole cross-section geometry, the calculation process can become computationally time consuming, leading to necessary simplifications within the models.

A more simplified model is shown in Figure 3-2 b), where the flanges and the web are modeled with shell elements, without a surface interception but with additional beam elements as square hollow sections of variable depth and wall thickness at the top and the bottom of the web. The beam elements are designed in such a way that they have the same area A and torsional moment of inertia I_T as the missing fillets between the web and flanges. This model approach was also used and verified in [168].

One further approach is the use of a shell-model with three plates representing the web and the flanges, which are intercepting in the centerline, see Figure 3-2 c). Therefore, the fillets are not modelled explicitly but are approximated by the overlap between the web and the flanges. Following this model assumption not all cross-section values can be taken into account precisely for hot-rolled I-shaped sections; welded profiles are mostly

excluded from this. In some cases, especially the torsional moment of inertia I_T can deviate, depending on the selected profile series, around 30% [169]. This can lead, in accordance to the observed problem, to lower capacity values e.g. in the case of lateral torsional buckling (LTB). However, for local instability problems, which were investigated throughout this report, members of shorter span are primarily not prone to LTB effects and therefore the above-mentioned modelling shortfall is negligible. For this reason, model c offers several strategical and numerical advantages e.g. higher computational efficiency and higher model homogeneity as applicable for both hot-rolled and welded I-shaped profiles.

Table 3-1: Used parameters for non-linear material model

Steel grade	E [N/mm ²]	f_y [N/mm ²]	f_u [N/mm ²]	ε_y [%]	ε_{sh} [%]	ε_u [%]	$\varepsilon_{sh}/\varepsilon_y$	E_{sh} [N/mm ²]	C_1
S355	210000	355	490	0.17	1.74	16.53	10.3	2283	0.38

In order to discuss the difference between the models, an HEA300 profile with a length of 800 mm and the steel grade S355 was selected and loaded with a normal force acting in the center of gravity or a constant moment. The material model for hot-rolled steel was chosen according to explanations in Section 2.4.3.1. Used parameters are summarized in Table 3-1. In a first step, a linear bifurcation analysis (LBA) was performed in ABAQUS for model a, b, and c. Table 3-2 displays the results of the obtained first eigenvalue for compression and bending, as well as calculated strain limits and corresponding maximum forces and moments according to CSM. The lowest eigenvalue occurs for model c for compression or bending, followed by model a and b.

The CSM results of the cross-section capacity for pure compression do not differ, although experiencing a slightly different CSM strain limit $\varepsilon_{csm}/\varepsilon_y$. This can be explained through the possible reached strain according to the CSM base curve, which lies for all models within the plateau region of the material model $\varepsilon_y \leq \varepsilon \leq \varepsilon_{sh}$. Figure 3-3 gives a clearer picture to this outcome. Figure 3-3 a) shows the CSM base curve and the areas, where the three models come to lie according to their slenderness. Figure 3-3 b) shows a strength dependent representation, where the x-axis is the CSM strain and the y-axis the back-calculated resistance corresponding to the material model. Since the resistance

of the profile comes to lie in the plateau region, no difference was identified. Nevertheless, the effect could be more significant for slender (transition between elastic range and plateau) or for very stocky profiles, where strain hardening could be misinterpreted.

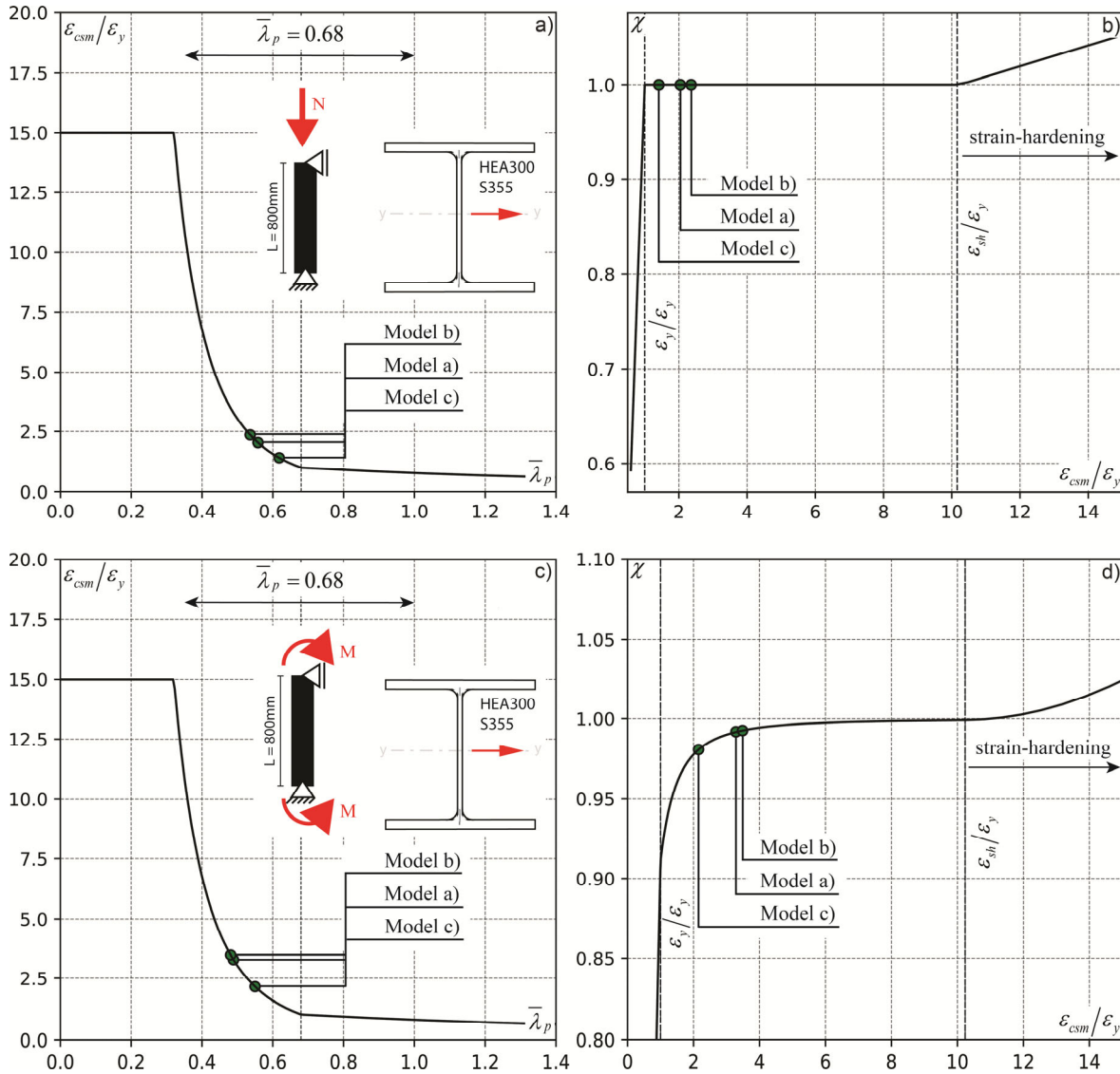


Figure 3-3: FE model influence for an HEA300, S355; a) CSM base curve, load case for compression; b) CSM based strength determination, load case for compression; c) CSM base curve, load case bending; d) CSM based strength determination, load case for compression

However, the latter would not be particularly noticeable here, since the incorporation of overstrength is a benefit per se and a clear advantage compared to EN 1993-1-1:2020 [48]. Further, the differences in the resistance calculation are not great, since the strain hardening gradient is significantly lower compared to the elastic range.

In the case of the moment resistance similar calculations were performed. The outputs regarding the CSM are summarized in Table 3-2. Figure 3-3 c) and d) shows the outcome in similar manner than for pure compression before. The difference in the reached moment resistance is more visible here, since the calculated CSM strain has a direct influence on the plasticized area over the heights of the cross-section. The biggest difference in the reached resistance, with respect to the different model approaches, would appear in the elastic range. Differences in the stocky range, especially the strain-hardening region, appear to be present but not significant for the overall method. Nevertheless, this effect can increase with a more non-linear material model as applied for cold-formed steel.

Table 3-2: Summary of simulation results for different model approaches

	Model a)	Model b)	Model c)
Eigenvalue [kN] compression	12876.80	13981.50	10505.00
Slenderness for compression	0.558	0.536	0.618
CSM strain limit for compression	2.042	2.360	1.414
$N_{pl,CSM}$	3993.75	3993.75	3993.75
$N_{pl,GMNIA}$	4017.00	4019.00	3814.40
Eigenvalue [kNm] bending	1842.03	1927.52	1479.28
Slenderness for bending	0.489	0.481	0.550
CSM strain limit for bending	3.284	3.485	2.151
$M_{pl,CSM,bending}$	487.00	483.36	481.53
$M_{pl,GMNIA,bending}$	491.70	492.60	467.20

Within a practical application for design, the method appears to be robust according to the comparison of the FE models studied here. Even if the user chooses a slightly unfavorable model for his design, this will not matter too much within the method itself. The differences in the load case for bending are around 1% for the considered profile. However, the differences may vary with the choice of other profiles, especially more slender ones. This circumstance should be investigated in further studies. Within academic comparisons, however, there may be larger differences between GMNIA shell calculations and CSM based comparisons. GMNIA results are additionally presented in Table 3-2. Hence, the CSM method considers different FE models of one selected profile indirectly by a prior slenderness calculation only. This is usually done by using additional free or

commercially available software. The subsequent calculated resistance will therefore always correspond to the models or experiments for which the CSM base curve was derived.

3.1.5 Conclusions

The purpose of Section 3.1 is to summarize, as a first step, selected and relevant drawbacks of the traditional and recent, more advanced design approaches presented in Chapter 2. In particular, Section 3.1.4 reflects the recent trend toward simulation-based solution approaches combined with advanced analysis methods. It highlights the importance of the chosen FE models in the wake of advanced analysis methods, not only for CSM, which serves as an illustrative example here, but more generally for "design by analysis" approaches in general. Although the differences are not critical to the design for the example shown, there can be significant variations depending on the local section slenderness, the profile geometry, and the material model used.

As the general trend is towards FE simulations, the focus of future tasks will be to select the "right" FE model and to be clear about the verification of these models using benchmark applications. In steel construction, this urgent requirement is addressed and included in a completely new EC3 part, the EN 1993-1-14 [72], Design assisted by finite element analysis. The treatment of topics, for strongly simulation-based approaches, such as FE modeling, validation and verification, or analysis are not only crucial, but also necessary within a generally applicable set of standards.

At this point, however, the question arises of whether this makes the method easier and more practical to use, despite precise model specifications. Specifications in themselves do not necessarily make modeling easier, but in engineering practice they can be more challenging in finding appropriate model validations and debugging. The logical conclusion is that software companies will have to adapt to these specifications in the near future. One possibility would be component-based modeling, as already practiced by the software company Idea StatiCa, especially with the newly introduced Idea StatiCa Member module. This means that the desired cross-section is only selected by the user and the higher-level modeling is taken from a software-inherent template, with any setting adjustments still to be made afterwards, i.e. boundary conditions, material parameters,

and FE discretization. In this way, a potential source of error is eliminated in the initial stages of modeling, simpler problem reconstruction with less scatter in the results is enabled, and thus time is saved at the simulation level. Nevertheless, these methods are still computationally intensive and so far limited to single components or parts. In order to apply such methods to entire structures, faster computational algorithms or advanced approaches are needed to speed up or partially replace the generally time-consuming modelling requirements and solution process, without losing accuracy and, ideally, even leading to accuracy gains. The following Section 3.2 gives a brief overview of possible *data-driven methods from the field of machine learning* as a viable path forward to overcome the mentioned shortcomings, and shows examples of already implemented applications in civil engineering.

3.2 New Approach: Machine and Deep Learning (ML/DL) in Structural Engineering

An alternative to analytical and semi-analytical design proposals are *data-driven methods*, predicated on machine-learning (ML) techniques, as they offer the possibility of creating "shortcuts" to a solution without an underlying, fully-developed analytical approach or, alternatively, a computationally intensive numerical simulation. These models typically require a certain amount of data to make reasonable predictions. This data is not easy to obtain, especially in the construction industry, and covers a wide spectrum as application areas, construction types, requirements and individual ideas vary. At the end of each project, there is always a unique product that is difficult to capture as a digital dataset due to the complex processes and numerous stakeholders involved. However, a paradigm shift can be observed due to advancing digitalization, which is not characterized by a significantly more digital data generation. Topics such as Building Information Modeling (BIM), Design by Analysis (DbA) and the broader acceptance of numerical methods are clearly in the foreground of developments in the structural engineering sciences, both at universities and in design and engineering software companies. This shows that it is already possible to digitally capture a large part of the design and construction process, generate usable data, and use it in a broader context. Data-driven

models are becoming increasingly important, enabling entirely new approaches and different ways of looking at problems. Over the past decade, a wide range of applications in the construction industry have been tested and found to work well. Current trends and thus additional examples are highlighted in this section.

3.2.1 Current trends in machine and deep learning

A variety of different Machine Learning (ML) models, here especially Deep Learning (DL) models, are available and used in all scientific and industrial fields. The most well-known applications in the public domain relate to machine vision for the development of autonomous driving and image generation or to text-based dialog systems, i.e., chatbots that generate text output depending on the input request. The current trends in machine learning and deep learning for civil engineering applications can be divided into several application areas, including the use of deep neural networks (DNN), convolutional neural networks (CNN) [170]–[173], support vector machine (SVM) [174]–[178], boosting algorithms (BA) [179]–[186] or random forest (RF) [187], and decision trees (DT). The main application areas relate to structural capacity prediction, fire resistance prediction, damage detection and monitoring, failure analysis and monitoring, structural analysis of truss structures, and mechanical property prediction. A particularly detailed summary of the current state of the art in machine learning for civil engineering, with about 580 references, was recently published by Thai [188]. It includes a general introduction to a wide range of topics related to ML as well as links to available datasets from civil engineering. Therefore, the reader is referred to [188] for a general overview of the topics and further information.

With respect to artificial neural networks (ANN), the following variants with corresponding model philosophies have gained increasing attention in recent years.

- i. **DNN:** Classical feed forward networks are used for the direct prediction of classes or float values as a target condition, using a set of input values/features from a space of available parameters. This prediction method is currently one of the most common strategies related to Deep Neural Network (DNN) applications. In its classical implementation, it is suitable for predicting problems by minimizing

a cost or loss function, usually using the mean square error (MSE) or cross entropy loss function for regression and multiclass classification problems, respectively.

- ii. **CNN:** Convolutional neural networks are of great interest for image based classification problems. The image is used as an input to generate the features for a fully connected classification network. The feature extraction is usually done with alternate layers of convolution and pooling.
- iii. **cVAE:** Conditional Variational Autoencoder are gaining popularity in generative design applications, providing additional advantages compared to normal DNN applications. The main reason for its use is the model architecture itself, providing a forward performance predictor for given design features (conceptually comparable to feed forward DNN models), as well as an inverse design features predictor conditioned on sets of performance requests. This optional solution method is particularly suitable in design tasks to exploit possible solution spaces for given problems.
- iv. **PINNs:** Physics-Informed Neural Networks use the DNN architecture incorporating physical laws by including partial differential equations together with a corresponding set of boundary and initial conditions as penalty terms in the loss function [189]. The idea behind PINNs is to use the neural network to approximate the solution to a partial differential equation (PDE) or a system of PDEs that describes a physical system. The network is trained using data from the physical system, and the loss function includes both a data-fitting term and a physics-based regularization term. The advantage of PINNs over traditional methods for solving PDEs is that they do not require explicit discretization of the PDE, which can be computationally expensive and difficult for complex systems. Instead, PINNs learn the solution implicitly by training the neural network using data from the physical system. Background references are provided in [190]–[193].

3.2.2 Selected application examples in the field of steel structures

A number of observations using different ML models throughout all fields of structural engineering has been performed within the last decades, testing its limits and opportunities. Some selected examples from structural steel design is referred to below.

In [194], DNNs were used to estimate the available rotation capacity of cold-formed rectangular and square hollow section steel beams. The used database for RHS and SHS profiles was collected from available experimental results from literature [27], [128], [195], [196]. In [197] and [198] DNNs were used to predict the flexural overstrength factor for I-shaped, as well as RHS and SHS steel beams; used datasets were collected from [44], [46], [47], [196], [199]–[207]. Further the overstrength factor for steel thin-walled circular hollow section beams was predicted using genetic programming (GP) and neural networks [198]. Available data was collected from experimental investigations published in [208]–[216]. It was shown that models based on DNN approaches could predict the flexural overstrength factor, as well as the rotation capacity with high accuracy.

Fonseca, in [217]–[219], developed and trained NN models to predict and obtain new data for the patch load behaviour, using different modelling and feature engineering approaches. In [220] an additional neuro fuzzy system was implemented to consider the difference in the beam structural collapse behaviour (web and flange yielding, web buckling and web crippling) in the form of a pre-set classifier, leading to more accurate results compared to existing code provision.

Predictions of the axial compression strength of steel members were investigated in [221]–[224] exploring the possibilities of artificial neural networks (ANN), boosting (XGBoost) and random forest algorithms, as well as support vector machine (SVM). The prediction performance for the buckling strength of steel members, corresponding to different instability cases for local [225]–[235], distortional [236]–[240], global [241]–[244] and lateral torsional buckling [245]–[247], was investigated using mainly ANN models. Application cases, where the flexural and torsional strengths of members was predicted is referred to in [198], [248]–[261]. Again, in most cases ANN models were used, dominating this field of applications.

3.3 Research Gaps

Building on the previous chapters, the above review of shortcomings of traditional methods and the possibilities presented by data-driven, machine-learning based approaches,

specific *research gaps* can be identified, which describe the currently missing knowledge that is i.) required to achieve the desired technological objective and/or ii.) may result as complementary insights from this thesis work.

As set out in Chapter 1, this thesis aims at developing an alternative method for the beam-element design of steel structures, which is able to capture buckling- and plasticity-induced nonlinearities, and, crucially, to accurately determine the structures' "real" plastic redistribution mechanisms and deformation capabilities. Thereby, Machine Learning techniques such as DNNs are to be used to augment the stiffness matrices of the traditional beam-element FEM implementation (Direct Stiffness Method – DSM) and include non-linear terms that account for the above inelastic effects. This method is termed "DNN-DSM" in this work and its development and successful implementation forms the working hypothesis of this doctoral dissertation.

The achievement of this goal brings forward a number of significant *research gaps*, which need to be addressed in the dedicated chapters of this thesis. The following, main research gaps were thereby identified.

Research Gap 1: data development from FEM simulations

The DNN-DSM method to be developed requires a thoroughly trained and validated artificial neural network for the prediction of non-linear stiffness terms at every loading step in structural components. The basis for this development is the availability of the corresponding training data, which must consist of many thousands, if not millions, of results for such stiffness terms, for various types of considered cross-section shapes, materials, load cases and load stages. Due to the cost and complexity of physical tests in structural engineering, it is impossible to develop this data purely experimentally. One working hypothesis in this thesis is thus that the corresponding data can be retrieved from localized numerical simulations, using shell elements. In a complex data development procedure, the thesis will thus need to address the validation of the FEM simulations against physical tests and explore the needed quality and quantity of data. The previous experimental findings of the project Hollosstab, during which over 140 full-scale physical tests on various types of structural hollow sections were performed, are used as the main starting point for this data development.

Research Gap 2: representation of the inelastic buckling behaviour of thin-walled steel members through beam-element stiffness matrices

Artificial Neural Networks have been used to predict various features and performance criteria in structural engineering, as described in Section 3.2.2. Some applications include the augmentation of stiffness matrices, mostly in the field of shell elements for composite structures. However, to the author's best knowledge, the present implementation, where the overall non-linear behaviour of structures is determined from DNN-predicted beam stiffness terms through "traditional" non-linear FEM matrix solution algorithms, has not been attempted in this form before. The approach presents several challenges in need of research, among them the analysis of required features of the DNNs, the need for subdivisions of the problem into various subsets and solution branches, and generally its implementation. The path from the training of the DNNs to the implementation in a bespoke stiffness matrix formulation and, finally, the validation against tests will allow to tackle this overarching research gap.

Research Gap 3: secondary knowledge gain on the behaviour of steel members:

Feature engineering of the produced dataset, as basis for ML-based predictions of the behaviour of such elements trained on a large synthetic dataset, can provide insights both for the method itself and for the wider topic of structural stability, as it allows to identify correlations and relationships between variables that have not previously been recorded or could not be exploited.

Part II

4

Deep Learning

Introduction, Overview and Concepts

Chapter 4 serves to provide a brief insight into machine learning as used in the context of this thesis. Note that this chapter is not a general introduction to this topic, but rather deals, with a depth deemed appropriate to understand the research methodology and output used in the context of the thesis. The interested reader is referred to the relevant scientific and formative literature for further information.

4.1 Terminology – Machine Learning in a Nutshell

4.1.1 Artificial Intelligence and Machine Learning

Learning in a general manner (in the explanation space of an “average human”) is associated with the acquirement of knowledge or skills, the memorization of information by repetition (intentional or incidental), coming along with a change in experience and behaviour based on individual experience in or with the environment.

In the context of machine learning, learning refers to the process by which a machine learning model improves its performance based on the given data. The core idea of “learning” in machine learning is that a chosen model learn from the available data rather than being explicitly programmed. In other words, the process of learning is an optimization process which tries to find the minimum in a given feature space by automatically identifying patterns, relationships and structures in the data. The most common learning types are presented in the following section.

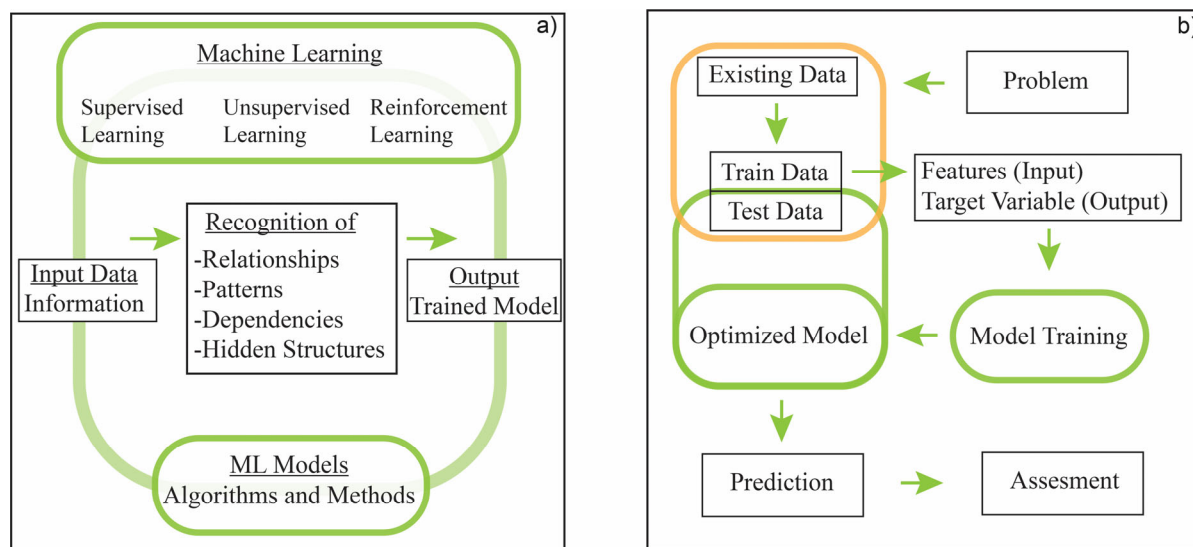


Figure 4-1: a) Classification of ML groups and independent pattern recognition; b) Conceptual ML workflow

Machine learning (ML) is a subfield of artificial intelligence (AI), but also a tool for other fields such as data mining [262], [263]. The term AI describes the ability of a machine or algorithm to mimic intellectual abilities such as problem solving, learning, and pattern

recognition. It includes all systems that act based on perceptions from the environment in a way that increases the probability of achieving a successful goal [3], [264].

Machine learning, as seen in Figure 4-1 a), is about computer systems learning to independently recognize patterns and relationships based on given data and to improve themselves without the need for additional programming. Parts of the program code are created by the computer itself. In doing so, machine learning uses mathematical methods, especially from statistics, to create code parts and models. Using the learned data and the resulting models, machine learning can be applied to new, unknown data sets to make predictions, decisions or inferences, and optimize processes [265].

A general workflow that applies to most models in the framework of supervised learning is presented in Figure 4-1 b). The starting point is a problem that lacks of an analytical solution, is computationally expensive or lacks of a general understanding. One main aspect of a successful ML application is existing data which the model is trained on. For this, the data is usually separated into a training and testing data set. Note, only the training data set is used for model optimization. The test data is exclusively used to validate the trained model. In term of supervised learning the data set consists of problem related features (input values) and known target values (output). After trained procedure the model is assessed with independent test and even new (unseen) data.

4.1.2 Structured and unstructured data

In general, the available data in the field of machine learning is commonly divided in two different types, i.e., structured and unstructured data.

Structured data is usually organized and ordered in a predefined manner, following a specific scheme in the format of tables or spreadsheets. This data form has fixed set of columns and rows. Each column represents a so called attribute or feature and each row a specific value of the feature. Therefore, a possible feature can be the thickness, representing many different cross-sections or the sensor data from an experiment recorded over a specific period of time.

On the other hand, unstructured data has refers to data that does not have a predefined format or organization. This data comes typically in the form of text, audio or pictures (as well as videos). In the case of a picture the relevant information is extracted by a decomposition of the picture using the information from each pixel, i.e., the RGB space. In convolutional neural networks this information is further processed by manipulating the data through convolutions, pooling functions and subsequently flattening into a feature space.

4.1.3 Subgroups of learning algorithms

Machine learning algorithms can be divided into three groups, i.e., supervised, unsupervised and reinforcement learning, all of which are ultimately concerned with forming or learning the mathematical function $f: X \rightarrow Y$, see Figure 4-1 a). The following three groups differ only in the quantities X and Y and the appearance of the data needed to learn the function. A brief description is given as follows:

- i. **Supervised learning** is a type of machine learning algorithm in which an AI model is trained on a labeled data set, i.e., the data set contains input data along with the corresponding correct output data. The goal of supervised learning is for the AI model to learn the underlying patterns and relationships between the input and output data so that it can accurately predict the output for new input data that it does not yet know. During the training phase, the AI model receives input data and the correct output data for reference. The model learns to recognize patterns and relationships within the data and adjusts its internal parameters to optimize its predictions based on the differences between the actual and predicted outputs. In supervised learning, there are two main types of problems that can be addressed, i.e., classification and regression. Classification is a type of problem where the goal is to predict a categorical label or class based on input features. The output layer is multidimensional and the target set Y is discrete [263]. During training, the model learns to identify patterns and relationships between the features and the labels, and to predict the correct label for new input data. In regression, continuous numerical values are expected as output. The output layer usually one-dimensional and the target set Y is continuous.

- ii. **Unsupervised learning** is a type of machine learning algorithm in which an AI model is trained on an unlabeled dataset, i.e., the dataset does not contain predetermined correct output values. The goal of unsupervised learning is to identify underlying patterns and relationships in the data without knowing in advance what the output should be. In unsupervised learning, the AI model is tasked with recognizing the inherent structure of the input data by identifying patterns and similarities between data points and clustering them based on those patterns.
- iii. **Reinforcement learning** is a type of machine learning algorithm that allows an AI model to learn through a process of trial and error. It interacts with an environment in a sequence of actions and observations. The model receives a reward or punishment based on the actions it performs and the results of those actions. The goal of the model is to learn to perform actions that lead to the highest cumulative reward over time by learning the best course of action through trial and error.

4.1.4 Overview of machine learning algorithms

According to the described learning subgroups above, different machine learning algorithms have been developed over the years and are present in the literature. Some of the most popular algorithms, associated with (deep) neural networks only, were partially described in Section 3.2.1 in the context of the research gap of this thesis. Apart from deep neural networks, plenty other algorithms exist in the framework of machine learning. An overview is presented in Figure 4-2. The most common techniques, which are currently used in civil engineering applications are linked to supervised learning and problem definitions corresponding to regression (prediction of float values) or classification (prediction of probabilities).

A clear overview of machine learning models and trends in civil engineering applications is provided in [188]. It contains a bibliometric study on the current literature related to ML methods for structural engineering applications, including results from 485 relevant publications since 1989 – the first relevant article was published by Adeli and Yeh on perceptron learning in engineering design [266]. The survey identifies that in 56% of all

applications (here always in the context of civil engineering application) neural networks are the most commonly used. This trend is followed by the family of boosting algorithms with 11% of all accounted application, with XGBoost as the most prominent representative. With respect to the applications, 38% are connected to structural members, 29% to material properties, 18% to damage detection and SHM (structural health monitoring via damage detection and condition assessment), 11% to analysis and design and 4% to fire design.

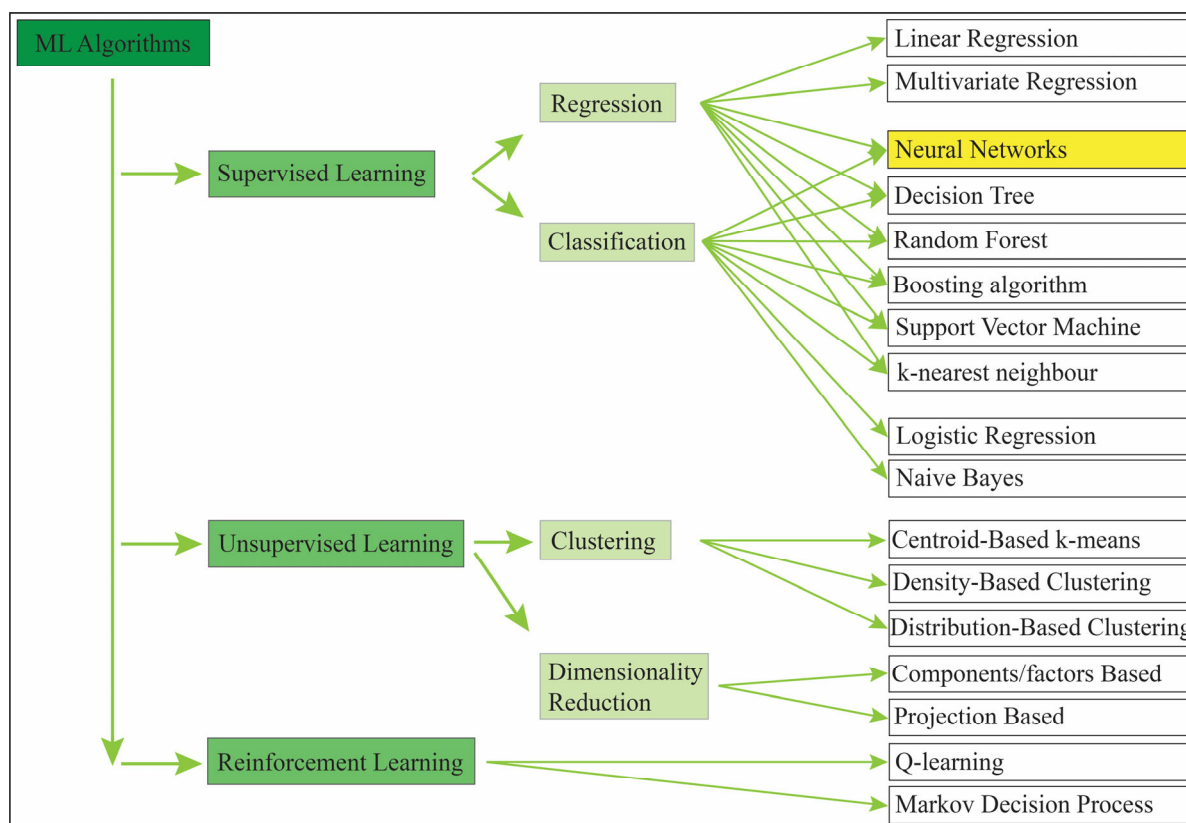


Figure 4-2: Machine learning algorithms from literature, partially based on [188]

4.2 Conceptual Introduction to Deep Neural Networks (Deep Learning)

4.2.1 Brief background information

In general, the idea of neural networks is not new and has its beginnings already in the 1940s through the work of McCulloch and Pitts [267] on "neurological networks". The

motivation for such methods lies in the logical description of the transmission of “impulses” between individual neurons within a larger nervous system, where each neuron simplistically consists of a soma and an axon. Pulse transmission occurs between the axon of one neuron and the soma of another neuron, which are connected by synapses that transmit (or fail to transmit) a signal depending on a threshold value. Later work by D. Hebb [268] led to the so-called "Hebb's learning formula", which can be described by the phrase "neurons that fire together wire together", meaning that the connection between neurons is strengthened when signals are transmitted together, which is consistent with the general rule of learning by repetition. After further developments, a paper by Marvin Minsky and Seymour Papert [269] was published in 1969, providing a detailed mathematical analysis of the perceptron, an early type of neural network for binary classification without hidden layers. The basic message of this work is that complex problems require more complex neural network architectures and thus more computational effort. This led to some disillusionment and, as a sum of further shortcomings, to the first, so-called "AI winter" in the late 1970s. After further ups and downs and advanced developments such as the multilayer perceptron (MLP) in the last decades, machine learning (ML) and especially deep neural networks (DNN) are now widely used in all technical application areas. This increasing popularity is fueled by access to large amounts of data, the availability of graphics processing units (GPUs), the development of algorithms, and easier access to the machine learning field - than decades ago - through the development of high-level libraries/APIs.

4.2.2 General representation of a neural network

4.2.2.1 General representation

A common representation of an artificial neuron (perceptron) is shown in Figure 4-3 a) and can be written as follows:

$$y(x) = a \cdot \left(\left(\sum W_n \cdot x_n \right) + b \right) \quad (4-1)$$

It consists of three main components, the weights, the bias and an activation function. The input parameters (features) are multiplied with randomly initialized weights, which are updated over a certain number of epochs during the training of the DNN model and are an indicator of the strength of a connection within a network. Parameters which do not affect the overall prediction are set over the training period to small values. The bias is an additional trainable value (zero or non-zero) which is added to the summation of the weighted inputs in a neuron. The neuron is mathematically represented through a single vector, which is passed to an activation function with an inherent predefined threshold. This concept can be further expanded to a more complex systems with more neurons and layers to increase the amount of trainable parameters for more non-linear problems, see Figure 4-3 b). All necessary components (weights, biases, activation functions) are presented in the following sections.

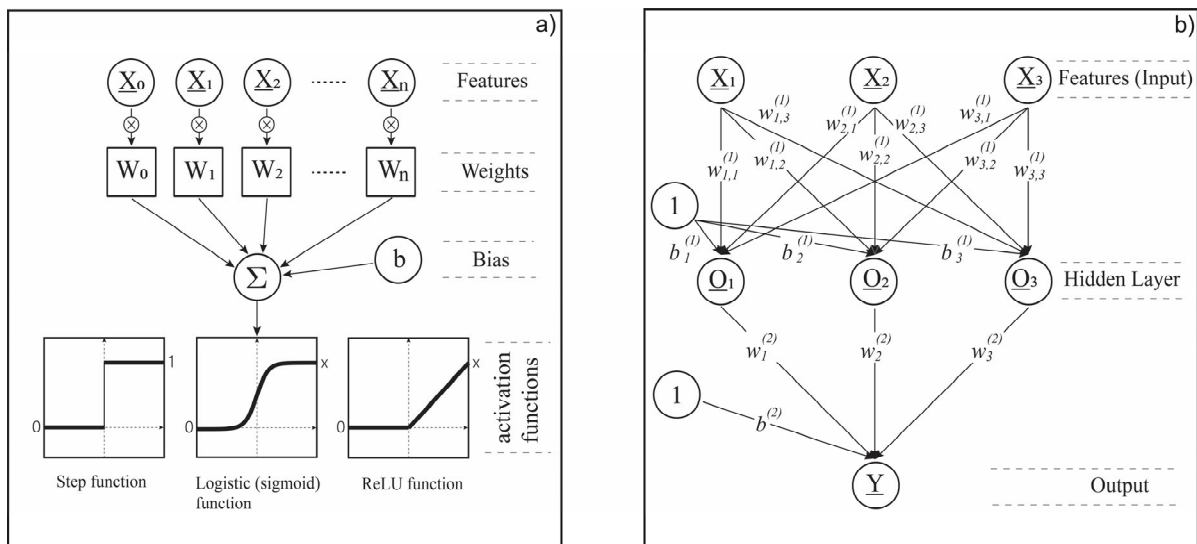


Figure 4-3: General representation of a) single-layer perceptron; b) multi-layer perceptron

4.2.2.2 Weights and biases

The weights of a deep neural network refer to the collection of numerical values assigned to the connections between the nodes (neurons) of the network, see Figure 4-3 b). These values determine how much the signals received by one neuron affect the signals sent to the next neuron. It is valid that the higher the absolute value of the weight of a neuron, the greater the influence of that neuron on the overall result. The weights

are updated (optimized) through a process called backpropagation, in which the network is trained with a set of labeled data (supervised learning). The optimization goal is to minimize the difference between the predictions and correct outputs.

The bias is an additional input value added to each neuron. It is represented as a constant value, often initialized to 1 or 0 in cases where it is to be neglected, and is not affected by the input data or weight. The bias is typically used to shift the neuron's activation function left or right to allow the network to learn more complex patterns in the data. In addition to the weights, the bias value is also adjusted by backpropagation during the optimization process.

4.2.2.3 Activation functions

The activation function is a mathematical function that converts the output of each neuron. It determines whether a neuron should "fire" and forward a signal to the next layer of the network based on the input it receives. Its purpose is to introduce nonlinearity into the network, allowing it to learn more complex relationships from the input data. Without an activation function only a linear transformation of input data is passed. The activation function should be differentiable, as this requirement is advantageous in weight optimization.

A number of activation functions are known in the literature [263]. Below are some activation functions that are frequently used.

- i. Sigmoid: A sigmoid function is an S-shaped curve that maps each input value to a value between 0 and 1. It is often used in binary classification problems. Unlike a pure step function, which can only represent false = 0 or true = 1, the sigmoid function also gives values in between, see Equation (4-2) and (4-3).

$$f(x) = \begin{cases} 0, & x < 0 \\ 1, & x \geq 0 \end{cases} \quad (4-2)$$

$$f(x) = \frac{1}{1 + e^{-x}} \quad (4-3)$$

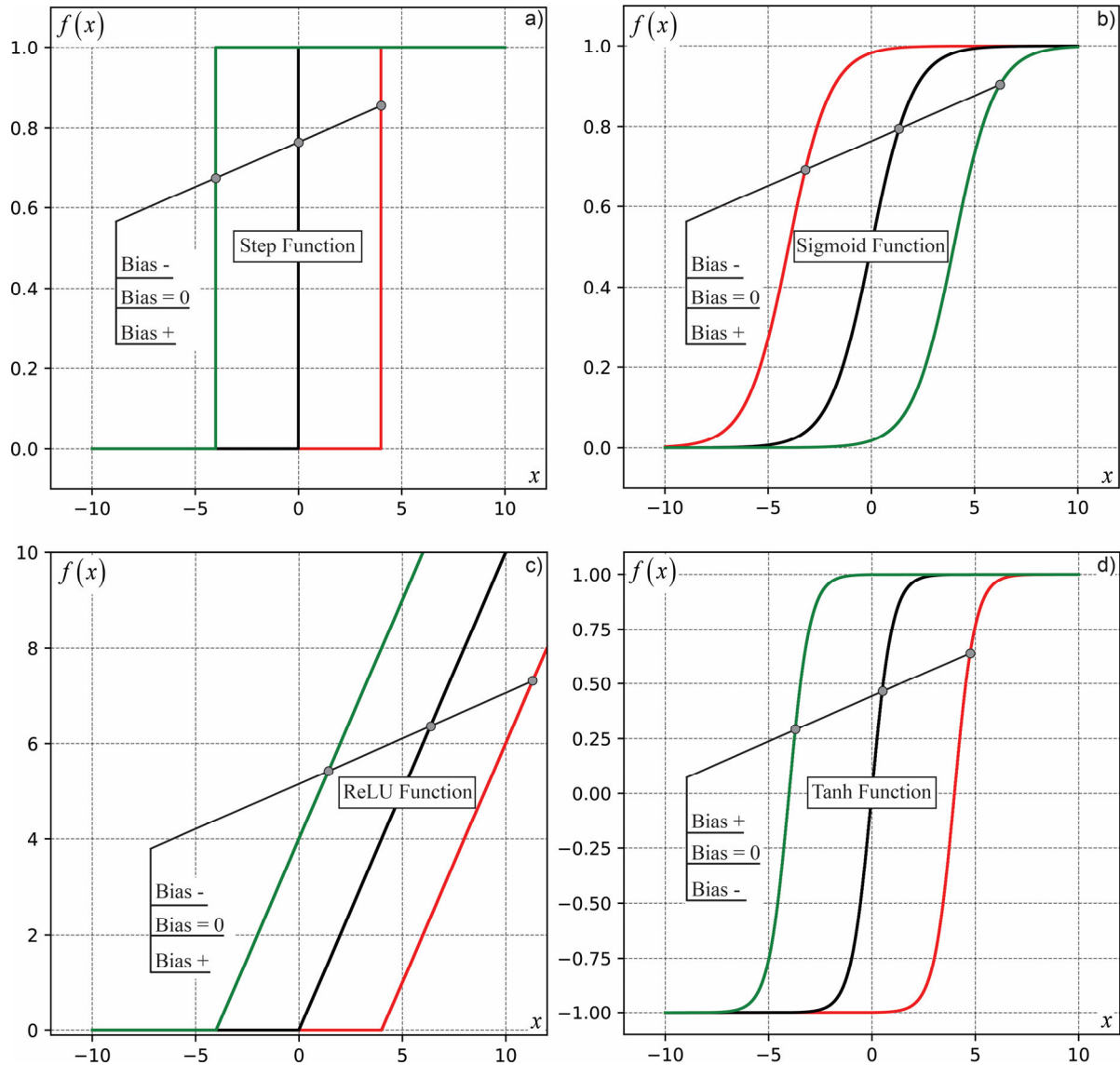


Figure 4-4: Common activation functions and influence of the bias

- ii. ReLU (Rectified Linear Unit): A ReLU (see Equation (4-4)) function returns the input value if it is positive and zero otherwise. It is often used in Deep Learning because it is computationally efficient and has been shown to be effective in many types of neural networks.

$$f(x) = \max \begin{cases} 0, & x < 0 \\ x, & x \geq 0 \end{cases} \tag{4-4}$$

- iii. Tanh (Hyperbolic Tangent): A Tanh function (see Equation(4-5)) is similar to a sigmoid function, but maps the input values to a range between -1 and 1.

$$f(x) = \frac{e^{2x} - 1}{e^{2x} + 1} \quad (4-5)$$

4.3 Optimization Procedure in Deep Neural Networks

4.3.1 Loss functions and performance evaluation

The chosen loss function plays a central role in updating the weights w and biases b of the a NN. It helps to determine the loss or error L after a training run. A deviation is calculated between an arbitrary true result y_i from the data set and the corresponding predicted result of the DNN \hat{y}_i , which is a measure of how far the output of the NN is from the desired response. An appropriate, problem dependent loss function is crucial for the optimization behaviour and steers the overall learning success. However, in terms of regression problems two very common error metrics are used as loss definitions, i.e., the mean squared error (MSE: Equation (4-6)) and the mean absolute error (MAE: Equation (4-7)).

$$MSE: L = \frac{1}{N} \sum_{i=1}^N (\delta_i)^2 = \frac{1}{N} \sum_{i=1}^N (y_i - \hat{y}_i)^2 \quad (4-6)$$

$$MAE: L = \frac{1}{N} \sum_{i=1}^N |\delta_i| = \frac{1}{N} \sum_{i=1}^N |y_i - \hat{y}_i| \quad (4-7)$$

The accuracy of regression based problems are generally measured with the R-squared (r^2) metric, also known as the coefficient of determination and provides information on how well the models fits to the compared data. In the context of deep neural networks, R-squared is calculated by comparing the predicted outputs of the DNN model \hat{y}_i with the actual true values y_i . It measures the proportion of the variance in the target variable that can be explained by the model. The R-squared value ranges from 0 to 1, with a higher value indicating a better fit and capturing the variability in the data. The calculation is represented through Equation (4-8). First the total sum of squares (TSS) is calculated, representing the total variability in the target variable. Then the residual sum of

squares (RSS) is evaluated, measuring the variability that remains unexplained by the DNN model. r^2

$$r^2 = 1 - \frac{RSS}{TSS} = 1 - \frac{\sum_{i=1}^n (y_i - \hat{y}_i)^2}{\sum_{i=1}^n (y_i - \bar{y}_i)^2} \quad (4-8)$$

where:

$y_i, \hat{y}_i, \bar{y}_i$ is the actual output, the predicted output and the standard deviation of the actual output

4.3.2 Gradient descent and backpropagation

The general learning/optimizing process in such a feed forward network is performed by using backpropagation as a technique to update the weights within a training period. Therefore, the Nabla-Operator and the chain rule are used to calculate the gradients of all nodes within a network (see Equation (4-9) and (4-10)).

$$\nabla = \begin{pmatrix} \frac{\partial}{\partial x_1} \\ \frac{\partial}{\partial x_2} \\ \vdots \\ \frac{\partial}{\partial x_n} \end{pmatrix} \quad (4-9)$$

$$\frac{\partial u}{\partial x} = \frac{\partial u}{\partial v} \cdot \frac{\partial v}{\partial x} \quad (4-10)$$

In order to “push” the calculation in the direction of the steepest descent a gradient method is used as follows:

$$x^{(j+1)} = x^{(j)} - \eta \cdot \nabla f(x^{(j)}) \quad (4-11)$$

where:

$x^{(j+1)}$ is the updated value, i.e. the weights and biases

η is the parameter or learning rate between 0 and 1, giving more stability to the used optimization method

∇f is the Nabla-Operator for partial derivative

While updating all weights and biases within a network a cost or loss function is used, which is minimized throughout the training and therefore calculated as the error between a predicted value \hat{y} of the DNN model and the true value y .

4.3.3 Influence of the amount of neurons

There is a correlation between the number of neurons and the chosen activation function. In the following, an example of this relation can be seen in Figure 4-5. The goal of the neural network is to learn the behaviour of the black non-linear curve. With a single neuron and the ReLU activation function, the neural network model cannot represent a polynomial behaviour with a sufficient accuracy (see Figure 4-5 a) red curve). The simple model lacks the flexibility to replicate the nonlinearity of the polynomial, representing just the ReLU activation function. When more neurons are added to the NN (see Figure 4-5 b), c), d)), multiple ReLU functions are superimposed to map the problem behaviour. With 8 neurons, the right-hand side of the polynomial is already very well represented. With 12 neurons in the NN model, the whole non-linear behaviour can be reproduced well within the area of interest. This means in this context, that with each additional neuron, the model gets closer to the desired target values.

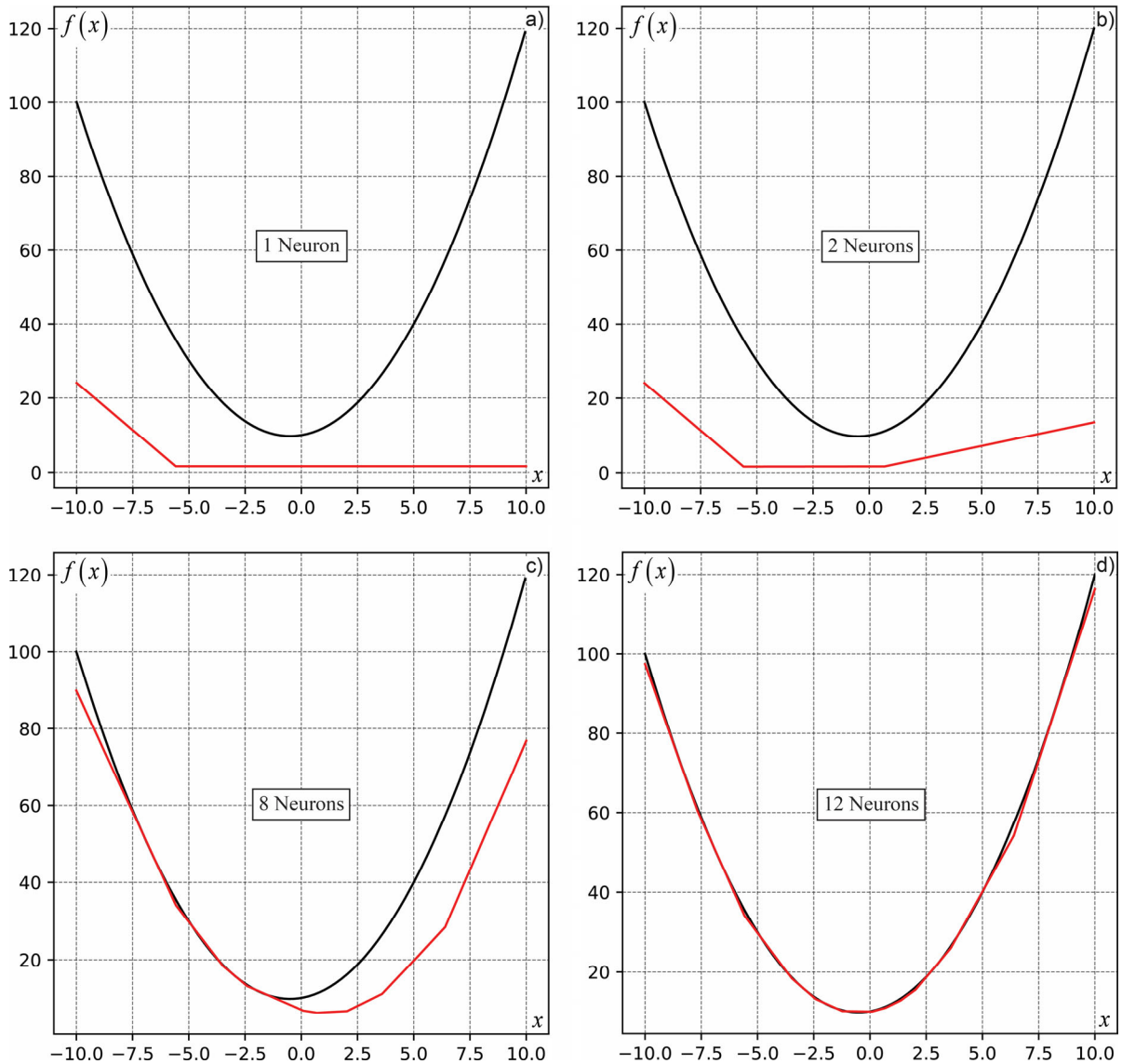


Figure 4-5: Influence of the amount of neurons on the prediction accuracy, ReLU activation function

4.3.4 Feature transformation

The overall estimated accuracy of a neural network is highly dependent on the quality and distribution of the input parameters. In many cases it is therefore necessary to transform or scale these values, using different methods like normalization (see Equation (4-12)) or standardization (see Equation (4-13)) as follows. This necessary procedure is often described throughout literature such as in [263].

$$\hat{x}^{(i)} = \frac{x^{(i)} - x_{\min}^{(i)}}{x_{\max}^{(i)} - x_{\min}^{(i)}} \quad (4-12)$$

$$\tilde{x}^{(i)} = \frac{x^{(i)} - \bar{x}^{(i)}}{\sigma} \quad (4-13)$$

where:

- $x^{(i)}$ is the x^{th} value of an input feature
- $\bar{x}^{(i)}$ is the mean value of an input feature
- σ is the standard deviation of an input feature

Data transformation eliminates the major problem of multiple features having different magnitudes, ranges and units by scaling them down to preset boundaries. Therefore, data normalization is used to scale the magnitudes of available features between the values of 0 and 1 (or -1 and 1), corresponding to the lowest and highest values. Standardizing the data means rescaling it, while the mean value is set to 0 and the standard deviation to 1. In a lot of engineering applications data standardization shows better performance evaluations, since outliers are taken better into account.

5

Finite Element Models

Investigations on Buckling Half-wavelengths, FE Assumptions and Simulations

Outline of the chapter:

This chapter provides background information on the verification and validation of finite element models from experimental investigations based on the Hollosstab project, which were subsequently used as the main source of data for the training of deep neural networks for the DNN-DSM method.

5.1 Experimental campaign in the project HOLLOSSTAB

The generalized slenderness based resistance method (GSRM), presented in Section 2.6, is strongly linked to the investigations carried out in the RFCS (Research Fund for Coal and Steel) funded project Hollosstab (2016-'19). The finite element models developed and employed in Hollosstab were validated on a large series of experimental tests. These models, and thus this validation work, form the basis for the FEM models employed in the present thesis, which are used herein for large-scale data generation on hollow section non-linear behaviour in Chapter 6 of the thesis. Thus, this chapter of the thesis provides background information on some key facts of the project, conducted experimental investigations (here only related to RHS/SHS profiles), auxiliary tests and subsequently the finite element modelling assumptions made for validation and calibration aspects in the framework of the HOLLOSSTAB project.

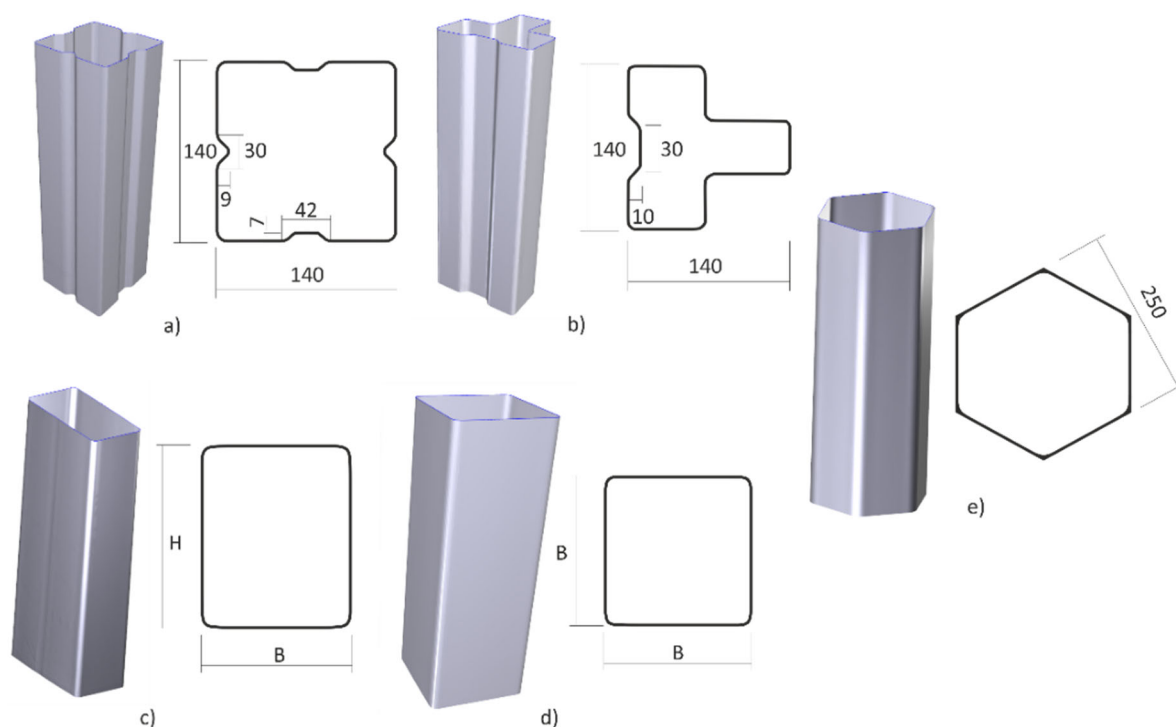


Figure 5-1: Used cross-sections within WP4 of the Hollosstab project, a) squared hollow section with stiffeners (SHS-S); b) squared hollow section with stiffeners and T-shape; c) rectangular hollow section (RHS); d) squared hollow sections (SHS); e) hexagonal hollow sections (Hex), adopted from [270]

The HOLLOSSTAB project produced a high number of experimental test results, i.e. results from stub column tests loaded with different N-M interactions, as well as results from

auxiliary tests to characterize the mechanical properties of used steel grades. Apart from classical experimental investigations additional 3D surface scans of whole specimens were taken and coupled with detailed evaluations of geometrical imperfections. The process of those investigations was documented and explained throughout several publications [2], [74], [162], [270]–[272] and project intern deliverables. A full overview of all work packages, their final outcomes and subsequent design proposals is provided within a final report [161] of the whole project.

5.1.1 Full scale tests

The full experimental campaign of the Hollosstab project was conducted at the laboratories of Bundeswehr University Munich (UniBW, Prof. Taras), Imperial College London (ICL, Prof. Gardner) and Istitute Superior Técnico in Lisbon (IST, Prof. Silvetsre) and included investigations on cylindrical (CHS), rectangular (RHS), squared (SHS), hexagonal and lip-stiffened hollow sections, with different steel grades ranging from S355 to S890, as well as lengths. The specimens were made in accordance to EN 10219 [5] (cold-formed cross-sections) and EN 10210 [4] (hot-finished cross-sections), see Figure 5-1 (also published in [270] and [2]).

The specimens were short or medium-length members subjected to pure compression, mono-axial bending and bi-axial bending (in a few cases). The used profiles for the full scale tests had varying thicknesses, load eccentricities, lengths and material properties. A summarizing overview is provided by Table 5-1. In the following, however, reference will only be made to the experiments conducted at the UniBW. This is mainly because the author personally participated in these experiments and the validation of the FE models used here is based on the same.

Table 5-1: Summary of varied parameters within experimental tests conducted at UniBW, ICL and IST, adapted from [161]

Parameter	Min	Max
Test eccentricity	0 mm	460 mm
Length	150 mm	800 mm
Steel grade	S355	S770
W or H length	50 mm	300 mm
Thickness	4 mm	8 mm

Figure 5-2 provides an overview of the test setup at UniBW for short members loaded eccentrically (see Figure 5-2 a)); the figure includes sketches of eccentricity application levels for applied N-M interactions (see Figure 5-2 b)) and a corresponding test setup representation for N-M-interactions (see Figure 5-2 d)).

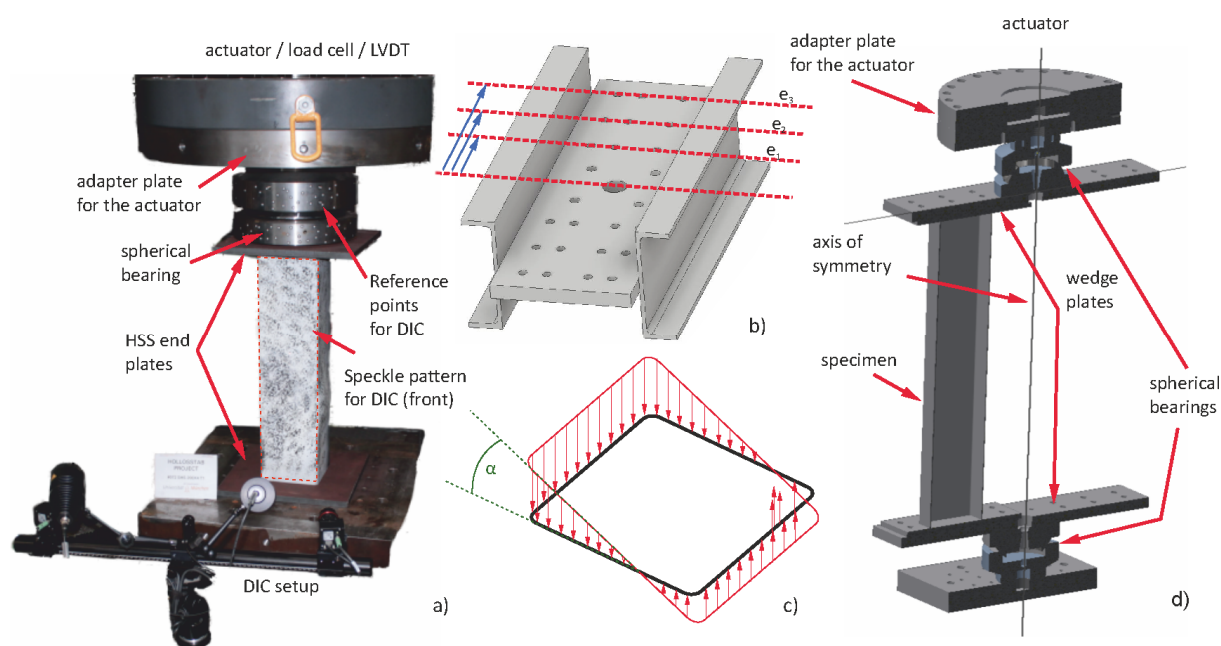


Figure 5-2: a) setup for the stub-column test; b) eccentricity level; c) tensional field induced by N-M-interaction; d) scheme of N-M-interaction test setup [161]

Table 5-2: Summary of tested cross-sections (WP4) at UniBW, adapted from [270]

Cross-section size	Steel grade	Class	Standard
SHS 140×140×4	S355	3	EN10219
SHS 200×200×5	S355	4	EN10219
SHS 200×200×8	S355	1	EN10219
SHS 200×200×4	S500	4	EN10219
SHS 200×200×5	S500	4	EN10219
RHS 300×150×6	S355	1-4	EN10219
RHS 300×150×8	S355	1-4	EN10219
SHS-S 140×140×2.5	S350GD	-	-
SHS-S 140×140×3.5	S350GD	-	-
SHS-T 140×140×2.5	HX460	-	-
SHS-S 140×140×4.0	HX460	-	-
HEX250×8.5	S355	-	EN10210

Full scale tests were sampled into 5 categories, depending on the load case and length of the used profiles, i.e. T1, T2, T3, T4 and T5. Test from T1 to T4 provide an increasing eccentricity with an equal profile length of 800 mm to induce N-M interaction. The eccentricities of T5 tests are in general equivalent to T3 tests, yet using a higher length of 2000 mm to display a global + local phenomena in the test procedure. Interactive behaviour was investigated this way. An overview of different eccentricities and lengths is provided by Table 5-3.

Table 5-3: Summary of test categories and specimen lengths (WP4) at UniBW, adapted from [270]

Test category	Top eccentricity in [mm]	Bottom eccentricity in [mm]	Specimen length in [mm]
T1	0	0	800
T2	9 – 64	0	800
T3	57 – 196	57 – 196	800
T4	232 – 457	232 – 457	800
T5	57 – 196	57 – 196	2000

5.1.2 Evaluation of local imperfections: Reverse engineering of specimen geometry

5.1.2.1 Set-up used for the measurements

The influence of local and global imperfections was already discussed in Section 2.1.6, pointing out the effects on the ultimate load bearing capacity, as well as the post-buckling behaviour and plastic hinge formation. The aim of investigating these influences was necessary and was approached as described in the following.

In order to measure the distribution of local geometric imperfections of entire specimens, a 3D laser-scanning technique was applied. The use of scanners lead to a non-contact, precise and relatively easy recording method of imperfections resulting in full scale 3D-surface scans containing a huge amount of measured points. To scan and record the spatial point clouds, a Zeiss 3D scanner was used. The data was initially processed in the software “Colin3D” [273], by Carl Zeiss Optotechnik GmbH, to make first refinements within the point quality, i.e. removing unnecessary points or filling holes. This prelimi-

nary step was later on replaced and performed directly in the software “Geomagic Design X” [274]. In all considered cases, the full-scale specimens were first 3D-scanned to later on reproduce the real geometry in numerical simulations. This procedure is commonly used to digitize an arbitrary geometry and optimize features within this geometry for further fabrication or production tasks (3D printing) and is in general termed as “reverse engineering”. The reverse engineering process used for the Hollosstab project is presented in the following section.

5.1.2.2 Derived reverse engineering work flow

The reverse engineering workflow can be split in two main procedures, dependent on the desired results. The direct “3D-Scan to FE-Modelling”, as the first procedure, requires a scanned surface in a point cloud format obtained from the test specimen, symbolizing the generated raw data. In order to use the scanned point cloud shape for the finite element model geometry an intermediate step is necessary, where a spline surface is generated. This step can be achieved by appropriate commercial software like Geomagic Design X [274], CloudCompare [275]. The real specimen geometry can subsequently be implemented into a FE based program in order to evaluate the laboratory test and assess the imperfections. This approach was already tested and performed successfully in [2], [276], [277][9], [10] and [11] using the commercially available FE Software ABAQUS [146].

The second reverse engineering procedure is labeled as “3D-Scan to Imperfection Analysis”, where the effective imperfections of the real specimen geometry are determined by using the scanned-surface data and comparing it with a CAD-Model of nominal or perfect geometry. This step symbolizes the initial imperfection analysis and gives an overview of the imperfections along the specimen (see Figure 5-3). Yet, at this analysis level, it is rather inaccurate to discuss the isolated magnitude of local imperfections, since effects like sagging and ovalization are inherently present. This particular problem is less of a problem in SHS and RHS profiles than in CHS profiles. To eliminate these particular effects or even being able to pick different “imperfection modes” out of the whole imperfection spectrum, it is necessary to make additional steps that commercial software does not necessarily provide. This strategy is further presented in Section 5.3 of this thesis.

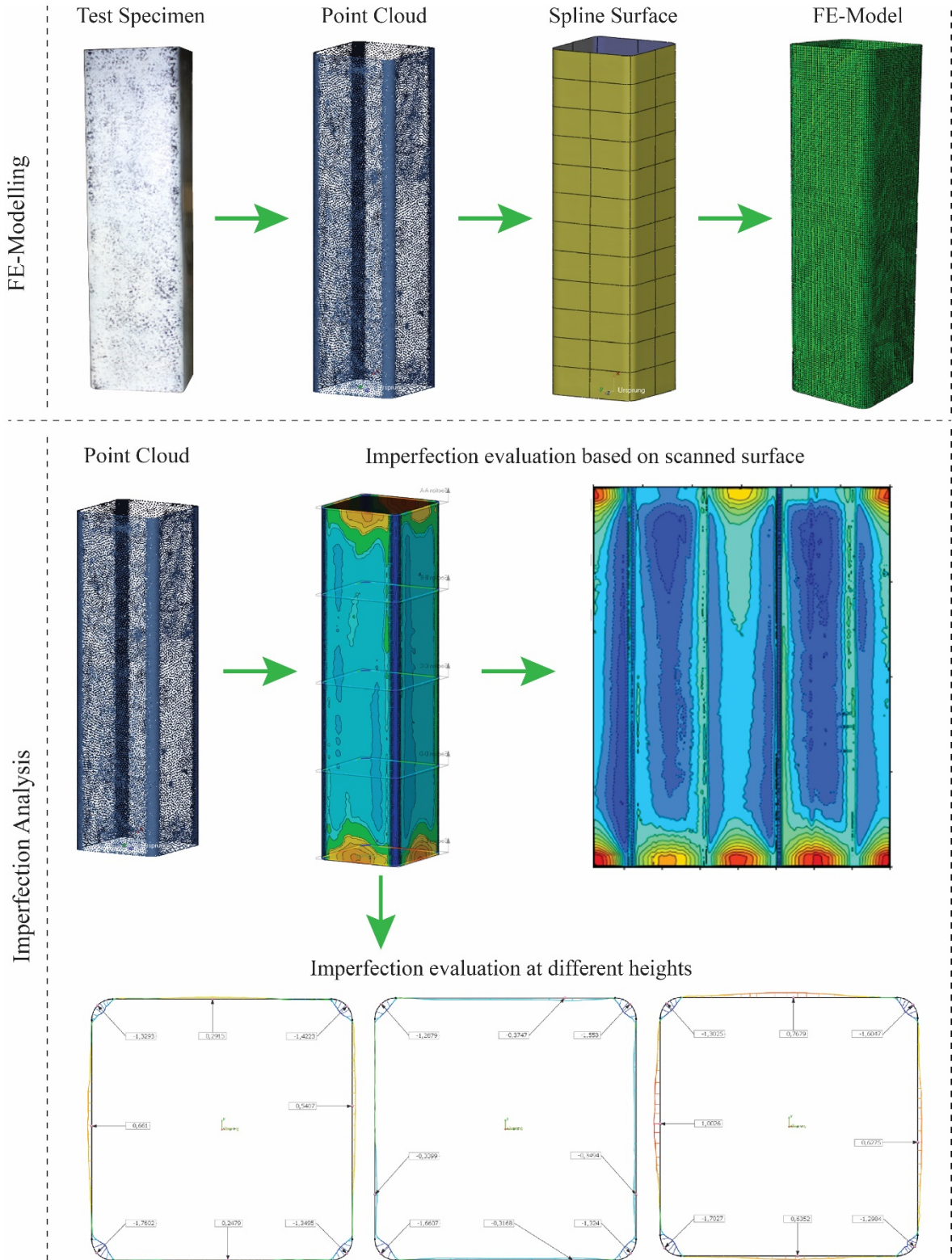


Figure 5-3: Applied reverse engineering workflows for the use in FE element simulations and imperfection evaluations

The procedure from above was performed to validate simulations from FE models against experimental results. Additionally, statistical evaluations of the 3D scan data, compared with shape deviations and tolerances from the nominal geometry (e.g. according to [4] and [5]), were carried out. The output of those comparisons was generated with the software “Geomagic Control X”. Such an output example is provided by Figure 5-3. The same representation was used within the Annex of Hollosstab deliverable D4.2 [270], which was initially evaluated and provided by the author of this thesis, and later on adapted by Toffolon [2] within the derivation of GSRM (see Section 2.6).

This relatively new method was already applied successfully in different projects e.g. [278], [279][7], [8] as part of an EU RFCS project “Combitube” for the evaluation of imperfections of spiral-welded steel tubes but also by [276], [277] in the outline of two industrial projects, conducted at the UniBW Munich, in the timeline between 2017 and 2019.

5.2 HOLLOSSTAB: Finite element modelling, validation and calibration

The overarching motivation for the conducted experiments and investigations from above served in general two main aspects, which are explained throughout this section. Those aspects follow two hierarchical steps of FE-model complexity. Models, used for the validation against experimental test are more complex, including a non-linear material model from tensile coupon tests and the real (scanned) 3D geometry. Further, models which were used for additional parametric studies were derived with simplified approximations, i.e. a perfect geometry with LBA based imperfections and generalized non-linear material models.

5.2.1 Validation against experimental tests

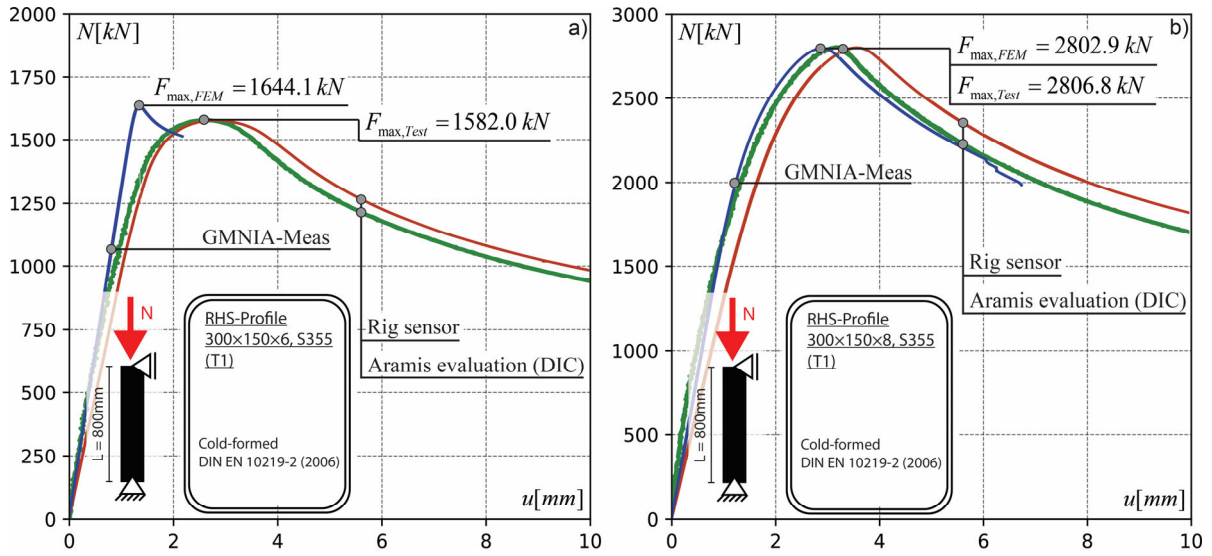


Figure 5-4: Validation of GMNIA-Meas models against experimental results, partially adopted from [2]

This step is performed to obtain the highest possible accuracy between GMNIA and corresponding test results. This step made use of the reverse engineering process from Section 5.1.2, to replicate the experimental test by using the measured geometrical shape (3D spline surface) of the cross-section and a real-stress strain relation. This type of GMNIA simulation is denoted as “GMNIA-MEAS” in the following explanations. For the numerical investigation the commercial software Abaqus [146] was applied. The shell based finite element models made use of linear isotropic shell elements with reduced integration formulation (S4R). The true, experimentally derived, stress-strain curve was used to validate each full-scale test. Note that the results of the coupon tests are usually expressed through engineering stress-strain relations and need to be converted to true stress-strain functions, see Equation (5-1) and (5-2) as follows:

$$\sigma_{true} = \sigma_{eng} \cdot (1 + \varepsilon_{eng}) \quad (5-1)$$

$$\varepsilon_{true} = \ln(1 + \varepsilon_{eng}) \quad (5-2)$$

Data from digital image correlation (DIC) was used to compare the measured deformations (shortening) as well as the buckling induced local failure between numerical simulations and experimental data. This consideration eliminates the influence of the test machine (elastic stiffness) as well as the test set up (slip). Using an appropriate discretization of the FE-model, as well as suitable boundary conditions, can lead to very small deviations of the ultimate load (<3%) obtained from simulations and experimental investigations. It was found that an even greater improvement on the accuracy of the models was provided by using the real imperfections (3D scanned surfaces), as well as the real material model (provided through tensile coupon tests). A representation of such comparisons is exemplary shown in Figure 5-4.

As a result of those investigations a minimum element amount of 60 elements in circumferential direction and 200 elements in longitudinal direction was found to be appropriate, leading to converging results of high accuracy. A statistical summary of those results is shown in Table 5-4.

Table 5-4: Summary of validated results from [2]

Tests	$F_{GMNIA-MEAS} / F_{Test}$	σ
12 stub-column tests (pure axial compression)	0.99	3.2%
48 stub-column and short beam-column tests	0.99	4.2%

5.2.2 Calibration of GMNIA parameters

The validation between GMNIA-MEAS and experimental test results enabled the calibration of simplified FE-models, which were used for parametric studies within the development of the GSRM approach. The simplified FEM models, denoted as GMNIA within the framework of the calibration process, made use of imperfection shapes extracted from linear buckling analysis (LBA) using the shape of the first eigenmode. The corresponding imperfection amplitude was scaled by a multiplying factor. Further use was made of material models based on derived models by Yun and Gardner for hot-rolled [6] and cold-formed [7] steel, respectively. Those material models were already described within Section 2.4.3, in the context of the CSM approach. Further, no residual stresses were taken into account, since the stress-strain formulation derived by Yun and Gardner

[[6] and [7]) was calibrated against a large pool of experimental results and inherently accounts for those effects.

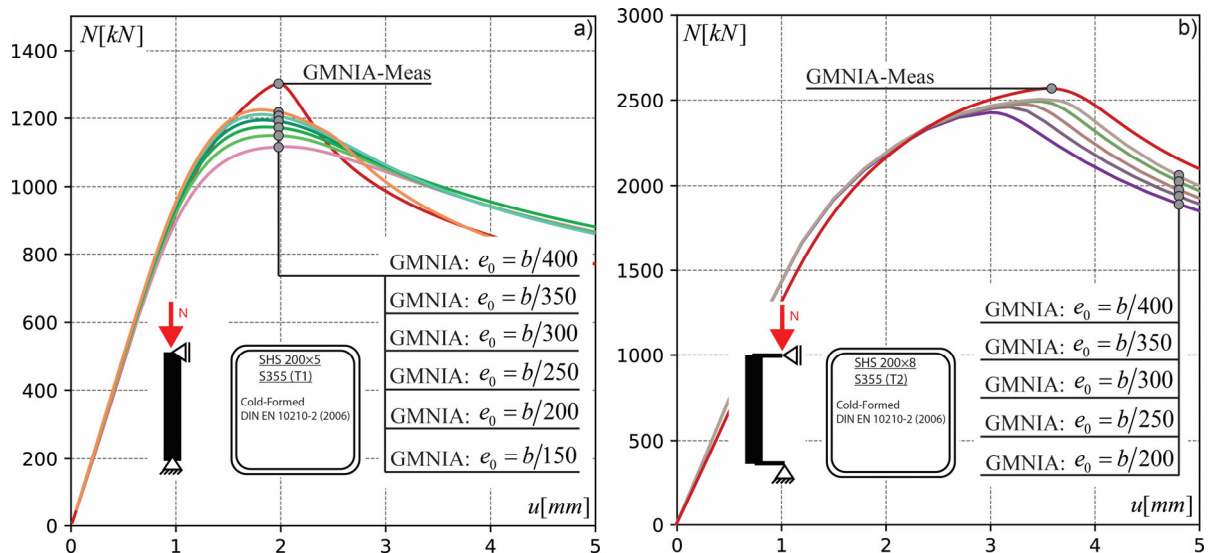


Figure 5-5: Calibration of the imperfection amplitude for a) SHS200×5, S355 (T1); b) SHS200×8, S355 (T2)

As mentioned, a necessary simplification of GMNIA-MEAS models was the transition from a scanned (real) geometry to imperfection shapes based on LBA simulations. Since the GSRM approach relies on the Winter [51] (in cases of local buckling) and Ayrton-Perry [280] (in cases of global buckling) formulation, a determining parameter is the shape and amplitude of the used imperfections. Therefore, the imperfection amplitudes required an approach on the local, as well as global level within the calibration process.

According to EN 1993-1-5, Annex C [11] the magnitude of local imperfections for the analysis of plate buckling may be assumed with a value of $e_0 = B/200$, where B is the smaller of the two corresponding dimensions of a rectangular hollow section. Nevertheless, referring to the findings of Rusch and Lindner [12], as well as the outcomes of the calibration of the FE-models, a determined amplitude of $B/400$ was found to be more suitable to represent the design curve for local buckling (“Winter curve”) [131] in numerical calculations, see Equation (2-75).

$$e_{0,L} = \frac{B}{400} \quad (5-3)$$

This conclusion was also made by the authors own investigations in [281], partially presented in Section 2.1.6.1. Global imperfection in cases of member buckling affect second order bending moments and influence the behaviour of global buckling. It was found that the global imperfection amplitude was suited according to Equation (5-4), where L is the length of the member. This value can be found throughout literature [282], [283] for column buckling. Further details on the calibration are provided by [2], [161], [270], [272], [284].

$$e_{0,G} = \frac{L}{1000} \quad (5-4)$$

5.3 Investigations on Buckling Half-Wavelengths

One main assumption within the current derivation strategy of the proposed DNN-DSM (Deep Neural Network Direct Stiffness Method) is a fixed, profile dependent local buckling length, which indicates the length of one corresponding finite beam element. This assumption is based on the plastic zone/area that is formed within the deformation process in a member subjected to arbitrary load conditions. It indicates its behaviour, in the pre- and post-buckling range and therefore describes its deformation potential e.g. rotation capacity. Since the models derived so far intend to represent a member behaviour ($L \geq 800mm$), additional investigations must be carried out with regard to the local lengths. Thus, this section focuses on the general assumptions for buckling half-wavelengths within the proposed shell finite element (FE) model from Section 5.2, serving as the starting point for the overall data generation, further data extraction and additional evaluation, i.e. in general terms feature engineering in Chapter 6.

The following buckling length considerations, which subsequently lead to the conclusions for the chosen FE model in Section 5.4, can be separated into several observation steps:

- i. Evaluation of half-wavelengths from experimental results of the Hollosstab project combined with 3D surface scan imperfection evaluations based on Fourier

series expansion and corresponding FE simulations. Assumptions and results are presented within Section 5.3.1.

- ii. Calculation of local half-wavelengths from analytical formulations derived by Fieber [67], [150], see Section 2.5.3.2. Additional GMNIA-Meas simulations on the basis of 3D scan surfaces from the Hollosstab project are performed to assess its impact on simulation results, see Section 5.3.2.
- iii. Subsequent conclusions for the plastic hinge length are proposed in Section 5.3.3.

Numerical simulations presented herein are based fully on investigations from the Hollosstab project, addressed briefly in in the framework of the GSRM approach in Section 2.6 and presented in Section 5.1. The investigations carried out consisted of non-destructive methods, where 3D surface scans of all specimens were made, and the actual experimental tests, in which the specimens were loaded until failure occurred. Numerical models derived from those surface scans (GMNIA-Meas) served for validation purposes against experimental test results, as well as generalized assumptions for the simplified FE-shell models. This procedure is described within Section 5.1.2.2. Additional project related information is provided in [270] along with conference papers and journal publications [285]. The correctness of these investigations is assumed, whereby the comparison between numerical simulations and experimental results is made here at individual points. It has to be noted that in all cases the results of the DIC (Digital Image Correlation) evaluations, representative for the performed full-scale tests, are used, allowing to directly neglect the machine stiffness of the test set-up for a better comparison with FE simulation results.

5.3.1 Preliminary investigations on buckling lengths

5.3.1.1 Background information on surface reconstruction based on Fourier series expansion

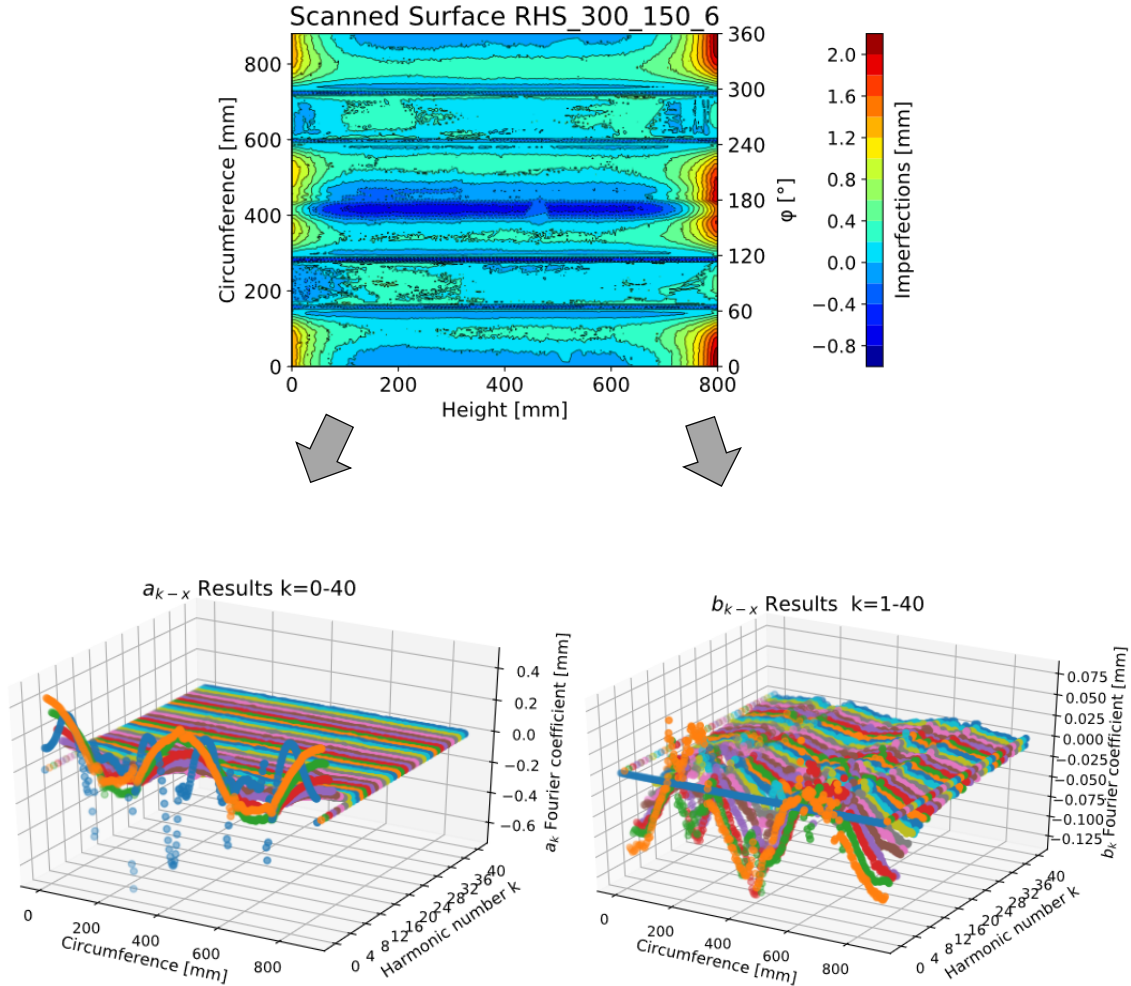


Figure 5-6: Calculated Fourier coefficients a_k and b_k for a RHS 300×150×6 profile, published in [286]

The reverse engineering steps described in Section 5.1.2 lead to an overall imperfection evaluation giving the deviation between the scanned and the perfect surface as an output. This “prepared” data is used as an input file for a python script, which was initially developed at UniBW Munich for investigations on CHS profiles [276] and then further evolved at ETH Zurich, Institute of Structural Engineering (IBK) Steel- and Composite Structures for investigations on RHS/SHS profiles [286].

The imperfection data of the considered specimen is first transformed or mapped to a flat surface by “unfolding” the hollow section along the circumference (see Figure 5-6 top). In this row form the scanned points, which form the surface of the specimen, are unevenly distributed. This has two main disadvantages for further FE simulations within the discretization process, as well as the calculation time of the non-linear problem, since there is no control over either the mesh size or the mesh orientation. This problem can be sufficiently solved by ordering the scanned points into a mesh-like structure, at best equal to the later FE discretization. Within the derived python script this interpolation was done by using the scipy library and there the griddata command to form a uniformly-spaced x (Height) – y (Circumference) grid. Furthermore, the scanned surface imperfections can be used for conclusions only to a limited extent, since many different imperfection shapes are superimposed at the same time, e.g. local imperfections combined with sagging and ovalization along the circumference. This circumstance was already shown within several publications [279], as well as own investigations in [277].

In order to distinguish between such forms within real scanned geometries a 1D full wave Fourier series expansion was implemented within the script. The general 1D Fourier series expansion expression is described by Equation (5-5). The additional Fourier coefficients a_0 , a_k and b_k are expressed through Equation (5-6) and (5-7), taking into account an initial function $f_{(x)}$, describing the slope between two scanned points along the surface. Hereby, it is accurate enough to assume a linear course between those points, which is approximated here by a straight line resulting in Equation (5-8).

Subsequently, by applying Equation (5-5) and calculating an arbitrary number of harmonic numbers for the Fourier coefficients, an imperfection spectrum for the given specimen is obtained (see Figure 5-6 bottom). Low harmonic numbers between 0 and 3 are usually related to global sagging and ovalization, whereas higher harmonic numbers are used to reconstruct local imperfections ([279], [277]).

$$w_{(x,y)} = \sum_{k=0}^K \left(a_{k,(y)} \cdot \cos \left(2 \cdot \pi \cdot k \cdot \frac{x}{x_{\max}} \right) + b_{k,(y)} \cdot \sin \left(2 \cdot \pi \cdot k \cdot \frac{x}{x_{\max}} \right) \right) \quad (5-5)$$

$$a_0 = \frac{1}{2 \cdot L} \int_{x_n}^{x_n+1} f_{(x)} dx; \quad a_k = \frac{1}{L} \int_{x_n}^{x_n+1} f_{(x)} \cdot \cos\left(\frac{n \cdot \pi \cdot x}{L}\right) dx \quad (5-6)$$

$$b_k = \frac{1}{L} \int_{x_n}^{x_n+1} f_{(x)} \cdot \sin\left(\frac{n \cdot \pi \cdot x}{L}\right) dx \quad (5-7)$$

$$f_{(x)} = m \cdot x + t \quad (5-8)$$

5.3.1.2 Performed investigations and results

Figure 5-7 a) to f) show the reconstructed surfaces using the Fourier coefficients from 0 to 5, one by one separately. Figure 5-7 g) and h) displays the sum of the reconstructed surfaces for the Fourier coefficients from 0 to 5 and from 0 to 40, leading to an increasingly precise surface, approximating the original scanned surface.

Calculating the coefficient of variation (cov) between the reconstructed and the scanned surface for rising harmonic numbers leads to an increasing accuracy with respect to surface similarity; $COV_{k0-k0} = 1.24\%$, $COV_{k0-k1} = 0.92$, $COV_{k0-k2} = 0.70$, $COV_{k0-k3} = 0.53$, $COV_{k0-k4} = 0.41$, $COV_{k0-k5} = 0.32$, $COV_{k0-k10} = 0.14$, $COV_{k0-k40} = 0.63 \cdot 10^{-2}$. The harmonic number 0 gives, due to its mathematical formulation, an average of the imperfections over the height of the specimen, therefore remaining constant along the height.

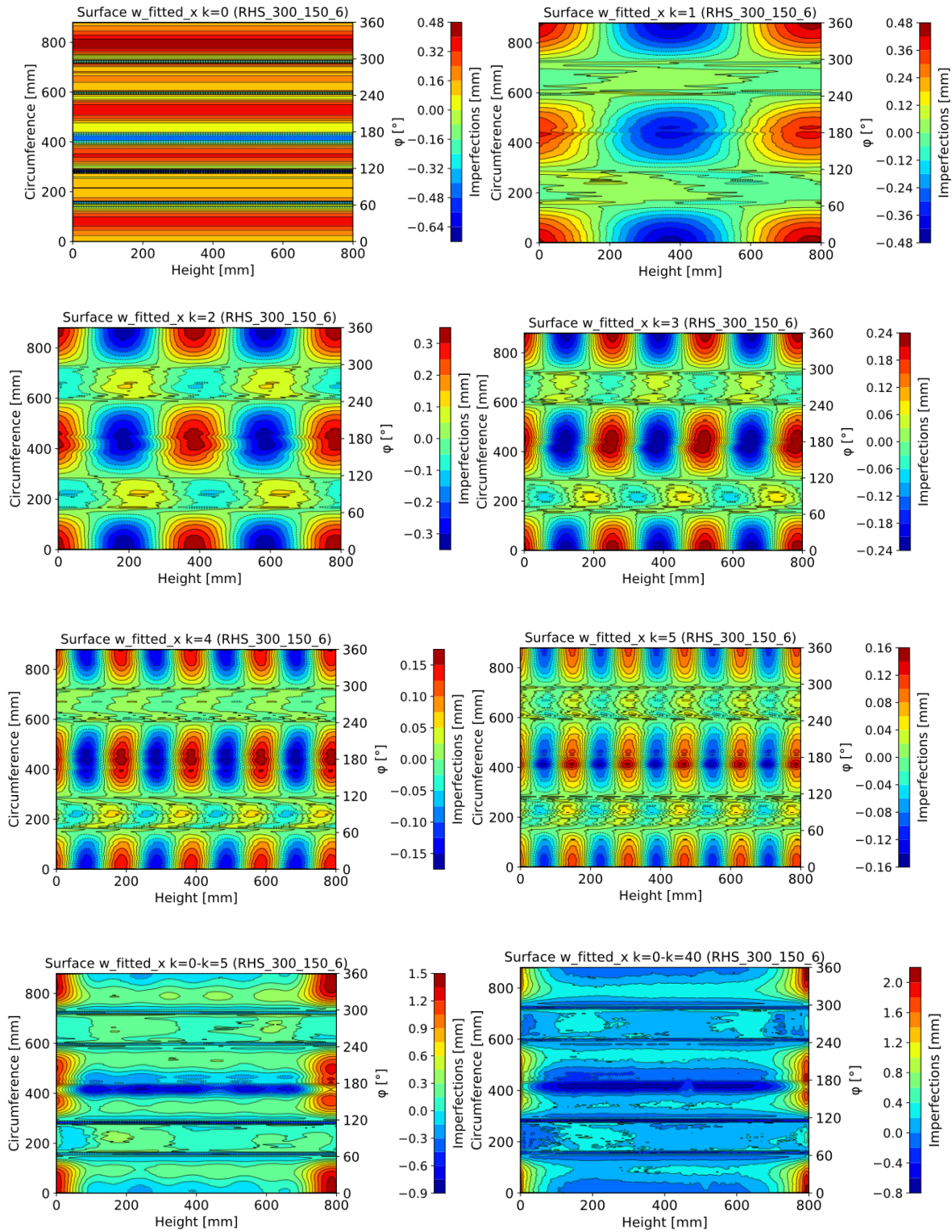


Figure 5-7: Compilation of reconstructed surfaces for different harmonic numbers

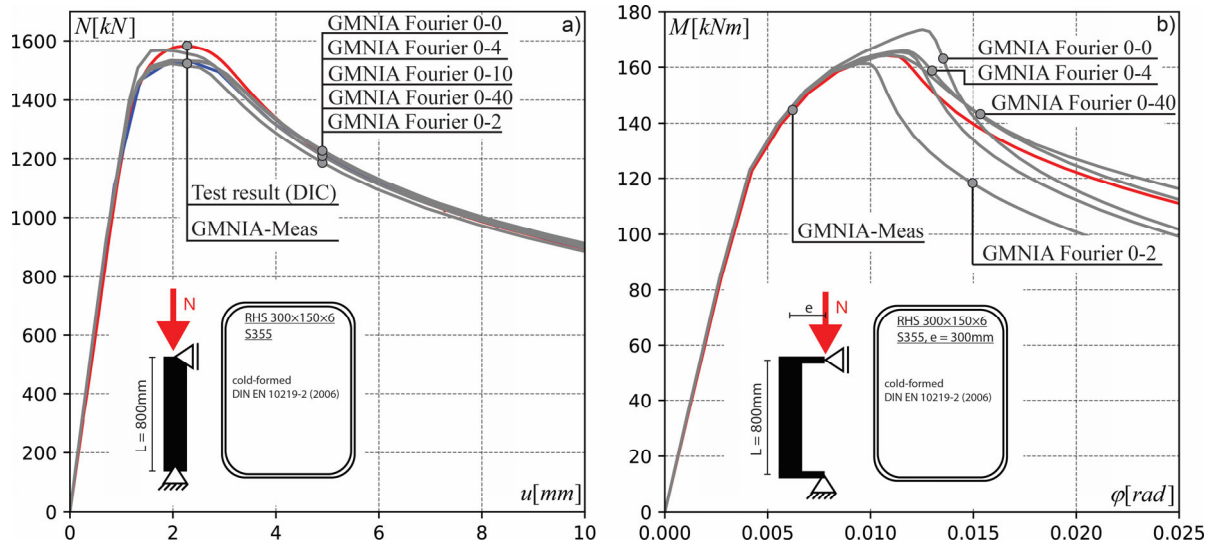


Figure 5-8: GMNIA results for ascending Fourier coefficients in comparison with GMNIA-Meas results

Figure 5-8 shows some results from GMNIA simulations taking different sets of ascending Fourier coefficients from $k = 0$ to $k = 40$ into account. Thus the dependence on the reconstruction accuracy can be shown for different load cases. In the case of a centric normal force only a low number of coefficients is needed to reproduce the behaviour from GMNIA-Meas simulations, i.e. the first four coefficients are sufficient enough, see Figure 5-8 a).

In Figure 5-8 b), where the load is introduced with an eccentricity of $e = 300\text{mm}$, the amount of necessary Fourier coefficients increases, showing the need for wave-lengths with a higher frequency, i.e. a higher harmonic number. In the case of the centric and eccentric load application the accuracy, regarding the force-displacement and moment-rotation-relation, respectively, increased with higher values of the harmonic number combinations, i.e., with lower half-wavelengths. However, sufficient results regarding the resistance and deformation could generally be achieved in a lower range between $k = 0$ and $k = 10$.

5.3.1.3 Assessment of combined harmonic numbers

This first results lead to further investigations on buckling forms with respect to harmonic numbers and the behaviour in the pre- and post-buckling range of hollow sections. Those outcomes were presented in [286] and [285] and are described as follows.

The calculations were performed by using the harmonic numbers from $k = 0$ to 5 separately to reconstruct, in each case, an imperfect surface based on just one individual harmonic number. Finally, dominant imperfection forms were identified for an RHS profile loaded by two different load cases, a centric and eccentric load application. To illustrate the influence of the eccentricity on the harmonic response spectrum an RHS profile was loaded with a higher eccentricity, leading to a shift towards higher amplitudes of the governing harmonic numbers.

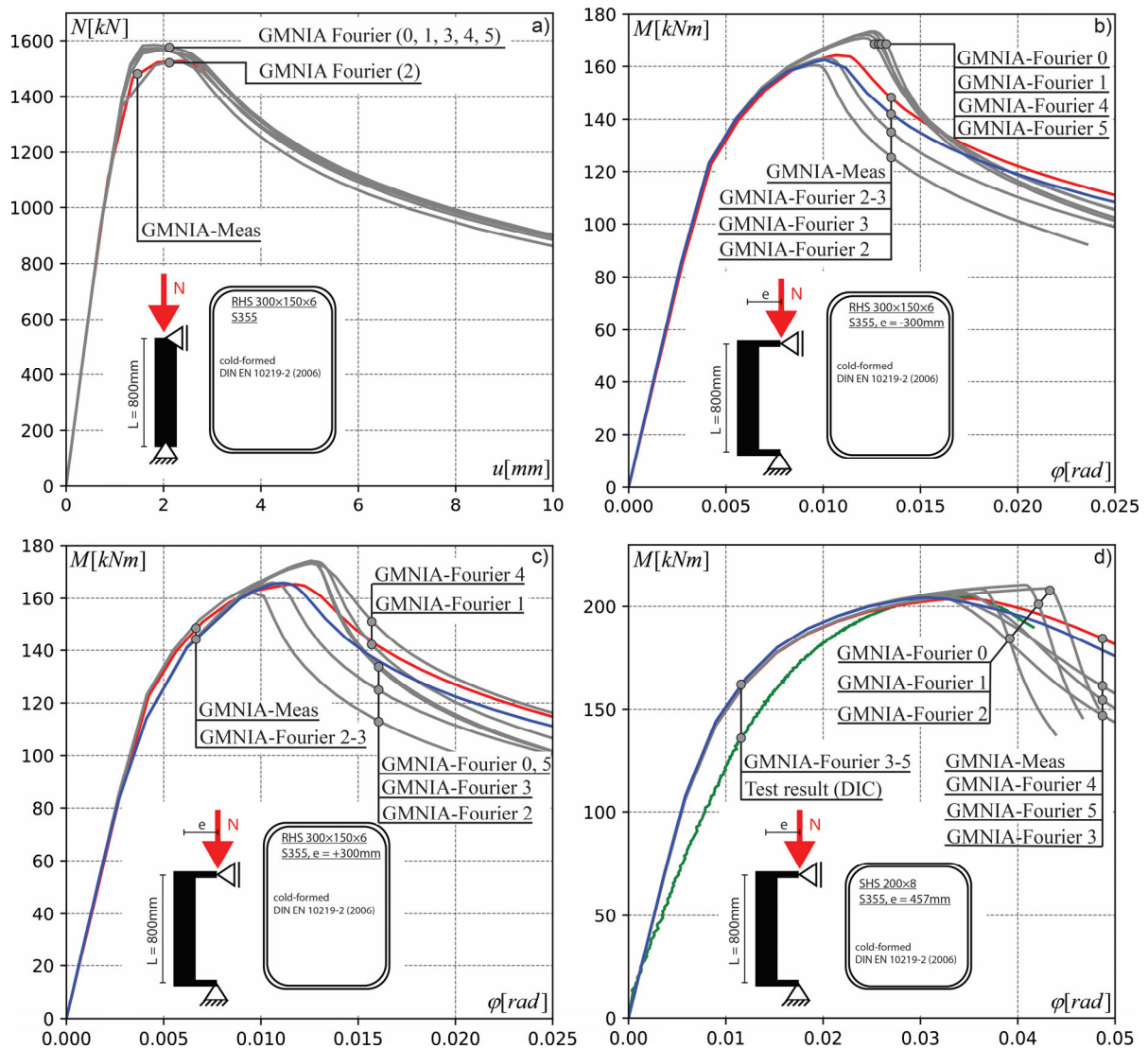


Figure 5-9: Comparison between individual harmonic numbers for an a) RHS 300x150x6 profile loaded in centric compression; b) RHS 300x150x6 profile loaded with an eccentricity of -300 mm in compression; c) RHS 300x150x6 profile loaded with an eccentricity of +300 mm in compression; d) SHS 200x8 profile loaded with an eccentricity of +457 mm

Figure 5-9 a) illustrates the results for different harmonic numbers from 0 to 5, i.e. different reconstructed surfaces, for the load case of centric compression. It is evident that, apart from slight differences in the maximum load, the resultant load deformation curves do not significantly differ. This applies to both, the pre-buckling as well as the post-buckling behaviour for the considered specimen. The difference in the maximum load is mainly caused by the different imperfection amplitudes of the used harmonic numbers. Nevertheless, it seems that the frequency of the buckling half-wavelength is only of minor importance in the case of pure compression. More crucial is the necessary member length that should be greater or equal to the buckling length to form the local failure mechanism.

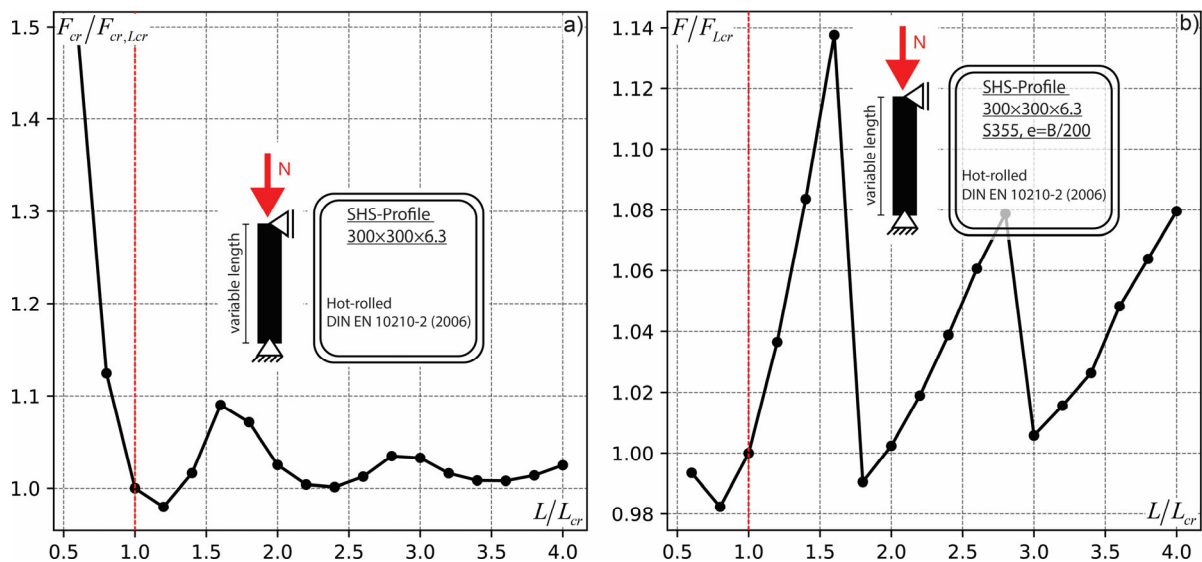


Figure 5-10: Comparison between different member lengths and their influence on a) LBA simulations; b) GMNIA simulations

This can be exemplarily illustrated as follows by using the results of LBA and GMNIA simulations for a member with varying lengths. An SHS300×6.3 profile was used with ascending member lengths from 150mm to 1000mm in 50mm steps. Figure 5-10 a) shows the corresponding LBA results. A normalized representation was chosen to explain the results. The x-axis shows the length L , normalized by the critical buckling length from L_{cr} . The critical buckling length was calculated with the analytical approach from the AACSM from Section 2.5.3.2. The y-axis shows the results for the critical buckling load F_{cr} , normalized by the critical buckling load $F_{cr,Lcr}$, which was read out for the model with the

critical buckling length L_{cr} . Note, the critical buckling length for an SHS300×6.3 was calculated to $L_{cr} = 250\text{mm}$. The critical buckling load appears to be the lowest near a local length of 250 mm to 300 mm or one of its multiples. Deviations between the minimum and maximum values start to decrease with an increasing length.

In addition, Figure 5-10 b) shows the GMNIA results from according simulations, where the first eigenshape from the LBA was used as a local imperfection form with a constant imperfection amplitude of $B/200$ according to EN 1993-1-5 [131] throughout all calculations. The maximum load bearing capacity from GMNIA results follows a similar logic, where the lowest capacity values are calculated with lengths between 200mm and 300mm or their multiples. Nevertheless, the differences within the reached maximum loads are not crucial and tend to decrease with bigger member lengths, comparable to the results from LBA calculations.

Figure 5-9 b), c) and d) illustrate moment rotation diagrams using different individual harmonic numbers for the reconstruction of the imperfect surfaces of the FE models. A cold-formed RHS300×150×6 (Figure 5-9 b), c)) and SHS200×8 (Figure 5-9 d)) profile are used to illustrate the shift towards “higher” harmonic numbers with increasing eccentricity. The eccentricity was set to $\pm 300\text{ mm}$ and 457 mm for the RHS and SHS profile, respectively. Overall, the shown moment-rotation curves appear more inconsistent and separated compared to the case of pure centric compression. In most cases the exclusive use of single individual harmonic numbers lead to large deviations within the moment-rotation behaviour, compared to GMNIA-Meas results (representing experimental test results).

It has been found that combinations of individual harmonic numbers are more appropriate to simulate the overall behaviour. In the case of the RHS profile (Figure 5-9 b) and c)) and an eccentricity of $e = \pm 300\text{ mm}$ for the load introduction – eccentricity was set along the profile height, so that the width (smaller profile dimension) is fully under compression – a combination between the second and the third harmonic number lead to GMNIA-Fourier results very close to the benchmark GMNIA-Meas curve. For the SHS profile (Figure 5-9 d)), a combination between the third, fourth and fifth harmonic number was appropriate to recreate the GMNIA-Meas moment-rotation behaviour.

Generally speaking, the impression arises that with increasing eccentricities the need for smaller half-wavelengths arises, i.e., higher harmonic numbers within the imperfection spectrum, to increase the accuracy compared to GMNIA-Meas calculations. In the case of bending, it means that a more complex local imperfection shape is needed to duplicate the “real” behaviour. These local half-wavelengths are in the geometric range of the cross-section dimensions. The lowest harmonic number in almost all investigated cases was $k = 2$, which is approximately corresponding to the bigger value of the width or the height of the cross-section. Sadowski [279] described that the critical terms in the harmonic analysis are usually not those with the largest amplitudes (typically low harmonics), but those with wavelengths close to that of the critical buckling mode (typically a high harmonic).

A comparable conclusion can be drawn from investigations made by Fieber [67] within the development of the CSM approach for members and frame systems, see Section 2.5. To account for redistributions and plastic hinge formations in a defined area, a so called “strain averaging” approach (see Section 2.5.2) was implemented. The length L_b of the plastic hinge is assumed to be the local buckling half-wavelength, being dependent on the profile geometry and the used load case. Those lengths can either be directly calculated by using the CUSFM software – resulting in so called signature curves (see Section 2.3) – or the analytical approach by Fieber [67], presented throughout Section 2.5.3.2. Using this approach exemplary within Figure 5-10 for the SHS300×6.3 profile, the calculated local critical buckling length is equal to $L_b = 250\text{mm}$, for the load case of pure compression, leading to a similar required minimum length resulting from Figure 5-10.

5.3.2 Buckling lengths from experimental investigations

Based on the investigations from above, an additional consideration of local buckling lengths with experimental tests and their evaluation regarding the geometry of the plastic hinge area can be made.

In particular, the geometries of the scanned profiles were used here, which were recorded and tested at UniBW in the framework of the Hollosstab project. The test program and the validation of the FE models have already been discussed in Section 5.1.

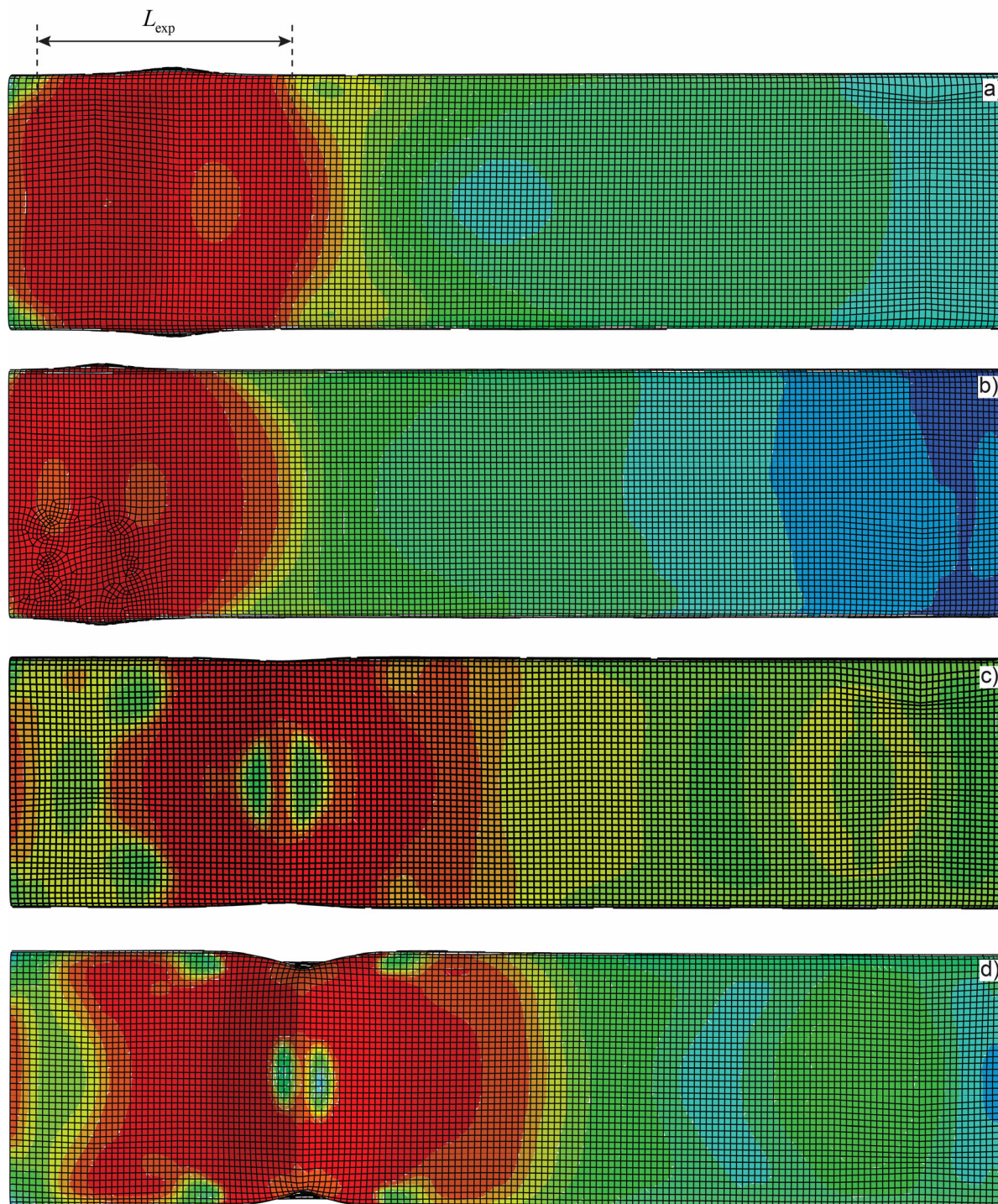


Figure 5-11: Simulated GMNIA-Meas buckling lengths for an SHS 200×5; a) T1; b) T2; c) T3; d) T4

Due to the close correlation between the experimental tests and the FE simulations – here denominated as GMNIA-Meas – using the real/scanned geometries for the modeling, the simulated results are used here for comparison purposes to determine the buckling lengths. The full scale tests were originally sampled into 5 categories, which depend on the load case and length of the used profiles, see therefore Section 5.1.1 and Table

5-3. Test with the denomination from T1 to T4 provide an increasing eccentricity with an equal profile length of 800 mm to induce N-M interaction. The eccentricities of test category T5 are in general equivalent to T3 tests, but using a length of 2000 mm to display a global + local phenomena.

In the following, the actual buckling lengths from GMNIA-Meas simulations are compared with theoretical buckling half-wavelengths, derived with analytical approximations from Fieber [67]. This comparison enables conclusions regarding the used member lengths within own FE models. The buckling lengths from GMNIA-Meas simulations were measured, therefore, the values for L_{exp} are not exact and describe more a tendency towards the dimensions of the plastic hinge area in a heuristic manner. Figure 5-11 shows this procedure for different eccentricities. The used profiles with the corresponding test eccentricities and measured (L_{exp}) buckling lengths, as well as calculated buckling half-wavelengths (L_b) are summarized in Table 5-5.

First, it should be noted that the measured buckling lengths L_{exp} from GMNIA-Meas simulations – note that those models are based on the scanned geometries – correspond in all cases to the larger profile dimension ($\max(H, W)$) of the used SHS/RHS. With increasing eccentricities, i.e. introduction of a planned N-M interaction, a certain decrease of the measured buckling length is observed. However, this effect is not significantly pronounced and could be neglected. Comparatively, the results according to the analytical formulations by Fieber [67] (see also Section 2.5.3.2) lead to buckling half-wavelengths that are in general smaller than the profile dimensions. Depending on the load case (N-M Interaction) the geometric deviations lie between 15% (compression) and 40% (bending dominated) compared to the biggest cross-section dimension (width or height of the profile). On the other hand, buckling lengths derived from GMNIA-Meas simulations are consistently closer to the bigger cross-section dimension with deviations between 0% and 20%.

Table 5-5: Comparison between local buckling lengths from experimental investigations (HOLLSSTAB) and critical buckling half-wavelengths [67]

Profile	Test eccentricity T [mm]	L_{exp} [mm]	L_b [mm]
RHS 300×150×6, S355	T1 = 0	295	254.47
RHS 300×150×6, S355	T2 = 17.9	274	254.47
RHS 300×150×6, S355	T3 = 57	250	254.40
RHS 300×150×6, S355	T4 = 297	250	224.57
RHS 300×150×6, S355	T5 = 57	270	254.40
RHS 300×150×8, S355	T1 = 0	305	254.47
RHS 300×150×8, S355	T2 = 17.4	280	254.47
RHS 300×150×8, S355	T3 = 57	253	254.40
RHS 300×150×8, S355	T4 = 232	250	228.70
SHS 140×4, S355	T2 = 14.6	152	116.2
SHS 140×4, S355	T3 = 137	121	110.36
SHS 140×4, S355	T4 = 312	120	103.07
SHS 200×5, S355	T1 = 0	182	166.00
SHS 200×5, S355	T2 = 20.9	179	166.00
SHS 200×5, S355	T3 = 107	170	162.91
SHS 200×5, S355	T4 = 457	170	146.74
SHS 200×8, S355	T1 = 0	197	166.00
SHS 200×8, S355	T2 = 20.9	193	166.00
SHS 200×8, S355	T3 = 107	193	162.45
SHS 200×8, S355	T4 = 457	193	146.74
SHS 200×4, S550	T1 = 0	195	166.00
SHS 200×4, S550	T2 = 63.0	190	166.00
SHS 200×4, S550	T3 = 107	190	162.53
SHS 200×4, S550	T4 = 457	200	146.74
SHS 200×4, S550	T5 = 107	200	162.45
SHS 200×5, S550	T1 = 0	200	166.00
SHS 200×5, S550	T2 = 63.9	190	166.00
SHS 200×5, S550	T3 = 107	190	162.76
SHS 200×5, S550	T4 = 457	190	146.74
SHS 200×5, S550	T5 = 107	190	162.06

5.3.3 Conclusions and assumptions for the plastic hinge lengths from own work

From the above investigations, general conclusions can then be drawn on the required local lengths of the corresponding FE models for the following simulation and subsequent data development:

- i. Using the mathematical approach of Fourier series expansion to recreate scanned surfaces, it was shown that only a limited number of harmonic numbers, corresponding to imperfection shapes from a sum of sine and cosine waves, is needed to recreate the overall behaviour of the FE model (GMNIA-Meas) based on the fully scanned geometry. In addition, a shift towards higher harmonic numbers, i.e. imperfection forms with higher frequencies (lower half-wavelengths), is obtained with an increasing moment.
- ii. The length of the member is a crucial factor within the determination of the critical elastic buckling load (LBA), as well as the maximum force from GMNIA simulations. Member lengths below the maximum dimension of the cross-section height or width can lead to results far above the critical bifurcation load and the actual load bearing capacity. Related own investigations on the choice of eigenmode shapes and their combinations for I-shaped and closed SHS/RHS profiles show a similar trend. Those results were published in [76] and related industrial projects in [75], [82].
- iii. Further, the investigated profile thickness range, as well as the steel grade do not significantly influence the buckling length within GMNIA-Meas simulations. Therefore, these parameters are neglected in further considerations of method development.
- iv. Plastic hinge lengths are not equal to buckling half-wavelengths from LBA simulations (CUFSM) or equivalent analytical solutions. In all investigated cases from Table 5-5, the necessary lengths L_{exp} to form a plastic hinge are bigger than the critical half-wave lengths L_b . The use of the latter can lead to GMNIA results that overestimate the actual local capacity.

As a conclusion to the results mentioned above, the local buckling length and therefore also the member length within the FE models are set equal to the larger dimension of

the height or the width ($\max(H, W)$) of the considered profile in each case for compression and bending. A description of the FE models is presented in Section 5.4.

5.4 Developed Finite Element Model

5.4.1 General description

The developed FEM models, as used throughout the remainder of this thesis, for data generation and subsequent DNN model training can be described as follows. All assumptions, except the local length of the models, are mainly based on the previous work from the Hollosstab project, as described throughout Section 5.2.

- i. The FE models make use of isoparametric shell elements with reduced integration of type S4R, with a mesh density of around 60 elements in circumferential and (depending on the total member length) 50 – 100 elements per meter in longitudinal direction.
- ii. The geometry of the profiles is based on code provisions of (EN 10210-2:2006 [4], EN 10219-2:2006 [5]) with a local length L (longitudinal direction) set as the bigger value of either the width W or the height H of the cross-section.
- iii. The loads and deformations are applied through defined reference points (RF-Points) which are located at the upper and lower edge of the cross-section (see Figure 5-12). These are connected through multiple point constraints (MPC-Pin formulation) to associated node sets along the upper and lower profile outer edge shown exemplary for the quarter range of the cross-section. This definition implies a pinned connection between the nodes at the extremity with regards to deformations and rotations, and a reference node at the centroid of the respective sections.
- iv. Non-linear material models for hot-rolled (bilinear + non-linear model) and cold-formed steel (two-stage Ramberg Osgood model) were implemented according to Yun and Gardner ([6], [7]), as well as Section 2.4.3, under consideration of Equation (5-1) and (5-2) for true stress-strain representations.

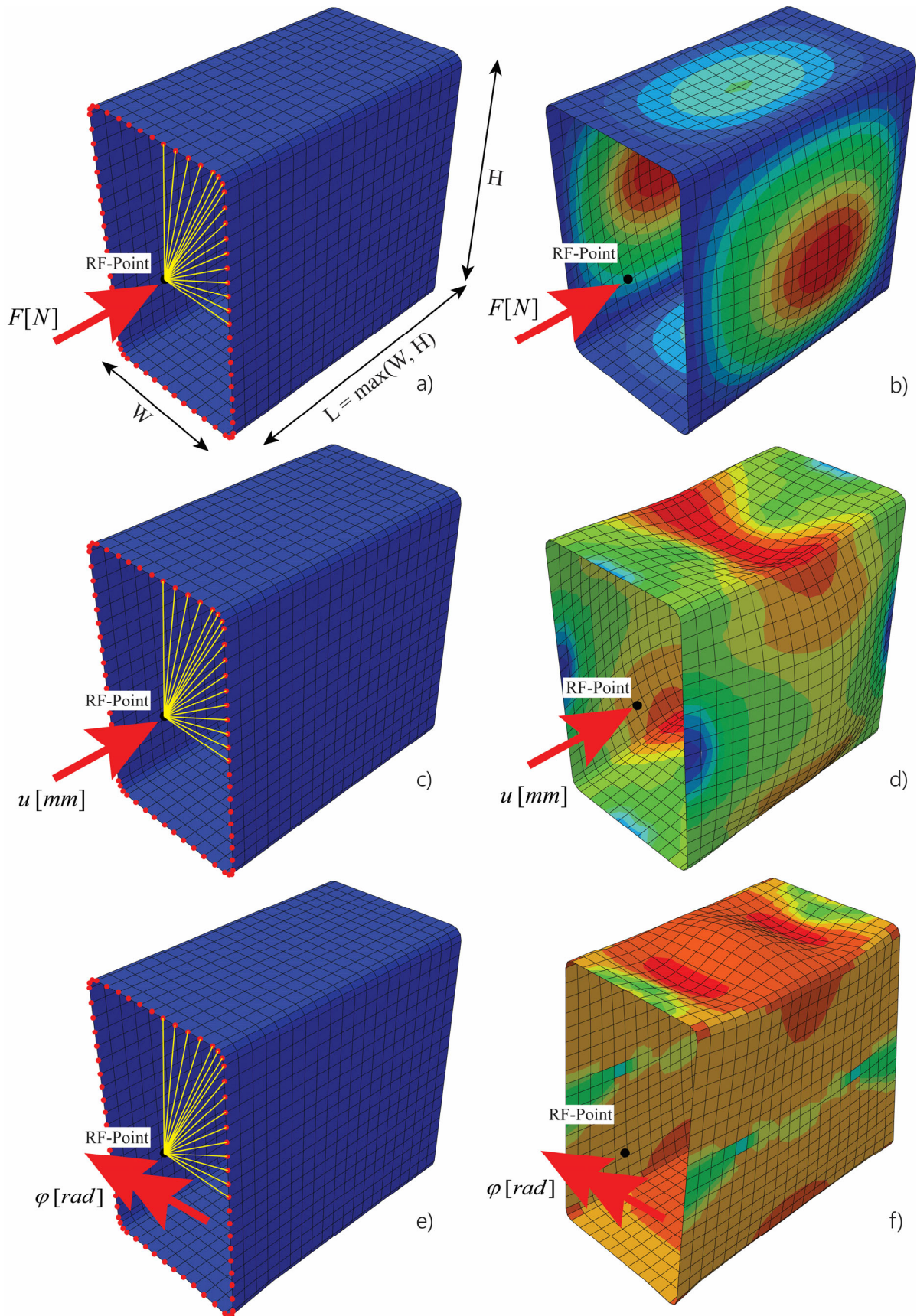


Figure 5-12: Exemplary illustration of FE models of an RHS section in compression and bending and their corresponding deformations; a), b) LBA compression; b), c) GMNIA compression; d), e) GMNIA bending

- v. Residual stresses were not explicitly considered in the Abaqus models. The overall validation of the Abaqus model is based on the described investigations from Section 5.2.

The basic process for the generation of the FEM-based training data sets is always performed in two steps.

- i. In a first step an LBA analysis is carried out in order to identify the elastic critical buckling resistance of the cross-section and the eigenshape as the critical imperfection form. The eigenshape is derived exclusively from the load case of centric compression and used in all further load cases as the initial imperfection form.
- ii. In a second step a GMNIA simulation is performed to determine an elasto-plastic buckling load – the realistic buckling resistance that considers both material and geometric nonlinearities – of the cross-section as well as the courses of the pre- and post-buckling range. The non-linear calculations in Abaqus were performed using the static general stress analysis.

5.4.2 Considered parameters and load cases

Table 5-6: Used profiles and parameters

Used Profiles	Number of Sections	Dimension Range c/t
SHS hot-rolled	106	8.0 – 47.62
SHS cold-formed	142	8.0 – 47.62
RHS hot-rolled	113	9.52 – 56.25
RHS cold-formed	165	12.5 – 55.55
Used Parameters	Number of Parameters	Values
Steel grade f_y	3	S355, S460, S700/S690
Material model (hot-rolled)	2	Bilinear + non-linear hardening model [6]
Material model (cold-formed)	2	Two Stage Ramberg Osgood [7]
Imperfection amplitude e_0	3	B/200, B/300, B/400
Abaqus Simulations		
LBA Compression		526
GMNIA Compression		9468
GMNIA Bending		9468

Within this thesis, serving as a preliminary step into the development of a novel data driven solution method for structural design, exclusively closed square (SHS) and rectangular (RHS) hollow sections are considered. This simplification is indeed needed throughout this development stage to prevent out of plane effects, i.e. lateral torsional buckling or distortional buckling effects, which occur mostly in open cross-sections (I-shaped or cold-formed open profiles). Therefore, the member behaviour in the 2D plane is evaluated. The required data for the evaluation of the DNN predictive models is based on European profiles from EN 10210-2 2006 [4] and EN 10219-2 2006 [5] for hot-rolled and cold-formed steel.

An overview of the used profiles is summarized in Table 5-6. In sum 526 profiles are evaluated, whereby, 219 are assigned to hot-rolled and 307 to cold-formed SHS and RHS profiles. Additional parameters were selected, such as three different steel grades (S355, S460 and S700/690), two material models in each case for hot-rolled and cold-formed consideration as well as three different equivalent local imperfection amplitudes ($B/200$, $B/300$ and $B/400$), which are scaled to the local buckling shape from LBA simulations. In total 18936 profiles with individual parameters are generated. This parameters form the basis for further LBA (linear buckling analysis) and GMNIA (geometrically and materially non-linear analysis with imperfections) simulations conducted in Abaqus. The subsequent data extraction and corresponding feature engineering steps are discussed and presented in Section 6.

Table 5-7: Used material properties according to EN 1993-1-1 [48], EN 1993-1-3 [287] and EN 1993-1-12 [288]

f_y [N/mm ²]	f_u [N/mm ²]	E [N/mm ²]
Hot-rolled steel		
355	490	210000
460	550	210000
690	770	210000
Cold-formed steel		
355	510	205000
460	550	205000
700	750	205000

The used material parameters for all Abaqus simulations are shown in Table 5-7. The advanced non-linear material models are based on investigations collected from literature and subsequently proposed as analytical formulations by Yun and Gardner ([6], [7]). The implemented models, i.e. a “bilinear plus non-linear hardening material model” for hot-rolled steel and a “two stage Ramberg Osgood material model” for cold-formed steel, are presented in Section 2.4.3 with additional background information and main parameter derivation. Their purpose within the proposed advanced non-linear simulation approach is primarily to match the experimental results (from both, literature and own investigations), used for comparison and validation of the DNN-DSM throughout Chapter 8.

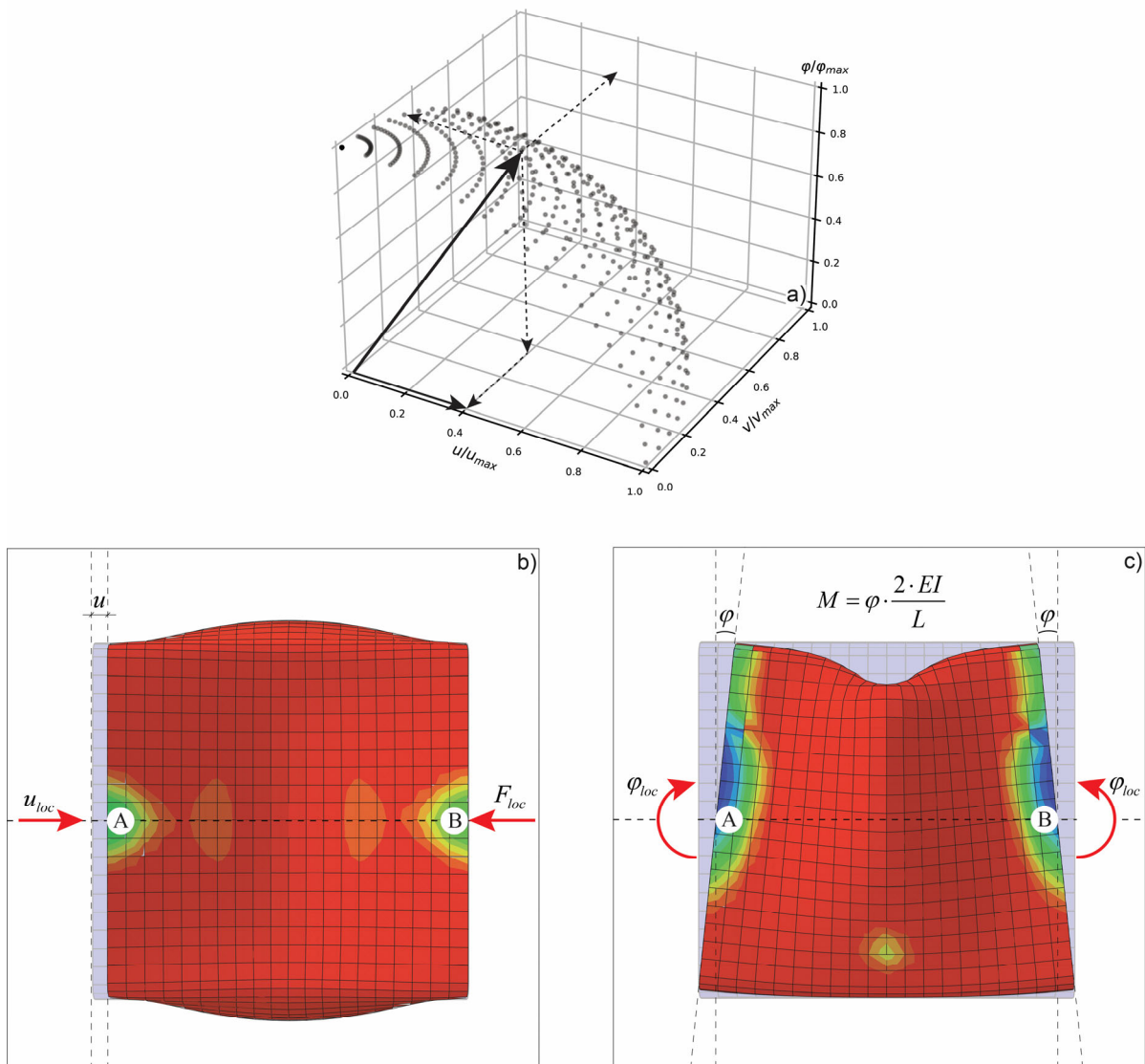


Figure 5-13: Considered load cases, a) pure compression; b) pure (constant) bending

Figure 5-13 a) shows a hypothetical 3D space of possible deformation scenarios, i.e. all possible combinations of longitudinal and transverse deformations (u_x, v_z) and additional rotations (φ_y) at a node of a beam element of a defined length loaded in plane (three degrees of freedom at each node). In the framework of this thesis, which is intended as a demonstration of the general feasibility of the DNN-DSM approach, longitudinal deformations u_x and end node rotations φ_y (see Figure 5-13 b) and c)) are considered. Beyond serving as a proof of concept, this simplification has also the decisive advantage that many general problems regarding data structure, density and post processing (feature engineering) can be tested on a much smaller scale with less computational effort.

6

Data Development

Data Basis and Feature Engineering

Outline of the chapter:

This chapter provides background information on all required steps from shell based FE simulations towards data sets, which are used for the training and testing of all presented DNN models. This models form the basis for the proposed DNN-DSM approach herein.

6.1 Data pre-processing

6.1.1 Data generation workflow and used software

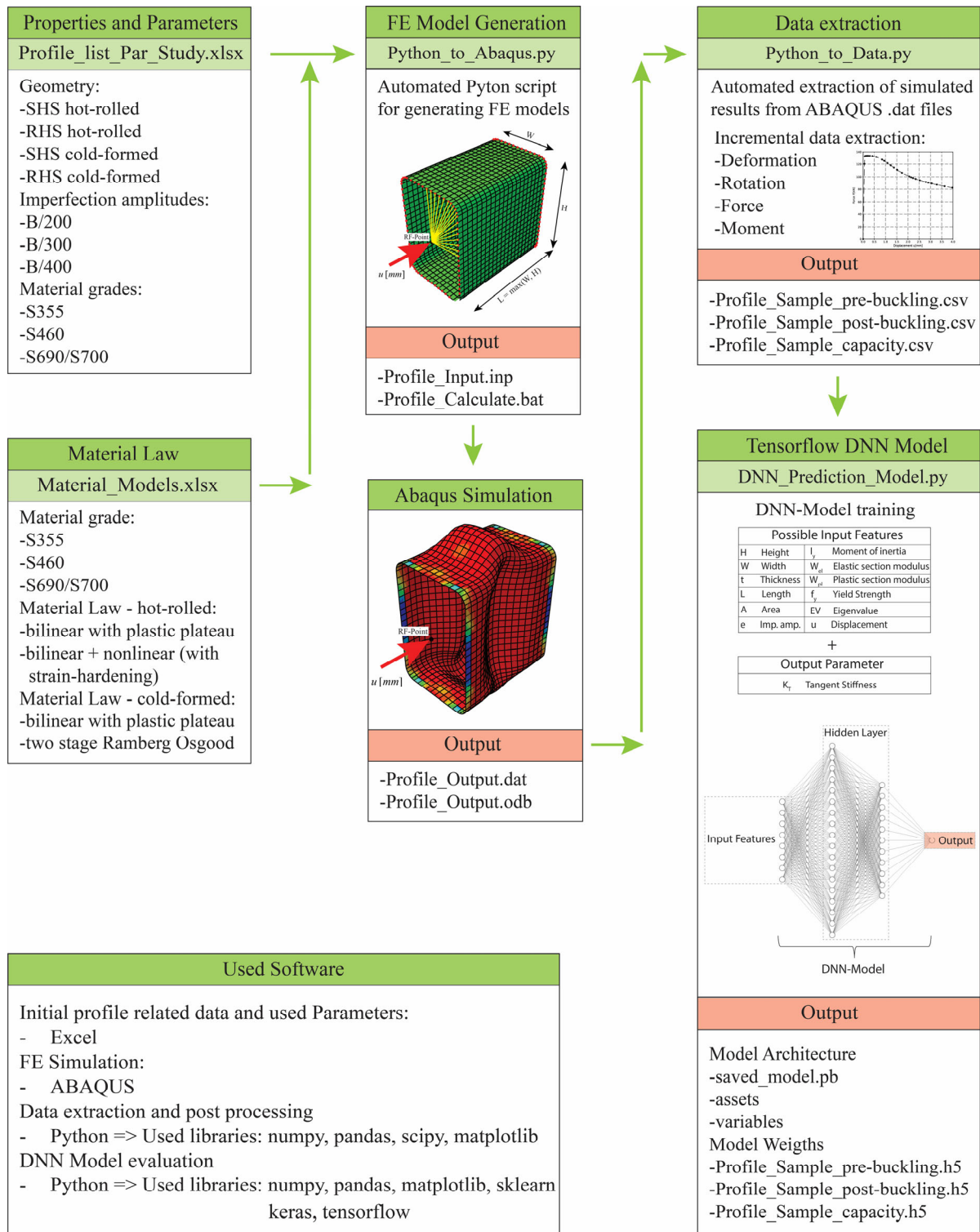


Figure 6-1: Data generation workflow and used software

The applied workflow for the generation of the data and its subsequent implementation to a DNN model is presented in Figure 6-1. All considered profiles (hot-rolled and cold-formed SHS/RHS profiles), additional variable parameters (in particular imperfection amplitudes and material grades), as well as the used material models were collected within two excel files “Profile_list_Par_Study.xlsx” and “Material_Model.xlsx”. A python code “Python_to_Abaqus.py” was written for an automated generation of ABAQUS .inp files for LBA and GMNIA simulations, using the information from the excel files. The ABAQUS simulations are initialized through a batch file (.bat) for an automated simulation process. An additional written python code “Python_to_Data.py” uses the .dat files from ABAQUS simulations to read out the results, i.e. incremental end deformations, incremental end rotations, as well as corresponding values for the force and the moment. The “Python_to_Data.py” code is coupled to “Profile_list_Par_Study.xlsx” in order to create a full data set with all contemplated features. The gathered information is summed up in .csv files. A third python code “DNN_Prediction_Model.py” is used to implement and train deep neural networks with the goal to accurately predict the incremental tangent stiffness K_T of the whole load-displacement or moment-rotation paths. In the course of the investigations, it was also necessary to make accurate predictions for the maximum force F_{max} and the maximum moment M_{max} achieved.

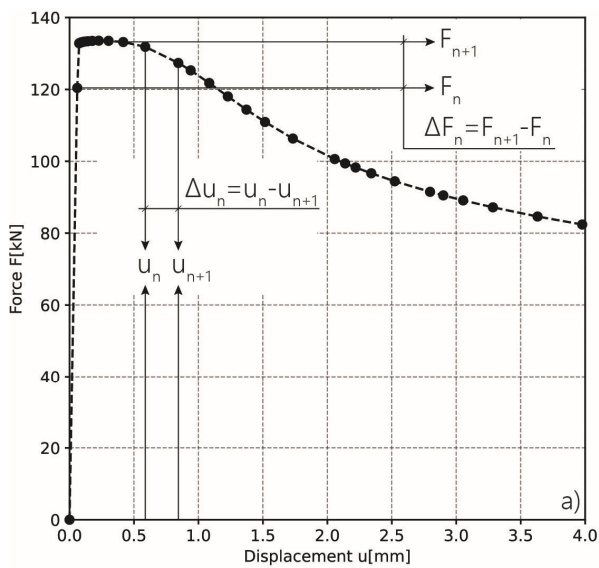
6.1.2 Data extraction

The generated data basis from Abaqus LBA and GMNIA simulations is used for the extraction of the input and output values. The LBA output is used to extract the cross-section dependent elastic critical buckling eigenvalue F_{cr} , corresponding only to pure compression in this thesis. In addition, the first local eigenshape is used as an initial imperfection shape. The GMNIA analysis results are used to extract the absolute and incremental deformation steps u_n and Δu_n and the corresponding differential force ΔF_n . This process of data extraction is exemplary shown by using a load-deformation representation from a GMNIA simulation, displayed within Figure 6-2 a). The simulated values determined this way are subsequently used to calculate the incremental tangent stiffness $K_{T,n}^N$ for the whole cross-section dependent pre- and post-buckling range, see Equation (6-1). The same procedure was applied to all extracted moment-rotations outputs for the calculation of the tangent stiffness $K_{T,n}^M$, see Equation (6-2). Figure 6-2 b) sum up the

extracted features used to develop the data sets. Overall, the features contain profile specific geometric and mechanical properties such as the profile height, width, thickness, moment of inertia, elastic stiffness etc., as well as the output value of the incremental tangent stiffness. Note that not all extracted features are necessary for a successful DNN model training. A feature importance evaluation is thus discussed in Section 6.2.5. Information on feature importance, data structure, distribution, as well as their effect on DNN model behaviour and accuracy are presented within Section 6.2.

$$K_{T,n}^N = \frac{\Delta F_n}{\Delta u_n} \tag{6-1}$$

$$K_{T,n}^M = \frac{\Delta M_n}{\Delta \varphi_n} \tag{6-2}$$



H	Height	I_y	Moment of inertia
W	Width	W_{el}	Elastic section modulus
t	Thickness	W_{pl}	Plastic section modulus
L	Length	f_y	Yield Strength
A	Area	EV	Eigenvalue
e	Imperfection amp.	K_T	Tangent Stiffness
u	Displacement		

SHS-Profiles
 Hot rolled
 DIN EN 10210-2 (2006)
 and
 Cold-formed
 DIN EN 10219-2 (2006)

RHS-Profiles
 Hot rolled
 DIN EN 10210-2 (2006)
 and
 Cold-formed
 DIN EN 10219-2 (2006)

Figure 6-2: Data extraction from non-linear Abaqus simulations; a) force-displacement relation for pure compression; b) potential features for pure compression; c) moment-rotation relation for pure bending; d) potential features for pure bending

6.1.3 Data structure

Below is a selection of the extracted data for longitudinal deformation and constant bending. The first 12 columns represent possible geometric and material features of the hollow section. These features are constant values for each record (record = the course of the numerical simulation of a single cross-section in Abaqus) in the data set. The features marked in orange, i.e. the longitudinal deformation u (compression) and the rotation θ (equal rotation at both ends), are changed within a record, typically with increasing values. The column marked in green shows the target variable (desired output/prediction), i.e. the incremental tangent stiffness for each calculation step.

Table 6-1: Used profiles and parameters

Compression													
H	W	t	L	A	I_y	$W_{y,el}$	$W_{y,pl}$	e	f_y	K_e	F_{cr}	u	K_T
40	40	2.6	40	3.82	8.8	4.4	5.31	0.2	355	2·106	1.2·106	-0.001	2·106
40	40	2.6	40	3.82	8.8	4.4	5.31	0.2	355	2·106	1.2·106	-0.002	1.6·106
40	40	2.6	40	3.82	8.8	4.4	5.31	0.2	355	2·106	1.2·106	-0.003	1.2·106
Bending													
H	W	t	L	A	I_y	$W_{y,el}$	$W_{y,pl}$	e	f_y	K_e	F_{cr}	θ	K_T
40	40	2.6	40	3.82	8.8	4.4	5.31	0.2	355	2·106	1.2·106	-0.01	2·106
40	40	2.6	40	3.82	8.8	4.4	5.31	0.2	355	2·106	1.2·106	-0.02	1.6·106
40	40	2.6	40	3.82	8.8	4.4	5.31	0.2	355	2·106	1.2·106	-0.03	1.2·106

where:

$H [mm]$ is the cross-section height

$W [mm]$ is the cross-section width

$t [mm]$ is the cross-section thickness

$L [mm]$ is the cross-section length

$A [cm^2]$ is the cross-section area

$I_y [cm^4]$ is the moment of inertia

- $W_{y,el} [cm^3]$ is the elastic moment of resistance
- $W_{y,pl} [cm^3]$ is the plastic moment of resistance
- $e [mm]$ is the local imperfection amplitude
- $f_y [N/mm^2]$ is the steel grade
- $K_{e,truss} [N/mm]$ is the elastic truss and beam stiffness
- $K_{e,beam} [Nmm/rad]$
- $F_{cr} [N]$ is the critical buckling load from LBA simulation
- u, θ is the applied deformation and rotation

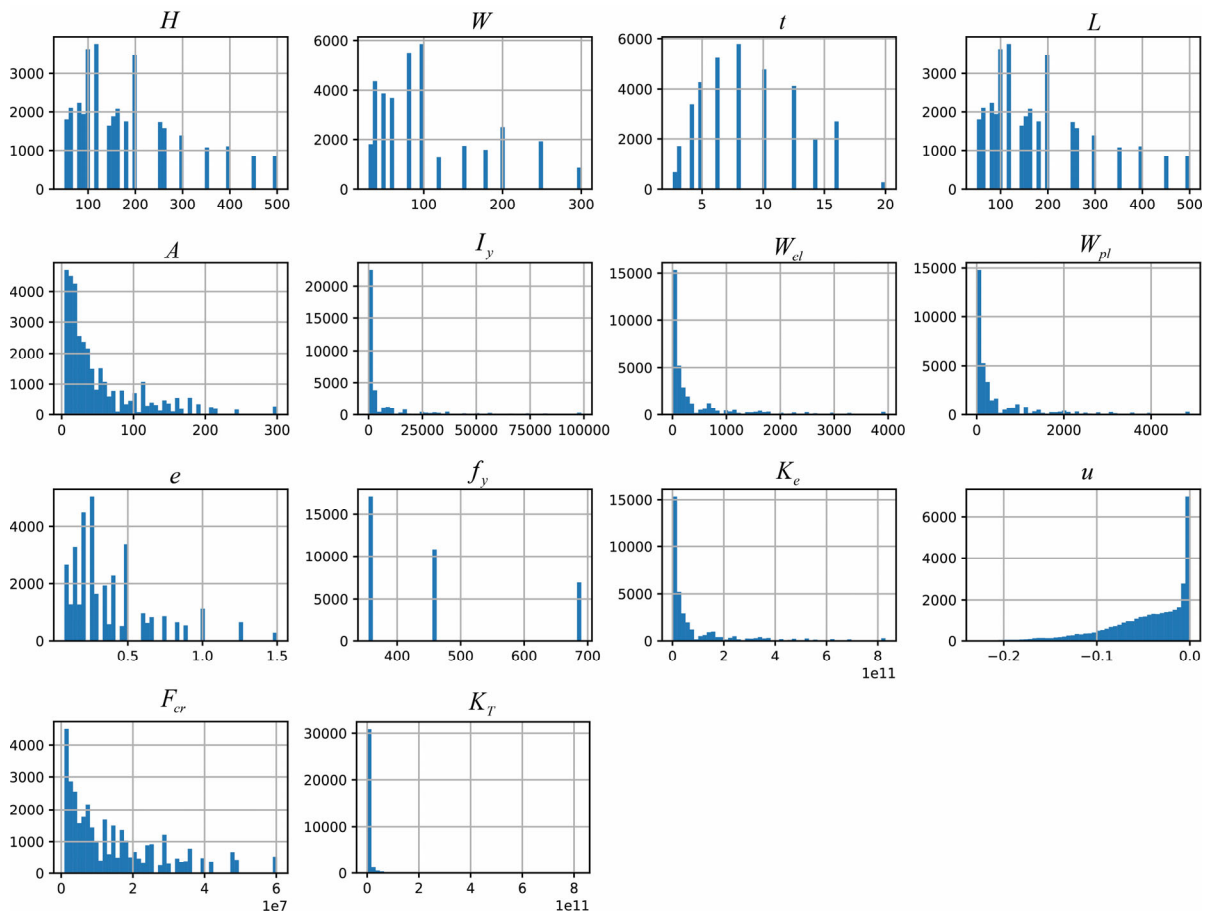


Figure 6-3: Exemplary representation of the data distribution for hot-rolled RHS profiles in the pre-buckling range

Figure 6-3 shows an example of the data distribution for hot-rolled RHS profiles in the pre-buckling range. Each feature is displayed individually.

The currently used data volume is shown in Table 6-2. Each individual number within the whole data set represent an entry, containing all possible features from Table 6-1. The whole data is split into pre- and post-buckling data sets, subdividing the predictions made later on in the different ranges. The cross-section capacity for each profile is represented in an extra data set, containing less data, since not the whole load-deformation/moment-rotation course is needed, but only the data at the point of the maximum reached load. The decision to split the data is made upon performed investigations from Section 6.2 in the following.

Table 6-2: Row entries in individual data sets

Profiles	Pre-buckling	Post-buckling	Cross-section capacity
Load Case: Compression (N)			
SHS Hot-rolled	315672	344282	954
RHS Hot-rolled	331982	424743	1008
SHS Cold-formed	308770	450012	1278
RHS Cold-formed	271554	490301	1485
Load Case: Bending (M)			
SHS Hot-rolled	251244	353110	954
RHS Hot-rolled	314352	205093	1008
SHS Cold-formed	212508	254254	1278
RHS Cold-formed	305676	384246	1485

6.2 Feature Engineering and Governing Results

The data quantity, its structure and density, appropriate feature sets or the data transformation strategy affect highly the accuracy of the output predictions of DNNs. The principle applies that *poor data quality will lead to inferior results*, in general independently of the computational level of the used method. However, of the methodology used in this thesis is the use of fully simulated data, leading to a very low scatter and the possibility of data reproduction and augmented extension.

Before choosing an appropriate DNN architecture, it was necessary to first investigate the data structure. This procedure is widely known under the term of “feature engineering” and includes different methods, starting with investigations on data quality and distribution, followed by necessary considerations of data normalization in the input and output layers, as well as investigations on feature importance, i.e. which input parameters has an impact on the optimization of DNN model. Thus, by using unsupervised methods like principle component analysis (PCA), to reduce the feature dimensionality, or the evaluation of the feature importance with decision tree based algorithms tendencies towards individual parameters are obtained.

The process of data analysis and interpretation is not structurally defined and does not necessarily follow a fixed sequence of operations. Since this process is highly iterative and many parameters are constantly changed, no clear hierarchy can be named within the individual modifications. Therefore, according to the principle of an ascending complexity, the most important adjustments are pointed out and summarized in the following subsections.

6.2.1 Preface to presented investigations

No direct reference information from previous research on parameters and their influence on the learning or prediction behaviour of DNN models in connection with load-deformation or moment-rotation data was available. For this reason, the considered parameters were chosen in order to minimize uncertainties, save computational time and primarily reduce their overall number. It shall be noted that the goal of this investigations was to verify the feasibility and performance of the proposed methodology, as opposed to fully verifying its accuracy and reliability. These investigations and their outcomes were previously published in [289]–[292] and form the basis for the studies presented here, with further research being carried out on the basis of the parameters from Section 5.4.2, i.e., the full set of hot-rolled and cold-formed RHS and SHS profiles from [4] and [5], as well as a non-linear material behaviour as proposed in [6] and [7].

6.2.2 Data set density

6.2.2.1 Data expansion

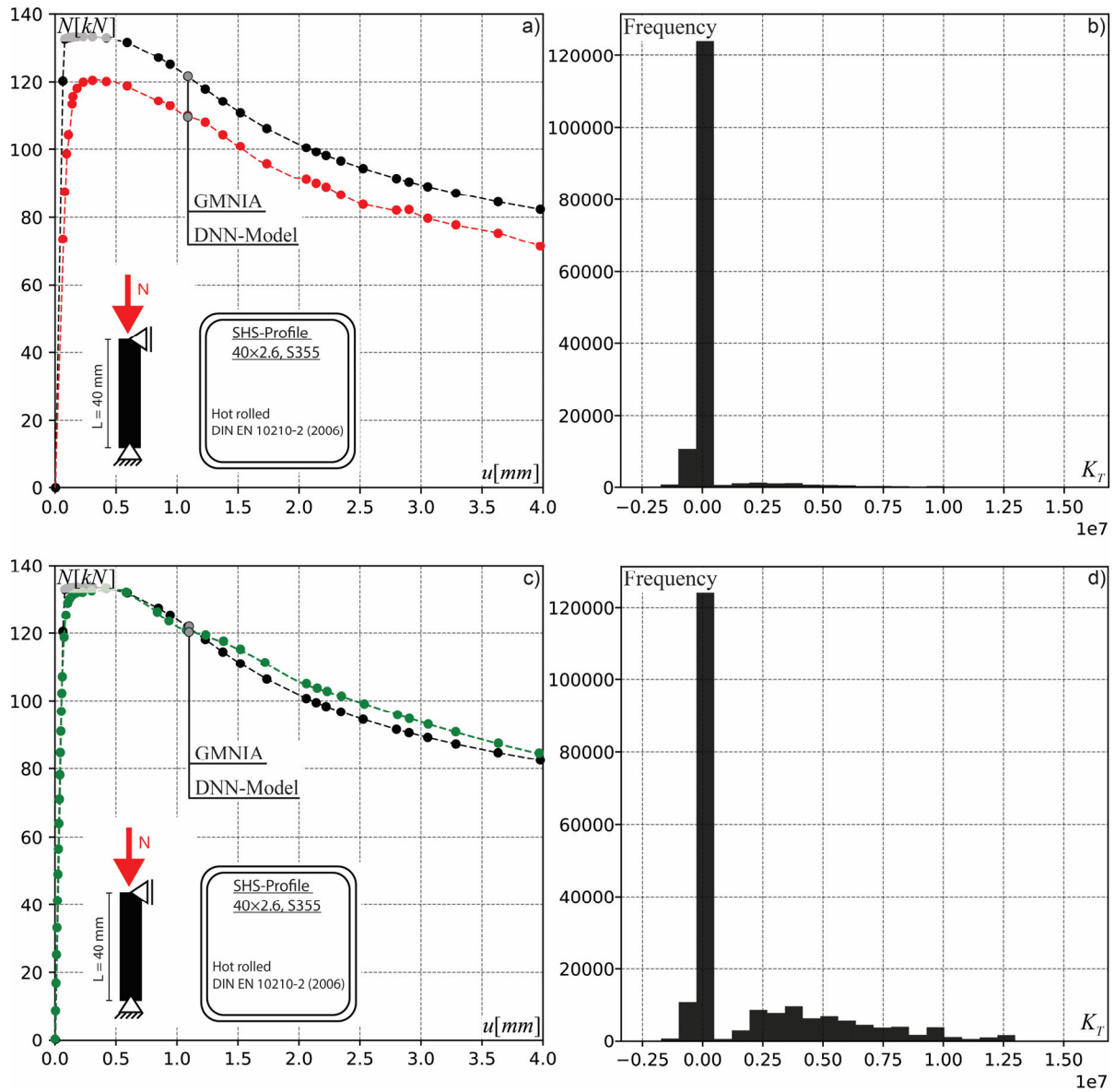


Figure 6-4: Comparison between simulated Abaqus GMNIA results and DNN model predictions for a different data density in the elastic range; a) DNN prediction for an SHS 40x2.6, S355, based on data set without data expansion; b) Histogram describing the tangent stiffness K_T based on data set without data expansion; c) DNN prediction for an SHS 40x2.6, S355, based on data set with data expansion; d) Histogram describing the tangent stiffness K_T based on data set with data expansion

Based on own investigations carried out to analyze the data density, structure and its influence on the performance on different DNN models, a clear outcome is obtained and

presented in Figure 6-4. The left side shows two load-displacement diagrams and the right side an associated frequency distribution of the tangent stiffness. The Abaqus GMNIA simulation is described by the black dotted curve and is considered here as the benchmark resistance. Each dot represents one increment of the numerical simulation. For the purpose of a better representation, the points were connected through interpolated lines. The red dotted line from Figure 6-4 a) symbolizes the predicted resistance, calculated with one DNN model by using the raw data set. This means that the displacement u had the same incremental distribution as provided by the Abaqus simulations. A profound difference between the black and the red curve can be obtained, especially in areas of small displacement in the pre-buckling range, i.e. high tangent stiffness. Due to this premature softening behaviour, the maximum load is predicted very inaccurately though. On the other hand, the course obtained in the post-buckling range is more precise, although the overall resistance is predicted too low. Figure 6-4 b) shows the frequency distribution of the tangent stiffness of the whole data set, including all investigated cross-sections.

The highest frequency is clearly reached around the value of zero. This range is attributed to the area near the maximum force of the load-displacement diagram, see Figure 6-4 a). The peak can be explained by the smaller increments chosen within the Abaqus simulation to achieve equilibrium in non-linear areas. On the other hand, relatively large incremental steps are made in the elastic range at the beginning of the calculation. Therefore, the different incremental step sizes along the load-displacement curve lead to an uneven distribution of data, resulting in predictions that are more accurate for regions with higher density. For this reason, high values of the tangent stiffness $K_T \approx K_e$, extracted from the start of every Abaqus simulation, are seen as outliers by the DNN models and are therefore difficult to predict precisely. Figure 6-4 c) shows an updated prediction, which is more accurate in representing the resistance within the pre-buckling range. A data enlargement was carried out by interpolating linear between the increments in the elastic range, i.e. the very first increments. Thus, leading to an artificially increased data density for the tangent stiffness of $K_T \gg 0$, as shown in the histogram of Figure 6-4 d). Overall, the expanded data set was increased by around 40 %.

Although this approach increases the prediction accuracy of the DNN models, the basic assumption to reduce the amount of calculated steps in Abaqus itself has a crucial drawback that becomes visible on a more global member scale within the DNN-DSM implementation. The following representations give an outlook on the prediction within the DNN-DSM approach, addressing the pre- and post-buckling behaviour dependent on different model assumptions to illustrate the effect, coming from the simplifications stated above.

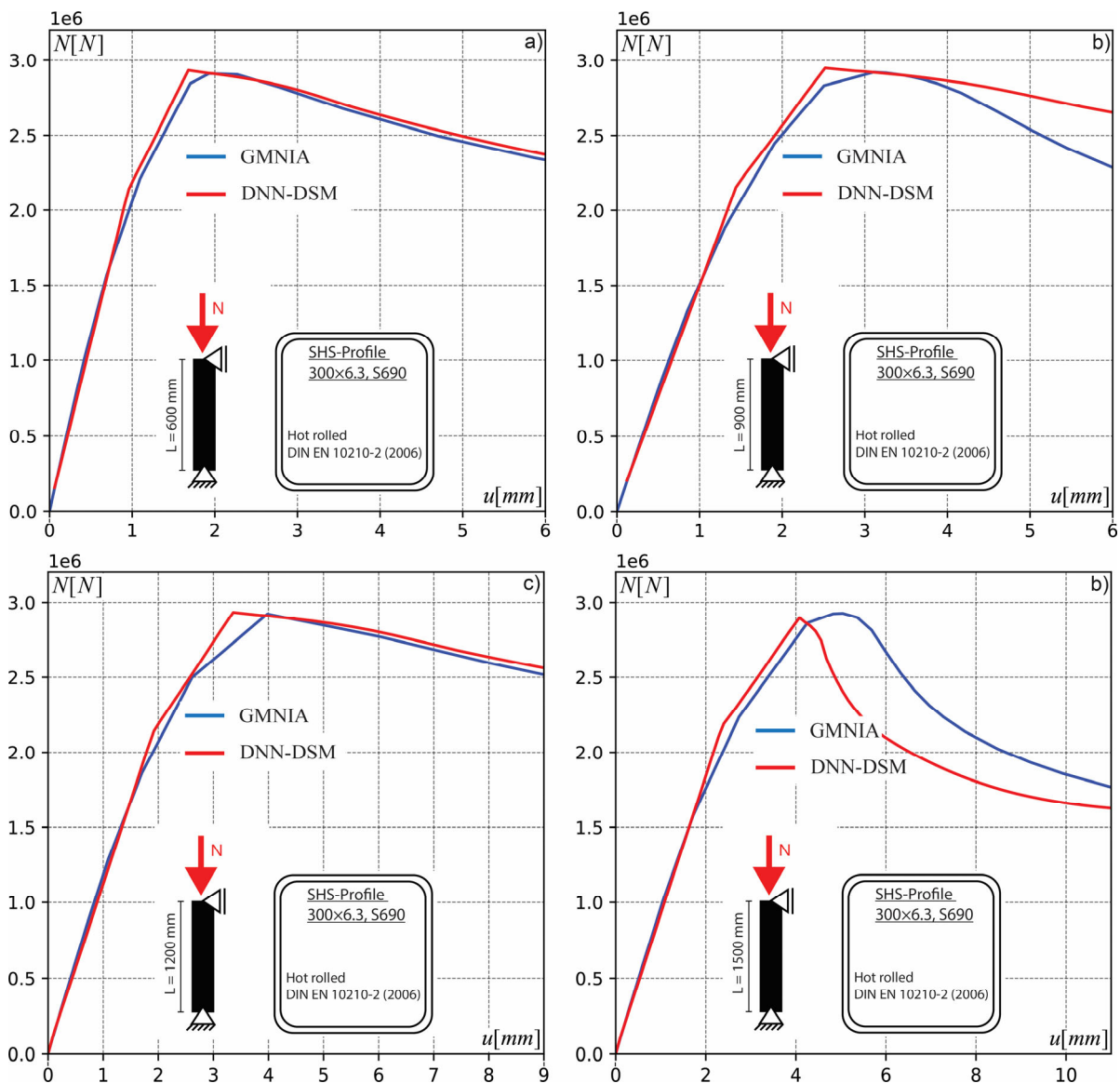


Figure 6-5: Comparison between GMNIA shell simulations and DNN-DSM prediction for a hot-rolled SHS300×6.3, S690 members, a) large solver steps, $L = 600$ mm; b) large solver steps, $L = 900$ mm; c)

Figure 6-5 shows an SHS300×6.3, S690 profile with the length of 600 mm (see Figure 6-5 a)), 900 mm (see Figure 6-5 b)), 1200 mm (see Figure 6-5 c)) and 1500 mm see Figure 6-5 d), loaded by pure compression. The x-axis describes the compression in axial direction and the y-axis the applied normal force. Curves in blue represent the FE-shell based GMNIA simulation. The red curves show the DNN-DSM recalculation. According to the current DNN-DSM approach the models are build up from local elements (beam elements), where the element length corresponds to the bigger value of the height or the width. The observations from Figure 6-5 mainly show that the overall non-linear load-deformation behaviour can be recalculated compared to the Abaqus GMNIA simulations in the pre- and post-buckling range. However, it is noticeable that with increasing member length, the maximum loads are well predicted, but the associated deformations are not accurately reproduced. This finding was only discovered during the course of implementation and comparative calculation, but has its origin in the assumptions made here, i.e., Abaqus solver settings resulting in a big step time.

6.2.2.2 Conclusions

As described in Section 6.2.2.1, assumptions were made within the solver step time, which lead to a computational reduction and fast results with the disadvantage of accuracy loss. This is illustrated through the load-displacement curves in Figure 6-6. Different solver setting were used for GMNIA (1) to GMNIA (3) simulations with increasingly smaller solver steps, i.e. an initial first step, a minimum step and a maximum step.

The minimum step was set constant to a very small value of $1e-20$, in order to make shore that the GMNIA calculation runs smoothly even for very slender cross-sections. The maximum step time was varied from 0.1 to 0.001 . The accuracy increases with decreasing steps and results in a more rounded non-linear curve behaviour. Further, a shift in the load bearing capacity towards higher deformations is visible. A maximum of around 15%, here exemplary shown for a hot-rolled SHS300×6.3 profile (s Figure 6-6 a)), is achieved by comparing GMNIA model (1) and (3). This difference potentially decreases with smaller step sizes. Comparing GMNIA model (2) and (3) only a difference of <1% is obtained.

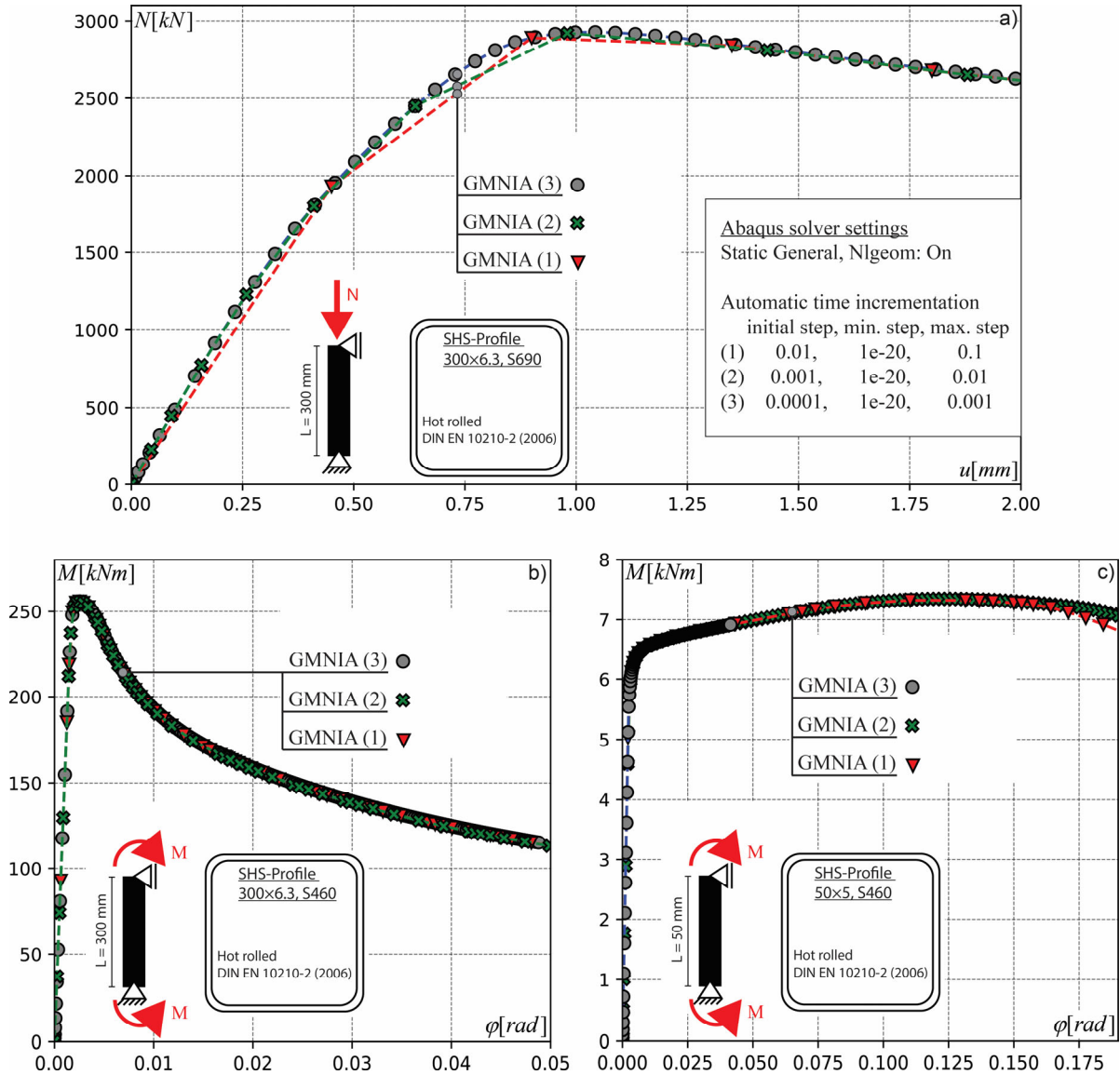


Figure 6-6: Load-displacement curves for different Abaqus solver step time setting

Therefore, to be numerically accurate and yet computationally time efficient, GMNIA model (2) solver settings are set to default to be used throughout data-set generation. To simplify the problem a similar behaviour is assumed for all other profiles and load cases, although, the effect of the capacity shift and the non-linear response was not visible for the case of a constant moment, see Figure 6-6 b) and c). In addition Figure 6-7 a), b), c), d) show the results with the adopted step time settings. The results show the same results in the pre- and post-buckling regions with an increasing accuracy towards the point of reaching the maximum force and corresponding deformation.

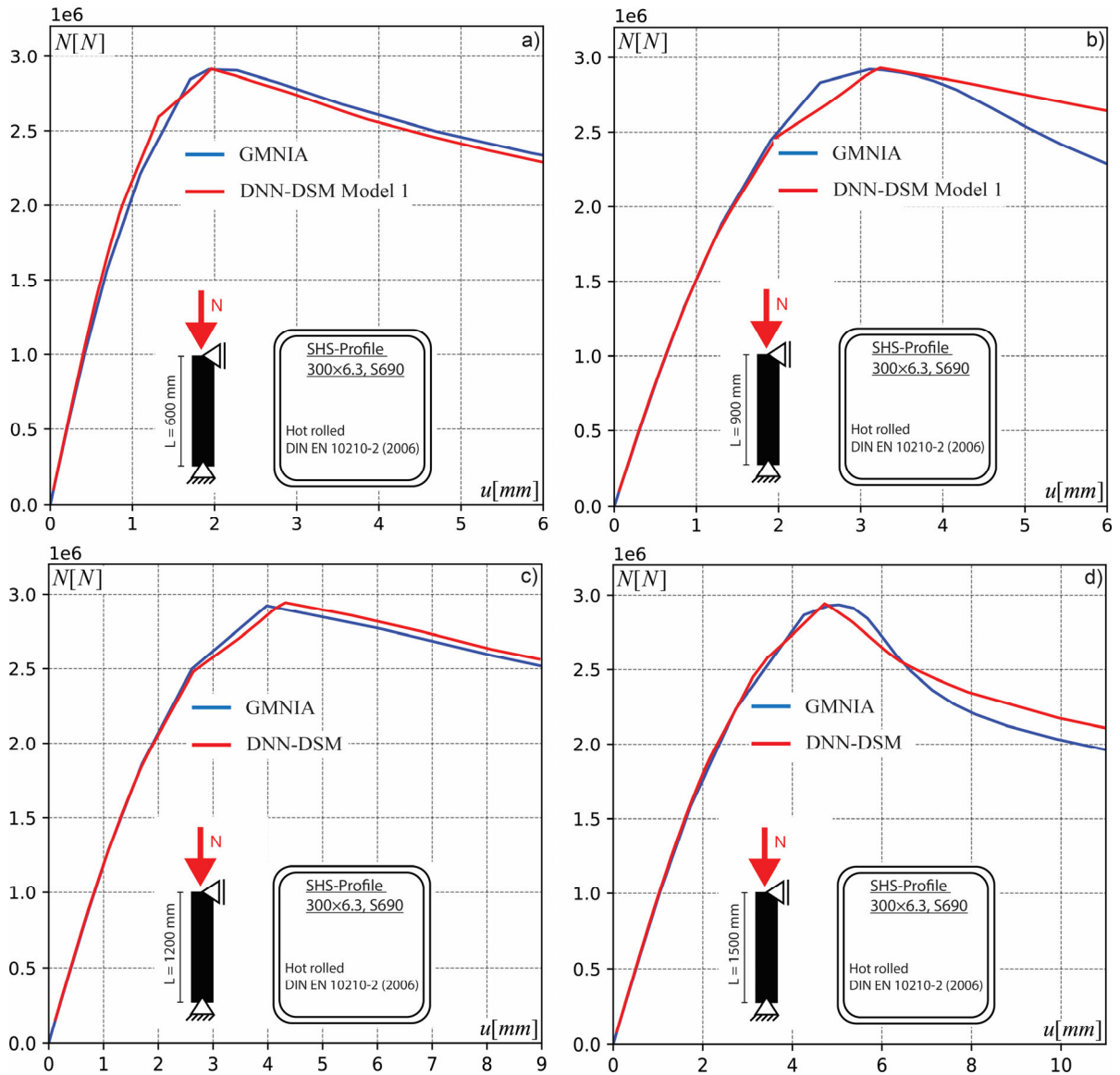


Figure 6-7: Comparison between GMNIA shell simulations and DNN-DSM prediction for a hot-rolled SHS300x6.3, S690 members, a) $L = 600$ mm; b) $L = 900$ mm

6.2.3 Data set splitting

Table 6-3: Split data sets according to profile, fabrication and the pre- and post-buckling range

Load Case: Compression (N)				
Prediction of the incremental tangent stiffness K_T				
Profiles	SHS		RHS	
Fabrication	hot-rolled	cold-formed	hot-rolled	cold-formed
Data sets	pre-buckling (1)	pre-buckling (1)	pre-buckling (1)	pre-buckling (1)
	post-buckling (2)	post-buckling (2)	post-buckling (2)	post-buckling (2)
Prediction of the maximum force N_{max}				
Data sets	load bearing capacity (3)	load bearing capacity (3)	load bearing capacity (3)	load bearing capacity (3)
Load Case: Bending (M)				
Prediction of the incremental tangent stiffness K_T				
Profiles	SHS		RHS	
Fabrication	hot-rolled	cold-formed	hot-rolled	cold-formed
Data sets	pre-buckling (1)	pre-buckling (1)	pre-buckling (1)	pre-buckling (1)
	post-buckling (2)	post-buckling (2)	post-buckling (2)	post-buckling (2)
maximum Moment M_{max}				
Data sets	load bearing capacity (3)	load bearing capacity (3)	load bearing capacity (3)	load bearing capacity (3)

Based on the outcomes of DNN model performance evaluations, additional adjustments were made with regard to the data structure. It was obtained that a splitting between hot-rolled and cold-formed SHS and RHS profiles and the pre- and post-buckling range led to a significantly better performance. The r^2 (r-squared) value (see Equation (4-8)) could be raised considerably up to $r^2 = 0.999$. Especially the prediction of the cross-section dependent maximum load F_{max} or moment M_{max} was met with a very high accuracy. The prediction output is further presented in Section 6.2.4 in the context of data transformation. The split data sets are shown in Table 6-3, below. The general split was necessary to improve the performance of the DNN-models, yet has a disadvantage in the prediction process of the whole non-linear response, disregarding the applied load case. Since the pre- and post-buckling range are no longer predicted by one neural network, the need for a third DNN model arises, which indicates the switch between this areas.

The third DNN-model predicts only the load bearing capacity as a condition in the calculation procedure within the DNN-DSM approach. Its methodology and implementation are presented in Chapter 7.

6.2.4 Data transformation

6.2.4.1 Transformation of input features

Figure 6-8 shows the difference between the performances of several DNN models based on normalized (see Equation (4-12)) and standardized (see Equation (4-13)) inputs. In each case, six randomly chosen feature combinations were taken into account. These will not be commented on further, as they serve for demonstration purpose only. The x-axis represents the number of epochs. These are in a general sense the number of repetitions in the training procedure. The y-axis describes the network accuracy using the measure r-squared (see Equation (4-8)), a statistical measure of the unexplained and the total variation.

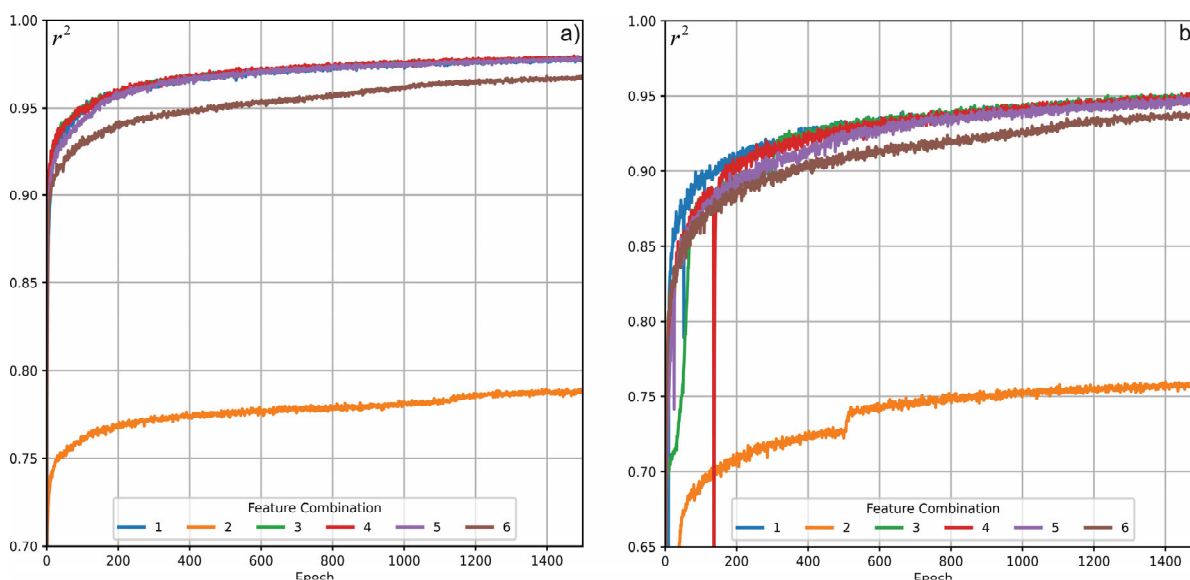


Figure 6-8: Training results for using a) standardized features; b) normalized features

The performance of DNN models with standardized feature combinations are summarized in Figure 6-8a). First, it can be noted that the r^2 value increases steeply straight from the beginning of the optimization process. Already after less than 50 epochs the value of $r^2 = 0.90$ is exceeded. After approximately 200 epochs, even the value of $r^2 = 0.95$

is passed for most feature combinations. On the other hand, Figure 6-8 b) shows the DNN model performance using normalized data sets. A direct comparison shows that the overall model accuracy is lower. Due to a flatter course between the first 200 epochs from the beginning, an $r^2 = 0.95$ can only be reached by the end of the optimization process around 1500 epochs. This difference underlines the choice of data standardization within further investigations and results presented in the following.

6.2.4.2 Prediction of the tangent stiffness K_T

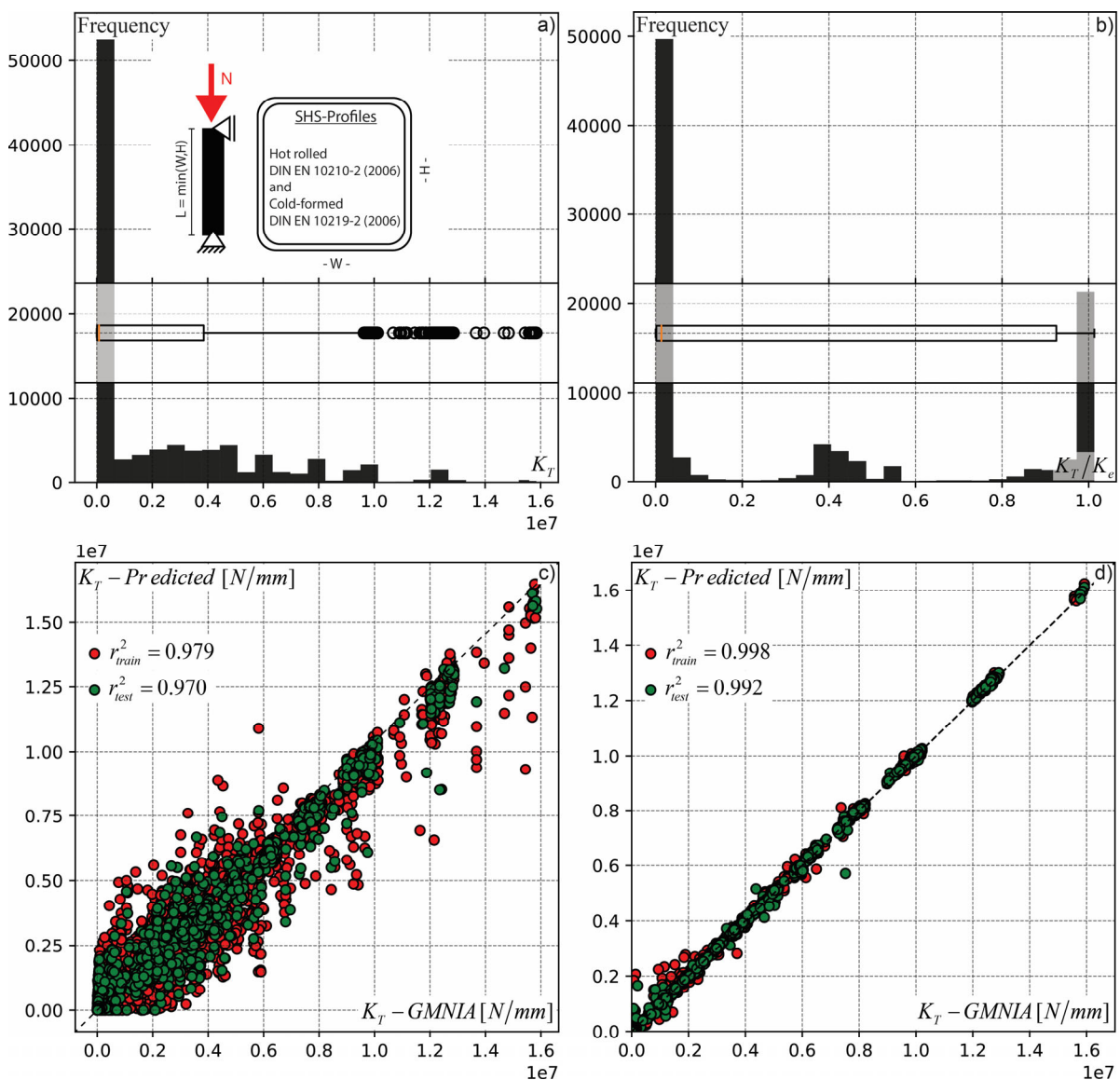


Figure 6-9: Output distribution for the subset of SHS hot-rolled profiles a) raw values of the tangent stiffness K_T ; b) transformed values of the tangent stiffness divided by the elastic stiffness K_T/K_e

An additional influence on the model performance is attributed to the chosen format of the predicted value within the output layer. Depending on its distribution within the data set, the accuracy can vary greatly within the predictions. The frequency distribution of the raw values of the tangent stiffness K_T , for hot-rolled SHS profiles in the pre-buckling range, is shown in Figure 6-9 a).

Values concentrated around zero represent the tangent stiffness ($K_T \ll K_e$) near the maximum reached resistance. However, all other values can be a combination of $K_T \approx K_e$ or $K_T < K_e$, attributed to the elastic initial range or an intermediate range with a propagating non-linear behaviour. This mixed tangent stiffnesses on the one side and the big difference in its magnitude (ranging between 0 and $1e7$) on the other side for the direct prediction of K_T (see Figure 6-9 a)), significantly affect the optimization process of the DNN model. Thus, in the investigations carried out, an $r^2 = 0.95$ was reached after approximately 1000 epochs and an $r^2 = 0.98$ after approximately 6000 epochs. Figure 6-9 b) shows the frequency histogram of the tangent stiffness K_T divided by the elastic stiffness K_e . The resulting distribution in this case is completely different from before, being clustered in mainly three parts due to the transformation. Values around zero are still attributed to the area near the maximum resistance. However, the cross-section dependent tangent stiffness in the elastic range ($K_T \approx K_e$) is now located close to the value of one. All other values of $K_T < K_e$ are in between these boundary ranges and are assigned to an increasing non-linear local behaviour. The prediction accuracy in this case is significantly higher. Thus an $r^2 = 0.99$ is already reached after approximately 200 epochs using the same DNN model architecture. Although the difference between the estimated accuracies is less than 2%, a higher scatter is obtained within the predicted stiffnesses using the raw output data in Figure 6-9 a). It must also be pointed out that the optimization process, measured in terms of the required epochs and the estimated associated model accuracy, was slower compared to the performance of DNN models based on the transformed data from Figure 6-9 b).

6.2.4.3 Prediction of cross-section resistance

A similar procedure applies for the prediction of the cross-section resistance, i.e. the peaks in the load-displacement curves. In general, it makes sense to start from a physically well-understood value, which is either the maximum reached peak load F_{max} or the calculated local buckling reduction factor $\chi = F_{max} / F_{pl}$. When considering these two data series, it makes sense to first look at their distribution. Therefore, Figure 6-10 a) and b) shows the frequency for the maximum load and the buckling reduction factor, respectively. From this, the following points can be specifically identified. It can be seen from Figure 6-10 a) that the maximum peak load for the majority of the profiles is highly distributed in the lower force range with an overall mean value of 2,851 kN. Additionally, the lowest and highest cross-section related peak load is equal to 93 kN and 20,5 kN, respectively. On the one hand, the distribution of the loads indicates that high values could partly be seen as outliers by the DNN, on the other hand, the big difference of the minimum and maximum values are a disadvantage, since this gap must be correctly covered by the weights and biases within the network. Therefore, it can make sense to rather normalize the prediction, which is done here by using the plastic cross-section capacity $F_{pl} = A \cdot f_y$ and calculate the buckling reduction factor χ . This consideration automatically minimizes the range between the values and changes the data distribution, see Figure 6-10 b). All values near the plastic resistance F_{pl} are therefore located around 1, which leads to a more meaningful representation; values below 1 can be addresses to more slender cross-sections, values around and above 1 to stocky cross-sections.

The consideration of both output parameters is shown within Figure 6-10 c) and d), respectively, to confirm the above stated arguments. Both figures represent the precision of the predictions reached after 1,000 epochs, made with the same neural network (presented in more detail within Sec. 4) and using the r-squared measure from Equation (4-8). A difference in the predictions can be obtained, although in both cases the r-squared valued are relatively high and could already be interpreted as sufficient enough. However, this is not least to the fact that we are dealing here with simulated values without a significant scatter. Yet, this problem is transferable and shows higher deviations obtained by using directly F_{max} as the predicted value, see Figure 6-10 c), rather than the

local reduction factor χ , see Figure 6-10 d). This subsequently underlines the before mentioned points.

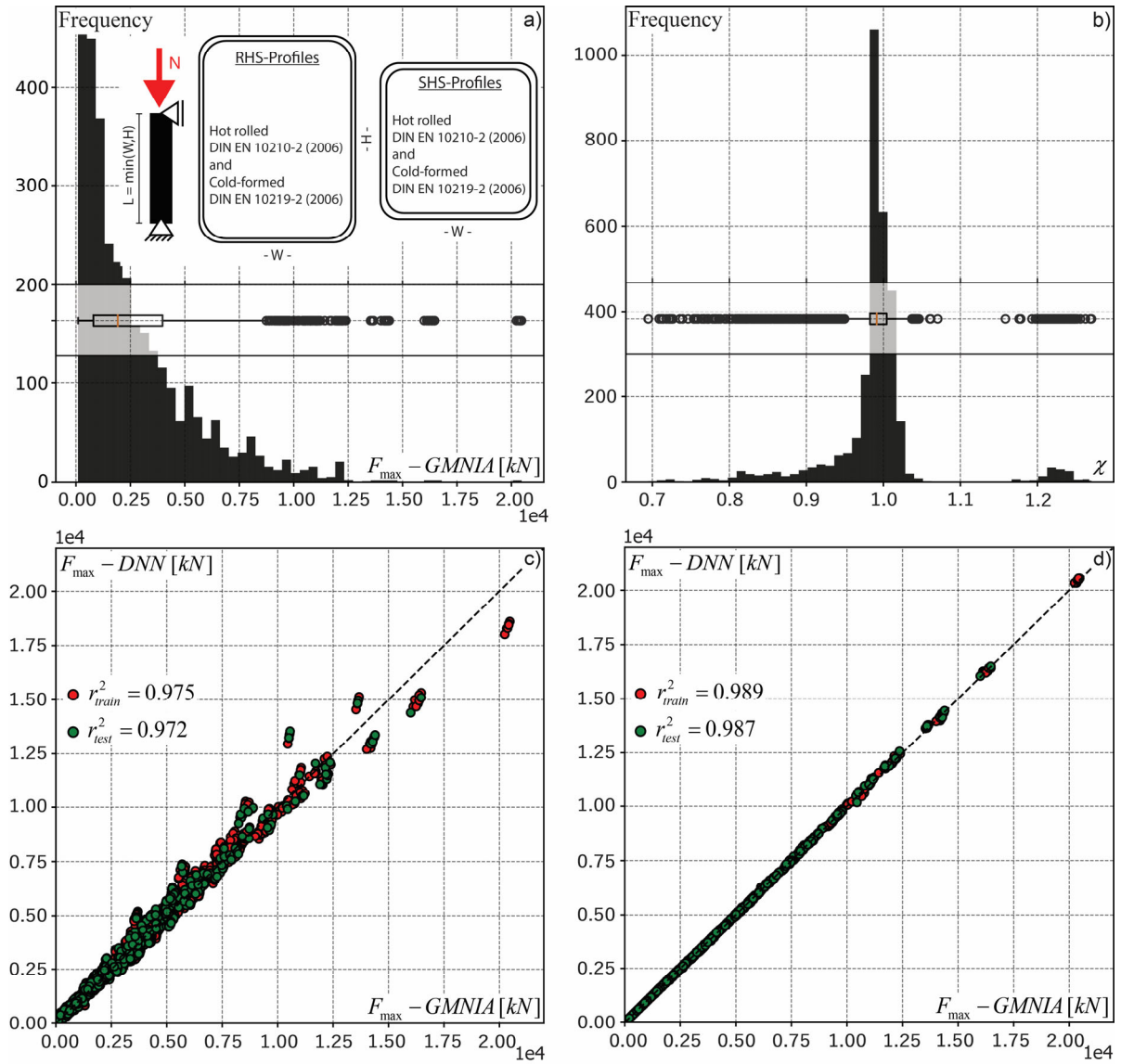


Figure 6-10: Frequency plots of the output values in different formats, a) raw output of F_{max} ; b) normalized output of $\chi = F_{max}/F_{pl}$ and true vs. predicted maximum; c) raw output of F_{max} ; d) normalized output of $\chi = F_{max}/F_{pl}$

6.2.5 Feature assessment

6.2.5.1 Feature interpretation

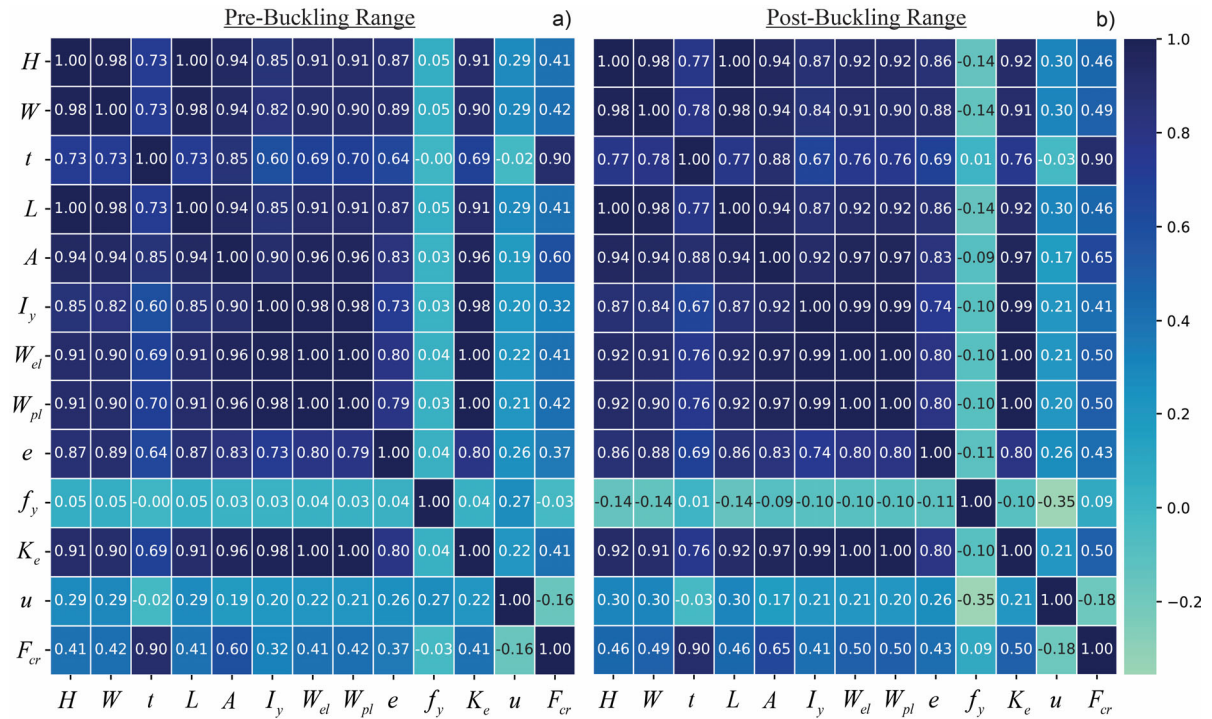


Figure 6-11: Correlation matrix for hot-rolled RHS profiles and the load case of compression, a) pre-buckling range; b) post-buckling range

A correlation matrix provides information on the coefficients of correlation between different features (input parameters) in a given data set and allows for an assessment of those. This step can help to reduce the dimensionality of the input parameters, or at least gain some insight into them within the pre-processing pipeline. Figure 6-11 shows such an output for the pre- and post-buckling data set for hot-rolled RHS profiles, loaded in compression. The matrix has the same number of rows and columns and corresponds to the chosen attributes. Here, 13 parameters, i.e. the profile height H , width W , thickness t , length L , cross-section area A , moment of inertia I_y , elastic moment of resistance W_{el} , plastic moment of resistance W_{pl} , imperfection amplitude e , steel grade f_y , elastic stiffness K_e , deformation u corresponding to centric compression, critical elastic buckling load F_{cr} , were selected. Values close to 1 (or -1) has a strong relationship and therefore correlate with each other, i.e., those values can be reduced since no additional infor-

mation is added to the solution. On the other hand, values closer to 0 has a weak relationship. In addition, negative values has a negative relationship leading to indirect proportional correlation.

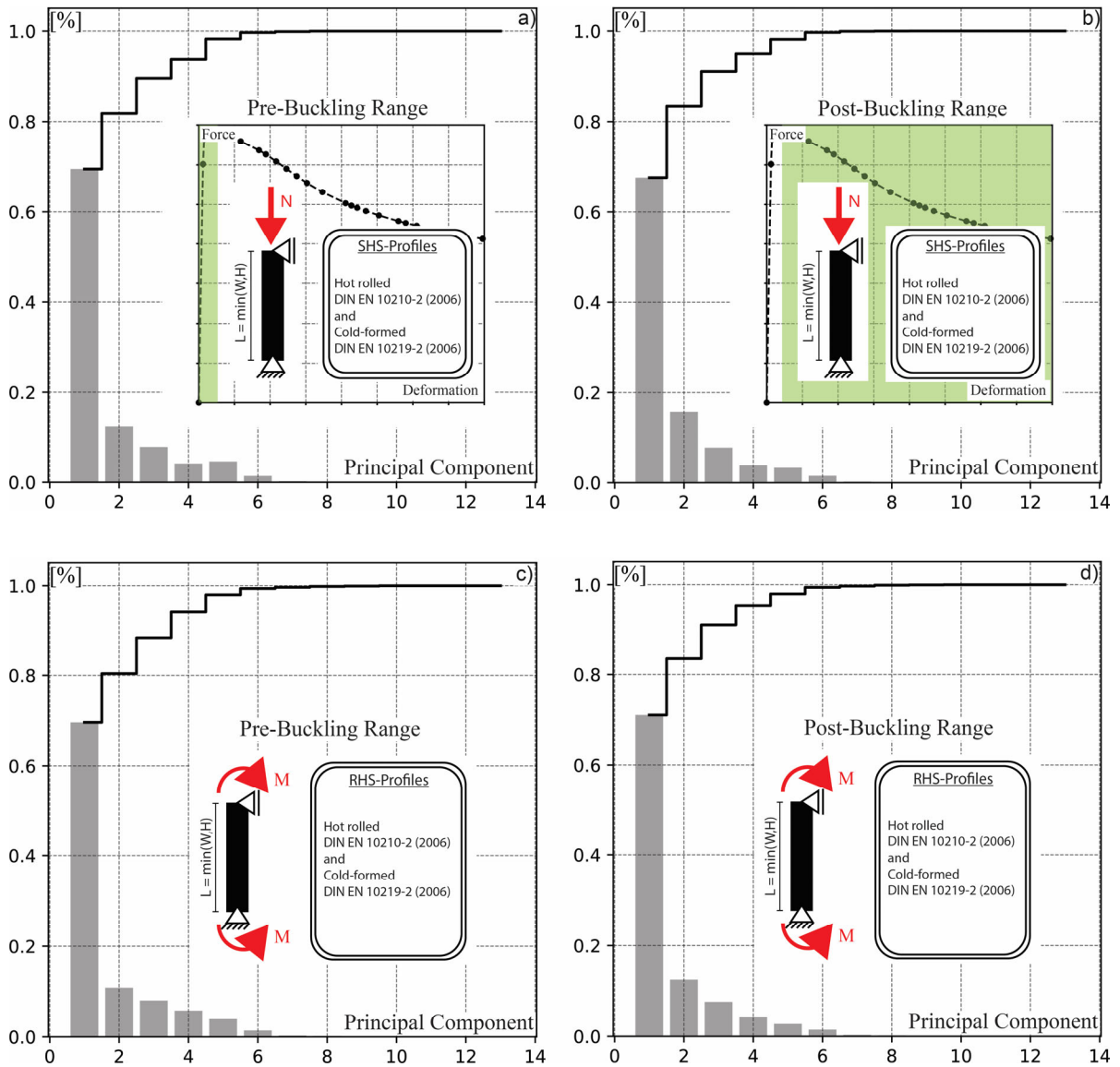


Figure 6-12: PCA for the data-set of hot-rolled SHS profiles; a) pre-buckling range; b) post-buckling range

Figure 6-11 a) and b) provide a similar information. Features highly correlating with each other describe the cross-section geometry (H , W , t , L) and additional cross-section values (I_y , W_{pl} , W_{el}). Features with a low correlation are attributed to mechanical properties like the steel grade f_y , the critical elastic buckling load F_{cr} and the deformation

(crushing) of the cross-section. These explorations provide good insight about the dependencies and serve to confirm the investigations conducted regarding feature importance.

An upstream principle component analysis (PCA) can provide information on the amount of parameters, by finding linear patterns between individual parameters. This method belongs to unsupervised learning techniques and is described in more detail in the following. Note, this step is not mandatory in the context of this thesis, but gives a better imagination for the present parameters and their interdependency, in order to assess the results from decision tree bases feature importance outputs. It assesses the possible potential to reduce the data due to dependencies.

Figure 6-12 shows the output of a PCA. Since the result between cold-formed and hot-rolled SHS and RHS profile is similar, in the following only the output for the set of hot-rolled SHS profiles is shown. The x-axis describes the amount of principal components, which number is equal to the selected features within the data set. Principle components can be described best as new variables, which are built as linear combinations of the initial variables. The initial 13-dimensional data is “squeezed” down to approximately 6 remaining components, see Figure 6-12 a) and b). The y-axis shows the normalized eigenvariance in percentage, calculated from the eigenvector of the covariance matrix. The covariance matrix aims to serve information on the relation between the variables of the input data with respect to their mean value.

Both diagrams within Figure 6-12 show similar results, but, and this point is more important, a high potential to reduce the number of dimensions (features). This information is used to draw the conclusion that several of the possible features are obsolete. Nevertheless, a PCA projects the original data onto the selected principal components to obtain the reduced-dimensional representation. This transformation preserves the most important patterns in the data while discarding less important information. The new output values differ from the physical variables and are not suitable at this level of method implementation. However, in the further development progress this step can make sense, in order to accelerate the method numerically.

In order to obtain information from the present data and make the machine learning model more easily interpretable, several strategies are provided. A common way of interpretation is the SHAP analysis, which allows to understand the contribution of each feature toward the impact on the prediction according to the value of the instance.

The SHAP output has the same dimensions as the data set used originally for the training of the model, i.e., the same amount of rows and columns, however, containing now the calculated SHAP values. The ML prediction for each instance $f(x)$ can be reproduced as the sum of the SHAP values plus a fixed base value, which is the mean value μ of the predicted output (normalized tangent stiffness or normalized cross-section capacity).

$$f(x) = \mu + \sum (\text{SHAP values}) \quad (6-3)$$

The global interpretation of the data set is explained in the followings with the help of beeswarm plots. This plots can be interpreted as more traditional feature importance bar plots as done in Section 6.2.5.2, but provide more information on the actual relationship to the predicted outcome. Figure 6-13 shows this output in a bar plot type with additional information on the value based model prediction, corresponding to each feature. All individual predictions are represented through a point along the bar for each feature. If several predictions have the same SHAP value impact, they are stacked on top of each other. This leads to areas with a larger accumulation of points.

The highest influence on the predicted outcome in the pre-buckling range (see Figure 6-13 a)), here the normalized incremental tangent stiffness K_T/K_e , is caused by the deformation u , the cross-section height H , the steel grade f_y and some additional cross-section values. The deformation u has a positive SHAP value prediction impact for very small values. This is a logical output, since the tangent stiffness K_T is the highest directly at the beginning of the deformation. With bigger deformation values, this impact starts to get negative in order to minimize the predicted outcome. It is noticeable, that the data density increases with higher deformations, i.e., the beeswarm plot for an individual feature is thicker (many predictions for an individual value) or thinner (less predictions for an individual value). This is basically the result of the step time regulation in Abaqus,

leading to smaller time increments in more non-linear load-deformation areas. A big impact can also be obtained from the height of the cross-section, which is clearly a geometrical delimitation between the learned predictions.

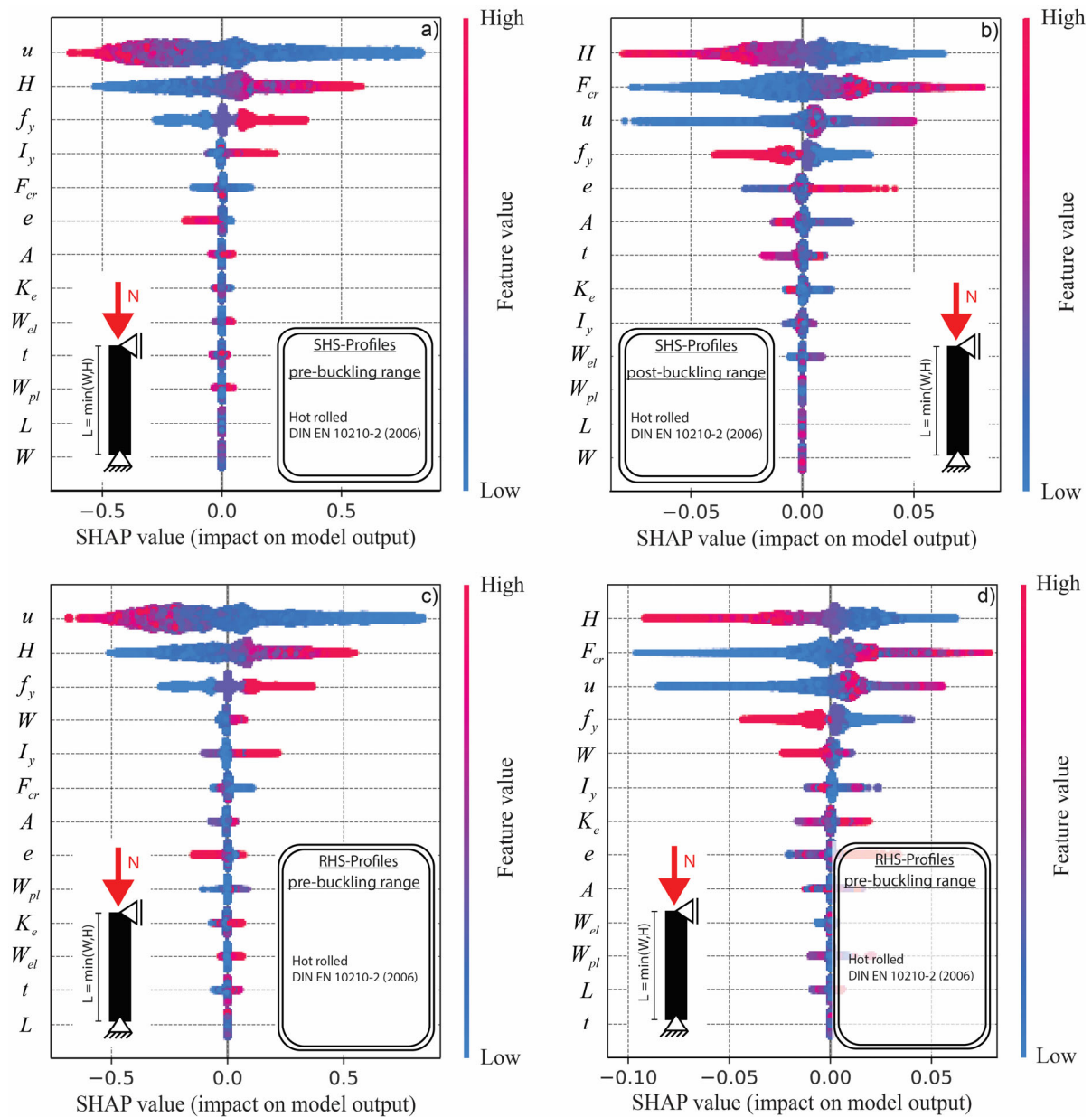


Figure 6-13: SHAP values for the load case compression and hot-rolled; a) SHS profiles in the pre-buckling range; b) SHS profiles in the post-buckling range; c) RHS profiles in the pre-buckling range; d) RHS profiles in the post-buckling range

Bigger cross-section dimensions lead consequently to higher stiffness values and vice versa. This behaviour is well captured by the model. The same logic applies to the steel grade or the imperfection amplitude. Surprisingly, the post-buckling behaviour is stronger affected by the cross-section height H and the critical elastic buckling load F_{cr} .

Nevertheless, the deformation has still a high influence on the tangent stiffness in the post-buckling range. Looking at the local imperfection amplitude e , the influence in the pre-buckling range is present but much less in comparison to the post-buckling range. This effect was also obtained throughout investigations on the post-buckling behaviour of RHS/SHS profiles in [285].

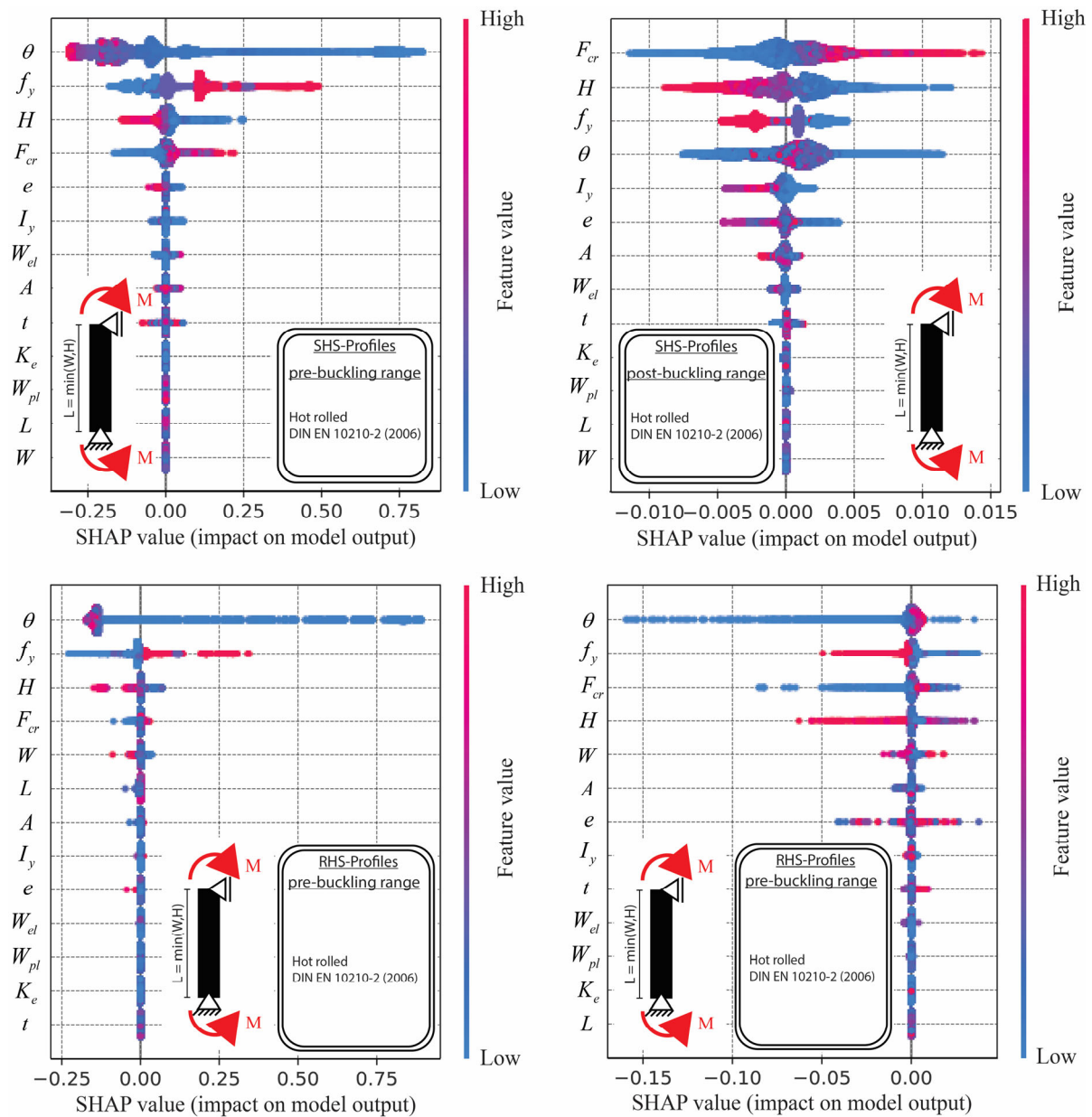


Figure 6-14: SHAP values for the load case bending and hot-rolled; a) SHS profiles in the pre-buckling range; b) SHS profiles in the post-buckling range; c) RHS profiles in the pre-buckling range; d) RHS profiles in the post-buckling range

Figure 6-14 shows the beeswarm plots for the load case of bending. Similar conclusions can be drawn for SHS profiles in the pre- and post-buckling range as for load case of pure

compression. On the other hand, the output for RHS profiles differs significant. The SHAP value impact linked to the rotation in the pre-buckling range is more separated, meaning that the scattered “line” is much thinner compared to the results for SHS profiles. This indicates that the general behaviour in the pre-buckling range is more diverse (non-linear). This applies in general to all features used in the SHAP value output for RHS profiles.

6.2.5.2 Feature importance

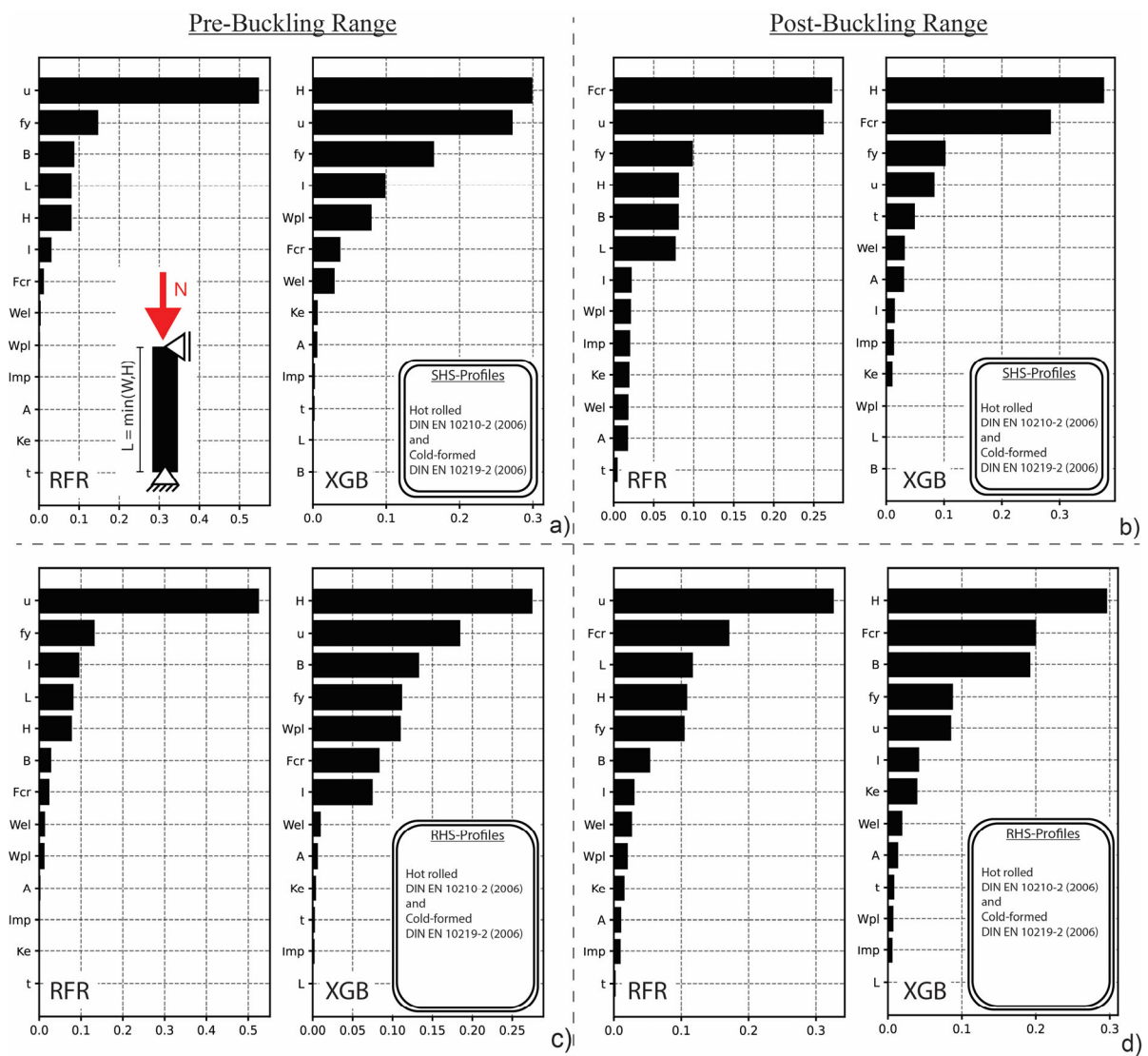


Figure 6-15: Evaluation of feature importance and comparison between the Random Forest model and the XGBoost model for compression a) pre-buckling range of SHS profiles; b) post-buckling range of SHS profiles; c) pre-buckling range of RHS profiles; d) post-buckling range of RHS profiles

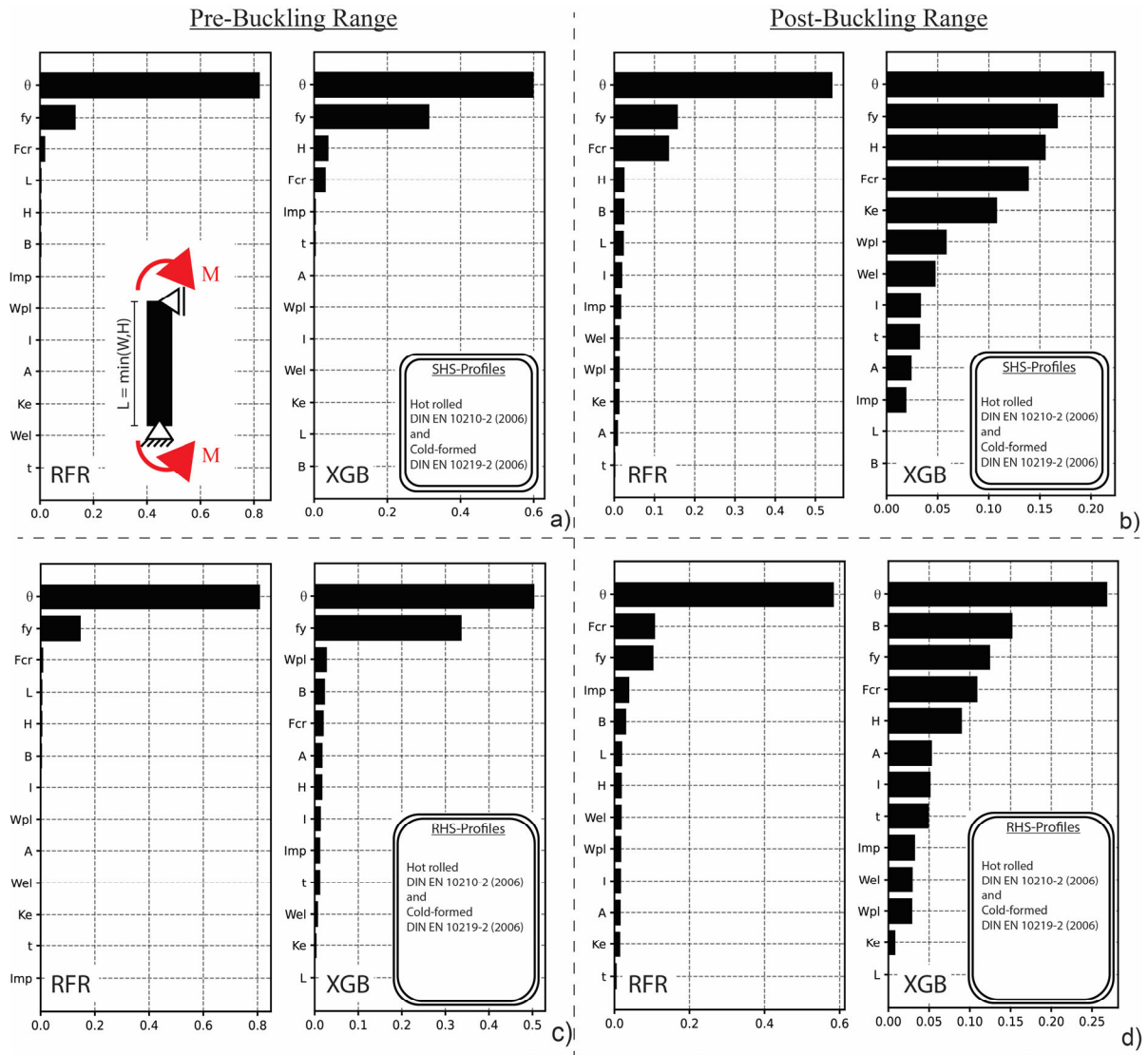


Figure 6-16: Evaluation of feature importance and comparison between the Random Forest model and the XGBoost model for bending a) pre-buckling range of SHS profiles; b) post-buckling range of SHS profiles; c) pre-buckling range of RHS profiles; d) post-buckling range of RHS profiles

ML and DL methods offer several approaches to detect features that have the most influence on the learning process. Carrying out a dedicated feature analysis has the advantage that input parameters that have no significant impact on the predictions are eliminated from the prediction process. Therefore, the calculation effort is reduced while the optimization process depends on fewer parameters. The most common way to seek for these parameters is the application of tree based algorithms. Decision trees are based on the logical structure of a tree, predicting the values through a sum of individual choices. Starting with the input values in a so called root, the data is split within different possible decisions (categorical decision for classification and quantitative decisions for regression problems). Following this principle to the end nodes of the model, a condition

or value is proposed. This procedure is highly powerful but prone to problems connected to data quality and tree complexity leading to an effect called overfitting. It occurs when the algorithm starts to capture noise, being too accurate on the training data due to a very deep tree structure. Therefore, the general approach goes lost, which leads to poor predictions on the base of unseen test data.

Further, two methodologies (Random Forest Regressor [187] and XGBoost Regressor [183]) were used in the following, which proved to be successful in the case of present data sets. The random forest algorithm is based on the general idea of a decision tree with the main difference of using not only one big tree to represent the problem, but rather a high number of simpler trees which are more general and therefore not as much affected by overfitting. The whole dataset is first subsampled (bootstrap sampling), meaning that a random number of features and data rows is used to build smaller data sets. This leads to a higher variety and a different data density. In the following, individual trees are build parallel leading to a large number of different predictions, which are gathered and averaged (bootstrap aggregating). In contrast, the XGBoost algorithm builds the trees not parallel to each other but uses a boosting technique. Thus, the trees (weak learners) are built sequentially so that each new tree corrects the error of the previous one (boosting).

Both algorithms were used to evaluate and plot the importance of the features of the SHS and RHS profiles in the pre- and post-buckling range, see Figure 6-15 (load case: compression) and Figure 6-16 (load case: bending). The abbreviation RFR is attributed to the Random Forest algorithm, while XGB is attributed to the XGBoost algorithm. The output of the feature importance is exemplary explained by Figure 6-15 a), using the data set of the SHS profiles (hot-rolled and cold-formed) in the pre-buckling range. All features are sorted according to their importance and displayed on the vertical axis. The importance itself is shown along the horizontal axis with the mean decrease impurity (also known as Gini index) computed for the Random Forest (RFR) and XGBoost structure (XGB). It is calculated as the total reduction of the impurity within a split, made by one selected feature on average over all trees within the forest. Apart from their order, the three most important features are the same, represented by the displacement u , the steel grade f_y and the height H or width W . In terms of SHS profiles the values for B , H

and L are identical. This also explains one main difference between these methods based on their structure. Since the Random Forest algorithm uses many individual trees, linear dependent features are not necessarily eliminated, as they are used independently within reduced data sets. For this reason, features B , H and L are listed with approximately the same importance (Figure 6-15 a) RFR). On the other hand, XGBoost (Figure 6-15 a) XGB) uses one sequential build of trees, so that equal features are eliminated throughout the optimization process.

Table 6-4: Estimated feature combinations for DNN models for the pre- and post-buckling range and the cross-section capacity

Load Case: Compression		
Prediction of the incremental tangent stiffness K_T		
	Pre-buckling range	Post-buckling range
SHS hot-rolled and cold-formed	$H, A, I_y, W_{el}, e, f_y, u, F_{cr}$	$H, t, A, I_y, W_{el}, e, f_y, u, F_{cr}$
RHS hot-rolled and cold-formed	$H, W, I_y, W_{el}, W_{pl}, e, f_y, u, F_{cr}$	$H, W, t, A, I_y, W_{el}, e, f_y, u, K_e, F_{cr}$
Prediction of the maximum force N_{max}		
SHS hot-rolled and cold-formed	$H, t, A, I_y, W_{el}, W_{pl}, e, f_y, F_{cr}$	
RHS hot-rolled and cold-formed	$H, W, t, I_y, W_{el}, W_{pl}, e, f_y, F_{cr}$	
Load Case: Bending		
Prediction of the incremental tangent stiffness K_T		
SHS hot-rolled and cold-formed	$H, W_{pl}, e, f_y, \theta, F_{cr}$	$H, I_y, W_{pl}, e, f_y, \theta, K_e, F_{cr}$
RHS hot-rolled and cold-formed	$H, W, A, I_y, W_{pl}, e, f_y, \theta, F_{cr}$	$H, W, t, A, I_y, W_{el}, e, f_y, \theta, F_{cr}$
Prediction of the maximum force M_{max}		
SHS hot-rolled and cold-formed	$H, t, A, I_y, e, Imp, f_y, F_c$	
RHS hot-rolled and cold-formed	$H, W, t, A, I_y, e, f_y, F_{cr}$	

Subsequently, the procedure of feature engineering requires the use of different methods, since the output can vary strongly and only the sum of reasonable results lead to a general tendency for the choice of important features and their combination. Furthermore, additional combinations of the selected features within the DNN models should be tested to determine differences in the performance and overall accuracy. Table 6-4 summarizes the chosen feature variations based on the outputs of Figure 6-15 and Figure 6-16. Subsequent model accuracy evaluation is presented in Chapter 8, in the context of method evaluation.

6.3 Hyperparameter tuning

In general, two types of parameters are distinguished within a deep neural network (feed forward network). The trainable parameters, which are changed throughout the optimization process, including the weights and the biases, and the preset hyperparameters, which do not change throughout the optimization process. This includes the general model architecture (amount of neurons and hidden layer), the chosen optimizer, an associated learning rate and the activation functions within the hidden layer, the batch size and additional regularization techniques. Without appropriate information on the DNN model performance, the computational effort needed for the estimation of possible hyperparameters is immense. For this reason, the problem was considered systematically by first exploring the parameters in a coarse pattern to come up with possible, still rough ranges of values. Consequently, these values were adjusted in finer intervals until suitable values were found.

Therefore, a total of 193 individual combination was tested within the framework of preliminary investigations using the Random Search Method. Random Search is in terms of ML one method to estimate decisive parameters, which can be suitable but do not necessary have to, since not all possible combinations are taken into account. The opposite would be the Grid Search Method were each parameter combination is tested. However, as there is not only one specific solution but rather a potential solution space of possible combinations of hyperparameters, this workflow is suitable in order to detect the overall tendencies within the DNN architecture.

Table 6-5: Initially considered parameters (Tuning 1)

Hyperparameter	Value Range	Configurations
Neurons per Hidden Layer	min = 5; max = 185; step = 18	11
Hidden Layer Combinations	min = 3, max = 6	4
Activation Function	ReLu, Sigmoid, Tanh	3
Dropout Rate	0.0, 0.1, 0.2, 0.5	4
Optimizer	Adam, Adamax, SGD	3
Learning Rate	0.0001, 0.001, 0.005, 0.01	4
Batch-Size	min = 32, max = 256, step = 32	8

All calculations were performed on the basis of a train and test philosophy, meaning that a specific data amount was used for the training (80%) and an additional independent amount for the validation process (20%). This procedure is crucial to detect problems like overfitting and the interpretation of the overall behaviour, assessing transferability to “unseen” data. The whole procedure of the hyperparameter tuning workflow is described next.

In the first step, different parameters were set up and initially investigated in a try and error process. This would be equivalent to a random search method. Since there were no clues at first on appropriate parameters, this procedure made sense at a certain point. Additionally, all the information from the previously described feature engineering assessments were not available at this moment and were investigated in parallel. All parameters initially considered are listed in Table 6-5. The biggest problem with a large number of parameters is logically the enormous time needed for the training of the networks and the uncertainty to find a suitable model by chance. If taking only the possible number of combinations, which results here purely from the number of hidden layers as well as the number of neurons, a total of 1,948,584 possible network structures is calculated. Nevertheless, the limitation of these parameters is suitable to develop a feedback for the behaviour of the models as well as for the actual problem.

Table 6-6: Considered parameters (Tuning 2)

Hyperparameter	Value Range	Configurations
Neurons per Hidden Layer	min = 9; max = 27; step = 9	3
Hidden Layer Combinations	min = 1, max = 4	4
Activation Function	ReLu	1
Optimizer	Adam	1
Learning Rate	0.0001, 0.0005, 0.001, 0.002	4
Epochs	1000	1
Batch-Size	128	1

Based on the philosophy that an unlimited number of suitable models may exist, parameters were eliminated in the next step which seemed to bring no or negative effect on the training behaviour and the neural network was reduced in size. A compact model

can on the one hand prevent overfitting problems, making dropout strategies unnecessary, and on the other hand speed up the training of the models. After each hidden layer the ReLu activation function was used.

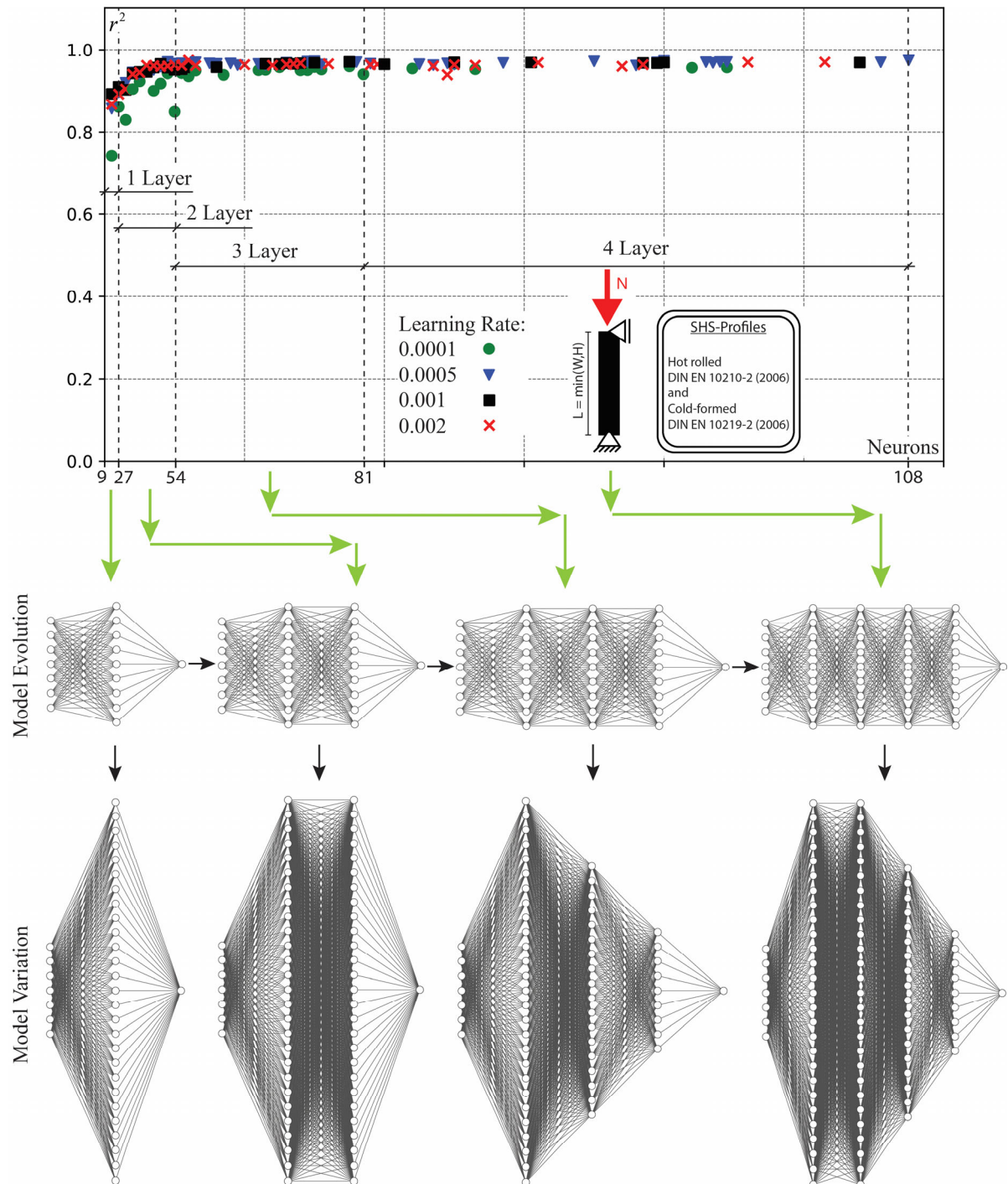


Figure 6-17: DNN model evolution and r-squared results

The optimizer was fixed to the Adam optimizer [293], as a results from the first hyperparameter evaluation. The goal of the second hyperparameter tuning was to get a conclusion about the best learning rate and to detect a tendency concerning the number of hidden layers. To accelerate the evaluation process, the number of epochs was limited to 1000 for all DNN models. All considered parameters are summarized in Table 6-6.

In sum, 127 randomly chosen combinations were tested. The evaluation process is presented in Figure 6-17, according to the different DNN model architectures, as well as different learning rates. It shows trends for the learning rates, but also for the number of hidden layers. The learning rate 0.0001 mostly provides the lowest results compared to the other 3 learning rates. For the learning rate 0.002, the results are significantly better and increase with the learning rate 0.0005 or 0.001. Looking at the 10 best combinations, 9 combinations have a learning rate of 0.0005 and only one combination has a learning rate of 0.001. In Figure 6-17 it can also be seen that from the models with one hidden layer, the lowest results for the averaged global r^2 are obtained. With 2 hidden layers, already higher results are obtained depending on the number of neurons in the hidden layers. The best results are obtained with 3 or 4 hidden layers. The hyperparameters of the best three models and their results are shown in Table 6-7.

Table 6-7: Best model summary from the hyperparameter evaluation (Tuning 2)

Hyperparameter	DNN Model 1	DNN Model 2	DNN Model 3
Neurons Hidden-Layer 1	27	18	18
Neurons Hidden-Layer 2	27	18	27
Neurons Hidden-Layer 3	18	18	27
Neurons Hidden-Layer 4	9	18	-
Activation Function	ReLU	ReLU	ReLU
Optimizer	Adam	Adam	Adam
Learning-Rate	0.0005	0.0005	0.0005
Epochs	1'000	1'000	1'000
Batch-Size	128	128	128
r^2	0.9741	0.9725	0.9718

In an additional step, a third hyperparameter evaluation was done, using a reduced set of hyperparameters according to the outcomes from the second tuning progress. The learning rate was set to a constant value of 0.0005 and the hidden layer combination was set to a minimum of 3 and a maximum of 4 hidden-layer. The goal was to investigate the accuracy outcomes with the Adamax optimizer [294]. A summary of the used parameters is presented within Table 6-8. In sum, 74 combinations were tested. Figure 6-18 describes the results by comparing the effect of different DNN model architecture (Figure 6-18 a)) and a comparison between the accuracy results calculated with the Adam and the Adamax optimizer (Figure 6-18 b)).

Table 6-8: Estimated hyperparameters

Hyperparameter	Value Range	Configurations
Neurons per Hidden Layer	min = 9; max = 27; step = 9	3
Hidden Layer Combinations	min = 3, max = 4	2
Activation Function	ReLU	1
Optimizer	Adamax	1
Learning Rate	0.0005	1
Epochs	1000	1
Batch-Size	128	1

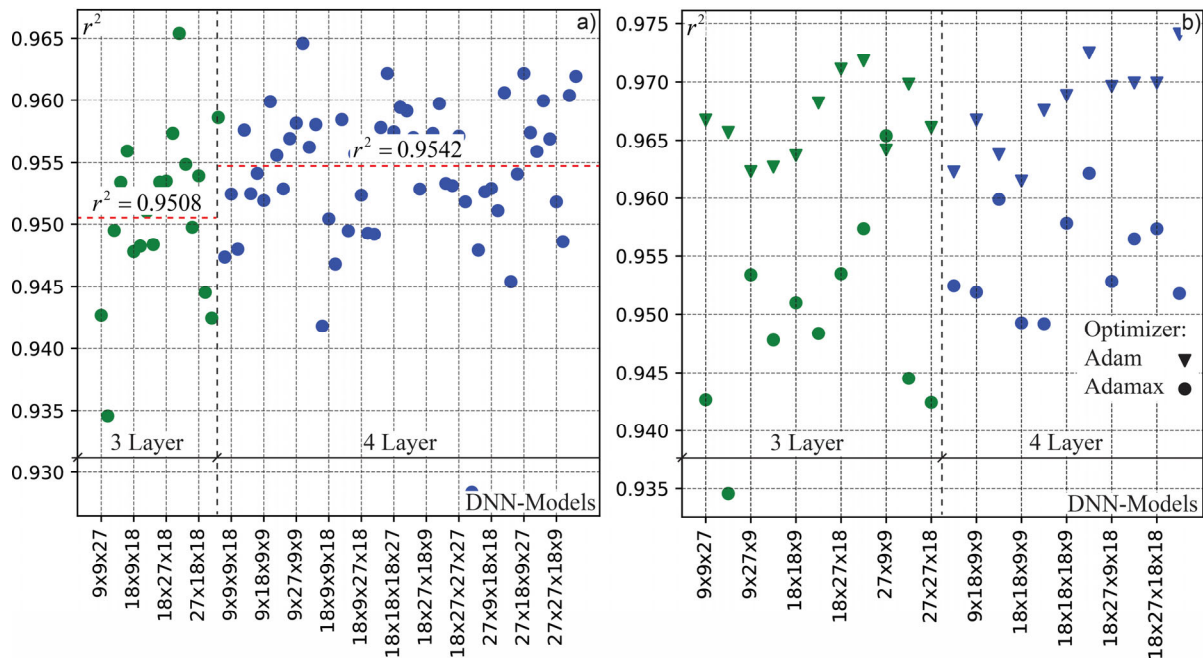


Figure 6-18: DNN model evolution and r-squared results

Figure 6-18 a) shows a clear tendency that the models with 4 hidden-layers tend to give better results than the models with 3 hidden layers. An averaged r^2 value of 0.9542 is reached for DNN models with 4 hidden-layers, being slightly higher compared to the DNN models with 3 hidden-layers.

To compare the used optimizers, accuracy results from hyperparameter tuning-2 with 3 and 4 hidden-layers, a learning rate of 0.0005 and the same DNN model architecture as those from hyperparameter tuning-3 were plotted in Figure 6-18 b). In total 22 DNN models could be compared. 11 models each have a mesh structure with 3 or 4 hidden-layers. A clear tendency towards the Adam optimizer is obtained, with an average of 3% higher r^2 values compared with the Adamax optimizer. In only one case the Adamax optimizer performed slightly better.

The subsequent DNN model that is applied on all other data sets for compression and bending is summarized in Table 6-9. It is equivalent to DNN model 1 from Table 6-6 and sufficient enough to make predictions throughout all data sets. A model accuracy evaluation is discussed in Section 8.

Table 6-9: Hyperparameters for final DNN model

Model Parameters	Selection
Hidden layer 1	27
Hidden layer 2	27
Hidden layer 3	18
Hidden layer 4	9
Activation function	ReLU
Optimizer	Adam
Learning rate	0.0005
Epochs	6000
Batch size	128

6.4 Conclusions

The overall prediction accuracy is strongly dependent on the data quality, the data amount and distribution, as well as the chosen machine learning model. Chapter 6 describes all necessary steps to receive accurate results with several deep neural network

feed forward models, to predict the non-linear local load-deformation/moment-rotation behaviour of RHS/SHS profiles made from mild and high strength steel.

The question of data quality within own data sets plays only a minor role, since the whole data development is based on FE simulations, therefore underlies in general a very low scatter. This step is only possible because the models used were calibrated on test results from experimental investigations. The corresponding procedure is described throughout Chapter 5. In general, the question of appropriate data quality would have a higher importance when using raw data from experiments.

A specifically high influence on the prediction accuracy was detected by three main data manipulation methods:

- i. The data density was obtained to be one important factor when prediction the pre-buckling range, especially of slender cross-sections. Since the data sets are based on GMNIA Abaqus simulations the solver step size varies while finding an equilibrium. A more linear behaviour is usually calculated with bigger steps, while a non-linear behaviour with much smaller increments in order to find a residuum. This results in different data densities within the data sets, leading to less data in linear regions. A simple solution to overcome such problems is to decrease the size of the increment in the solver setting.
- ii. The splitting of the data sets into separate pre- and post-buckling ranges improved the prediction accuracy for both. This modification step made sense for the current neural network architecture, since only positive or negative tangent stiffnesses need to be predicted by corresponding models.
- iii. A particular importance is set in the transformation of the data set input and output features. The input features were standardized using Equation (4-13). This important step brings the input features into similar data ranges leading to an unbiased optimization procedure. The output parameters were additionally normalized; the prediction of the tangent stiffness was improved by using a normalized representation with K_T/K_e ; the prediction of maximum forces and moment by using the following expression $\chi = F_{max} / F_{pl}$ and M_{max} / M_{pl} , respectively.

Apart from data manipulation, the question of appropriate feature combinations is an important task which is necessary to improve the overall performance and reduce the amount of features to accelerate the optimization process. Different methods were used to come up with combinations and assess the importance of features. A more general

feature interpretation can be found in Section 6.2.5.1, where different methods like PCA or SHAP analysis interpretation were used to obtain pattern in the data and the potential to reduce it. The PCA analysis showed a high potential to reduce the data due to linear dependencies between the features. The SHAP analysis output showed different patterns within the features in the data sets. The driving parameter is logically the deformation or rotation, depending on the considered load case. In addition the geometric parameter (Height H , Width W , Moment of inertia I_y) and the material parameters (yield strength f_y) played for all cross-section an important role. The geometric local imperfection amplitude, on the other hand, was important in the load case for compression but less important for pure bending. Further, the critical buckling load F_{cr} (always extracted from Abaqus LBA simulations for pure compression) has almost no influence on the training performance in the pre-buckling range but a high influence in the post-buckling region.

The overall assessment of the feature importance was done through random forest and XGBoost models. The feature importance can be taken as an output of those models (see Section 6.2.5.2) and is a very effective way to obtain the most influential features. Feature combinations were additionally tested throughout the hyperparameter tuning in different neural network models and are presented in Table 6-4.

Part III

7

DNN-DSM Methodology

Concept, Implementation and Limitations

Outline of the chapter:

Chapter 7 presents the general idea behind the DNN-DSM methodology developed and studied in this thesis: it discusses its implementation within a code based explanation, as well as the limitations of the scope considered in this thesis. The DNN-DSM method consists of connecting and integrating two approaches for the prediction of the non-linear mechanical performance of steel structures as they approach the ultimate limit state: *(i)* a data driven machine learning approach based on deep neural networks (DNN), and *(ii)* an analytical or numerical, well-known methodology, i.e. the direct stiffness method (DSM). DNN models, its functionality and the background were already described in Chapter 6 of this thesis. Therefore, the present chapter takes a closer look on the general implementation of the DSM method. After this introduction, the link between DNN models and the DSM approach is presented and described in a more general manner.

7.1 Preface to the Direct Stiffness Method (DSM)

7.1.1 Introduction

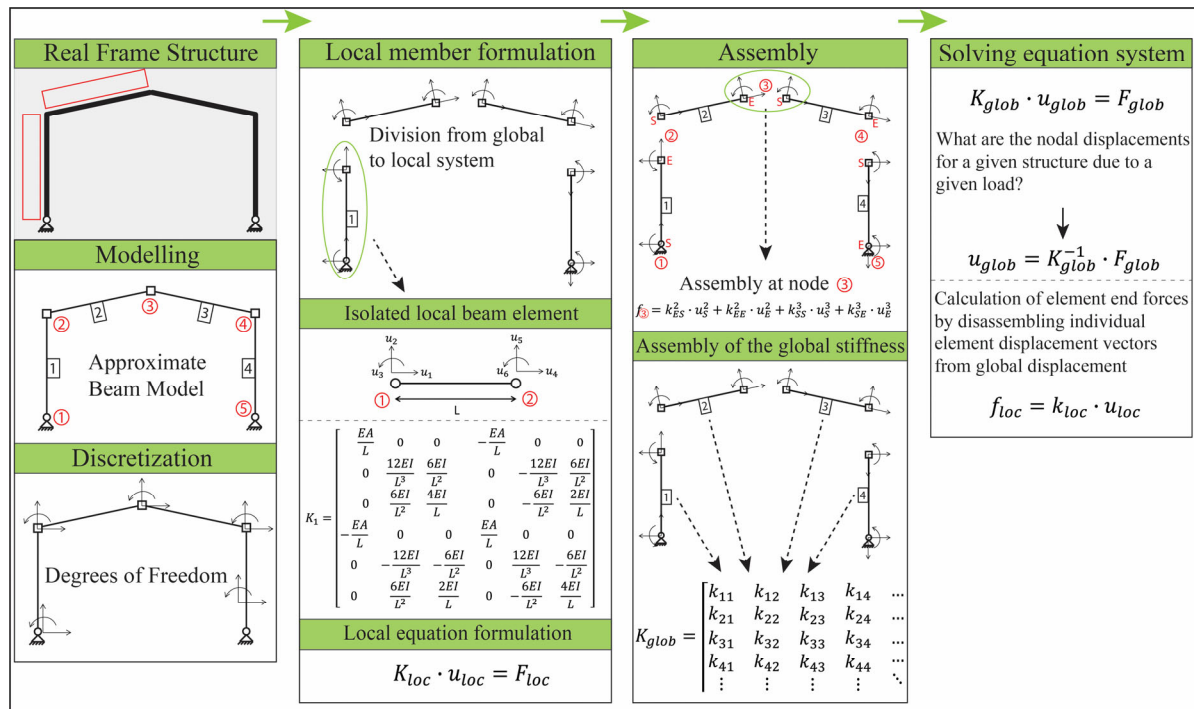


Figure 7-1: General workflow of the direct stiffness method (DSM), shown for 2D elastic 1st order frame analysis.

The Direct Stiffness Method (DSM) is one of the basic numerical implementation approaches in finite element method (FEM) applications. In general, FEM is a method for breaking down a complex problem/domain into smaller elements that are interconnected and assembled to form an approximation to the original structure. The DSM approach was first introduced by Turner [295] in 1959. It was the starting point for the development of the finite element method, which is one of many other methods within CSSM (computational solid and structural mechanics) spatial discretization techniques.

The DSM is a calculation method in which forces or deformations can be calculated via a matrix formulation, based on the stiffness properties of individual beam elements and their mutual interaction. The numerical calculation procedure is described as follows for the 2D in-plane case and a linear static analysis (Th.I.Ord.). It is partially based on the work flow described in [296].

- iv. Divide structural system into elements. Define all nodes and add the connectivity information between the elements and their cross-section properties.
- v. Calculate for each element the local stiffness matrix. Here one can distinguish between truss and beam elements, subjected to normal forces only or a combination of normal forces and moment.

$$\bar{K}_{e,Truss} = \frac{EA}{L} \cdot \begin{bmatrix} 1 & 0 & -1 & 0 \\ 0 & 0 & 0 & 0 \\ -1 & 0 & 1 & 0 \\ 0 & 0 & 0 & 0 \end{bmatrix} \quad (7-1)$$

$$\bar{K}_{e,Beam} = \begin{bmatrix} \frac{EA}{L} & 0 & 0 & -\frac{EA}{L} & 0 & 0 \\ 0 & 12\frac{EI}{L^3} & 6\frac{EI}{L^2} & 0 & -12\frac{EI}{L^3} & 6\frac{EI}{L^2} \\ 0 & 6\frac{EI}{L^2} & 4\frac{EI}{L} & 0 & -6\frac{EI}{L^2} & 2\frac{EI}{L} \\ -\frac{EA}{L} & 0 & 0 & \frac{EA}{L} & 0 & 0 \\ 0 & -12\frac{EI}{L^3} & -6\frac{EI}{L^2} & 0 & 12\frac{EI}{L^3} & -6\frac{EI}{L^2} \\ 0 & 6\frac{EI}{L^2} & 2\frac{EI}{L} & 0 & -6\frac{EI}{L^2} & 4\frac{EI}{L} \end{bmatrix} \quad (7-2)$$

- vi. Convert loads acting within the elements into equivalent nodal forces (element node vector)
- vii. Transform the local stiffness matrix of each element into a global stiffness matrix. Therefore, the local stiffness matrix needs to be rotated from the local to the global coordinate system first. This is done through Equation (7-3), with the rotation matrix for truss (see Equation (7-4)) or beam elements (see Equation (7-5)).

$$K_e = R_e^T \cdot \bar{K}_e \cdot R_e \quad (7-3)$$

$$R_{e,Truss} = \begin{bmatrix} \cos(\theta) & \sin(\theta) & 0 & 0 \\ -\sin(\theta) & \cos(\theta) & 0 & 0 \\ 0 & 0 & \cos(\theta) & \sin(\theta) \\ 0 & 0 & -\sin(\theta) & \cos(\theta) \end{bmatrix} \quad (7-4)$$

$$R_{e,Beam} = \begin{bmatrix} \cos(\theta) & \sin(\theta) & 0 & 0 & 0 & 0 \\ -\sin(\theta) & \cos(\theta) & 0 & 0 & 0 & 0 \\ 0 & 0 & 1 & 0 & 0 & 0 \\ 0 & 0 & 0 & \cos(\theta) & \sin(\theta) & 0 \\ 0 & 0 & 0 & -\sin(\theta) & \cos(\theta) & 0 \\ 0 & 0 & 0 & 0 & 0 & 1 \end{bmatrix} \quad (7-5)$$

- viii. The global force vector is defined based on the acting loads from (iii). The bearing reactions are entered as unknowns in the force vector.
- ix. Account for geometric boundary conditions, i.e. end supports and restraints, in the global stiffness matrix as well as the global force vector. Columns and rows connected to a fixed support can be eliminated to reduce the global stiffness matrix. Equation (7-6) shows the general system of equations. By taking the inverse of the global stiffness matrix the unknown system deformations can be calculated using Equation (7-7).

$$K_{sys} \cdot U_{sys} = F_{sys,ext} - F_{sys,int} \quad (7-6)$$

$$U_{sys} = K_{sys}^{-1} \cdot (F_{sys,ext} - F_{sys,int}) \quad (7-7)$$

- x. Calculate internal forces in the nodes for each element. The known nodal deformations are rotated back to the local system and multiplied with the local element stiffness.
- xi. Calculate internal forces inside the elements using shape functions.

For calculation according to 2nd order theory (Th.II.Ord.) the steps from 1st order theory (Th.I.Ord.) need to be performed first. Following this, the calculation is started again at point (ii), where additional geometric element stiffness matrices are calculated for the

element forces from point (vii) according to Th.I.Ord. \bar{G}_{beam} from Equation (7-8) shows the general approximation of the terms by a Taylor series.

$$\bar{G}_{Beam} = \begin{bmatrix} 0 & 0 & 0 & 0 & 0 & 0 \\ 0 & \frac{6}{5} \cdot \frac{N}{L} & \frac{1}{10} \cdot N & 0 & -\frac{6}{5} \cdot \frac{N}{L} & \frac{1}{10} \cdot N \\ 0 & \frac{1}{10} \cdot N & \frac{2}{15} \cdot N \cdot L & 0 & -\frac{1}{10} \cdot N & \frac{1}{30} \cdot N \cdot L \\ 0 & 0 & 0 & 0 & 0 & 0 \\ 0 & -\frac{6}{5} \cdot \frac{N}{L} & -\frac{1}{10} \cdot N & 0 & \frac{6}{5} \cdot \frac{N}{L} & -\frac{1}{10} \cdot N \\ 0 & \frac{1}{10} \cdot N & -\frac{1}{30} \cdot N \cdot L & 0 & -\frac{1}{10} \cdot N & -\frac{2}{15} \cdot N \cdot L \end{bmatrix} \quad (7-8)$$

A global geometric stiffness matrix is formed according to point (iv) and summed up with the global stiffness matrix (see Equation (7-9)). K_{sys} represents the system stiffness from Th.I.Ord. and G_{sys} the additional part from Th.II.Ord.. According to point (vi) the unknown system deformations are solved by Equation (7-10).

$$K_{sys} + G_{sys} \quad (7-9)$$

$$U_{sys} = (K_{sys} + G_{sys})^{-1} \cdot (F_{sys,ext} - F_{sys,int}) \quad (7-10)$$

The eigenvalue problem is described through the homogeneous matrix equation below, see Equation (7-11). The eigenvalue is expressed by α_{cr} and the corresponding eigenvector by u .

$$(K + \alpha_{cr} \cdot G) \cdot u = 0 \quad (7-11)$$

7.1.2 Application of deformations

If the applied action is not a nodal force but a nodal deformation within a system, the determination of the total deformation vector has to be done, e.g., by means of a so-called "penalty method". For this purpose, a fictitious penalty element is formed with the following global stiffness and force vector.

$$K^i = w_i \cdot v_i^T \cdot v_i \quad (7-12)$$

$$F^i = w_i \cdot v_i^T \cdot b_i \quad (7-13)$$

where:

w_i is a weight with the property $w_i > 0$. In general cases this value is set to a high number. In the framework of this work the weight is set to $w_i = 1e15$.

v_i is a matrix with the column length equal to the number of restrained degrees of freedom and the row length equal to the number of all degrees of freedom. The matrix is filled with ones at the spots according to the restrained degrees of freedom.

b_i is a vector equal to the length of the number of restrained degrees of freedom, containing the acting node deformation.

All further deformations, resulting from the acting nodal deformation, are then solved with the following Equation (7-14).

$$u_{penalty} = \left(K + \sum_{i=1}^m K^i \right)^{-1} \cdot \left(F + \sum_{i=1}^m F^i \right) \quad (7-14)$$

7.2 Deep Neural Network Direct Stiffness Method (DNN-DSM)

7.2.1 General idea

As described in detail in previous chapter, plasticity and (even more importantly) local (plate) 2nd-order effects and instabilities lead to a pronounced nonlinearity of the load-deformation behaviour of steel elements as they approach the ultimate limit state. The DNN-DSM methodology makes use of machine learning techniques (deep neural networks – DNN) to predict the non-linear stiffness matrix terms in a beam-element formulation suited for implementation in the standard Direct Stiffness Method (DSM). By doing so, the accuracy and precision of elasto-plastic, geometrically non-linear shell element analysis can be combined with the computational efficiency of beam element analysis, taking into account local slenderness dependent instability phenomena directly in the beam-element analysis process.

In the method, DNN models are used to predict tangent stiffnesses, dependent on the local element end deformations or rotations. The training of this models is based on the results from finite element simulations, the features and validation of which are described in Section 5.4 and presented in Section 6.1. The finite element shell models are designed in such a way that only local buckling is the driving instability phenomena for all investigated cross-sections. The underlying assumptions for the local length of the models was discussed in Section 5.3. The main goal of the finite element simulations was the calculation of the non-linear load-deformation and moment-rotation behaviour in the pre- and post-peak load range. Incremental tangent stiffnesses for each calculated step are extracted from these simulations and form the target values on which the DNN models were trained, to make predictions based on absolute local beam element deformation and rotation. The predicted incremental tangent stiffnesses are implemented within a DSM based approach, presented and discussed in the following sections.

7.2.2 Limitations and Assumptions

The DNN-DSM approach presented herein is in a preliminary design phase and does not cover all profiles and load cases commonly used in civil engineering applications. Since

the derived work serves as a primarily a feasibility check, it is limited to the boundary conditions listed below.

- i. The used profiles are limited to closed rectangular RHS and square SHS hollow sections. This eliminates out of plane instability effects like lateral torsional buckling (LTB) and reduces the problem to a 2D space.
- ii. The implemented elements are limited to 6 degrees of freedom (dofs), 3 at each end connected to a longitudinal and transverse deformation and an in plane rotation.
- iii. The prediction of the tangent stiffness according to bending is simplified through the assumption of equal constant rotation at both ends of the element.
- iv. Predictions are associated to compression and bending only. An N-M interaction is assumed according to EN 1993-1-1 [48].
- v. Shape functions according to Euler-Bernoulli beam theory.

7.2.3 Implementation for truss elements

The DNN-DSM makes use of the implementation from Section 7.1 to predict a local non-linear tangent stiffness matrix $K_{T,loc,pred}$ according to a given nodal deformation u_{loc} . The applied local deformation is an accumulation of incremental deformation steps $\Delta u_{loc}^{i+1} = u_{loc}^{i+1} - u_{loc}^i$ on the local element level. An exemplary procedure description with the two first calculation runs is shown within Figure 7-2.

Equation (7-15) describes the calculation of an incremental force $\Delta F_{loc,pred}^{i+1}$ according to an absolute deformation at a current time step u_{loc}^{i+1} . In this consideration, $f(X)$ is the prediction done by the pre-trained DNN model. X is the 2D matrix describing the data set in an Euclidean \mathbb{R}^2 space with $X \in \mathbb{R}^{n \times m}$, corresponding to the used model features as individual entries. The displacement vector $u_{loc} \in X$ is part of the entries within the used features space.

$$\Delta F_{loc,pred}^{i+1} = f\left(X\left(u_{loc}^{i+1}\right)\right) \cdot K_{e,loc} \cdot \Delta u_{loc}^{i+1} \quad (7-15)$$

$$K_{T,loc}^{i+1} = f\left(X(u_{loc}^{i+1})\right) \cdot K_{e,loc} \tag{7-16}$$

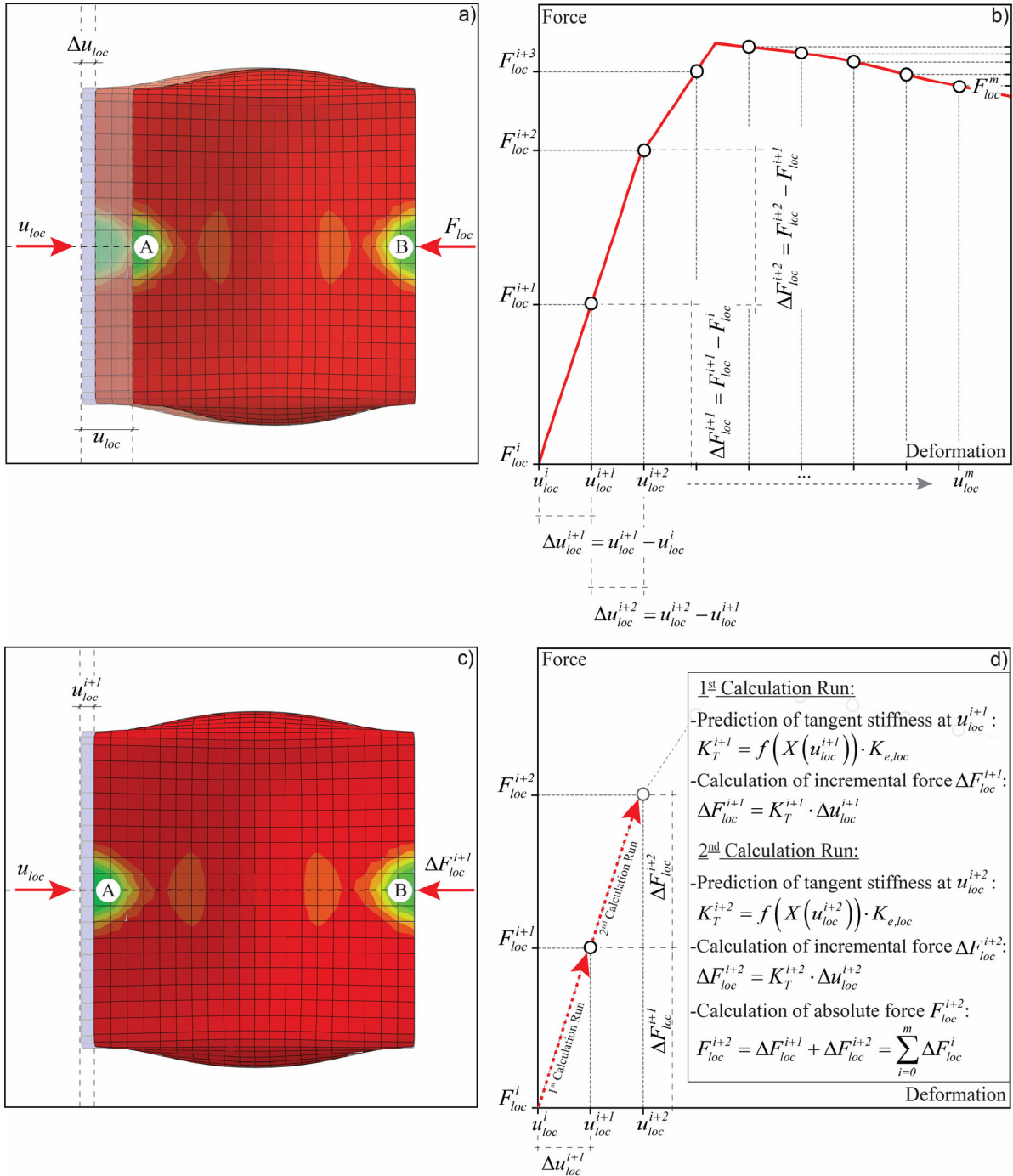


Figure 7-2: a) Deformed shape of an SHS FE shell model; b) Load-deformation curve and description of incremental deformation steps; c) Incremental deformation of an SHS FE shell model; d) Explanation of first two calculation steps

In more general terms, the calculated absolute force F_{loc} at any given local element displacement $u_{loc}^i \in \{i, m\}$ can be described by the following equation. The process stops when a maximum preset input displacement is reached.

$$F_{loc}^{i+1} = \sum_{i=0}^m K_{T,loc}^{i+1} \cdot \Delta u_{loc}^{i+1} \quad (7-17)$$

The same procedure applies in the pre- and post-buckling deformation range. The expressions from above need to be reshaped into the DSM format, according to the description from Section 7.1.

$$\begin{bmatrix} \Delta F_1 \\ \Delta F_2 \\ \Delta F_3 \\ \Delta F_4 \end{bmatrix} = f(X(u_{loc})) \cdot \frac{EA}{L} \cdot \begin{bmatrix} 1 & 0 & -1 & 0 \\ 0 & 0 & 0 & 0 \\ -1 & 0 & 1 & 0 \\ 0 & 0 & 0 & 0 \end{bmatrix} \cdot \begin{bmatrix} \Delta u_1 \\ \Delta u_2 \\ \Delta u_3 \\ \Delta u_4 \end{bmatrix} \quad (7-18)$$

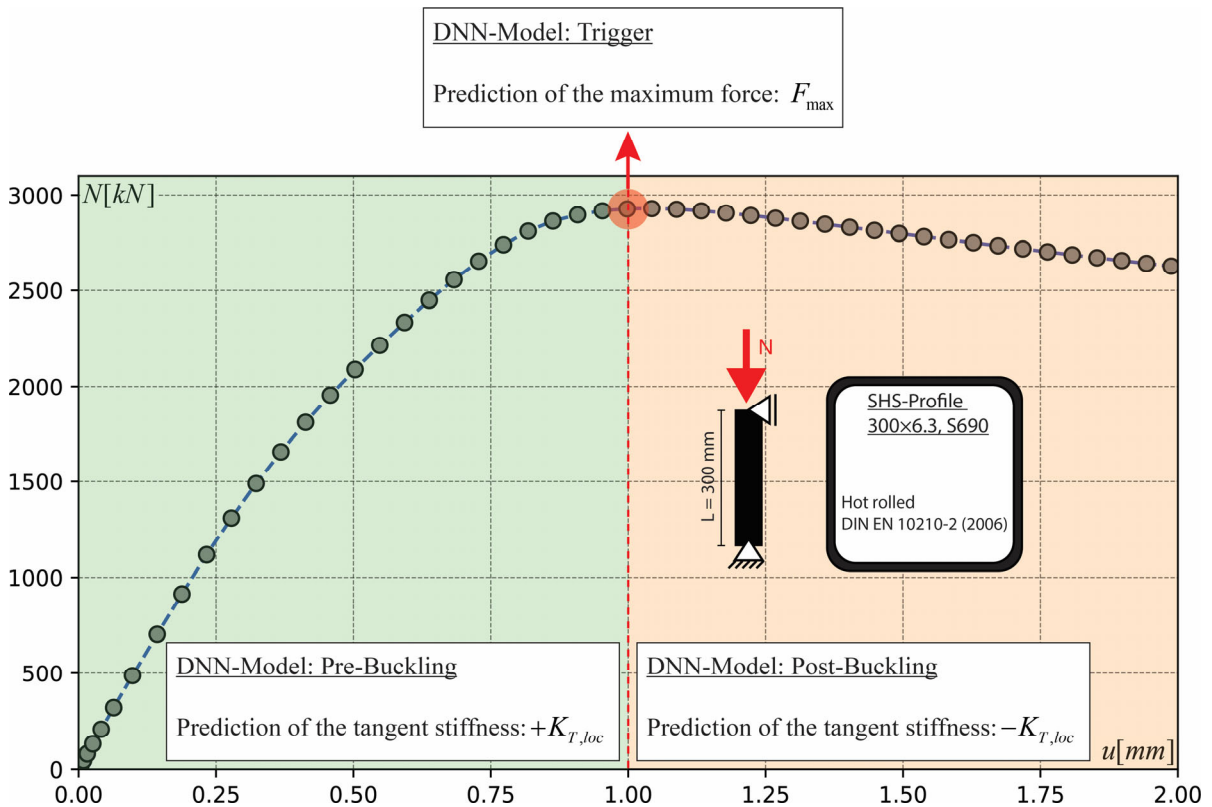


Figure 7-3: Ranges of the three DNN-models used for prediction

To predict the entire load deformation path in the pre- and post-buckling range, three DNN-models are needed. The first model predicts only the tangent stiffness in the pre-buckling range, the second model predicts the maximum force of the member under compression and is considered as a triggering predictor to introduce a stop condition. After reaching the threshold of the maximum force the third DNN-model is used to predict the tangent stiffness in the post-buckling range. The condition of the each local element, i.e. weather the element is in the pre- or the post-buckling range, is stored in an identity matrix for each predicted step to be able to switch between the models. Figure 7-3 describes the areas where the three models are active.

7.2.4 Beam implementation

7.2.4.1 Implementation

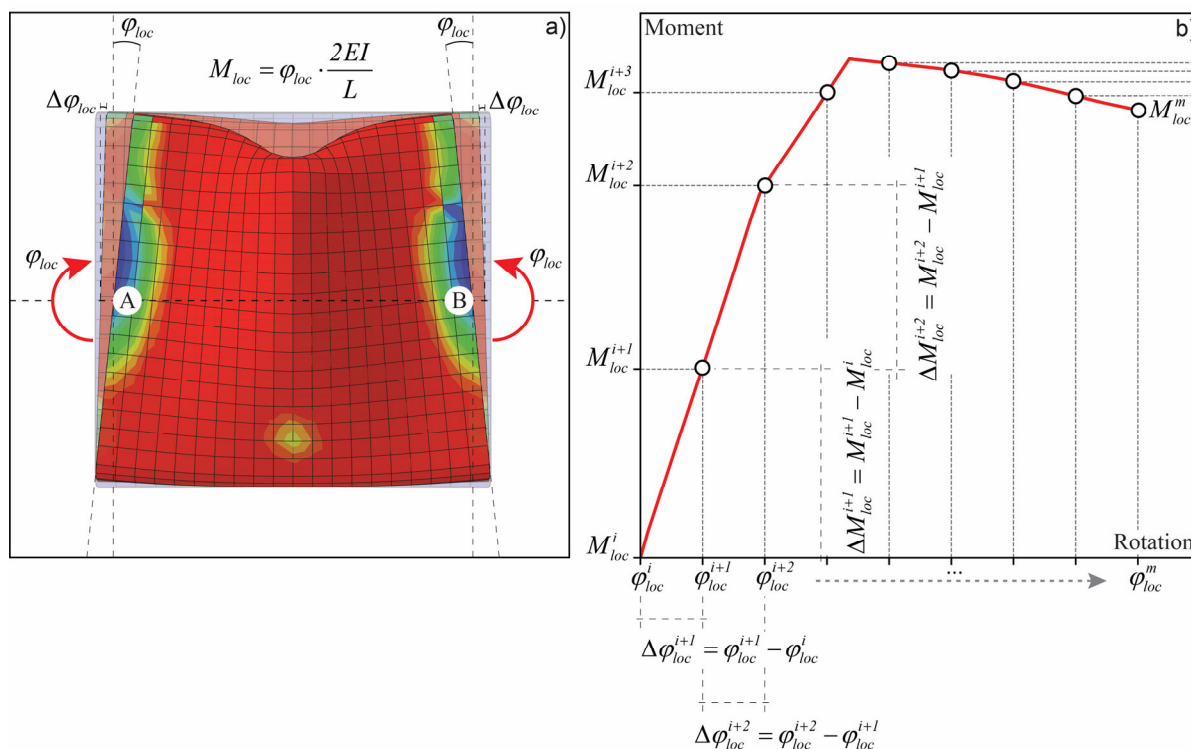


Figure 7-4: a) Deformed shape of an SHS FE shell model; b) Moment-rotation curve and description of incremental deformation steps; c) Incremental deformation of an SHS FE shell model; d) Explanation of first two calculation steps

The implementation for in-plane bending cases and 2D beam elements follows a similar approach by modifying the local beam element stiffness matrix according to a given local

rotation φ . Note that the rotation is one main input feature for the DNN model prediction. The corresponding definition of the rotation φ for an element is stated in Figure 7-4 a). Within the framework of the presented method an equal constant rotation at both ends is always assumed. The resulting constant moment along the element length L is defined through Equation (7-19). This formulation is assumed only in the elastic range.

$$M_{loc} = \varphi_{loc} \cdot \frac{2EI}{L} \quad (7-19)$$

The general notation for the elastic local beam element stiffness is represented by Equation (7-20). Further, the stiffness component for constant bending is factored out to be more in the line with the general implementation idea.

$$\bar{K}_{e,beam} = \frac{2EI}{L} \begin{bmatrix} \frac{6}{L^2} & \frac{3}{L} & -\frac{6}{L^2} & \frac{3}{L} \\ \frac{3}{L} & 2 & -\frac{3}{L} & 1 \\ -\frac{6}{L^2} & -\frac{3}{L} & \frac{6}{L^2} & -\frac{3}{L} \\ \frac{3}{L} & 1 & -\frac{3}{L} & 2 \end{bmatrix} \quad (7-20)$$

As was described for the truss elements, the nonlinearity of the load-deformation path is introduced by modifying the elastic stiffness matrix by a modification scalar $f(\underline{X})$, which is a function of the current deformation state (vector “ \underline{X} ”) and is predicted by the trained DNN in the model. *It shall be noted that the assumption of a proportional modification of all stiffness terms involved with bending is a severe one, and is mechanically only acceptable for short elements for which the nonlinearity is not affected by shear. For the methodology and the application scope as used in this thesis, this limitation is however acceptable.*

For in-plane bending, the predicted incremental force vector is thus written as follows, following the approach as used for truss elements in Equation (7-15). Note that $\varphi_{beam,mean}$ is the mean (average) rotations at both ends of the beam, i.e. node A and B

from Figure 7-4. The mean rotation is back calculated from system element rotations based on a globally acting load case.

$$\begin{bmatrix} \Delta V_{beam(AB)} \\ \Delta M_{beam(AB)} \\ \Delta V_{beam(BA)} \\ \Delta M_{beam(BA)} \end{bmatrix} = f\left(X(\varphi_{beam,mean})\right) \cdot \frac{2EI}{L} \begin{bmatrix} \frac{6}{L^2} & \frac{3}{L} & -\frac{6}{L^2} & \frac{3}{L} \\ \frac{3}{L} & 2 & -\frac{3}{L} & 1 \\ -\frac{6}{L^2} & -\frac{3}{L} & \frac{6}{L^2} & -\frac{3}{L} \\ \frac{3}{L} & 1 & -\frac{3}{L} & 2 \end{bmatrix} \cdot \begin{bmatrix} \Delta v_{beam(AB)} \\ \Delta \varphi_{beam(AB)} \\ \Delta v_{beam(BA)} \\ \Delta \varphi_{beam(BA)} \end{bmatrix} \quad (7-21)$$

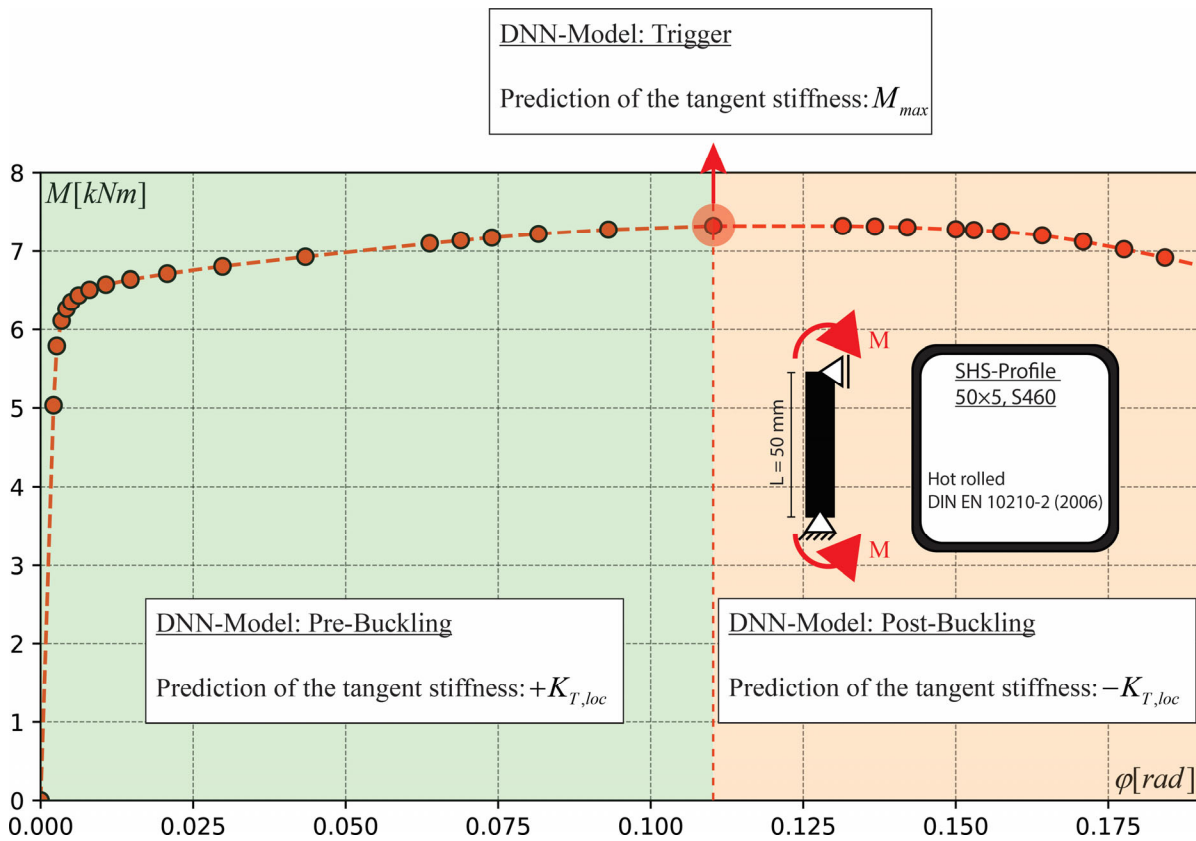


Figure 7-5: Ranges of the three DNN-models used for prediction

Again, the prediction of the whole moment-rotation path, i.e. the pre- and post-buckling range, is based on the same basic approach as for the truss element: two DNN models are used to predict the tangent stiffness in the pre- and post-buckling range and a third one to predict the maximum cross-section dependent capacity M_{max} . It is used as a triggering network to switch between the predictions in the ascending and descending path.

Figure 7-5 describes the areas where the three models are active, exemplary for an SHS 50×5 profile, S460, loaded by constant bending.

7.2.4.2 Prediction Workflow

To provide a general overview of the implemented prediction algorithm, Figure 7-6 shows in a simplified manner the implemented workflow within the code. Following explanations describe some steps of the procedure in more detail:

- i. Based on the DSM implementation, in a first step the system is initialized with cross-section dependent properties, the global system geometry and connectivity assignment, as well as a load case.
- ii. An elastic element stiffness is initialized and assembled to a global system stiffness matrix to provide a starting condition.
- iii. According to the system stiffness, the applied incremental deformation Δu is distributed along the system by using the penalty method from Section 5.1. The output is a displacement vector for all active system dofs.
- iv. A mean rotation in every element is calculated from the moments acting along the system. The mean moment is simply calculated from the evaluated moments at both ends of the element, see Equation (7-22). The mean rotation is calculated with Equation (7-23).

$$M_{mean} = \frac{M_A + M_B}{2} \quad (7-22)$$

$$\varphi_{mean}^{i+1} = \frac{I}{f(X(\varphi_{mean}^i))} \cdot \frac{M_{mean} \cdot L}{2 \cdot EI} = \frac{M_{mean}}{K_{T,pred}} \quad (7-23)$$

- v. The mean rotation is subsequently used to predict the updated local element tangent stiffness. This is done for every element of the system. Equation (7-24) summarizes this step.

$$K_{T,beam}^{i+1} = f\left(X\left(\phi_{mean}^{i+1}\right)\right) \cdot \frac{2EI}{L} \begin{bmatrix} \frac{6}{L^2} & \frac{3}{L} & -\frac{6}{L^2} & \frac{3}{L} \\ \frac{3}{L} & 2 & -\frac{3}{L} & 1 \\ -\frac{6}{L^2} & -\frac{3}{L} & \frac{6}{L^2} & -\frac{3}{L} \\ \frac{3}{L} & 1 & -\frac{3}{L} & 2 \end{bmatrix} \quad (7-24)$$

- vi. The global tangent stiffness matrix is assembled and used in an update step to distribute the applied incremental displacement Δu within the system. This loop is repeated until a pre-set threshold value is reached. Here, it is exclusively a matter of meeting the system stiffness as well as possible in order to distribute the corresponding deformations correctly within the system.
- vii. As described in Section 7.2.3, with the help of Figure 7-2, the load bearing capacity needs to be checked for every incremental step to identify whether the tangent stiffness predictions need to be performed in the pre- or post-buckling range. The identity of each element, i.e. pre-buckling range is equal to 0 and post-buckling to 1, is stored within a matrix for every calculated step.
- viii. Finally, the updated system properties are calculated and the next incremental deformation step Δu is applied.

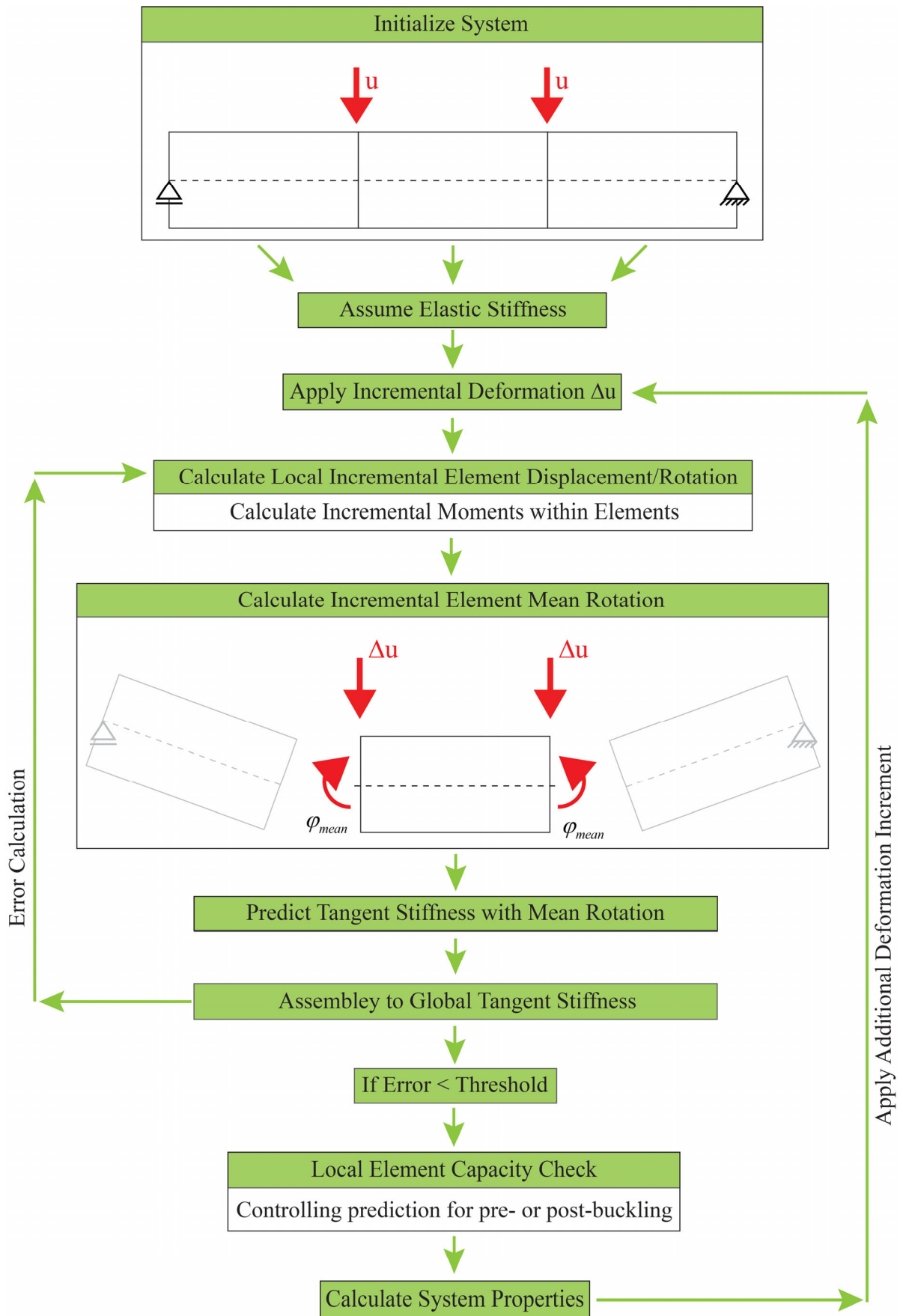


Figure 7-6: Implemented workflow for bending

7.2.5 Simplified implementation of beam-column behaviour

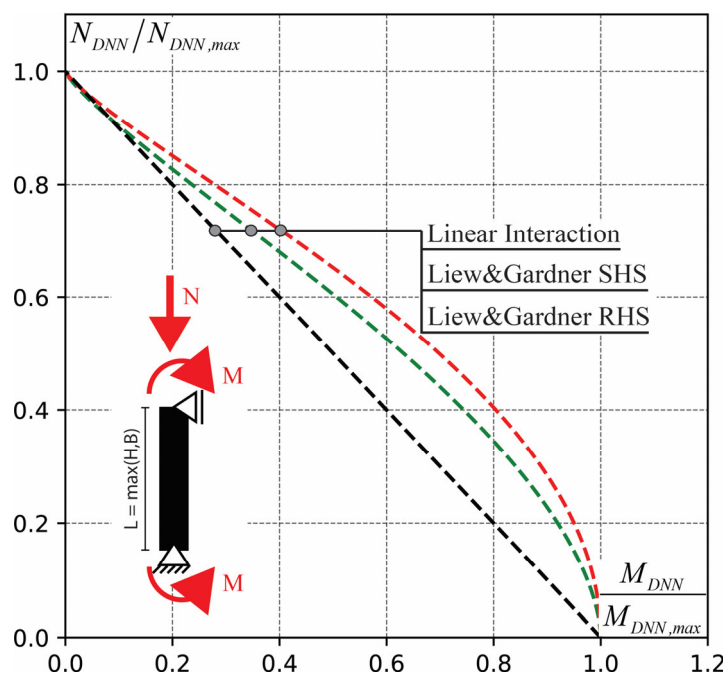


Figure 7-7: N-M interaction formulations according to Liew and Gardner [108]

In this thesis, the interaction of compression and bending moments was not studied in detail by dedicated data creation and training. However, a simplified approach for the consideration of this interaction by considering the training for bending capacities to be “scalable” to a reduced bending resistance, and considering the interaction formulation for squared hollow sections according to EN 1993-1-1 [48] might be used as a “trigger” and “scaling” factor. Yet, other interaction formulations, such as the one presented in Section 2.4.5.3, Equation (2-56) [108], can also be applied to the prediction process.

The main difference to the truss and beam implementation only, is the adjustment of the triggering forces, i.e. the load bearing capacity connected to compression and bending. This point is illustrated in Figure 7-3 and Figure 7-5, which separates the pre- and post-buckling range predictive models. The prediction process is adjusted as follows. According to a calculated mean moment M_{mean} within the incremental prediction process, the triggering load bearing capacity for compression $N_{DNN,max}$ is modified with Equation (7-25). The formulation is adopted from Equation (2-56), yet the forces and moments are normalized by the predicted maximum capacities $N_{DNN,max}$ and $M_{DNN,max}$. Figure 7-7 shows N-M interaction relations according to [108].

$$N_{DNN,max}^* = N_{DNN,max} \cdot \sqrt[{\alpha_y}]{I - \left(\frac{M_{mean}}{M_{DNN,max}} \right)^{b_y}} \quad (7-25)$$

The required stiffness terms are formulated using the overall beam stiffness representation shown in Equation (7-2). Here, the DNN model predictions for compression X_T and bending X_B are multiplied with the corresponding stiffness terms, see Equation (7-26).

$$K_T = \begin{bmatrix} X_T \frac{EA}{L} & 0 & 0 & -X_T \frac{EA}{L} & 0 & 0 \\ 0 & X_B 12 \frac{EI}{L^3} & X_B 6 \frac{EI}{L^2} & 0 & -X_B 12 \frac{EI}{L^3} & X_B 6 \frac{EI}{L^2} \\ 0 & X_B 6 \frac{EI}{L^2} & X_B 4 \frac{EI}{L} & 0 & -X_B 6 \frac{EI}{L^2} & X_B 2 \frac{EI}{L} \\ -X_T \frac{EA}{L} & 0 & 0 & X_T \frac{EA}{L} & 0 & 0 \\ 0 & -X_B 12 \frac{EI}{L^3} & -X_B 6 \frac{EI}{L^2} & 0 & X_B 12 \frac{EI}{L^3} & -X_B 6 \frac{EI}{L^2} \\ 0 & X_B 6 \frac{EI}{L^2} & X_B 2 \frac{EI}{L} & 0 & -X_B 6 \frac{EI}{L^2} & X_B 4 \frac{EI}{L} \end{bmatrix} \quad (7-26)$$

7.2.6 Second order implementation

In order to account for second order effects, the geometric stiffness matrix, as proposed in Section 7.1.1 and Equation (7-8), is added to the formulation from Equation (7-2), ending up in Equation (7-10). The bending terms are reduced with increasing normal forces leading to lower stiffnesses and higher deformations and rotations of the global system.

$$\alpha_{cr} = \frac{F_{cr}}{F_{Ed}} \quad (7-27)$$

Global imperfections linked to out-of-straightness on the member level and out-of-plumbness on the frame level can directly be applied by solving the eigenvalue problem

from Equation (7-11). The output leads automatically to an α_{cr} , described by Equation (7-27), and an eigenvector providing the information of the eigenshape of the structure. This eigenshape is used as an initial imperfection applied to the perfect system and account for second order effects. The parameter α_{cr} on the other hand is used to assess, whether global imperfections on the member or system level need to be applied. Limit values are provided by EN 1993-1-1 [48] for members prone to flexural buckling and frames affected by instability caused through sway effects, i.e. second-order $P-\Delta$ effects need to be included. For flexural buckling a limit value of $\alpha_{cr} \geq 25$ has to be fulfilled in order to ignore instability. This limit corresponds to the plateau value of European flexural buckling curves for members. According to EN 1993-1-1 [48], frames need to meet the condition of $\alpha_{cr} \geq 10$, if designed elastically, and $\alpha_{cr} \geq 15$ in terms of plastic design. A slightly higher limit value is defined to account for material yielding and the corresponding loss of stiffness.

To capture both effects, the $P-\Delta$ and $P-\delta$ ($P-\Delta-\delta$), i.e. out-of-straightness and out-of-plumbness, in one second-order analysis different options are available.

- i. The $P-\Delta$ effect is generally accounted for in a geometrically non-linear analysis through sway-mode imperfections.
- ii. The incorporation of the $P-\delta$ effect is performed by two commonly used procedures. Member imperfections are accounted for through member buckling checks based on non-sway effective lengths; member imperfections are explicitly modelled. Stability effects are therefore directly captured in the calculation and do not require further stability checks. Instead, only cross-section verification is applied to the most heavily loaded section [69].

8

Method Evaluation

Verification and Validation

Outline of the chapter:

This chapter is dedicated to the evaluation of the performance of the developed and trained DNN-DSM algorithm by means of demonstration examples. In a first verification step, the standard, 2D DSM implementation is verified by comparing its results against those given by a commercial, elastic beam analysis software. Subsequently, the model validation is carried out by comparing the non-linear DNN-DSM load-deformation predictions with numerical analyses using shell-element models, with otherwise similar assumptions regarding (nominal) material and imperfection definitions. Finally, the DNN-DSM predictions are compared physical test results from the literature or the Hollosstab test series, with the aim of assessing the capability of the method to make predictions in parameter ranges that are outside of the immediate training range. The considered tests include short columns and beam-columns as well as statically determinate and indeterminate beams. The results confirm the viability and potential of the DNN-DSM approach, while also highlighting the need for further developments before maturity of the method is reached.

8.1 Verification in the elastic range

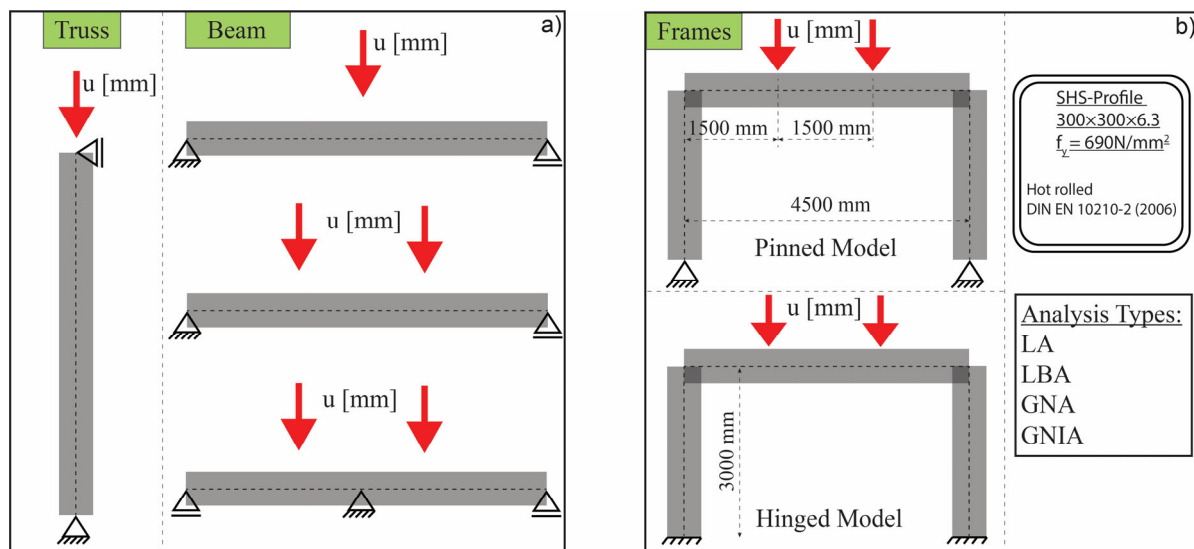


Figure 8-1: Schematic representation of verified models

In a first step, the author's standard DSM implementation using Python was verified by comparisons with predictions given by a commercial software, Cubus [297]. Different models of truss-and frame-type structures were thereby considered. The considered models and analysis methods are schematically shown in Figure 8-1. LA, LBA, GNA and GNIA calculations were performed. A general description of those analysis approaches was given in Section 2.2. The estimated differences between the author's and CUBUS results were not significant (below 0.1%) for the models in part a) of the figure and are therefore not described in detail for all models. Only minimally larger differences were obtained for the frame models from Figure 8-1 b), in particular for the GNIA analysis, therefore this result is shown in more detail here. A pinned and hinged frame were thereby considered, with an SHS300 profile of 6.3 mm wall thickness and a steel grade with $f_y = 690 \text{ N/mm}^2$. Figure 8-2 shows the results for the pinned model. The results for both models are summarized in Table 8-1. The estimated error [%] is shown for different analysis approaches. Note that the LBA output (eigenvalue, eigenshape) is not explicitly shown, but rather implemented as an initial geometric imperfection in the GNIA.

Considering the obtained results, the author's own 2D DSM implementation was assumed to be verified and correct.

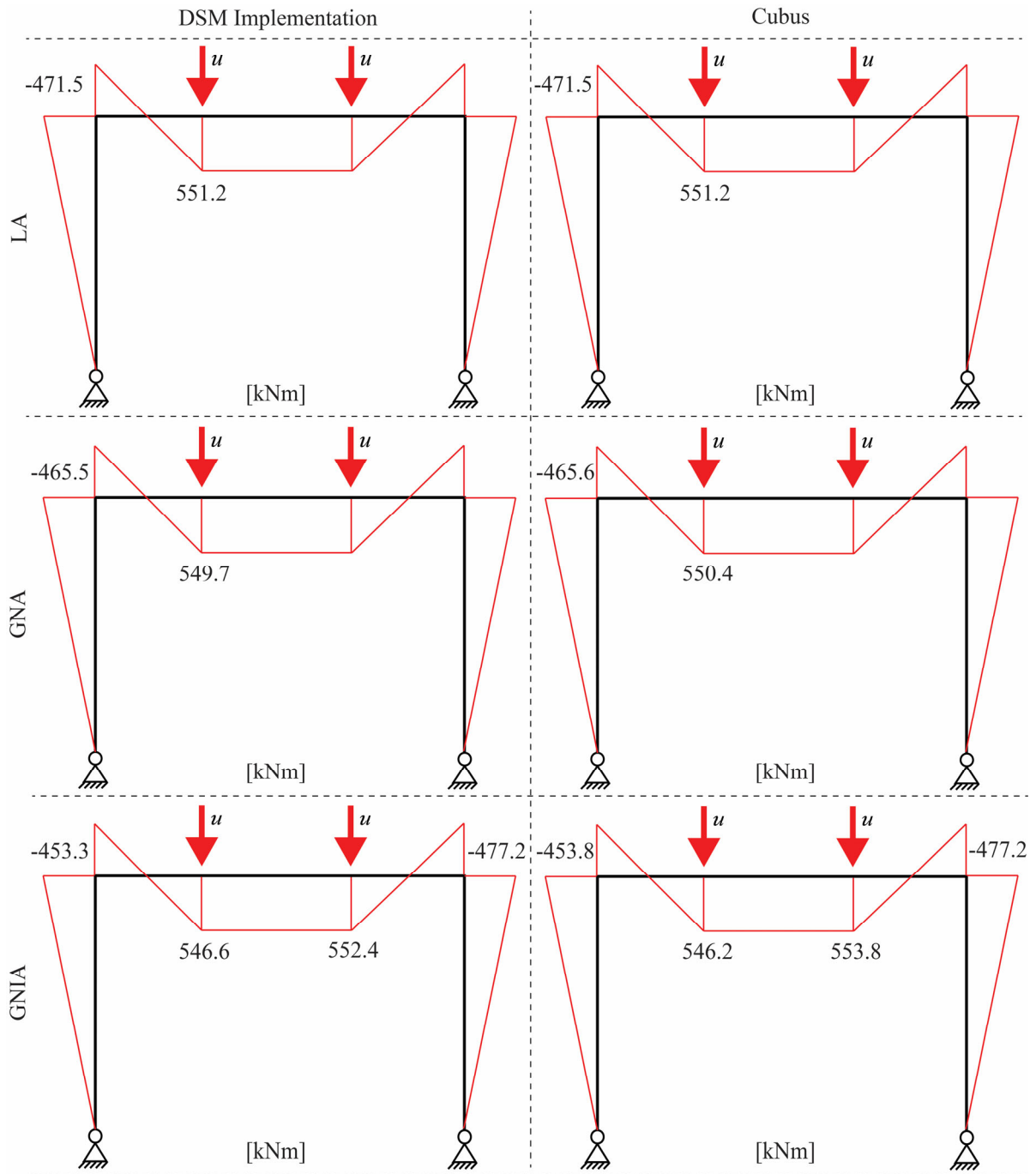


Figure 8-2: Analysis comparison for a hinged frame between own DSM implementation and Cubus [297]

Table 8-1: Verification results

Used Models	LA	LBA	GNA	GNIA
Error in [%]				
Frame Hinged	0.00	0.19	0.13	0.073
Frame Clamped	0.00	0.34	0.15	0.11

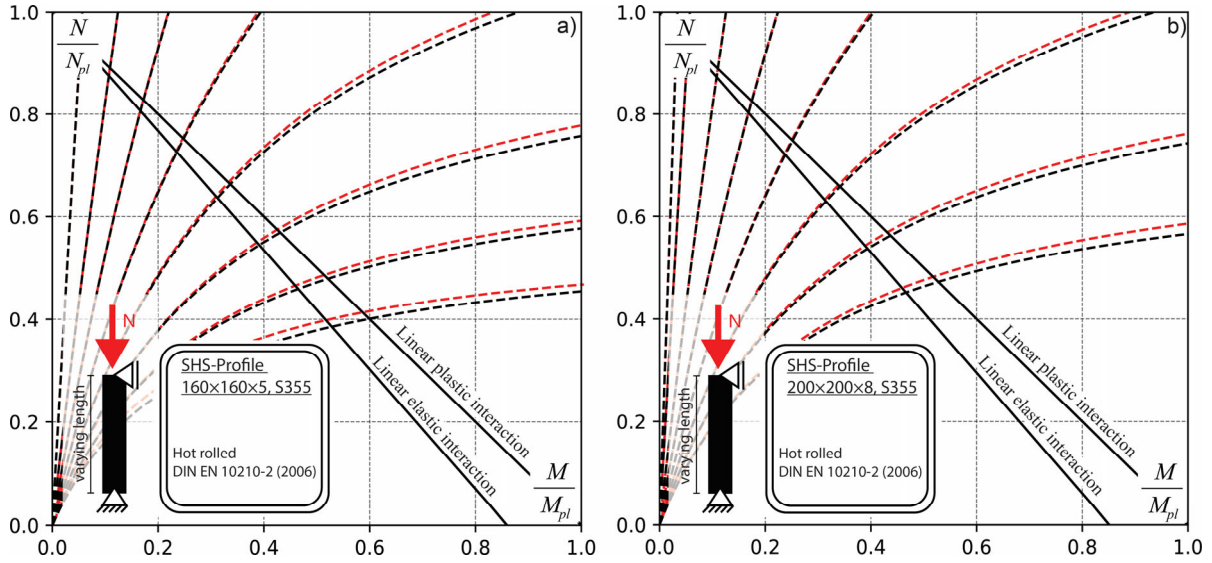


Figure 8-3: Comparison between second order DSM results and theoretical second order moment in a linear cross-section interaction diagram

$$M_{Th.2.Ord.} = \frac{N \cdot e_0}{1 - \frac{N}{N_{cr}}} \quad (8-1)$$

Figure 8-3 represents the second order column resistance (GNIA) with the linear elastic and plastic cross-section failure criterion under axial load and second order moment according to Equation (8-1). The comparison with own second order DSM calculations is within the scope of acceptance around an estimated error of around 1.0%.

8.2 Cross-section verification

The verification results on the cross-sectional level are shown and discussed in Section 8.2.1 and Section 8.2.2. Section 8.2.1 shows the “direct” DNN model predictions of the cross-section resistance for bending or compression. Note, that this prediction procedure does not need the general DNN-DSM implementation, described previously in Chapter 7. The predictions are done for every individual profile, resulting in one normalized output value for each cross-section (normalized cross-section resistance), see Section 6.2.4.3. This models are used in the DNN-DSM model as trigger values (thresholds)

to switch between the pre- and post-buckling range. However, they are excellent for determining individual resistances due to their accuracy and efficiency, as described in the following.

Section 8.2.2 shows results, which are still on the cross-sectional level, but, with the big difference to Section 8.2.1, not based on the prediction of only one resistance value. Instead the whole load-displacement/moment-rotation curve is described by predicting incremental tangent stiffnesses and stepwise back calculating the forces and moments for the whole range.

8.2.1 Cross-section capacity

The general DNN model architecture was presented in Section 6.3 and is used for all predictions done here. All necessary features are summarized in Table 6-4 of Section 6.2.5.2, distinguishing between different profile geometries and fabrication routes. The overall prediction accuracy is very high, with an averaged r^2 value of 0.99 resulting from the data sets used for training and testing of the models. A representation of GMNIA results and the predicted DNN model values are shown for some selected profile series, in compression or bending, in Figure 8-4.

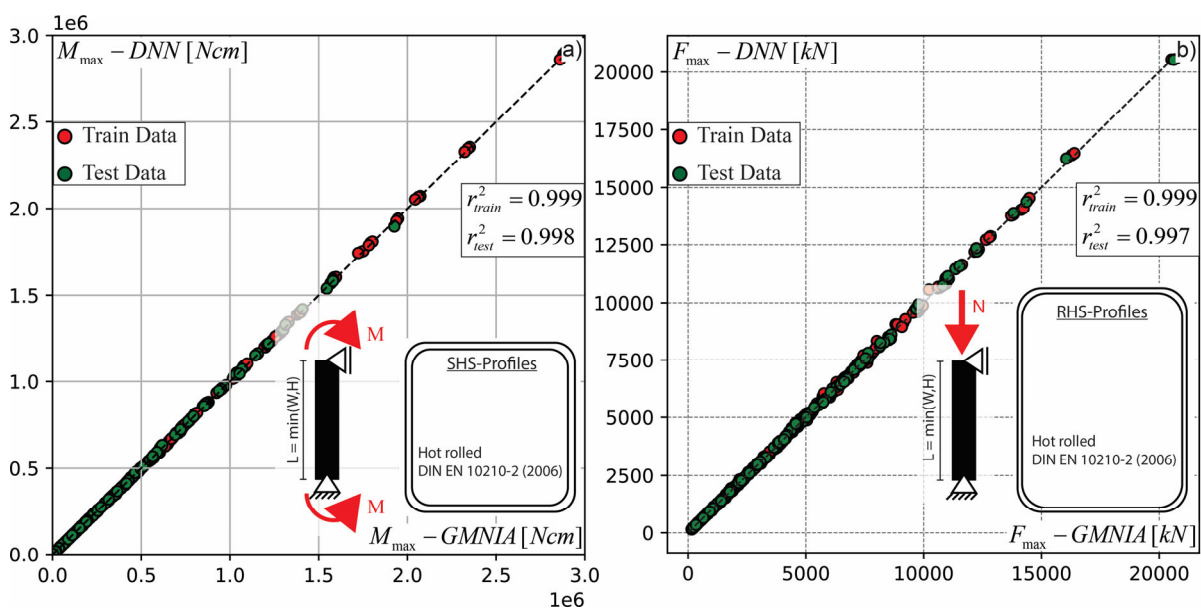


Figure 8-4: Comparison of DNN prediction and shell FE simulations for cross-section capacity in, a) bending, SHS hot-rolled; b) compression, RHS hot-rolled

Further, the made predictions are compared with FE shell results and the resistance curves from EN 1993-1-5 [131]. The results are summarized in Figure 8-6 and Figure 8-7, using the normalized representation format for buckling, where the x-axis is the relative local slenderness and the y-axis the buckling knock down factor. Simulations and predictions are plotted on top of each other to showcase the accuracy achieved by such models.

In addition, Figure 8-5 displays a comparison of GMNIA shell FE simulations and the results obtained with the AA-CSM by Fieber [67], collected for RHS and SHS cross-section in compression or bending. Regardless of the very good match, this diagram is intended to show the difference between a CSM based approach and DNN prediction from Figure 8-6 and Figure 8-7 in the following. The AA-CSM follows the results from FE beam analysis. The termination criterion is the obtained CSM strain limit, individually for each cross-section by calculating a local slenderness. Local imperfections are indirectly taken into account by the CSM base curve. Since the curve is a calibrated best fit solution and includes both compression and bending, scatter from shell based GMNIA solutions cannot be reproduced. For both cases, the results in Figure 8-5 follow a narrow prediction course, being in some cases slightly conservative or optimistic compared with shell FE.

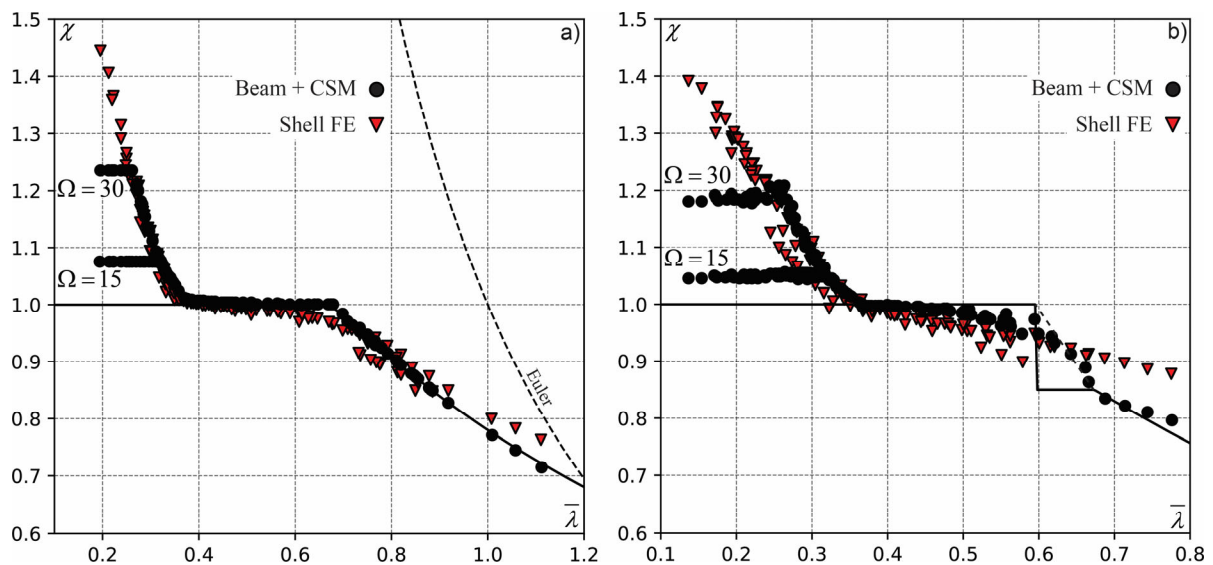


Figure 8-5: Cross-section capacity predicted by shell FE models, AA-CSM [67] with strain limits and EN 1993-1-1 [48] for SHS/RHS profiles for, a) pure compression; b) pure bending; adopted from [67]

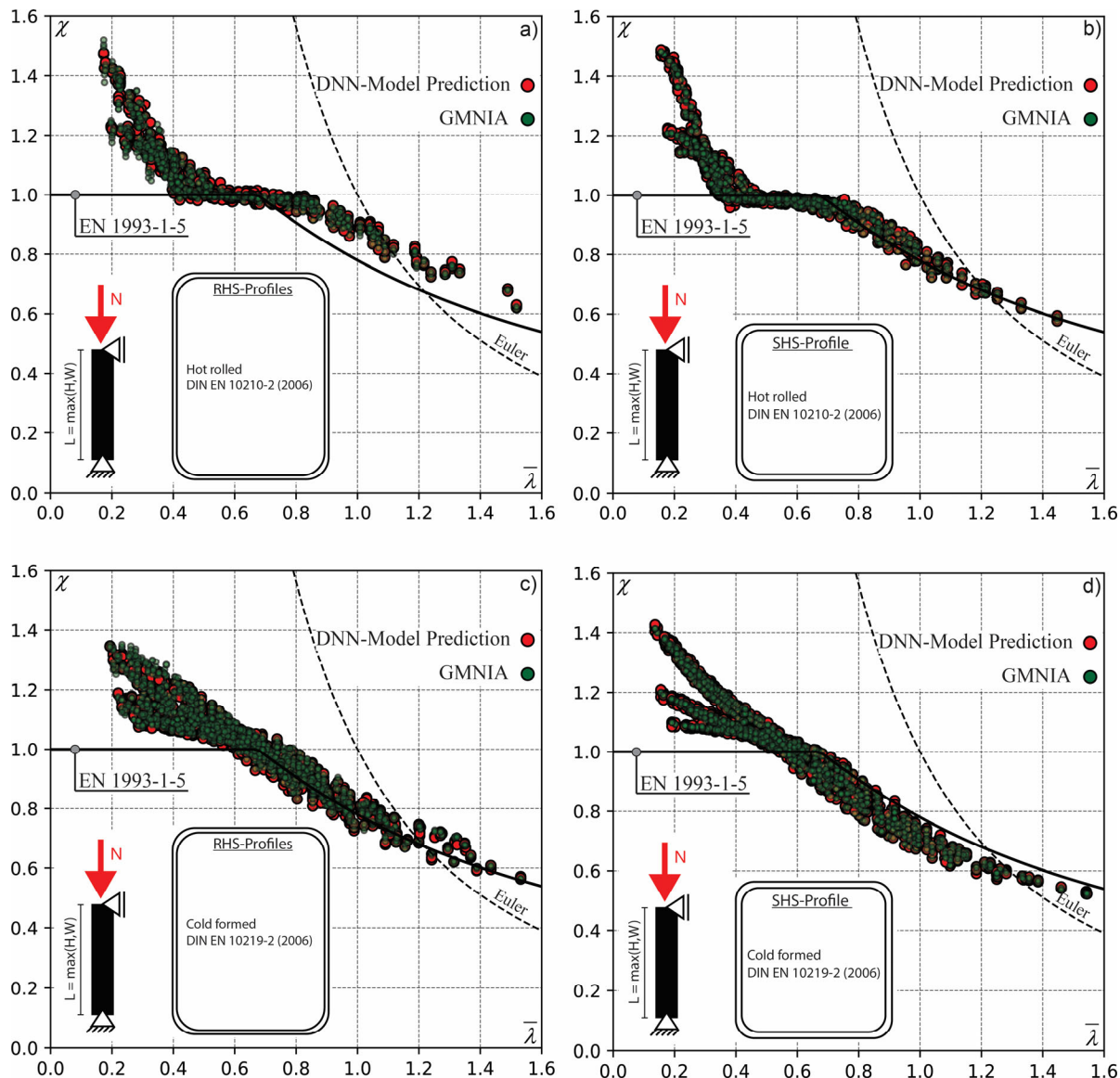


Figure 8-6: Prediction of the cross-section capacity for all investigated profiles, load case: compression

The used DNN model is presented in Table 6-9, additional features for prediction in Table 6-4. Figure 8-6 and Figure 8-7 show the results for hot-rolled and cold-formed RHS and SHS profiles. In regions, where the cross-section would be classified as class 1 or 2, strain hardening is clearly visible while showing its positive effects in a much higher load bearing capacity compared to EN 1993-1-5. In more slender regions the cross-section capacity follows the buckling curves for the load case of pure compression, see Figure 8-6 a) to d). For the load case of pure bending the predicted values are always above the buckling curve in slender areas. This is mainly addressed to mutual effects of the cross-section plates in bending, leading to higher capacities even for a higher relative slenderness, i.e., beyond the plastic plateau.

The three different steel grades for hot-rolled and cold-formed steel are clearly visible in the capacity prediction in the plastic region through a capacity separation into three branches. The higher branch is addressed to the steel grade of S355 and the lower branch to S690/S700. This makes sense, since the strain hardening ratio decreases for high strength steel compared to mild steel. Beyond the plateau no clear separation is visible between steel grades and imperfection amplitudes and the branches fall basically into one overall capacity prediction.

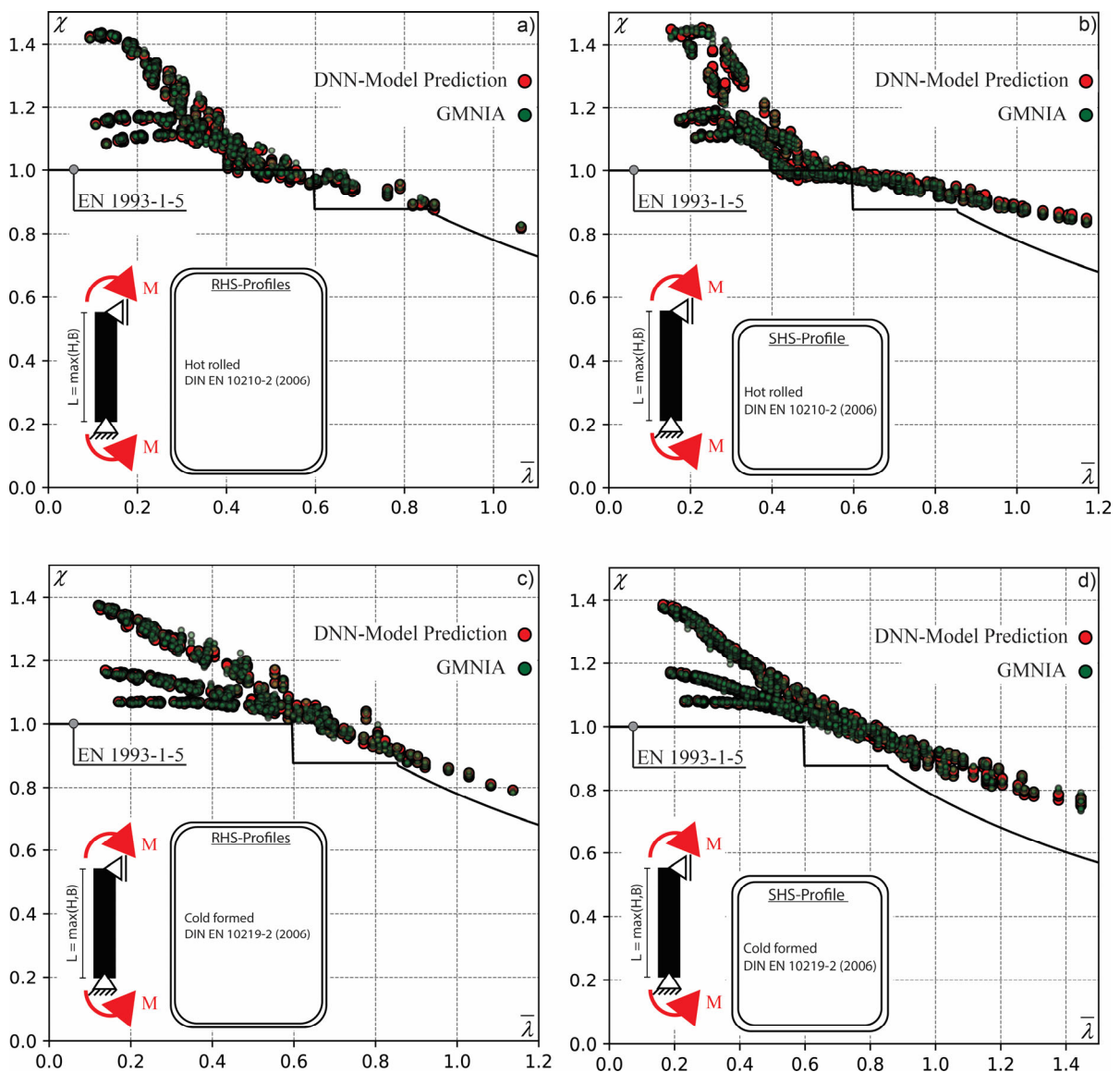


Figure 8-7: Prediction of the cross-section capacity for all investigated profiles, load case: bending

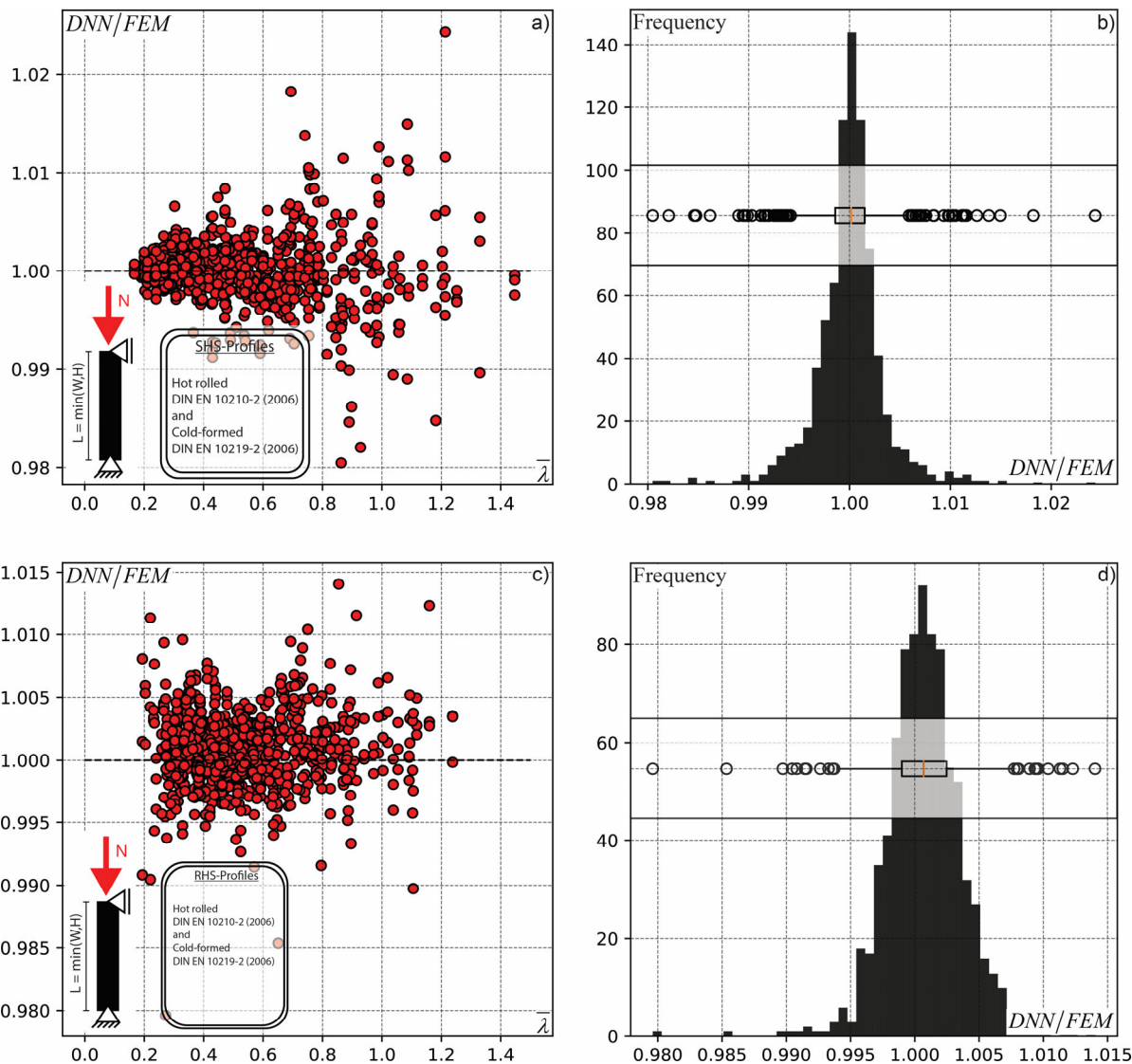


Figure 8-8: Comparison between DNN model predictions and GMNIA simulations, load case: compression

A more evident accuracy comparison can be drawn from Figure 8-8 and Figure 8-9 for compression and bending, respectively. Figure 8-8 a) and b) show a summarized representation for all hot-rolled and cold-formed SHS and RHS profiles. The x-axis displays the relative local slenderness, the y-axis a direct comparison between the predicted results and the target values (non-linear Abaqus GMNIA simulations) resulting in a normalized manner. The deviations for compression are in some individual cases around 2%, in all other cases below. Additional frequency plots explain the distribution of the predictions according to their error, see Figure 8-8 b) and d). The same representation was chosen for the load case of pure bending in Figure 8-9, leading to overall similar results.

All statistical results are summarized in Table 8-2, leading to the overall conclusion of a very high model accuracy for the prediction of the cross-section capacity. Thus, the 95% confidence describes the level of certainty within a calculated prediction interval of 95%. Here the calculated interval values are close between 1.00, which would indicate a perfect result. This results applies to the load case of pure compression and pure bending to the same extent.

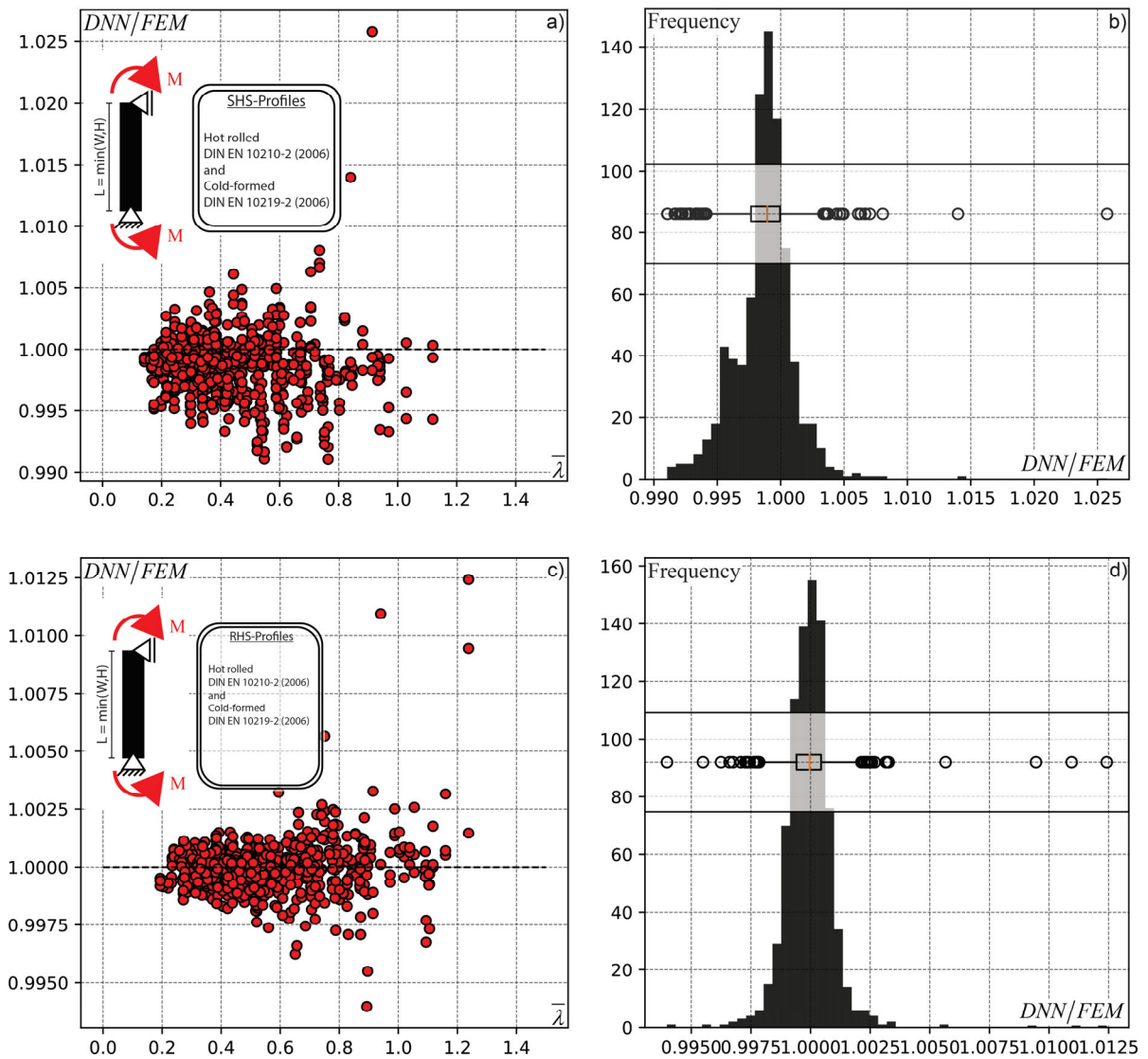


Figure 8-9: Comparison between DNN model predictions and GMNIA simulations, load case: bending

To conclude this evaluation a final remark is made towards the enormous time advantages. Each profile series (106 SHS hot-rolled profiles, 142 RHS hot-rolled profiles, 113 SHS cold-formed profiles, 165 RHS cold-formed profiles) has three parameters for the steel grade and the local imperfection amplitude. The **DNN model prediction** takes

around **4 to 6 second** to predict **all values** of each profile list. Note, this procedure does not involve the DNN-DSM algorithm and is only based on the tensorflow implementation. This is far beyond the calculation velocity recorded for the Abaqus calculations. Neglecting the modelling time, always two calculations need to be performed: LBA and GMNIA. The **LBA** takes around **5 to 10 seconds** to estimate the first eigenmodes. The **GMNIA** around **20 to 40 seconds** for each profile. To be fair, the DNN model used herein only predicts a discrete point (maximum force or moment) on the load-deformation/moment-rotation curve and not the whole course.

Table 8-2: Summary of the accuracy evaluation for cross-section capacity

DNN Models: Compression				
Profiles	μ	σ^2	cv	95% confidence
SHS hot-rolled and cold-formed	1.00	1.24e-5	0.003	0.999-1.000
RHS hot-rolled and cold-formed	1.00	9.26e-6	0.003	1.000-1.001
DNN Models: Bending				
SHS hot-rolled and cold-formed	0.998	6.25e-6	0.0025	0.999-0.999
RHS hot-rolled and cold-formed	1.00	1.076e-6	0.001	1.000-1.001

8.2.2 Cross-section behaviour

The outputs of the used models are verified and discussed in the following. Estimated accuracies of the DNN models are presented within Figure 8-10 and Figure 8-11. The x-axis is representing the simulated results from shell FE and the y-axis the predicted values from the DNN models. Figure 8-10 a) and c) and Figure 8-11 a) display exemplarily the overall prediction of the tangent stiffness K_T for hot-rolled and cold-formed SHS, as well as RHS profiles in the pre-buckling range, subjected to compression or bending. Note, this values are used as initial inputs for the calculation of forces, accumulated over the deformation (see Equation (8-2)):

$$F_n = F_{n-1} + K_{T,n} \cdot \Delta u_n \quad (8-2)$$

Predictions in the pre-buckling range replicate in most cases the GMNIA results with a high accuracy, although a higher scatter for lower tangent stiffnesses is obtained. In general, a low stiffness is present when reaching the maximum force or moment of a cross-section. A high stiffness, on the other hand, is always present in the beginning of the deformation/rotation. Therefore, the network will recognize a prediction pattern in the beginning more easily, than for progressed deformations/rotations. Depending on the slenderness of the cross-section, the load bearing capacity is reached at very different states. Thus, predictions tend to be more diffuse in this regions.

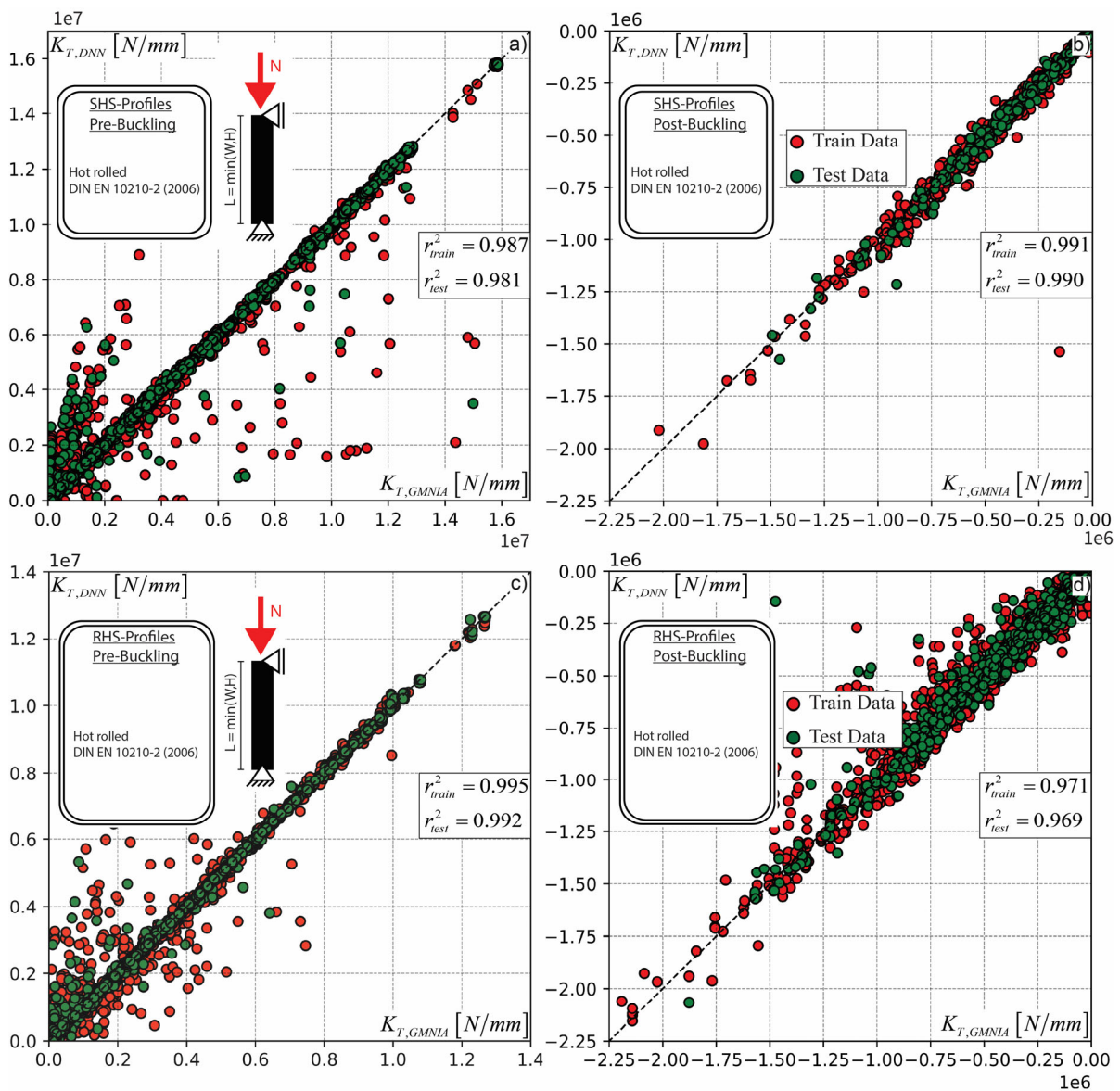


Figure 8-10: Comparison of simulated ($K_{T,GMNIA}$) and predicted ($K_{T,DNN}$) results of the incremental tangent stiffness for the load case compression and, a) hot-rolled SHS profiles in the pre-buckling range; b) hot-rolled SHS profiles in the post-buckling range; c) hot-rolled RHS profiles in the pre-buckling range; d) hot-rolled RHS profiles in the post-buckling range

Corresponding post-buckling prediction comparisons are shown in Figure 8-10 b) and d). The prediction scatter increases for the post-buckling range, resulting in slightly lower R-squared values. This is due to a clearly non-linear behaviour for the whole range, not following the same logic as in the pre-buckling range, with a high stiffness directly in the beginning and a decrease with higher deformation/rotations. Depending on the profile slenderness, the load-deformation/moment-rotation behaviour can vary strongly after reaching the peak load, by suddenly dropping in stiffness or being more ductile.

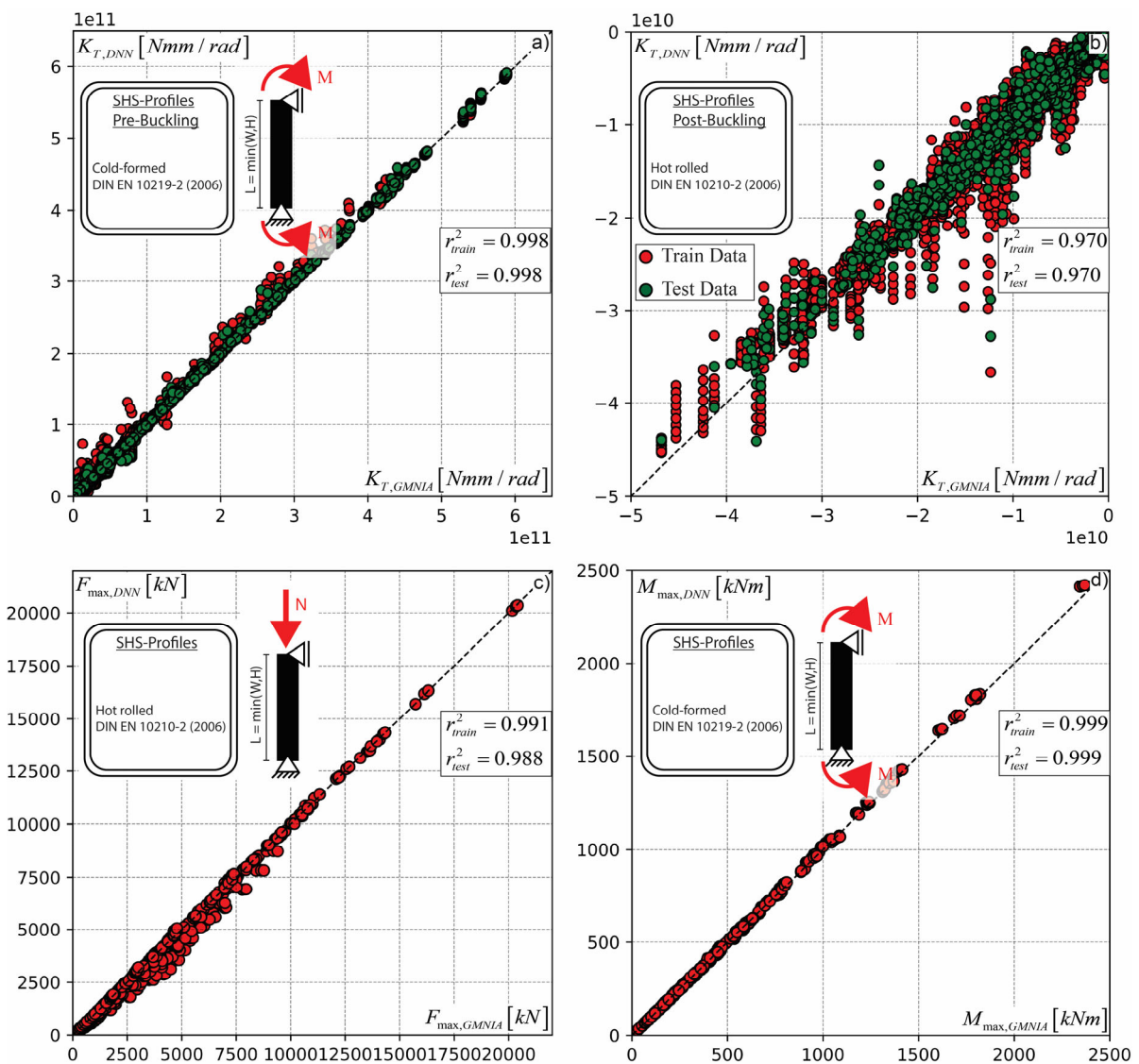


Figure 8-11: Comparison of simulated ($K_{T-GMNIA}$) and predicted (K_{T-DNN}) results of the incremental tangent stiffness for bending of cold-formed SHS profiles; a) pre-buckling range; b) post-buckling range; c) and d) comparison of maximum loads calculated from stiffness predictions

Table 8-3: Summary of the accuracy evaluation for cross-section capacity

DNN Models: Compression		
Profiles	r_{train}^2	r_{test}^2
SHS hot-rolled pre-buckling	0.987	0.981
SHS hot-rolled post-buckling	0.991	0.990
RHS hot-rolled pre-buckling	0.995	0.992
RHS hot-rolled post-buckling	0.971	0.969
SHS cold-formed pre-buckling	0.999	0.999
SHS cold-formed post-buckling	0.993	0.993
RHS cold-formed pre-buckling	0.999	0.999
RHS cold-formed post-buckling	0.975	0.974
DNN Models: Bending		
SHS hot-rolled pre-buckling	0.987	0.985
SHS hot-rolled post-buckling	0.959	0.957
RHS hot-rolled pre-buckling	0.992	0.992
RHS hot-rolled post-buckling	0.978	0.973
SHS cold-formed pre-buckling	0.998	0.998
SHS cold-formed post-buckling	0.970	0.970
RHS cold-formed pre-buckling	0.999	0.999
RHS cold-formed post-buckling	0.983	0.984

Despite the high R-squared values shown in Figure 8-11 a) and c), a certain scatter is present which might imply high inaccuracies in the calculation of the forces (see Equation (8-2)). Therefore, the load-displacement and moment-rotation curves of the considered hot-rolled and cold-formed SHS profiles are calculated in the pre-buckling range, by accumulating all forces/moment calculated with the predicted values of the tangent stiffness. Therefore, the trained DNN models were used for the prediction in the pre-buckling range. Figure 8-11 c) and d) explains the comparison of these results by isolating only the maximum load F_{max} . Thus, it was assumed that the overall error is most present by the end of every cross-section dependent load-displacement curve. It can be seen that the outliers of the presented cases has a rather low influence on the estimated maximum force F_{max} . The associated r^2 value lies in both cases, for compression or bending, around 0.99 for training and testing data. This can be attributed to the fact that the predicted values of K_T are based on the incremental distribution from Abaqus simulations.

This results in the fact that deviations within the tangent stiffness lead to small differences in the accumulated force.

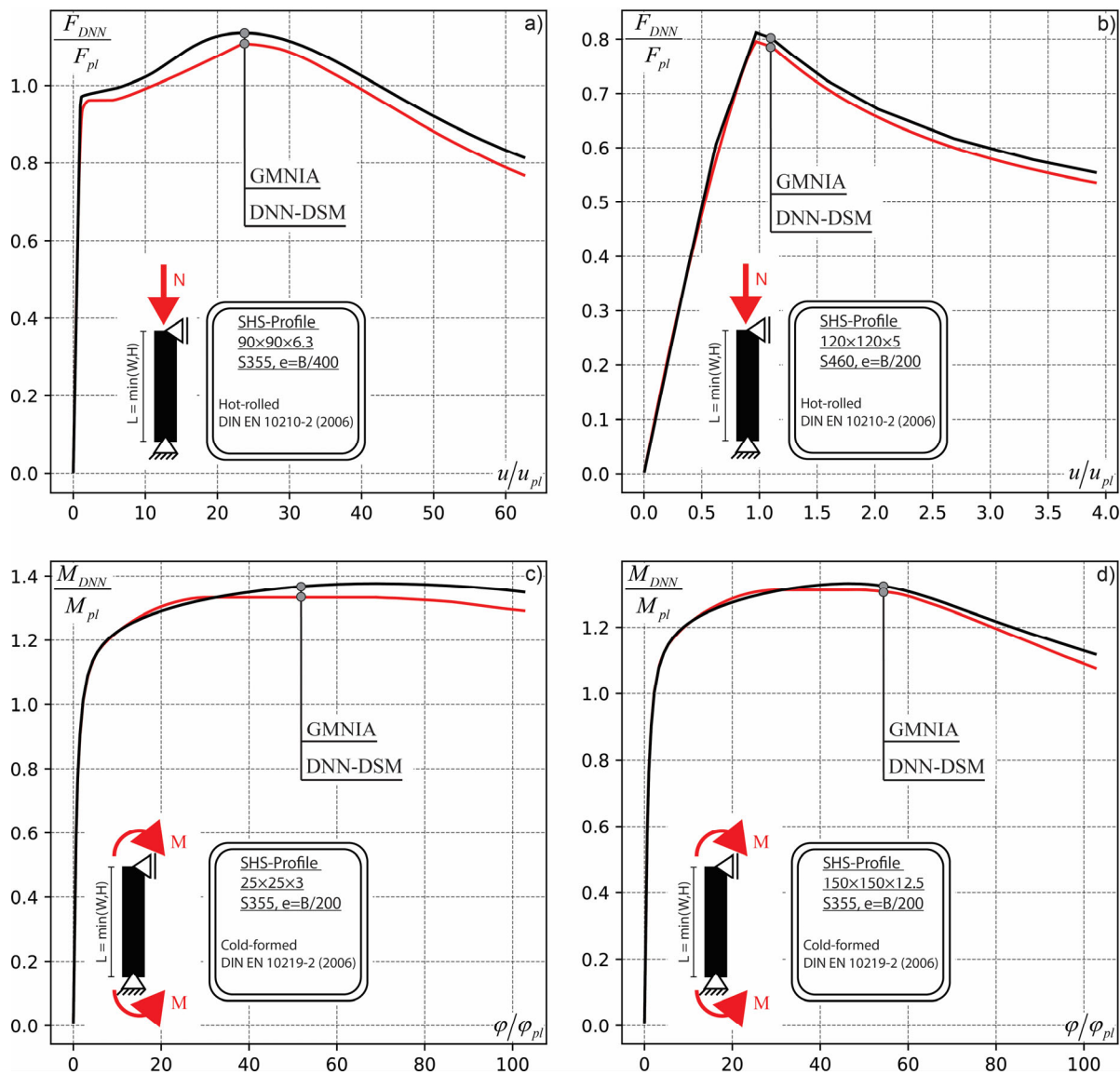


Figure 8-12: Comparison of load-displacement/moment-rotation curves between GMNIA and DNN prediction for the pre- and post-buckling range in compression or bending; a) and b) comparison of hot-rolled SHS profiles loaded in compression; c) and d) comparison of cold-formed SHS profiles loaded in bending

Figure 8-12 provides results from the overall prediction in the pre- and post-buckling range for some individual profiles. Figure 8-13 a) and b) shows the results obtained for hot-rolled SHS profiles loaded in compression. In general, the overall prediction is accurate enough to replicate the non-linear load-displacement behaviour. More slender cross-sections, such as the shown SHS120×5 profile in Figure 8-12 b), are predicted mostly with a higher accuracy, since no plateau and strain hardening region needs to be

predicted. A general observation was that the DNN model tend to learn a straight or more rounded behaviour much better without intermediate kinks. Therefore, profiles from Figure 8-12 c) and d) showed a much closer match with the GMNIA curves.

Figure 8-13 displays additionally the prediction of the full load-displacement range of 954 hot-rolled SHS in compression and 1278 cold-formed SHS profiles in bending. A normalized representation was chosen within the axes. This definition has the considerable advantage that all curves are displayed and compared in a scale independent manner. Therefore, the pre- and post-buckling range is plotted along its local slenderness, the predicted force/moment (N_{Pred}/M_{pred}) is divided by the plastic cross-section capacity N_{pl}/M_{pred} and the corresponding displacement/rotation u/φ divided by u_{pl}/φ_{pl} , the theoretical plastic deformation. Figure 8-13 illustrates that the pre- and post-buckling range of various profiles of different slenderness, steel grade, manufacturing process and load case can be predicted with a good accuracy. This was in general demonstrated within the explanations and figures in this section. Subsequently, this three-dimensional information forms the basis for the implementation of the DSM beam formulation.

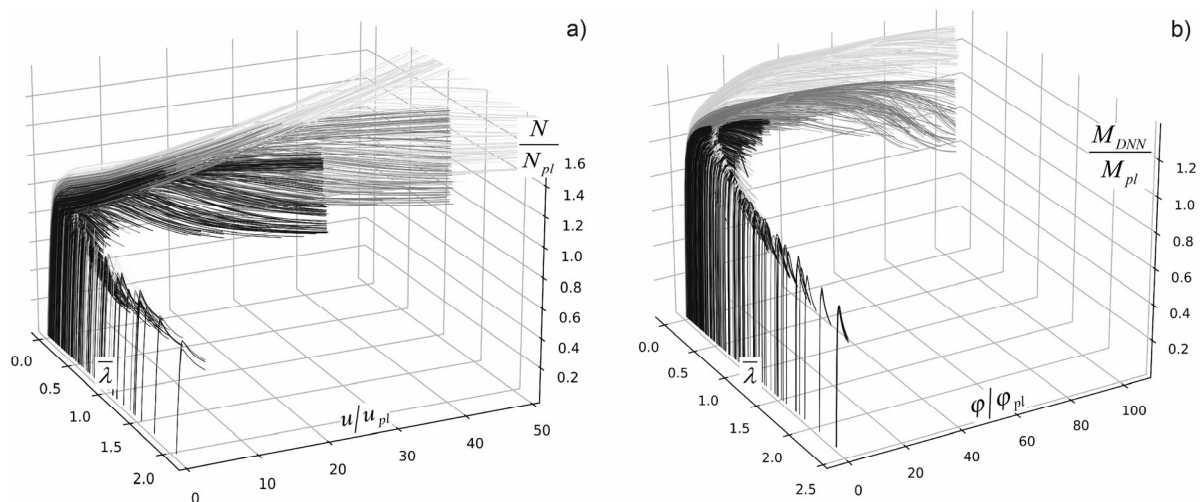


Figure 8-13: Predicted pre- and post-buckling range for a) hot-rolled SHS profiles in compression; b) cold-formed SHS profiles in bending

8.2.3 Prediction sensitivity

8.2.3.1 Feature scatter

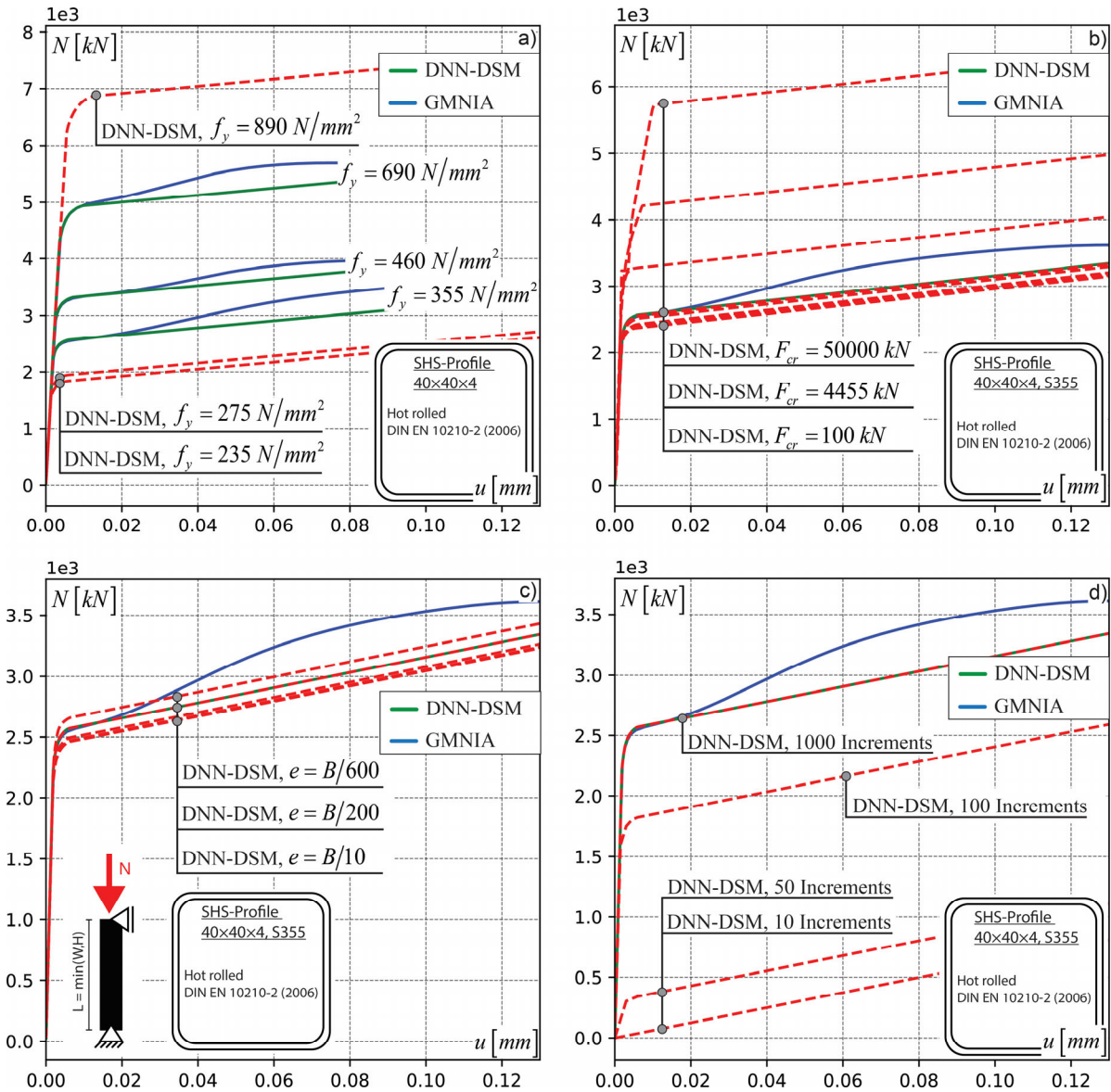


Figure 8-14: Comparison of predictions beyond the predefined data set boundaries for a hot-rolled SHS40x4 profile and the load case compression, varied parameters are a) yield strength; b) the critical elastic buckling load; c) the imperfection amplitude; d) the incremental step size

Section 8.2.1 focuses on the presentation of the prediction accuracy made by the DNN model for the tangent stiffness K_T . In addition, full load-deformation and moment-rotation curves are calculated from those predictions to show the general comparison with GMNIA simulations. For that purpose, the predictions done by the DNN models were

generated by using exactly the input features that were also used to train and test the models, i.e., nominal values for the geometry and the material properties.

In reality, the required input features can vary strongly from the nominal values. The steel grade can be obtained from tensile coupon test, the imperfection amplitude as well as the geometry measured directly from the real specimen, the critical buckling load can be obtained from a slightly different FE model. Therefore, the sensitivity towards a robust prediction procedure is tested in the following. The features f_y , F_{cr} , e and u are changed to explore regions beyond the boundaries of the data sets and their influence on the DNN model predictions. This was done here exemplary for one profile, summarized in Figure 8-14 for the load case of compression. The corresponding prediction are done on the cross-sectional level for one augmented bar element.

Figure 8-14 a) displays the load-deformation curves for a hot-rolled SHS40x4 profile, for the steel grade S355, S460 and S690. Blue solid lines correspond to the GMNIA simulation, green solid lines to the DNN model predictions and the red dashed lines to the changed parameters. Changing the yield strength beyond the trained boundaries, in this case below S355 or above S690, leads to reasonable results, following the logic of the load-deformation from the learned yield strength values.

Figure 8-14 b) shows the differences when using the “wrong” critical elastic buckling load. Here, the wrong critical buckling load would be every value besides the one calculated in Abaqus for compression and the assumed FE model. Using any different software with slightly different model assumptions would automatically lead to a difference. This problem can be avoided if the values are determined automatically within the program without any user intervention. The results show that critical buckling values below the actual value ($F_{cr} = 4455 \text{ kN}$) do not strongly affect the behaviour. Taking as an input feature $F_{cr} = 100 \text{ kN}$, which is only 2.24% (44 times smaller) of the actual critical buckling value, results in a small deviation of around 3%. On the other hand, taking higher critical buckling values result in significantly larger calculated forces. A nine times higher buckling load leads to 150% bigger values and an eleven times bigger critical buckling load to 200% bigger results. Although these values are very extreme, they depend on the chosen unit load in the LBA. Thus, misinterpretations may well occur, which will have to be solved program-internally.

Figure 8-14 c) illustrates the predictions based on different imperfection amplitudes. Note, the imperfections amplitudes which were used for the training of the models are $B/200$, $B/300$ and $B/400$. Yet, changes beyond this values result in reasonable predictions, following the course of the trained load-deformation curves in a logical manner, without overshooting over proportionally.

Figure 8-14 d) describes predictions made with a different amount of total increments. It is important to understand, that the DNN models are exclusively trained on the increments, i.e. deformations or rotations, that were extracted from the shell FE Abaqus models. However, taking always exact the same increments for the predictions in the DNN-DSM procedure is not possible, since the deformations are applied arbitrary and distributed stiffness dependent along the system. Using very small steps sizes (many increments) leads to a prediction close to the actual trained result, here demonstrated with 1000 increments. Decreasing the number of increments is only logical to improve the efficiency of the DNN-DSM algorithm. This, however, leads to inaccurate results, since the predicted stiffness may partially miss the elastic stiffness range and result in too low capacities. An extreme example is shown here by using only ten increments, completely unable to describe the non-linear load-displacement curve. Since this effect is an essential part of the method, this aspect is further discussed in Section 8.2.3.2.

8.2.3.2 Step size effect

The incremental step size has a significant influence on the accumulated prediction accuracy within the load-deformation path. This effect is independent of the used profile, material model, imperfection amplitude or load case. An exemplary explanation is given in the following, based on the load case of centric compression.

The incremental step size, equivalent to the incremental nodal deformation, is discussed in Figure 8-15 regarding on its influence on the prediction with respect to the GMNIA simulation. The x-axis is always showing the nodal displacement, the y-axis the corresponding force at each increment. The ground truth is given by the GMNIA simulation, here shown as a black line. The green line is the DNN model prediction in the pre-buckling range, using exactly the same deformation steps as extracted from the Abaqus FE shell calculation, i.e., the data that the DNN model was trained on. The dotted grey lines

represent the DNN-DSM calculation, using a different amount of incremental deformations until reaching a defined loading level. All diagrams show exclusively the pre-buckling deformation range.

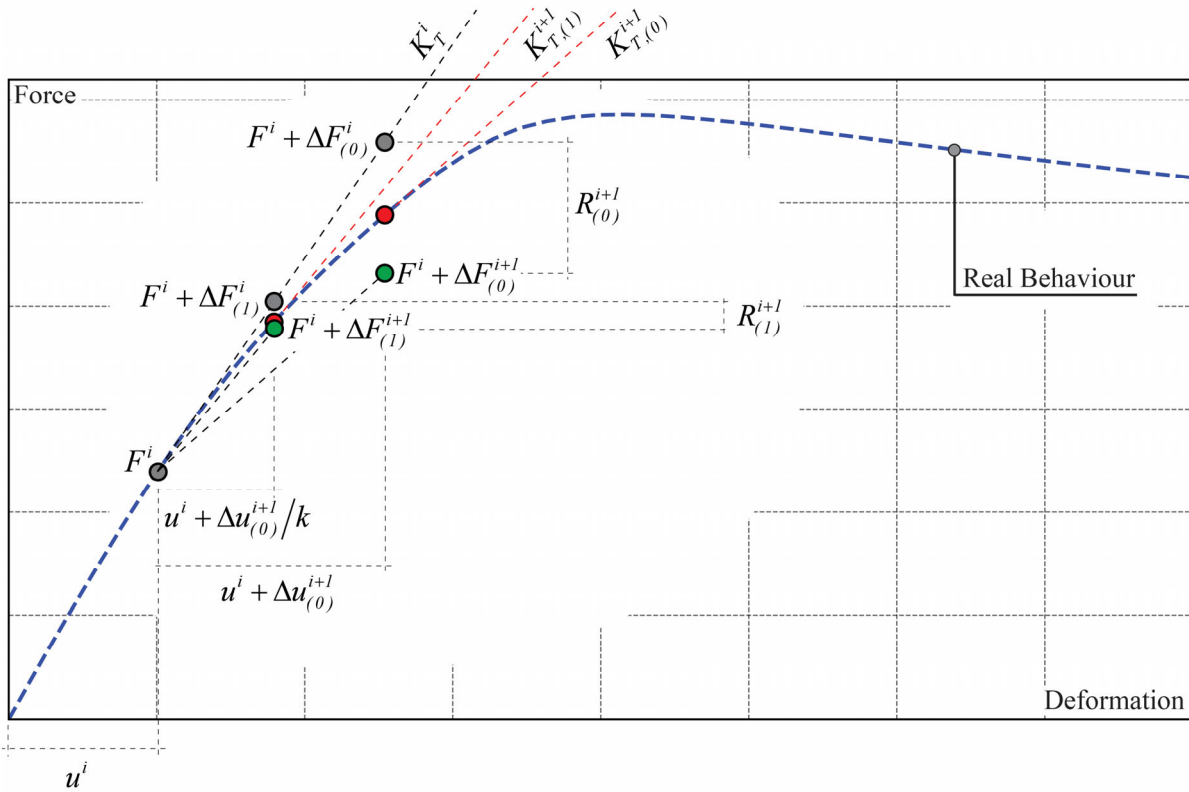


Figure 8-15: Dynamic step size optimization

A clear influence can be drawn from the size of the incremental deformation. With decreasing step size the accuracy of the prediction start to decrease. This is illustrated through Figure 8-16 a), b) and c), where the step size decreases from 20 to 4. This can be explained through the following steps. The prediction for K_T^i is done by using an absolute deformation at a current deformation of u^i . Therefore, at points with stiffness jumps, i.e. a kink in the load-deformation curve (the same applies for the moment-rotation relation), predictions with too large step sizes may lose stiffness too early.

To avoid this problem, a step size optimizer can be introduced, in which the step size is dynamically adjusted dependent on an error definition from the residuum. Figure 8-15

explains briefly this procedure. Starting from an arbitrary point on the true load-deformation curve (blue dotted line) at the location u^i and F^i .

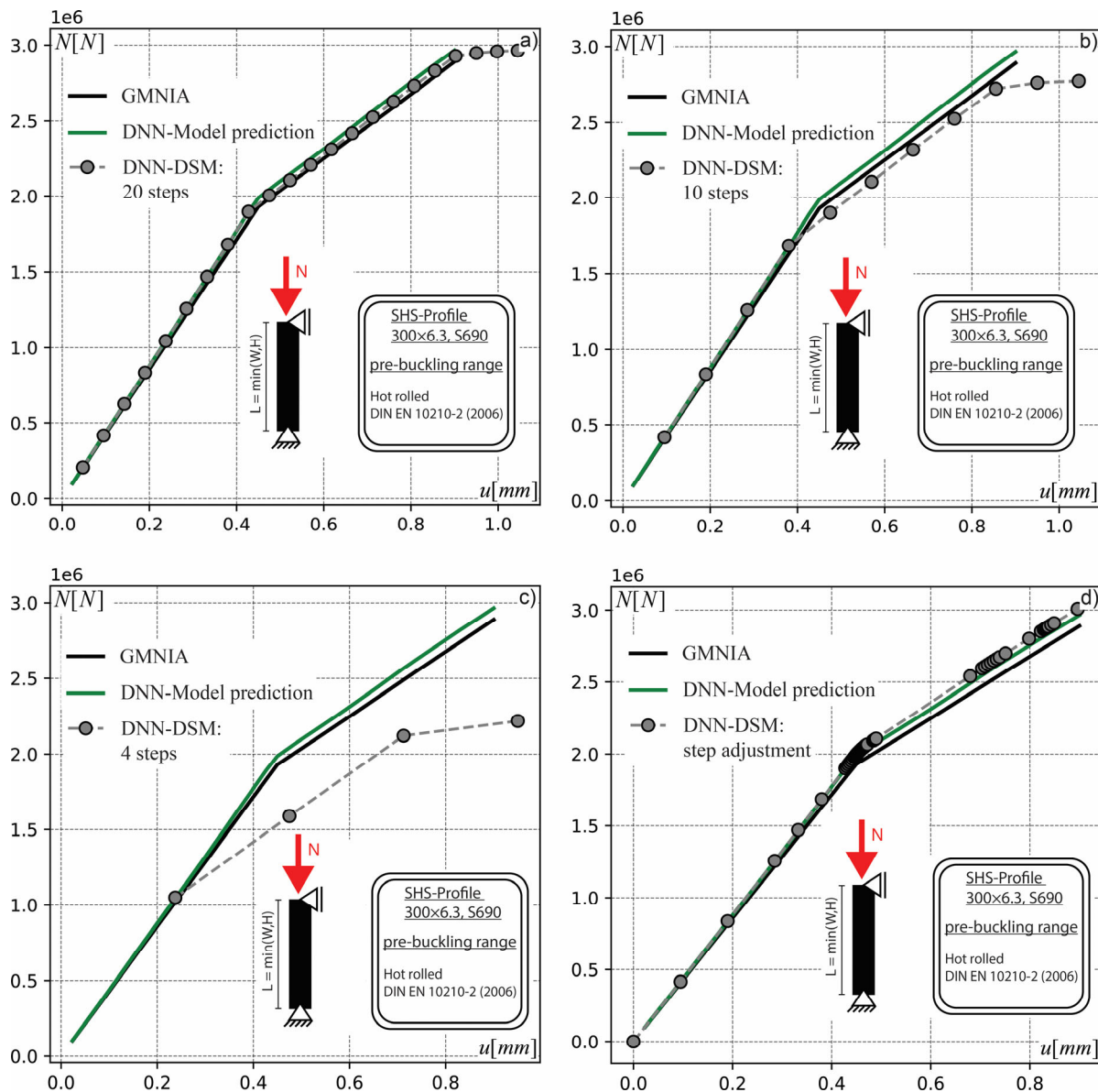


Figure 8-16: Influence of the amount of steps on the prediction accuracy of the load deformation path; a) 20 steps; b) 10 steps; c) 4 steps; d) dynamic step optimization

The prediction of the tangent stiffness $K_{(0)}^{i+1}$ is done with the updated absolute deformation $u^i + \Delta u_{(0)}^{i+1}$, while $\Delta u_{(0)}^{i+1}$ is assumed to be an arbitrary incremental deformation. The desired true force is represented through the red point on the blue dotted line and the predicted force through the green point at $u^i + \Delta u_{(0)}^{i+1}$. Corresponding to it, the grey point represents the force, which is calculated by assuming the tangent stiffness K_T^i from

the previous step. The residuum is an error function and can be calculated with Equation (8-3), although other definitions are possible.

$$R^{i+1} = \left| \frac{(F^i + \Delta F^i) - (F^i + \Delta F^{i+1})}{(F^i + \Delta F^i)} \right| \leq \text{threshold} \quad (8-3)$$

If the calculated error is bigger than the defined threshold value, the incremental deformation step $\Delta u_{(0)}^{i+1}$ is minimized by $\Delta u_{(0)}^{i+1}/k$, where $k = 2$. The factor k is free to choose. The new tangent stiffness $K_{(1)}^{i+1}$ is now calculated at a smaller deformation $u^i + \Delta u_{(0)}^{i+1}/k$, leading to a smaller residuum compared to the previous step $R_{(1)}^{i+1} < R_{(0)}^{i+1}$.

In the context of Figure 8-16 d) the step size was halved ($k = 2$) if the calculated residuum is higher than a predefined threshold value. This automatically leads to an accumulation of calculations in areas with larger stiffness changes and thus an increase in computational effort. Nevertheless, this strategy enables a save computational propagation with a small number of steps in areas with a comparable stiffness and still a high prediction accuracy.

8.3 Verification of Isolated Members

8.3.1 Isolated members in compression

Figure 8-17 and Figure 8-18 show GMNIA simulations and DNN-DSM recalculations of an SHS300×6.3, S690 profile with the length of *600 mm* (see Figure 8-17 a)), *900 mm* (see Figure 8-17 b)), *1200 mm* (see Figure 8-18 a)) and *1500 mm* (see Figure 8-18 b)) loaded in pure compression. The results are shown by a load-deformation relation. The blue curves always represent the results from the performed GMNIA simulations. The imperfection shapes were estimated from LBA simulations by assuming the first eigenmodes as the critical one. The imperfection amplitude was set to $B/200$ in all cases according to EN 1993-1-5 [131]. Above each diagram is a representation of the FE model and its buckling shape during failure. In addition, the assumed DNN-DSM models used for the recalculation are shown in order to identify model influences on the pre- and post-buckling behaviour.

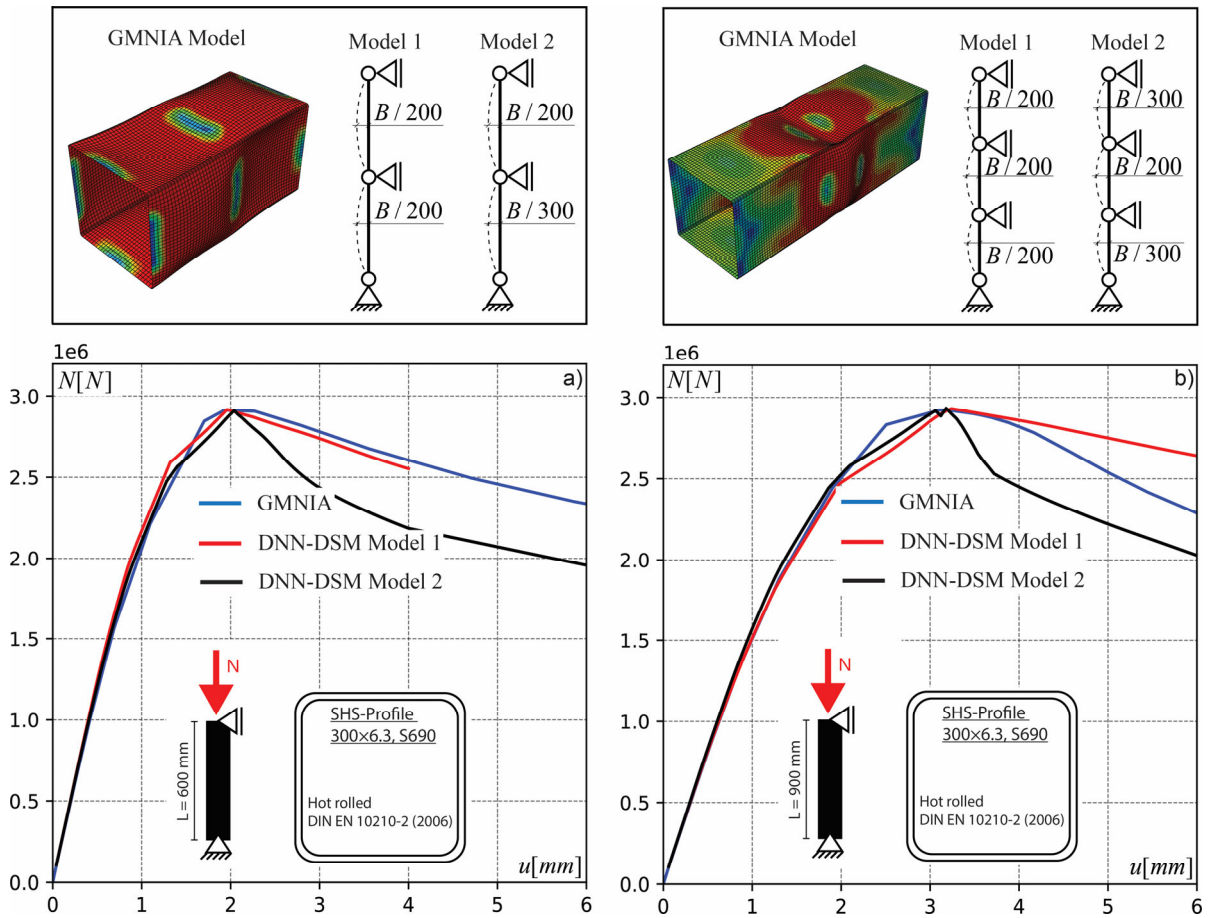


Figure 8-17: Comparison between shell FE and DNN-DSM models of different lengths; a) $L = 600\text{mm}$; b) $L = 900\text{mm}$

In the FE shell-based GMNIA simulation, the case of the 600 mm long member (see Figure 8-17 a)) shows constant buckling over the entire length, with two main local buckling fields forming. Thus, the deformation of the whole member is more pronounced in the post-buckling region due to the distribution of deformations over the entire length. A similar behaviour can be achieved with DNN-DSM model 1, with an equivalent imperfection amplitude of $B/200$ in all elements. In addition, model 2 uses two different imperfection amplitudes, $B/200$ and $B/300$, in order to achieve buckling in only one beam element. This leads, in particular, to a larger drop of the load-deformation curve within the post-buckling range. This behaviour is somehow logical, since the deformations are not distributed over the whole member length, but are concentrated in one field.

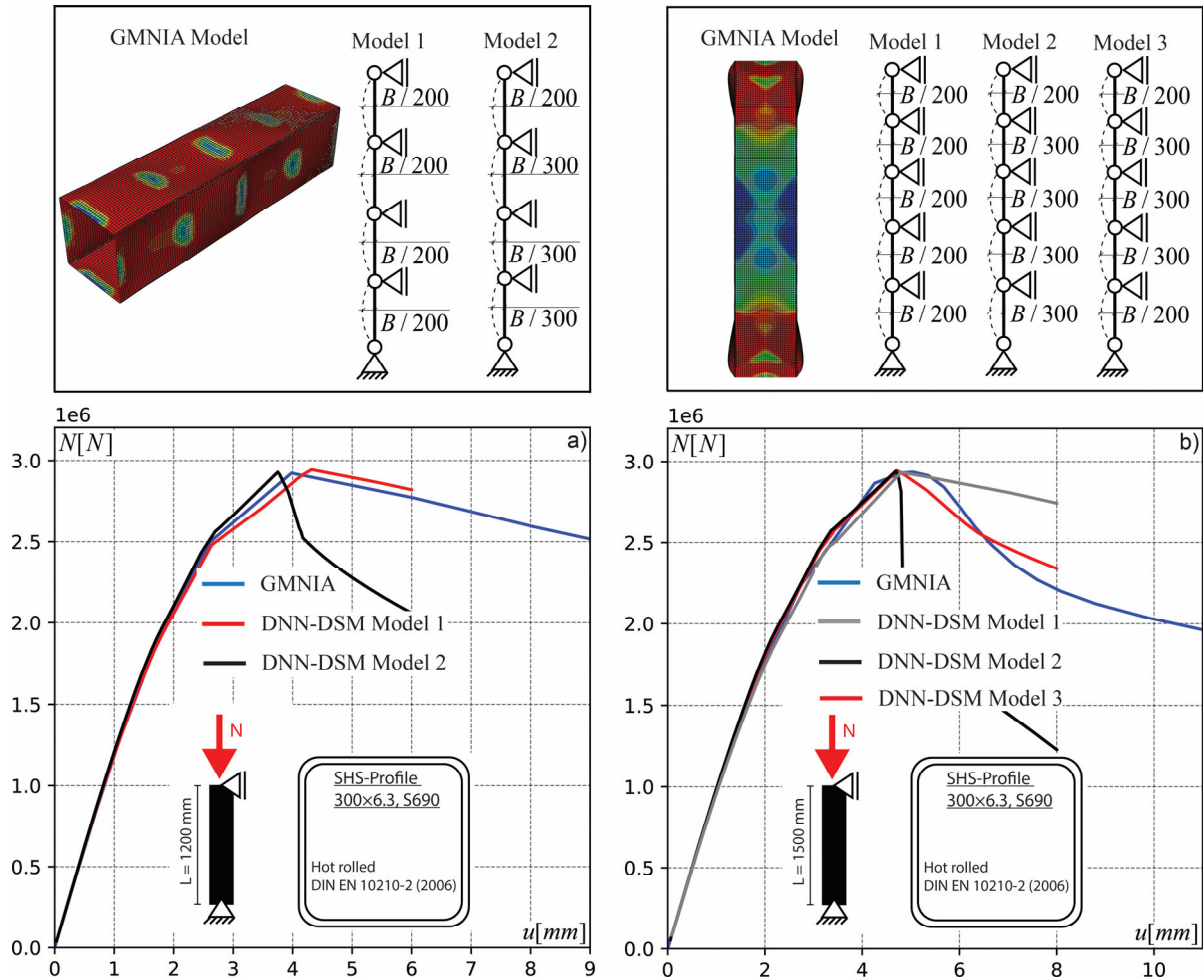


Figure 8-18: Comparison between shell FE and DNN-DSM models of different lengths; a) $L = 1200\text{mm}$; b) $L = 1500\text{mm}$

A slightly different behaviour was observed for the member length of $L = 900\text{ mm}$. Figure 8-17 b) displays the results for the GMNIA simulation, where local buckling is clearly more concentrated in one area. This mainly affects the post-buckling behaviour, which appears more compressed with a greater reduction in stiffness. In comparison, DNN-DSM model 2 (local buckling in one beam element) leads to more conservative results, with a sharper drop of resistance in the post-buckling. However, no differences in the pre-buckling range between DNN-DSM model 1 and model 2 were identified. A similar behaviour, as shown in Figure 8-17 a), was observed for the member length of $L = 1200\text{ mm}$ and shown in Figure 8-18 a). Again, local buckling occurs over the whole length of the member, leading to a pronounced post-buckling behaviour. This behaviour is then best reproduced by DNN-DSM model 1, assuming equivalent imperfection amplitudes for in all beam element within the prediction. Figure 8-18 b) indicates the results for the member length of 1500 mm . Two buckles, at the top and the bottom occurred within the

GMNIA simulation. According to this, 3 different DNN-DSM models were implemented to observe the overall load-displacement prediction. DNN-DSM model 1 uses an equivalent imperfection amplitude with $B/200$. DNN-DSM model 2 uses two imperfection amplitudes, $B/200$ and $B/300$ in order to force the model to buckle exclusively in one field. DNN-DSM model 3 uses the same imperfection approach as model 2, with the difference that buckling is introduced in the upper and lower element only.

In all cases it was slightly more conservative to choose the model with only one local buckling field, i.e., buckling of one beam element. The pre-buckling behaviour remains the same compared to the other DNN-DSM models, but the post-buckling behaviour is less pronounced and more affected by a higher drop in the resistance within a smaller overall deformation. For this reason, all recalculations in Section 8.4.1 are performed exclusively on the basis of a DNN-DSM model with a local buckling formation in one element along the whole member.

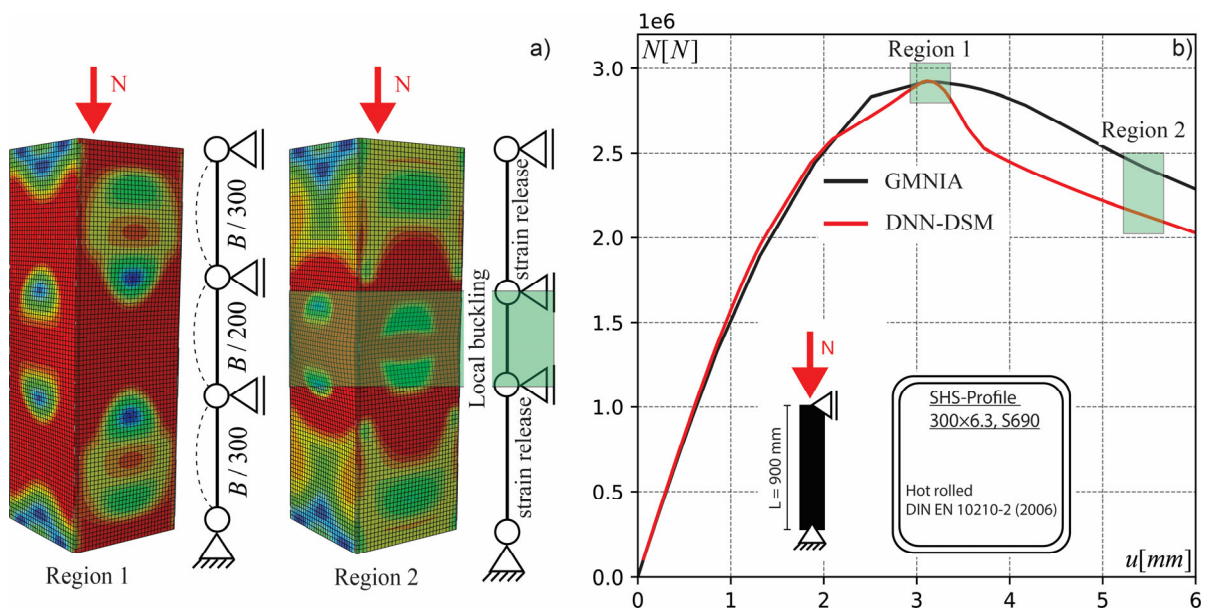


Figure 8-19: a) Comparison of redistributions of strains; b) corresponding load-displacement curve of a hot-rolled SHS300x6.3 profile, S690, loaded in compression

Figure 8-19 provides an interesting redistribution effect, which was obtained during the performed calculations on truss systems. The same SHS300x6.3 profile, as the one chosen for model considerations in Figure 8-17 and Figure 8-18, was used here. The length of the member is equal to $L = 900$ mm. Thus, three beam elements are used to build the DNN-DSM model. A corresponding shell FE model is shown in Figure 8-19 a). Figure 8-19

b) provides the load-displacement curves from GMNIA simulation and DNN-DSM predictions. Two regions are highlighted as “Region 1” and “Region 2”, indicating the peak load and some deformation stage in the post-buckling range. The GMNIA model is fully compressed, almost equally along the whole length, right before reaching Region 1. Right after, it starts to develop a local buckle, leading to a release of strains in the outer regions and to an over proportional increase of strains in the local buckling field. The same behaviour was obtained in own DNN-DSM predictions. By assuming the middle field with a slightly higher imperfections, one can force the model to buckle directly in the middle element. During the calculation the same behaviour is obtained, where the outer beam elements are released from strains and the middle beam element developing local buckling and taking the whole applied deformations.

8.3.2 Isolated members in compression with global second order effects

The DNN-DSM approach as developed in this thesis is currently limited by several assumptions, which were presented in Section 7.2.2. In particular, some of those limitations need to be addressed first in order to clarify the DNN-DSM algorithm, modified for consideration of global (column-type) second order effects.

The DNN models were not trained for combined load cases. Therefore, an N-M interaction is not accounted for in the stiffness terms. Instead, the assumption is made on the cross-sectional resistance level, according to the N-M interaction formulation by Liew and Gardner [108] from Section 7.2.5, to scale the cross-section compression resistance to a corresponding moment value. A further assumption in the calculations here, is that only the elastic bending stiffness terms were chosen for the predictions. This comes mainly from the fact that the members are dominated by normal forces and nonlinearities according to bending are not dominant. To conclude, the predictions presented in the following Figure 8-20, use a **simplified N-M interaction** to scale the predicted cross-section capacity and **elastic bending stiffnesses**. For this reason, the comparisons are mainly qualitatively, in order to show the already existing possibilities and advantages.

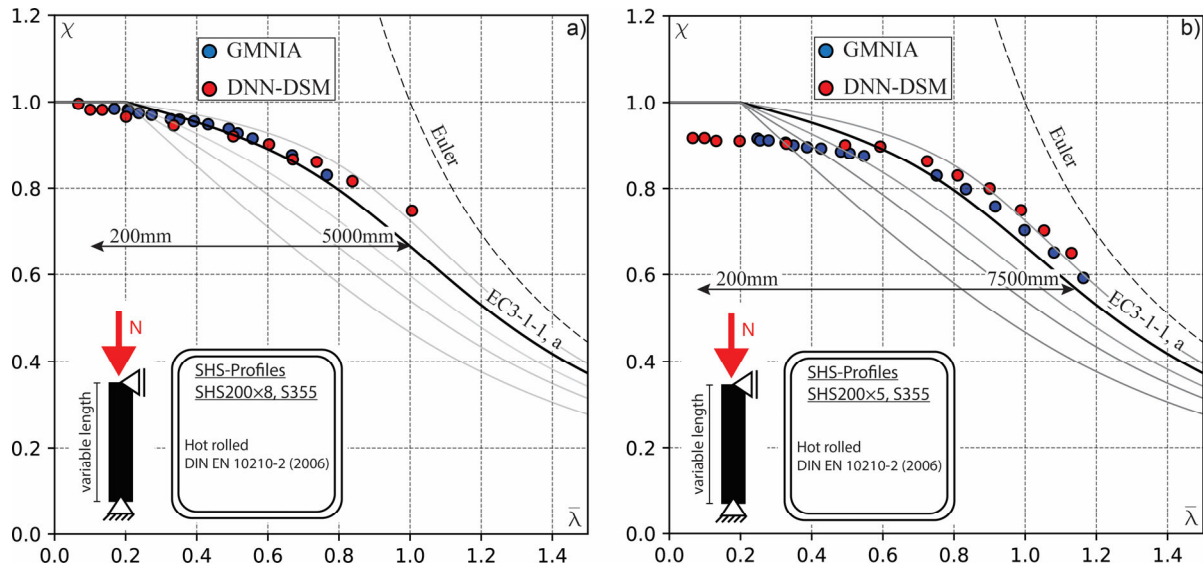


Figure 8-20: Comparison of FE shell simulations with DNN-DSM predictions with second order effects; a) hot-rolled SHS200×8 profile, S355; b) hot-rolled SHS200×5 profile, S355

Figure 8-20 show comparisons between advanced shell FE simulations and DNN-DSM predictions with second order effects. The GMNIA shell models are based on the FE model assumptions from Section 5.4. Two eigenforms are combined, a local and a global buckling shape to account for local and flexural buckling. Note, the GMNIA results from Figure 8-20 were published in [75], [76] in a slightly different representation, but are well suited for comparisons made herein. However, in the context of the above mentioned publications, different imperfections amplitudes were chosen than proposed in EN 1993-1-1 [48]. The imperfection amplitude for local buckling was set to $B/400$ (see Equation (2-11)), and for flexural buckling to $L/1000$. In both diagrams the GMNIA results follow closely flexural buckling curve for hot-rolled SHS profiles.

Figure 8-20 a) shows the results for a hot-rolled SHS200×8 profile with the steel grade S355. The local slenderness of the profile is equal to $\bar{\lambda} = 0.53$, therefore still in the plateau region of the local buckling curve from EN 1993-1-5 [131] ($\bar{\lambda} < 0.674$), meaning that local buckling is not the dominant instability criterion. The results reflect this, as the full cross-section capacity is reached in the plateau region of the buckling curve for flexural buckling. Similar results can be replicated with the DNN-DSM, although slightly different imperfection amplitudes had to be used for flexural buckling with a value of $L/250$ in order to achieve similar results in more slender regions. Simulations presented in Figure 8-20 b) follow the same considerations for a hot-rolled SHS200×5 profile. The local cross-section slenderness is equal to $\bar{\lambda} = 0.84$ and beyond the local buckling plateau from

EN1993-1-5. Local buckling affects the overall cross-section capacity, which is also present in the results, since the full cross-section capacity is not reached in the plateau region for flexural buckling. This effect is captured directly by the DNN-DSM, showing a big advantage in the design procedure in contrast to the GMNIA simulation. It is important to understand that this effect is often not necessarily captured by the GMNIA simulation. This is related to the simulation procedure within such advanced analysis methods, which are basically all based on LBA calculations for eigenvalue and eigenform extraction. Depending on member length and the local cross-section slenderness, the need for combined eigenforms might become relevant. However, this circumstance is not explicitly addressed in code provisions such as EN 1993-1-14 for FE design, and therefore always a potentially error prone task.

Qualitatively, it can be said that the DNN-DSM is able to reproduce the results from GMNIA, despite the assumptions mentioned above. However, this step requires further evaluations and an actual interaction relationship between the stiffness terms.

8.3.3 Isolated members in bending

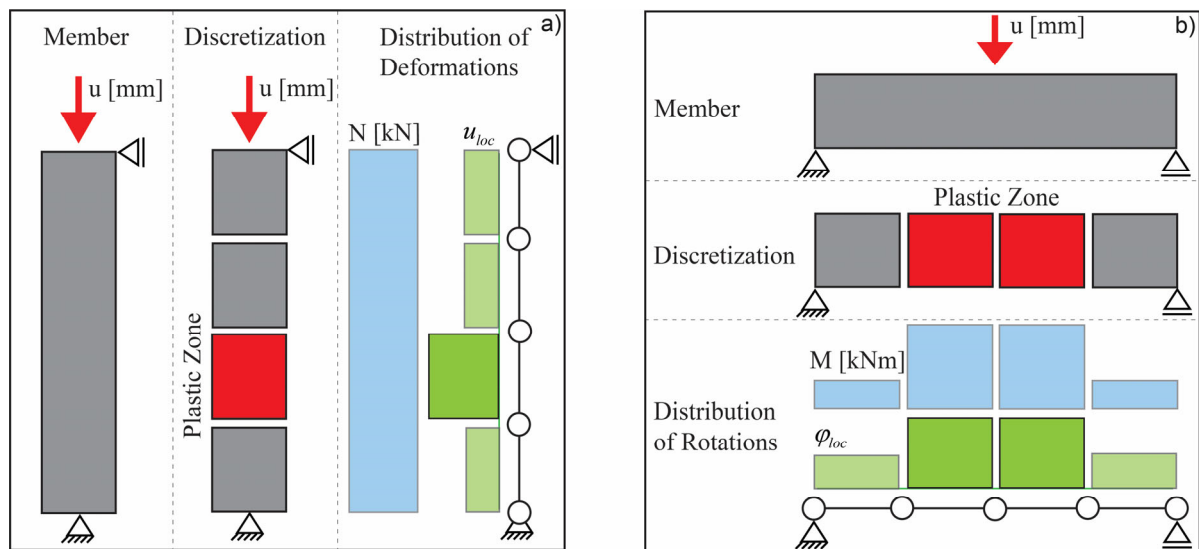


Figure 8-21: DNN-DSM Model approaches for a) truss models; b) beam models

In the course of AA-CSM (see Fieber [67] and Section 2.5.2) a strain averaging approach was presented, which takes the mean strain within an estimated buckling length (half-wavelength) to account for a more realistic behaviour in the plastic zone. It is therefore required that the discretized beam elements are equal or smaller than the buckling half-wavelength. The difference within the DNN-DSM approach here, is that the assumed buckling length (discussed and presented throughout Section 5.3 and 5.4) is equal to the local FE shell model length from Abaqus and is automatically the length of an implemented beam element (beam element length = buckling length) The strain averaging is not explicitly calculated but is rather directly accounted for in the DNN model prediction.

Isolated members in bending are evaluated exemplary, comparing shell finite element GMNIA simulation results and equivalent DNN-DSM model calculations. Figure 8-22 shows the results for three-point bending, Figure 8-23 for four point bending, comparing the estimated load-deformation curves from shell FE and DNN-DSM. The shell FE models are build up on the assumptions made in Section 5.4, i.e. shell element type, cross-section geometry, discretization, imperfection amplitudes. MPC beam constraints were first generated along the edges and coupled to reference points at each end of the member, to generate a relatively simple pin type boundary condition.

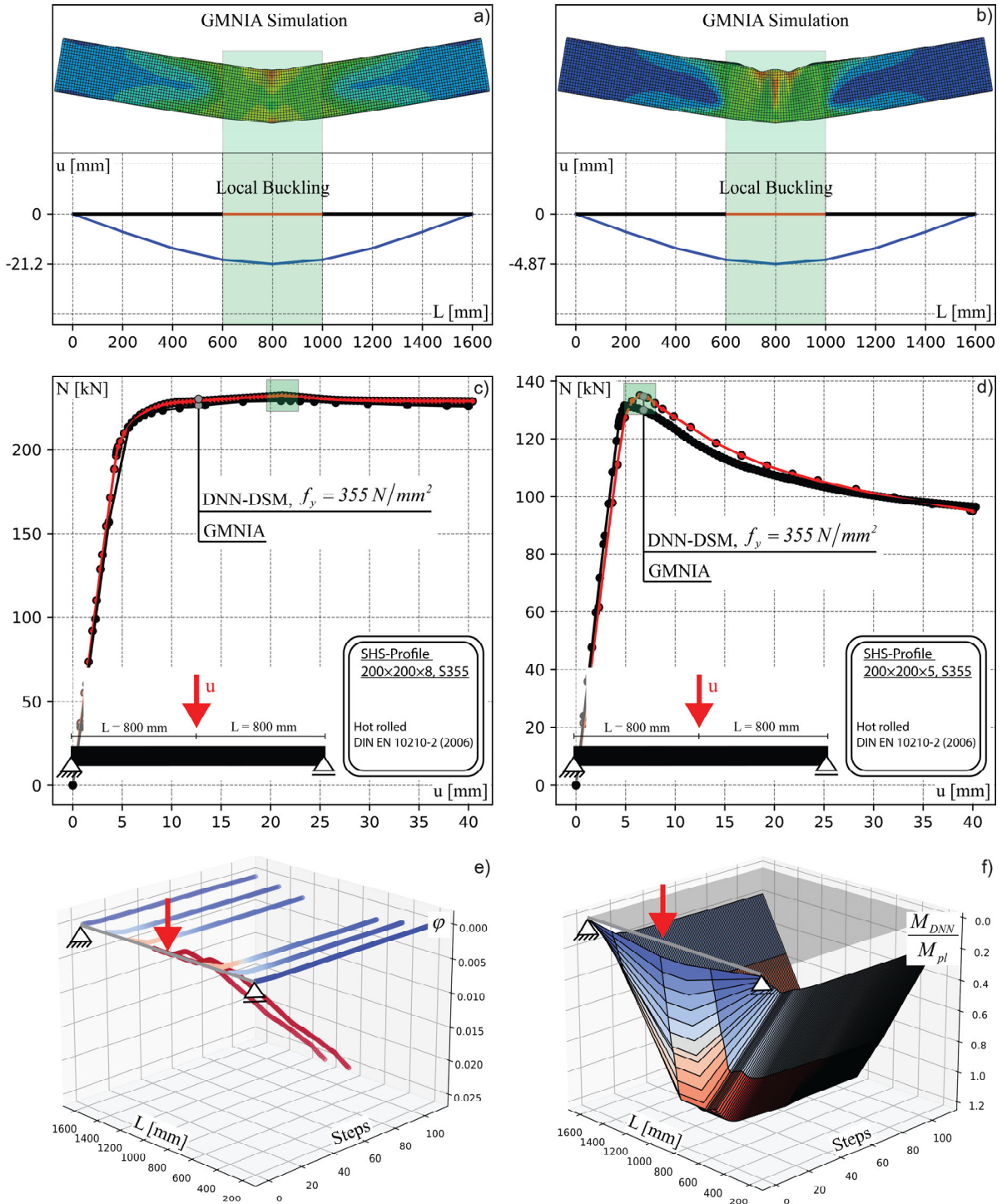


Figure 8-22: Comparison of load-deformation results between shell FE and DNN-DSM predictions for three point bending for a hot-rolled SHS200×8 and an SHS200×5 profile made from S355; a), b) deformed members at peak load (scaled); c), d) comparison of load-deformation curves; e) 3D representation of local element rotations; f) 3D representation of global moments corresponding to the calculated step and plotted along the member length

System deformations were introduced through reference points, which were coupled to several individual nodes on the upper flange of the cross-section. This procedure was chosen according to investigations in [28], to simulate a more realistic load introduction

and prevent failure to local crushing. Note that deformations were introduced in order to be able to calculate the post-buckling range. Member length was chosen to fit with the local beam element lengths, which are bound to the longer cross-section dimension. Two simulations were done for each model, first an LBA to estimate imperfection shapes, second a fully non-linear GMNIA with local imperfections and a non-linear material behaviour with strain hardening. The material model corresponds exactly to the one used for the GMNIA calculation results used for DNN model training.

Results for three-point bending are presented in Figure 8-22 for two profiles, SHS200x8 and SHS200x5, hot-rolled with the steel grade S355. Figure 8-22 a) and b) show output deformations from Abaqus and the DNN-DSM predictions. Both Abaqus models form a local buckle around the load introduction area. The DNN-DSM replication uses only 8 elements, at each node 2 dofs (vertical displacement and rotation), leading to a total of 18 dofs for the whole system. Note that the Abaqus model uses 77298 dofs, in order to calculate the non-linear load-deformation curves from Figure 8-22 c) and d). A very close result can be recalculated with the DNN-DSM approach. The elements around load introduction reach their maximum cross-section dependent capacity and go into post-buckling, which leads to the overall drop of the loads. Deviations of maximum forces are below 3% for this particular case. Corresponding deformations deviate stronger from each other. In the case of the SHS200x5 profile the DNN-DSM approach lies 30% above the GMNIA shell FE results. This might be drawn back on effects not included in the DNN-DSM, like local crushing in the load introduction area or a slightly smaller local hinge area that could affect the overall behaviour. Figure 8-22 e) shows in a 3D plot the local rotations for each beam element along the member length and the corresponding calculated step. The two middle elements, which are loaded to most, develop directly from the beginning the highest local rotations. Figure 8-22 f) shows the corresponding moment diagram according to the calculated steps.

The overall system behaviour was replicated successfully with the DNN-DSM, predicting the pre- and post-buckling range in less computational time compared to the Abaqus simulations. The DNN-DSM algorithm was finished after approximately 150 sec, the Abaqus calculation after around 240 sec, for the case of three point bending. This time

includes only the actual calculation. Taking into account the modelling effort would lead to significantly bigger differences.

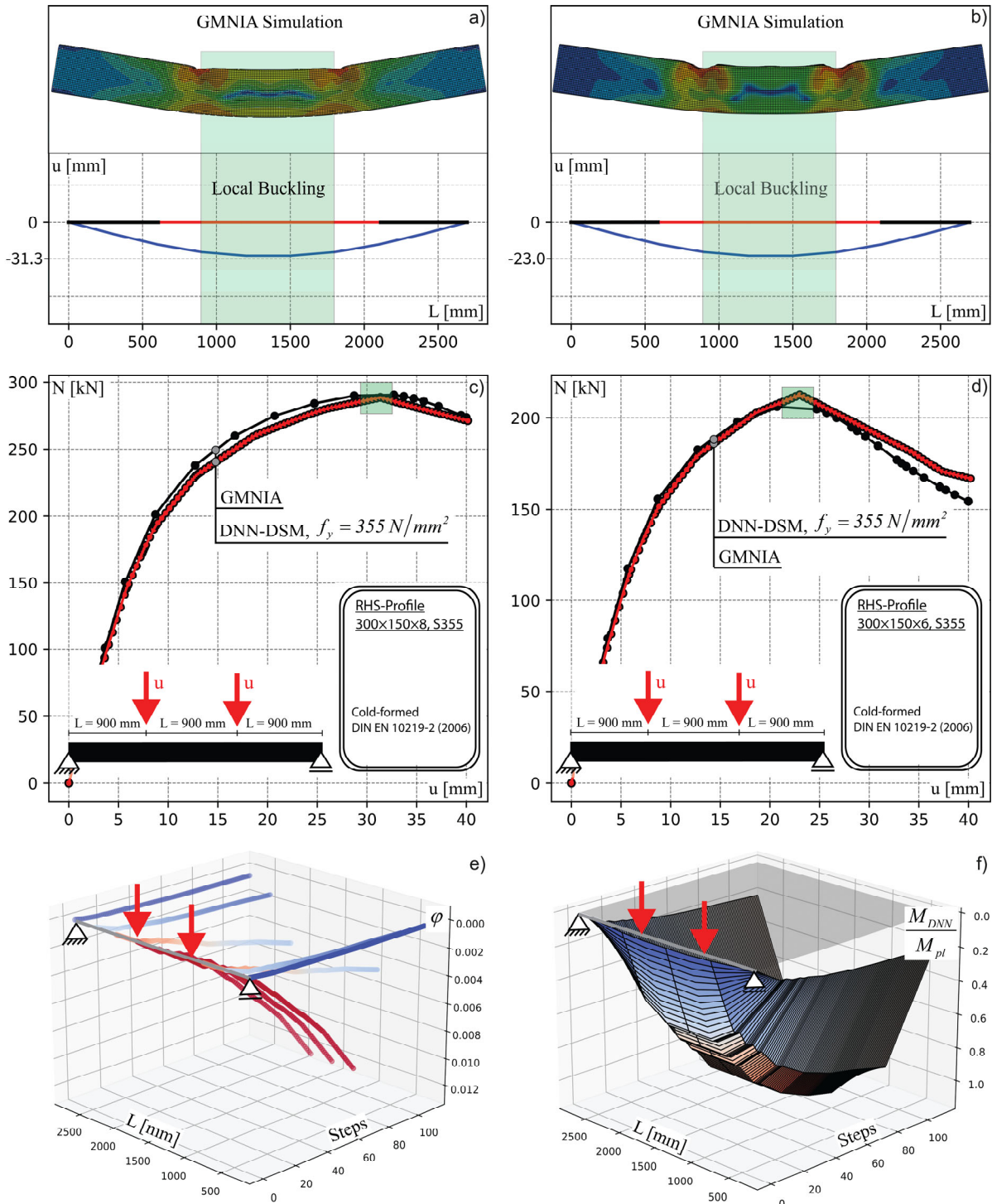


Figure 8-23: Comparison of load-deformation results between shell FE and DNN-DSM predictions for four point bending for a cold-formed RHS300×150×8 and an RHS300×150×6 profile made from S355; a), b) deformed members at peak load (scaled); c), d) comparison of load-deformation curves; e) 3D representation of local element rotations; f) 3D representation of global moments corresponding to the calculated step and plotted along the member length

Figure 8-23 shows the results of four point bending simulations in the same manner as for the three point bending comparison. GMNIA deformation plots are displayed against DNN-DSM deformations for two cold-formed profiles, RHS300x150x8 and RHS300x150x6 and the steel grade S355. The DNN-DSM replication uses 9 beam elements with a total of 18 dofs. The Abaqus model on the other hand contains 146358 dofs. In contrary to three point bending, where mostly the beam elements around the load introduction area were strongly deformed while reaching post-buckling, all element in between load introduction are affected by plastic deformation and reaching post-buckling in the four-point bending simulation. Figure 8-23 c) and d) shows the comparison between the load-deformation paths from GMNIA shell FE simulations and DNN-DSM predictions. Again, a high accuracy is reached for the maximum capacity, as well as corresponding deformation. However, Figure 8-23 d) shows a slightly bigger difference of the reached loads, where the deviations lie between 4% to 5%. This is caused through the effect of a concentrated load introduction in the GMNIA analysis, as local buckling directly at the point of load application cannot be completely excluded for slender profiles. This effect cannot be captured with the DNN-DSM approach, leading to higher calculated capacities. Nevertheless, a good agreement between GMNIA and DNN-DSM prediction is given. The total runtime could be halved with own recalculations compared to the Abaqus simulations.

8.4 Validation against Experimental Results

8.4.1 Stub column tests

In the following subsections the DNN-DSM approach is compared with experimental results and GMNIA simulations from literature. Comparisons of stub column test are based on investigations by Gardner et al. [195] and Toffolon [2]. These are presented separately in the following Section 8.4.1.1 and 8.4.1.2, designated as test series 1 and 2.

The corresponding DNN-DSM model assumptions are shown in Figure 8-24. The specimen lengths in the test by Gardner et al. [195] are always four times the bigger cross-section dimension (height or width). Thus, the DNN-DSM models could be built up from four beam elements of the chosen length and always matched the specimen length from

the tests, see Figure 8-24 a). On the other hand, specimens in the test series evaluated by Toffolon [2] has always the fixed length of 800 mm . Therefore, it is not always possible to match exactly the experimental lengths by the chosen length of DNN-DSM elements. In the chosen DNN-DSM implementation, a specimen with the cross-section dimensions of 200×200 has a local beam element length of 200 mm . Four of those elements would thus exactly match the specimen length of 800 mm . However, a specimen with the cross-section dimensions of 300×150 has a beam element length of 300 mm . Three elements lead to a member length of 900 mm , which slightly exceed the actual specimen length of 800 mm . For the purposes of the validation to be carried out here, this length difference was ignored, as the buckling deformations were considered to be located only within one buckling half sine wave length.

Table 8-4: Considered profiles and properties from [2], [195]

	Profile	Test Set-Up	$f_{y,nom} [N/mm^2]$	$f_{y,exp} [N/mm^2]$
TEST SERIES 1 Gardner et al. [195]	S355; SHS 40×40×4-HR	Stub Column (SC)	355	496
	S235; SHS 40×40×4-CF	SC	235	410
	S355; SHS 40×40×3-HR	SC	355	504
	S235; SHS 40×40×3-CF	SC	235	451
	S355; RHS 60×40×4-HR	SC	355	468
	S235; RHS 60×40×4-CF	SC	235	400
	S355; SHS 60×60×3-HR	SC	355	449
	S235; SHS 60×60×3-CF	SC	235	361
	S355; SHS 100×100×4-HR	SC	355	488
	S235; SHS 100×100×4-CF	SC	235	482
TEST SERIES 2 Toffolon [2]	S355; SHS 140×140×4-CF	SC	355	430
	S355; SHS 200×200×5-CF	SC	355	401
	S355; SHS 200×200×8-CF	SC	355	475
	S500; SHS 200×200×4-CF	SC	500	563
	S500; SHS 200×200×5-CF	SC	500	557
	S355; RHS 300×150×6-CF	SC	355	429
	S355; RHS 300×150×8-CF	SC	355	451

In physical tests of stub columns, it is typical to observe a concentration of buckling deformations in a part of the element the length of which roughly matches the length of a

single buckling half-wave. In order to lead to such a concentration local buckling exclusively in one DNN-DSM beam element, one such element along the modelled member was considered to have a higher initial imperfection amplitude than the rest of the beam elements. For the comparisons in this chapter, the failing element was modelled with an imperfection amplitude of $B/200$. The remaining beam elements were given the input of an imperfection amplitude of $B/400$. B was chosen according to Equation (2-10).

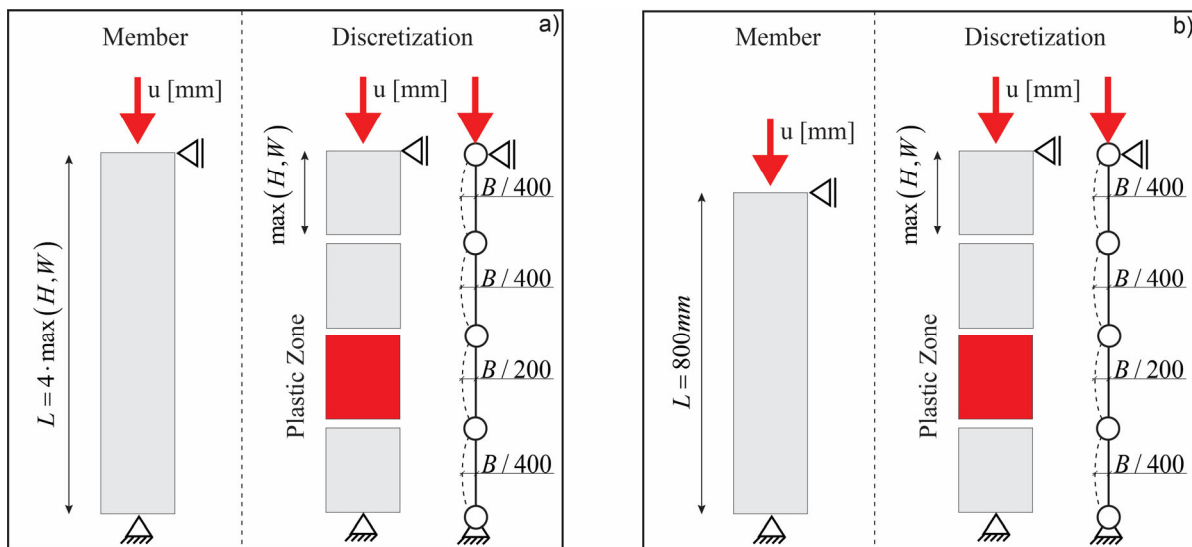


Figure 8-24: DNN-DSM model discretization, a) model assumptions for comparisons in Section 8.4.1.1 (test series 1); b) model assumptions for comparisons in Section 8.4.1.2 (test series 2)

8.4.1.1 Test series 1

As a first test series for validation, stub column test results by Gardner et al. [195] were first compared against DNN-DSM predictions with the models trained on GMNIA specimens. The global length of the DNN-DSM model was covered by four beam elements. This exactly corresponds to the specimen length from the tests. As stated above, it was assumed that local buckling is introduced only in one element along the length of the model. Figure 8-25 shows a comparison between the load-deformation curves from the tests and own DNN-DSM based recalculations for four selected specimens. The dashed and the continuous line both represent test results, as each test was repeated twice with specimens created from the same hollow section. The red dotted lines show the results of the DNN-DSM calculations. In all cases, two yield strength values were accounted for, i.e., the nominal value $f_{y,nom}$ and the experimentally derived yield strength $f_{y,exp}$. The x-

axis represents the displacement u in the longitudinal direction, normalized by the measured total member length L_{exp} . In order to exclude global effects throughout the tests, L_{exp} was chosen to be 4 times the bigger value of the cross-section height or width. The y-axis describes the reached normal forces, normalized by the plastic normal force N_{pl} , calculated with the yield strength σ_y from tensile coupon test. This comparison allows one to follow up on the analyses from Section 8.2.3 and assess prediction outside the data space.

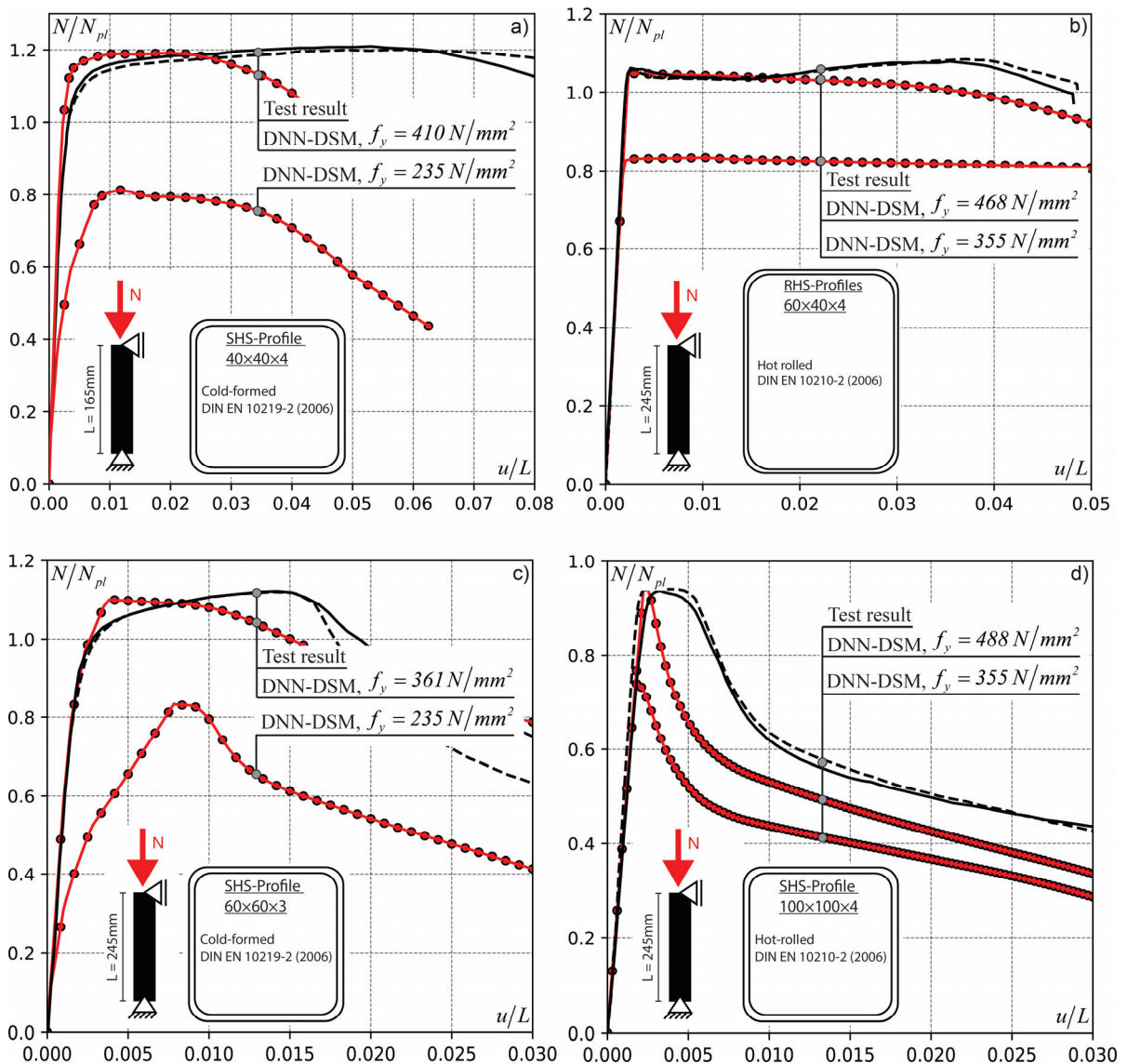


Figure 8-25: Comparison between stub column test results by Gardner et al. [163] and DNN-DSM recalculations

Table 8-5 shows the summarized results of all 10 stub column test for test series 1. In order to exclude gross outliers in the experimental campaign, two analyses were performed on specimens of the same type, i.e., same geometry and material properties. However, this is not further considered, since the estimated deviations are too small to make a difference in the comparisons made here.

Table 8-5: Considered profiles and properties from [195]

Profile	$f_{y,nom} [N/mm^2]$	$\frac{F_{max,DNN-DSM}}{F_{max,exp}}$	$\frac{u_{max,DNN-DSM}}{u_{max,exp}}$
	$f_{y,exp} [N/mm^2]$		
S355; SHS 40×40×4-HR	355	0.72	0.64
	496	0.94	0.03
S235; SHS 40×40×4-CF	235	0.74	0.17
	410	1.05	0.08
S355; SHS 40×40×3-HR	355	0.70	0.03
	504	0.81	0.05
S235; SHS 40×40×3-CF	235	0.61	0.21
	451	0.93	0.11
S355; RHS 60×40×4-HR	355	0.82	0.30
	468	0.96	0.07
S235; RHS 60×40×4-CF	235	0.64	1.13
	400	0.97	0.14
S355; SHS 60×60×3-HR	355	0.71	0.10
	449	0.95	0.12
S235; SHS 60×60×3-CF	235	0.79	0.55
	361	1.04	0.27
S355; SHS 100×100×4-HR	335	0.71	0.56
	488	0.99	0.69
S235; SHS 100×100×4-CF	235	0.61	1.24
	482	1.04	0.44

Predictions made by using the nominal yield strength $f_{y,nom}$ lead in all cases to conservative results: as expected and must be the case, the load-deformation curves are far below the test results when the nominal yield stress is considered and the measured one far exceeds the nominal value. This is not surprising, since the experimentally estimated material properties from tensile coupon tests in [195] are significantly higher compared

to the nominal values, which were used to train the DNN models. Thus, adapting the experimental yield strength values in the prediction process leads to results closer to the tests, with a maximum deviation of the maximum forces of around 7% (see Table 8-5).

Regarding the general shape of the load-displacement curve, it can be observed that the DNN-DSM prediction and the experimental curves are generally satisfactorily close in the elastic and non-linear range up to the first peak when the experimental value of the yield strength is considered, while in the post-buckling range the match is far less satisfactory. This can be attributed to a variety of factors, among which is the great importance of the exact distribution of imperfections in the physical specimen for the post-buckling behaviour.

The behaviour of DNN-DSM recalculations is less ductile with maximum loads reached earlier. However, the course in the pre-buckling range is very similar to the one obtained experimentally. The comparison of the course in the post-buckling range is less accurate and strongly linked to the actually-present imperfections. This effect was investigated and discussed in [285] by the author. Good matches with the real load-displacement behaviour as observed in physical tests, particularly in the post-buckling range, are therefore very hard to capture and would require a better knowledge of the real geometry of the specimens, a detailed material model and an accurate representation of geometrical imperfections. Nevertheless, in some cases, see Figure 8-25 b) and d), the pre- and post-buckling curves can be simulated well along the whole deformation. This is mostly attributed to two effects, (i) strain hardening is not reached and the behaviour in the pre-buckling range is more elastic, plastic redistributions are not present; (ii) local buckling has formed in only one concentrated region.

8.4.1.2 Test series 2

This section presents some of the experimental results from the Hollosstab project and compares them to DNN-DSM predictions, which were carried out as described in the previous sections. The project Hollosstab itself was presented in the course of the finite element assumptions in Sections 5.1 and 5.2. The comparisons made here build up on

the experimental investigations and evaluations by Toffolon [2]. In the project, stub column and short member tests were performed, the latter with different eccentricities. A summary of all test and parameters is presented in Table 5-1, Table 5-2 and Table 5-3. In the following, only the T1 test (pure compression, i.e. stub columns) are used for comparison purposes. All specimens have a total length of 800 mm , disregarding the cross-section dimensions. This allowed the investigation of local buckling only, without global effects. In the DNN-DSM models, which in this section make use of elements of fixed length, it was attempted to approximate length of 800 mm . Some DNN-DSM model lengths were in some cases slightly longer than the 800 mm of the tests. Assumptions from Section 8.3.1 were used to cause local buckling in only one beam element of the whole model.

Table 8-6: Considered profiles and properties from [2] – stub column test series 2

Profile	$f_{y,nom} \left[\frac{N}{mm^2} \right]$	$\frac{F_{max,DNN-DSM}}{F_{max,exp}}$	$\frac{F_{max,DNN-DSM}}{F_{max,GMNIA}}$	$\frac{u_{max,DNN-DSM}}{u_{max,exp}}$	$\frac{u_{max,DNN-DSM}}{u_{max,GMNIA}}$
	$f_{y,exp} \left[\frac{N}{mm^2} \right]$				
S355; SHS	355	0.76	0.72	0.60	0.55
140×140×4-CF	430	0.88	0.83	0.62	0.57
S355; SHS	355	0.81	0.76	0.57	0.58
200×200×5-CF	401	1.00	0.94	0.75	0.76
S355; SHS	355	0.73	0.70	0.44	0.45
200×200×8-CF	475	0.93	0.90	0.45	0.46
S500; SHS	500	0.80	0.77	0.67	0.95
200×200×4-CF	563	0.85	0.82	0.65	0.93
S500; SHS	500	0.73	0.71	0.55	0.77
200×200×5-CF	557	0.79	0.77	0.55	0.77
S355; RHS	355	0.92	0.89	0.68	1.27
300×150×6-CF	429	1.03	0.99	0.67	1.24
S355; RHS	355	0.72	0.72	0.71	0.77
300×150×8-CF	451	0.87	0.87	0.78	0.85

Figure 8-26 shows the load-deformation curves of some selected profiles. In this case, for test series 2, the black solid lines represent the physical test results. Finite element shell based GMNIA simulations, using the 3D-scanned specimen geometry and the measured material stress-strain relationship (from coupon tests) are represented by the black dashed lines. The procedure to derive these GMNIA models within Hollosstab was

described in Section 5.1.2 and involves 3D full scale surface scans and reverse engineering procedures to derive finite element models. Both lines thus indicate the state on which the validation of FEM-models in the Hollosstab project is based on and was carried out. It is therefore suitable for the present comparisons with the DNN-DSM predictions, since the results of not self-performed GMNIA calculations are available and not subjected to a self-produced bias. The two red dotted lines in each diagram represent the DNN-DSM recalculations for two different yield strength values, i.e., the nominal $f_{y,nom}$ and experimentally $f_{y,exp}$ derived values.

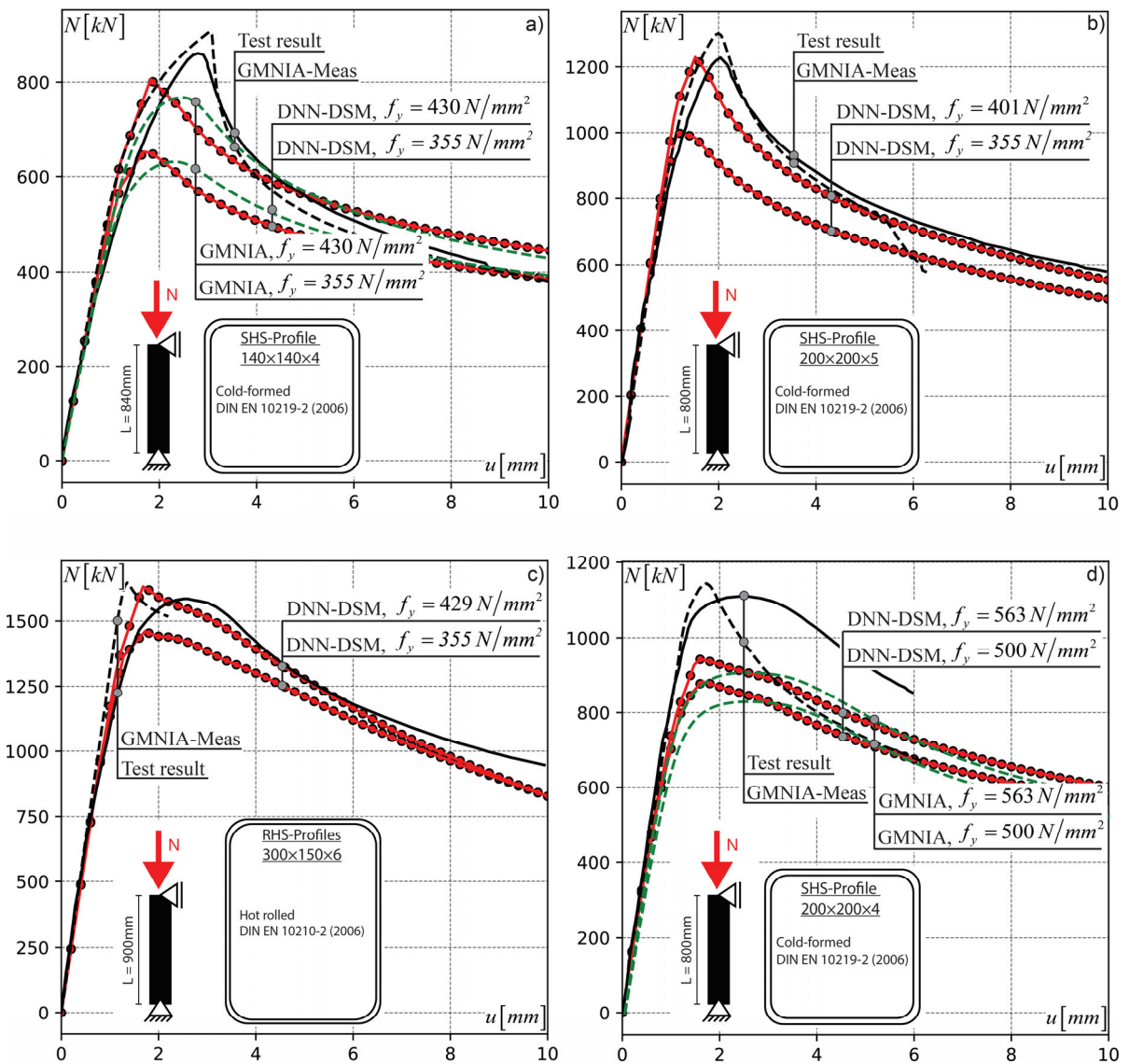


Figure 8-26: Comparison between stub column test results by [2] and DNN-DSM recalculations for test series 2 (from Hollosstab project)

Compared to the results of stub column test form Section 8.4.1.1, the presented comparison in Figure 8-26 shows a better correlation with the load-deformation curves from tests in two of the four shown cases, see sub-figures b) and c). The comparison for these two cases shows that the behaviour in the pre- and post-buckling range is matched well, albeit differences remain in the reached maximum loads and corresponding deformations. Again, as must be the case, deviations between the maximum reached load bearing capacities become smaller when using the yield strength $f_{y,exp}$ from tensile coupon tests. The comparison between DNN-DSM calculations and GMNIA simulations (black dashed line) show a somewhat closer resemblance: like the DNN-DSM predictions, the GMNIA simulation results show a slightly stiffer behaviour in the pre-buckling range and feature a steeper stiffness deterioration in the post-buckling range.

Regarding the sub-figures a) and d), it can be observed that the peak load is relatively strongly underestimated for both the 140x4 and 200x4 SHS section. In order to better understand this deviation, for these particular cases a second type of GMNIA calculation was performed, this type introducing imperfection shapes derived from LBA calculations and with amplitudes of $B/200$, as is assumed for the DNN-DSM models. The corresponding results are plotted with dashed green lines (for the nominal and measured yield stress). As can be seen in the figures, these additional GMNIA calculations match the peak load of the DNN-DSM curves much more closely, while the deformations at this peak load are larger. The latter effect can be attributed to the fact that multiple buckling half-waves were assumed to have the same imperfection amplitude of $B/200$ in these additional GMNIA calculations, thus leading to a “softer” behaviour as the ULS load is approached. In summary, it can thus be stated that even the cases with larger differences in peak loads between DNN-DSM vs. physical and numerical test (with measured imperfections) is explicable: it can be assumed that the physical specimens in this case had far smaller and less inconvenient imperfection amplitudes than what would be assumed by introducing an LBA-based shape with amplitude $B/200$. Again, the results highlight the significance of imperfection amplitudes in capturing the local buckling behaviour of stub column tests. They additional confirm the viability of the DNN-DSM method.

A summarized representation of the maximum forces and corresponding deformations for the entire test series is given in Table 8-6, thus showing the comparison of test results

and GMNIA simulations against DNN-DSM calculations. Again, the nominal yield strength $f_{y,nom}$ and the experimentally derived yield strength $f_{y,exp}$ were taken into account. Deviations of the maximum forces between tests and DNN-DSM calculations go up to 28% when using the nominal yield strength and 21% when using the experimental value for the yield strength. On average these are 22% and 9%, respectively. Thus, overall, the DNN-DSM results based on data from GMNIA models and simulations with imperfection amplitudes and shapes based on LBA buckling shapes can be stated to be always conservative for the results of this test series, based on their current training. A comparison with GMNIA results leads to slightly higher deviations, since the GMNIA values were slightly higher than the test results in all cases.

8.4.2 Bending tests

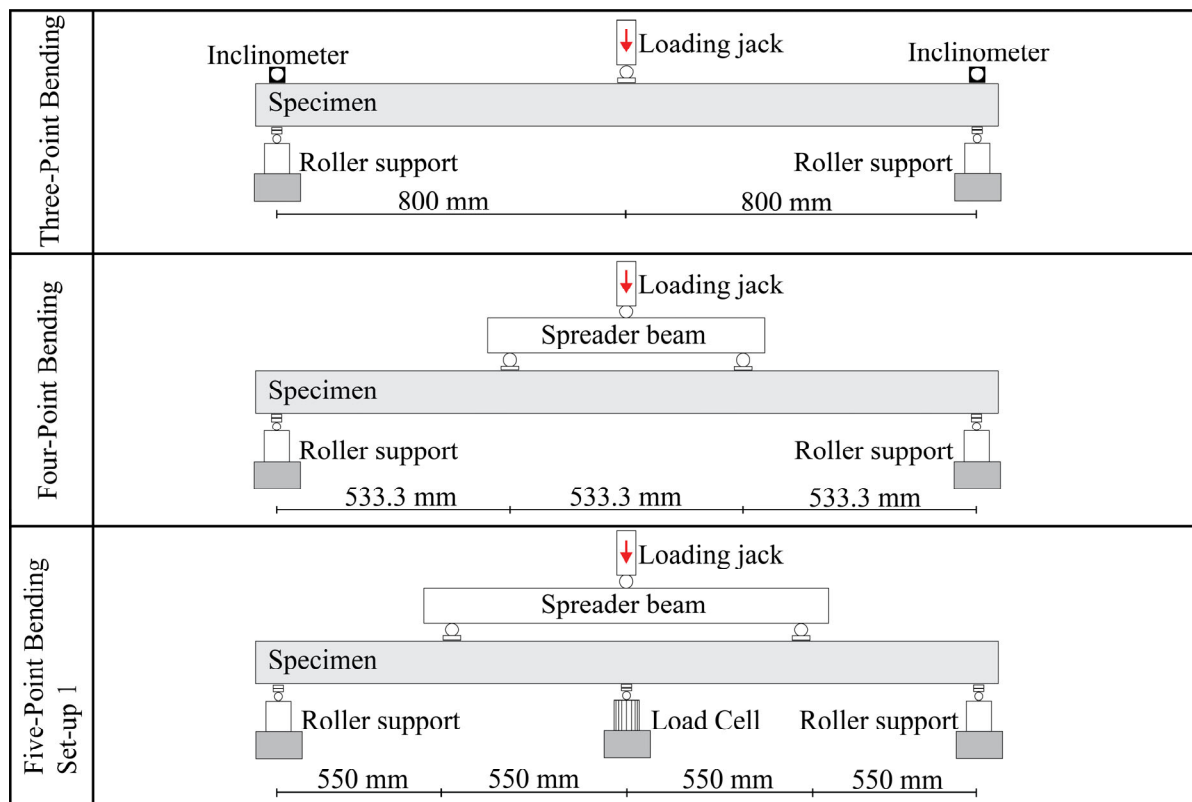


Figure 8-27: Schematic representation of bending test set-ups, adopted from [163]

The validation of the DNN-DSM approach against experimental results from three-point, four-point, and five-point bending tests is presented in Sections 8.4.2.1, 8.4.2.2 and 8.4.2.3, respectively. All test results are based on publications by Gardner et al. and Wang

et al. [163], [195]. For detailed information on the test setup, material properties, and geometric measurements, the reader is referred to these references. A general test set-up for all considered bending tests is provided by Figure 8-27. Furthermore, Table 8-7 shows a summary of results for all considered cases. The cross-sections are labeled according to their nominal steel grade, geometry, and fabrication (HR = hot-rolled; CF = cold-formed). The abbreviations for the test setup correspond to the three-point (3PB), four-point (4PB) and five-point (5PB-1) bending tests performed, which are summarized in the following diagram (see Figure 8-27). Note that the experimental test series from [195] includes two five-point bending test set-ups, with a varying load introduction distribution. However, within the performed investigations only test set-up 1 was used.

Table 8-7: Considered profiles and properties from [163], [195]

	Profile	Test Set-Up	$f_{y,nom} [N/mm^2]$	$f_{y,exp} [N/mm^2]$
Gardner et al. [195]	S355; SHS 40×40×3-HR	3PB; 5PB-1	355	504
	S235; SHS 40×40×3-CF	3PB; 5PB-1	235	451
	S355; SHS 40×40×4-HR	3PB; 5PB-1	355	496
	S235; SHS 40×40×4-CF	3PB; 5PB-1	235	410
	S355; RHS 60×40×4-HR	3PB; 5PB-1	355	468
	S235; RHS 60×40×4-CF	3PB; 5PB-1	235	400
Wang et al. [163]	S460; SHS 50×50×4-HR	3PB; 4PB	460	523
	S460; SHS 50×50×5-HR	3PB; 4PB	460	505
	S460; SHS 90×90×3.6-HR	3PB; 4PB	460	500
	S460; SHS 100×100×5-HR	3PB; 4PB	460	511
	S460; RHS 100×50×4.5-HR	3PB; 4PB	460	498
	S460; RHS 100×50×6.3-HR	3PB; 4PB	460	498
	S690; RHS 50×50×5-HR	3PB; 4PB	690	759
	S690; RHS 90×90×5.6-HR	3PB; 4PB	690	774
	S690; RHS 100×100×5.6-HR	3PB; 4PB	690	782
	S690; RHS 100×50×5.6-HR	3PB; 4PB	690	777
	S690; RHS 100×50×6.3-HR	3PB; 4PB	690	799

Own investigations required a slight adjustment within the actual beam lengths, depending on the used profile. As described in Section 8.4.1, the local beam element lengths correspond to the larger cross-section dimension of the profile height or width, see also

Figure 8-24 b). Adjustments can be made by introducing short, elastic elements in regions of low stress, or by ignoring minor total length differences.

8.4.2.1 Three point bending

The results and recalculations of the three-point bending tests are presented in the following. Firstly, a comparison between experimental results from [163], [195] and DNN-DSM models is carried out. Secondly, a comparison between validated FE-shell models and experimental results, both from [163], against own DNN-DSM prediction is performed.

Figure 8-28 shows the results of the comparison between experimental results (black line) and DNN-DSM recalculations (red dashed line). The x-axis represents the normalized rotation θ/θ_{pl} , where θ is the theoretical mid-span “rotation” or slope change, defined as the sum of the two end rotations from the installed inclinometers in the experimental campaign in [163]. In own recalculations, the rotation at the supports was extracted for every calculated step and summed up. θ_{pl} is the sum of the plastic rotation at the supports, back calculated from the theoretical value for M_{pl} (according to elastic theory) at the mid-span. However, for the normalized representation along the x- and y-axis in Wang et al. [163], θ_{pl} was calculated from the measured geometry and material properties from tensile tests, and for the determined values of the plastic moment M_{pl} . Thus, these values were adopted directly from [163] and [195] for the comparisons made in Figure 8-28 and Figure 8-29. For each DNN-DSM prediction two yield stress values are used, i.e. the nominal yield stress $f_{y,nom}$ and the experimentally derived yield stress $f_{y,exp}$ from corresponding tensile coupon test. The main purpose is to investigate whether the trained DNN models are able to interpret yield stress values for which they were not trained, since the yield stress is one main feature of the DNN input parameters.

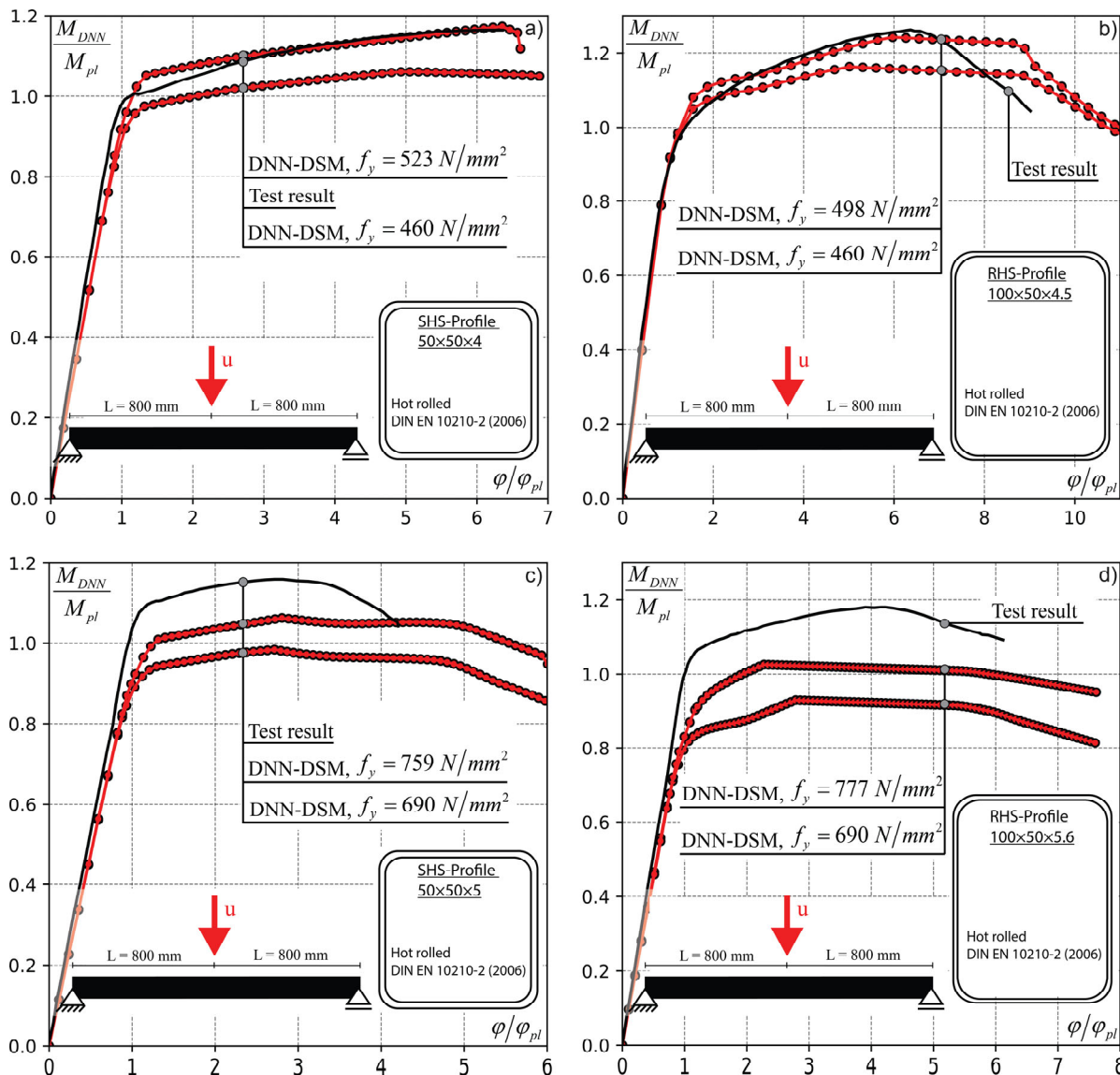


Figure 8-28: Comparison between test results from three-point bending by Wang et al. [163] and DNN-DSM recalculations for RHS/SHS profiles made from steel grade S460 a), b) and S690 c), d)

Each prediction is represented in one of the diagrams of Figure 8-28. In most cases, the experimentally derived yield stress $f_{y,exp}$, within the input features of the DNN model, leads to close prediction of the maximum moment capacity, whereby the nominal yield stress $f_{y,nom}$ to results far on the safe side. The moment-rotation curves from the DNN-DSM recalculations have a reasonable shape and largely resemble the test results. Especially the stiffness in the elastic range and the shape of the curve in the non-linear of the pre-buckling phase match - in individual cases - very close the experimental results (Figure 8-28 a) and b)). The curves in the post-buckling area are reasonable, but cannot be fully verified with the tests, since the required data is often missing due to an

early test termination. However, it is not always possible to match the experimental result. Figure 8-28 c) and d) shows relatively poor results in comparison, with deviations of around 20% in force. This can have in general many possible origins, such as effects from the test set-up, the actual non-linear material behaviour which is not part of the predictions or the local imperfection amplitudes, which in reality deviate from theoretical eigenshapes. These effects were not further investigated but are part of ongoing evaluations.

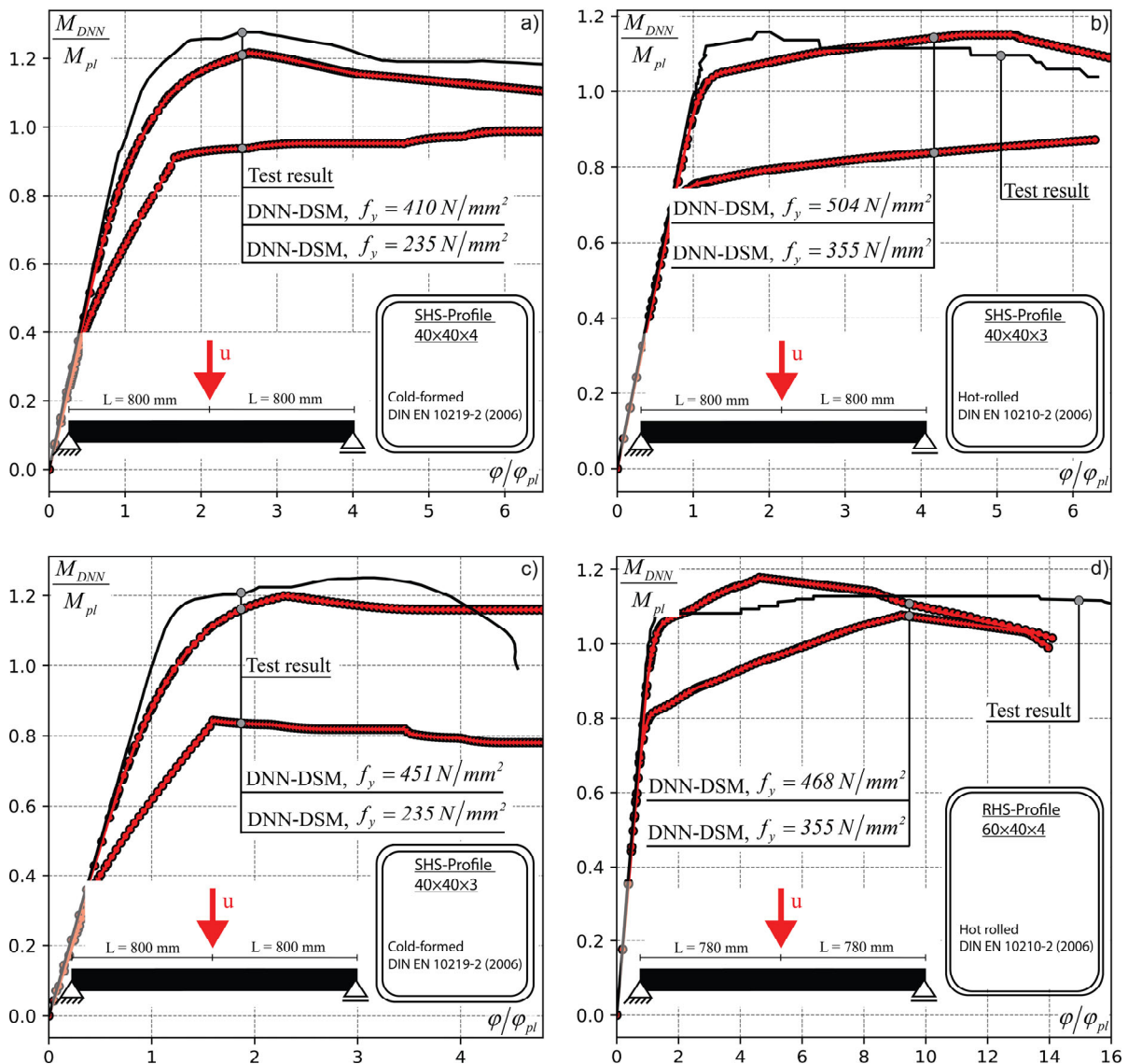


Figure 8-29: Comparison between test results from three-point bending by Gardner et al. [195] and DNN-DSM recalculations for steel grade S460 a), b) and S690 c), d)

The same type of comparisons were made for the three-point bending experimental results collected from Gardner et al. [195], which comprised both hot-rolled and cold-

formed RHS/SHS profiles, summarized in Table 8-8 and exemplary shown in Figure 8-29. Following the same logical interpretation as before, similar conclusions can be drawn. Own recalculations with nominal yield strength values $f_{y,nom}$ are more conservative compared to experimentally derived properties for the yield strength $f_{y,exp}$. The shapes of the moment-rotation curves are always comparable and in some cases very close to the experimentally derived curves, as shown for Figure 8-29 a) or b).

Table 8-8: Comparison of the results from three-point bending tests by [163], [195] and DNN-DSM

Profile	$f_{y,nom} \left[\frac{N}{mm^2} \right]$	$\frac{M_{\max,DNN-DSM}}{M_{\max,exp}}$	$\frac{\theta_{\max,DNN-DSM}}{\theta_{\max,exp}}$
	$f_{y,exp} \left[\frac{N}{mm^2} \right]$		
S355; SHS 40×40×4-HR	355	0.86	1.98
	496	0.99	0.79
S235; SHS 40×40×4-CF	235	0.70	1.12
	410	1.01	2.87
S355; SHS 40×40×3-HR	355	0.81	3.41
	504	0.99	2.80
S235; SHS 40×40×3-CF	235	0.65	0.90
	451	0.96	1.25
S355; RHS 60×40×4-HR	355	0.97	1.85
	468	1.06	1.45
S235; RHS 60×40×4-CF	235	0.60	0.31
	400	0.87	-
S460; SHS 50×50×4-HR	460	0.91	0.78
	523	1.00	1.00
S460; SHS 100×100×5-HR	460	0.78	0.31
	505	0.87	0.35
S460; SHS 90×90×3.6-HR	460	0.95	0.81
	500	1.05	0.86
S460; SHS 100×50×4.5-HR	460	0.79	0.89
	498	0.97	1.05
S690; SHS 50×50×5-HR	690	0.85	1.25
	759	0.92	1.30
S690; SHS 100×100×5.6-HR	690	0.74	0.77
	782	0.87	0.83
S690; SHS 100×50×5.6-HR	690	0.79	0.66
	777	0.87	0.55

Further, the maximum loads and corresponding rotations are compared with the experimentally derived data. This comparisons are summarized in Table 8-8. Two discrete values along each moment rotation curve, the maximum moment and the corresponding rotation, are compared with each other.

Deviations of the maximum forces between tests and DNN-DSM calculations lie between 5% and 40%, when using the nominal yield strength. This deviations decreases when using the experimental value for the yield strength and lie between 1% and 13%, with only minimal deviations on the unconservative side even for the latter type of material model. A comparison of the corresponding rotations is subjected to a potentially greater scatter than the reached forces. The reached force is mainly influenced by the material model, the imperfection amplitude and the boundary conditions, assuming that the idealized model geometry is close enough to the real geometry. On the other hand, the rotations are much more influenced by additional factors, such as the buckling length, the imperfections shape and amplitude as well as the onset of material yielding. This effects were partially investigated throughout the numerical calibration process by Wilkinson in [27] and own simulations in in [285].

Table 8-9: Comparison of the results from GMNIA simulations by Wang et al. [163] and DNN-DSM predictions

Profile	$f_{y,nom} \left[N/mm^2 \right]$	$\frac{M_{max,DNN-DSM}}{M_{max,GMNIA}}$	$\frac{\theta_{max,DNN-DSM}}{\theta_{max,GMNIA}}$
	$f_{y,exp} \left[N/mm^2 \right]$		
S460; SHS 50×50×5-HR	460	0.90	1.13
	505	0.99	1.19
S460; SHS 100×50×6.3-HR	460	0.97	0.77
	498	1.02	0.85
S690; SHS 90×90×5.6-HR	690	0.95	0.94
	774	1.08	1.52
S690; SHS 100×50×6.3-HR	690	0.96	0.94
	799	1.09	0.81

In the next step, the results from tests and corresponding GMNIA simulations by Wang et al. [163] were compared against DNN-DSM predictions. The comparison shows that the results from DNN-DSM agree well with the GMNIA results. In particular, the stiffness

in the region prior to buckling is well satisfied, as is the load-carrying capacity in all profiles considered. The maximum moment obtained is always slightly lower when using the nominal yield strength $f_{y,nom}$. On the other hand, using the yield strength derived from experiments $f_{y,exp}$ leads overall to uncertain results. The corresponding rotations are safe in most cases for the nominal yield strength. The post-buckling behaviour is too pronounced compared to the GMNIA results, where the curves have a stronger drop after reaching the maximum moments. Table 8-9 shows additionally the comparison of reached maximum loads for both simulations, GMNIA and DNN-DSM, and corresponding rotations.

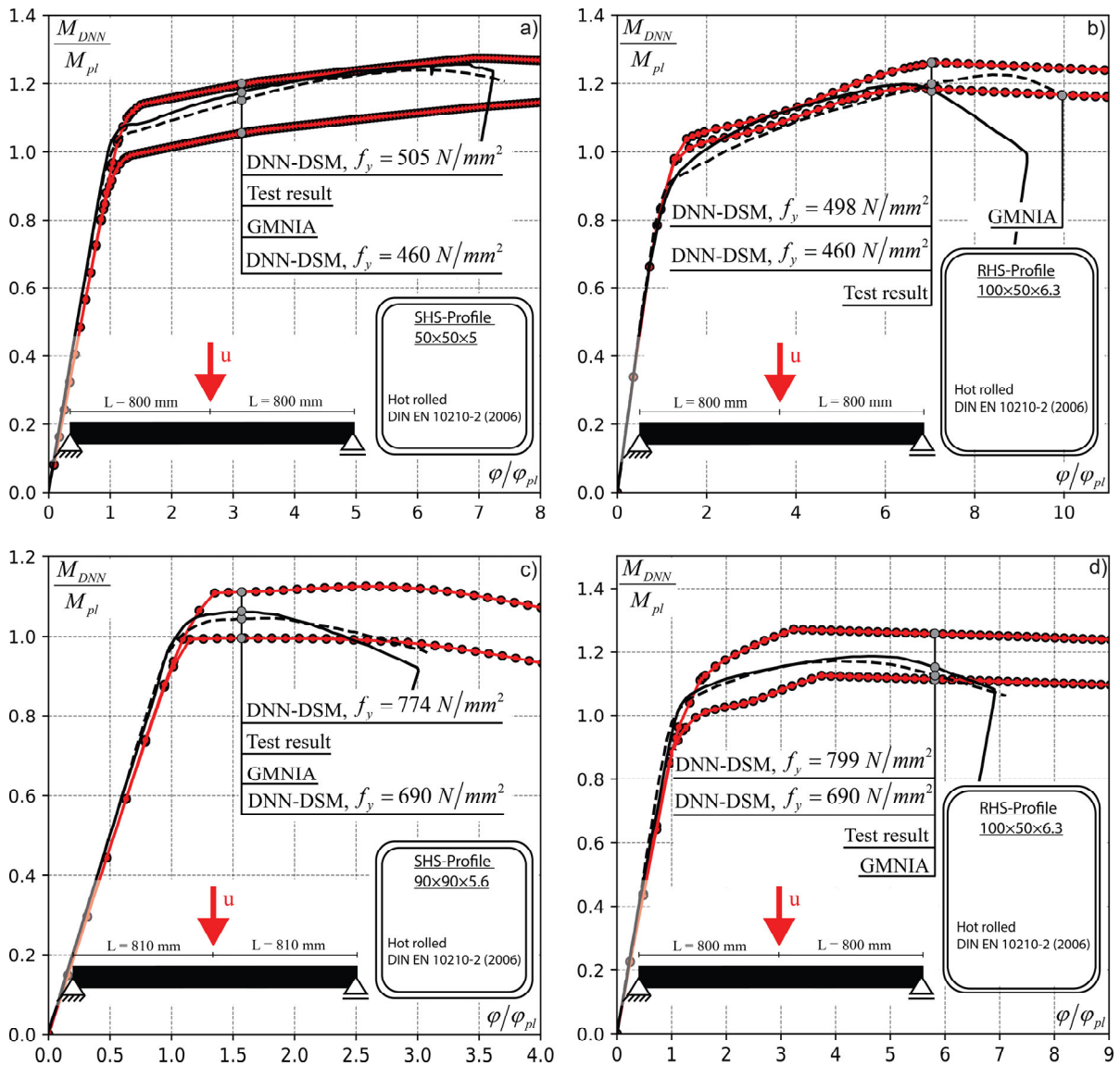


Figure 8-30: Comparison between test results from three-point bending and FE GMNIA simulations by [163] and DNN-DSM recalculations for steel grade S460 a), b) and S690 c), d)

8.4.2.2 Four point bending

The comparisons between experimental test results and DNN-DSM based recalculations for the considered four-point bending tests are presented in Figure 8-31 and Figure 8-32 for the steel grade S460 and S690, respectively.

The pure comparison between experimental results and DNN-DSM recalculations shows a good agreement. In all cases considered (Figure 8-31, Figure 8-32), the rising branch in the elastic region is matched without significant deviations. With the onset of plasticity and thus a significantly more non-linear behaviour, deviations occur, but within acceptable limits. The recalculations are mostly more conservative than the experimental results with basically lower maximum loads.

Table 8-10: Comparison of the results from four-point bending tests by Wang et al. [163] and DNN-DSM predictions

Profile	$f_{y,nom} [N/mm^2]$	$\frac{M_{max,DNN-DSM}}{M_{max,exp}}$	$\frac{\kappa_{max,DNN-DSM}}{\kappa_{max,exp}}$
	$f_{y,exp} [N/mm^2]$		
S460; SHS 50×50×4-HR	460	0.94	3.81
	523	1.15	3.67
S460; SHS 90×90×3.6-HR	460	1.03	1.00
	500	0.95	0.53
S460; SHS 100×100×5-HR	460	0.82	-
	505	0.90	-
S460; RHS 100×50×4.5-HR	460	0.99	-
	498	1.04	-
S690; SHS 100×100×5.6-HR	690	0.82	1.17
	782	0.91	1.13
S690; RHS 100×50×5.6-HR	690	0.86	1.32
	777	0.96	0.81
S690; RHS 90×90×5.6-HR	690	0.84	1.89
	774	0.93	4.06

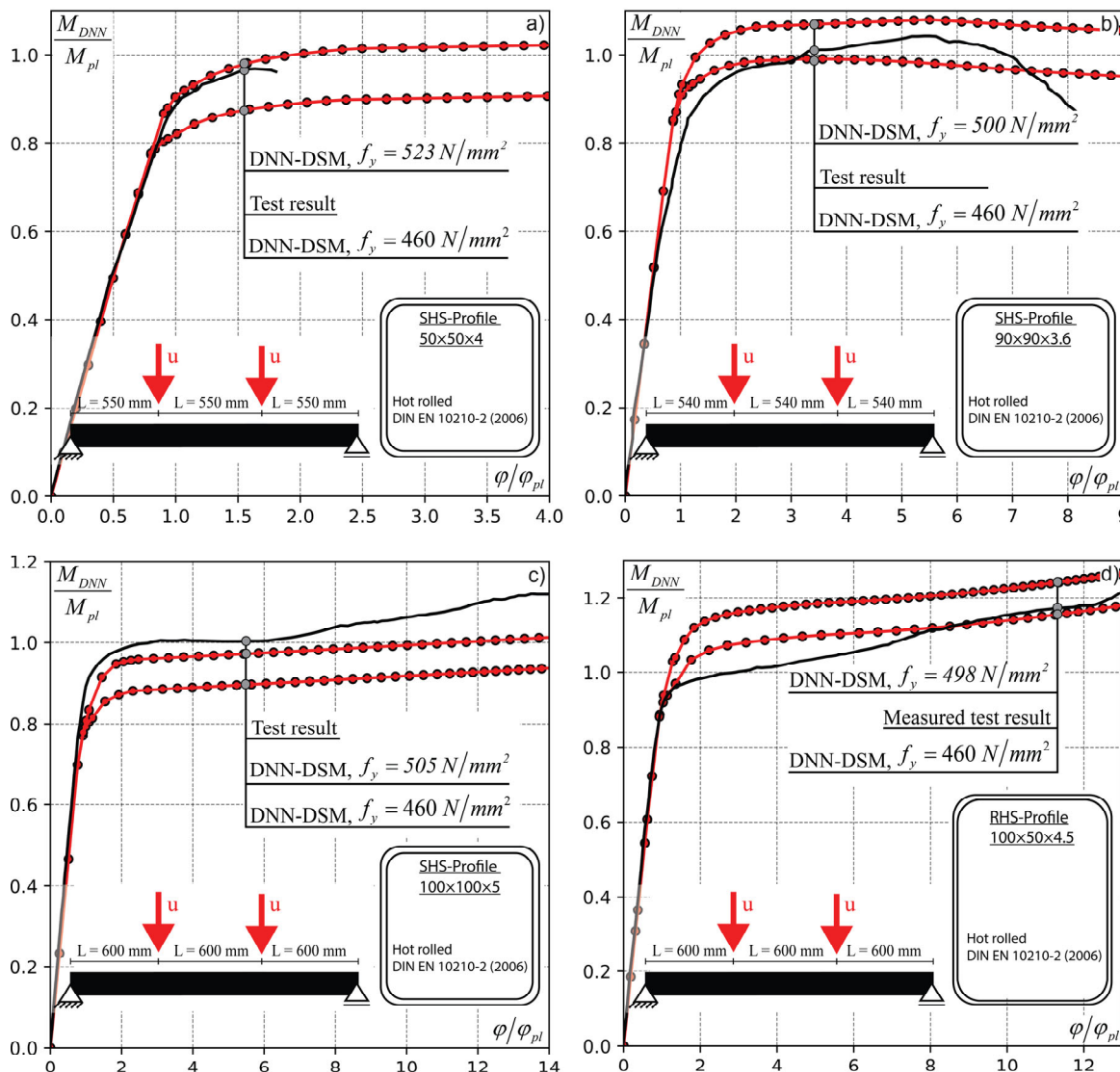


Figure 8-31: Comparison between test results from four-point bending by Wang et al. [163] and DNN-DSM recalculations for steel grade S460

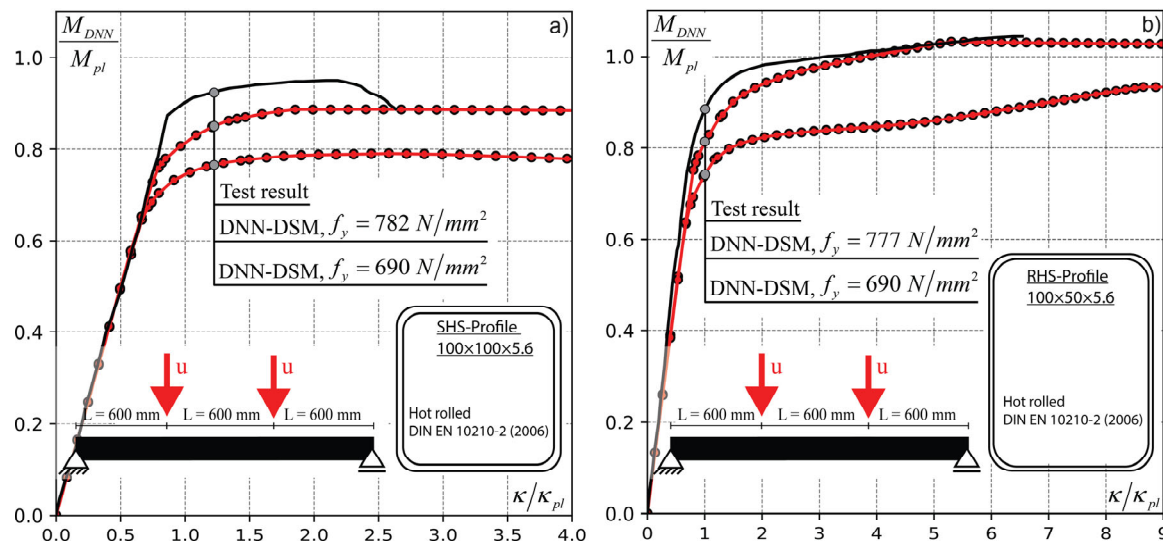


Figure 8-32: Comparison between test results from four-point bending by Wang et al. [163] and DNN-DSM recalculations for steel grade S690

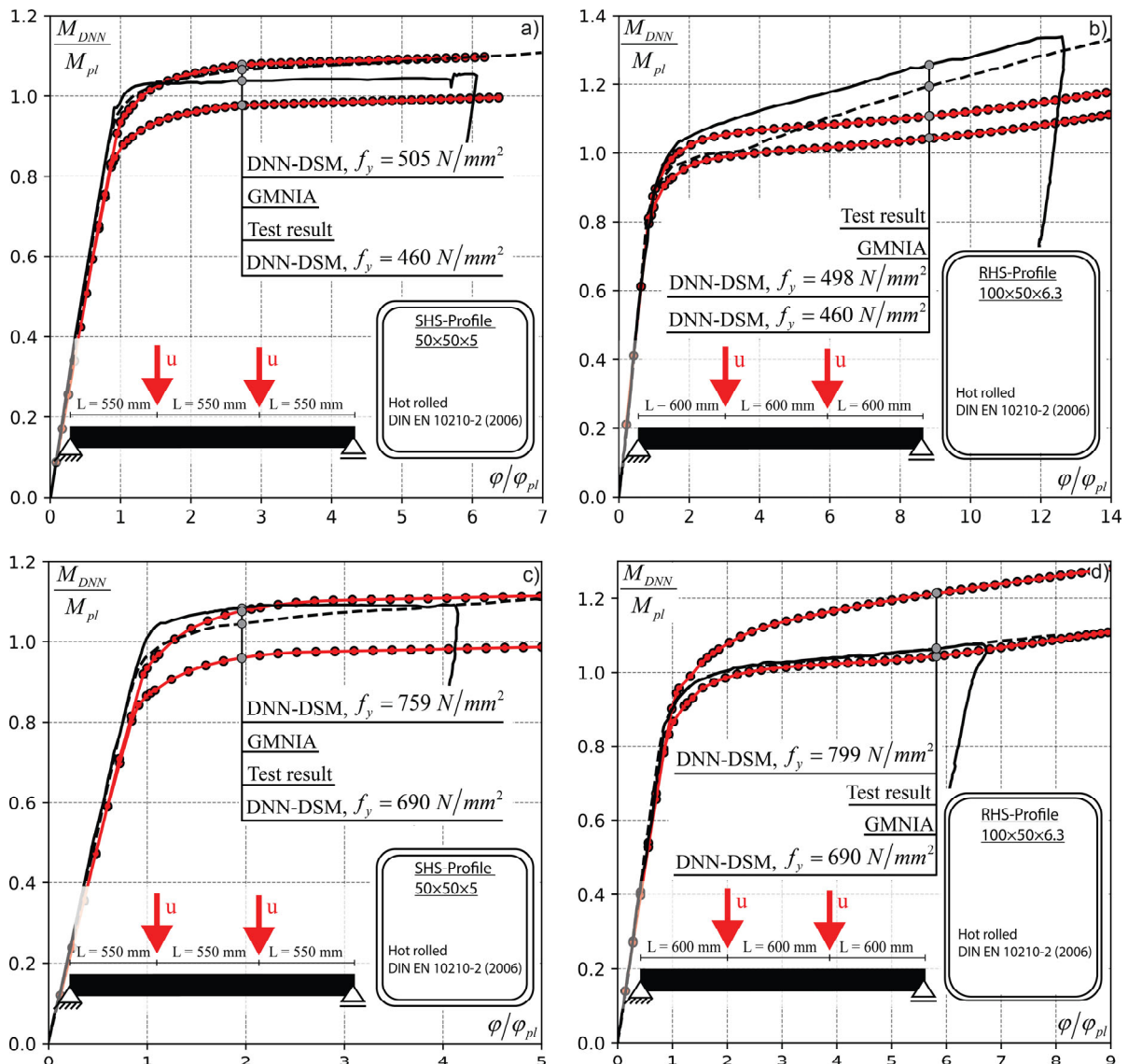


Figure 8-33: Comparison between test results from four-point bending and FE GMNIA simulations by Wang et al. [163] and DNN-DSM recalculations for steel grade S460 a), b) and S690 c), d)

In addition, a comparison between experimental results and validated shell based GMNIA simulations from Wang et al. [163] was performed and illustrated in Figure 8-33. Once again, in each case, the DNN-DSM predictions were performed with the nominal and experimentally determined values for yield strength, $f_{y,nom}$ and $f_{y,exp}$. Again, the DNN models were only trained on the nominal yield strength values and not the experimentally derived ones. The focus here is on the GMNIA calculations, which were primarily developed to match the experiments as accurately as possible, for the purpose of subsequently performing parameter studies, in [163]. It can be seen that the results from the GMNIA simulations and the predictions of DNN-DSM are largely in agreement. In Figure

8-33 a), c), and d), the numerical and predicted simulations are almost on top of each other. In Figure 8-33 b), the course in the ascending branch agrees only partially, since the effect of strain hardening is not quite as pronounced as in the GMNIA calculation or in the experiment. In all cases, using the nominal yield strength value as an input feature leads to more conservative results than the actual yield strength value from experiments.

However, the DNN are once again able to capture the effect of the higher yield strength, resulting from the trained (nominal) input features and extrapolate it on the unseen (experimentally derived) values.

Table 8-11: Comparison of the results from GMNIA simulations by Wang et al. [163] and DNN-DSM

Profile	$f_{y,nom} \left[\frac{N}{mm^2} \right]$	$\frac{M_{max,DNN-DSM}}{M_{max,GMNIA}}$	$\frac{\kappa_{max,DNN-DSM}}{\kappa_{max,GMNIA}}$
	$f_{y,exp} \left[\frac{N}{mm^2} \right]$		
S460; SHS 50×50×5-HR	460	0.93	-
	505	1.01	-
S460; RHS 100×50×6.3-HR	460	0.89	1.06
	498	0.95	1.22
S690; SHS 50×50×5-HR	690	0.89	1.04
	774	1.00	1.01
S690; RHS 100×50×6.3-HR	690	0.89	1.02
	799	1.00	0.89

8.4.2.3 Five point bending

The evaluation of the five point bending test from [195] follows the same procedure as for the three and four point bending test before. The general test set-up is presented in Figure 8-27 of Section 8.4.2. Figure 8-34 shows the comparison of the curves from test results and DNN-DSM predictions. The x-axis shows the member end-rotation in [rad]. For DNN-DSM based representations the calculated theoretical values was used. The y-axis represents the applied force, normalized by the theoretical plastic collapse load F_{coll} . The values for the collapse load were directly taken from [195] to normalize the DNN-DSM results.

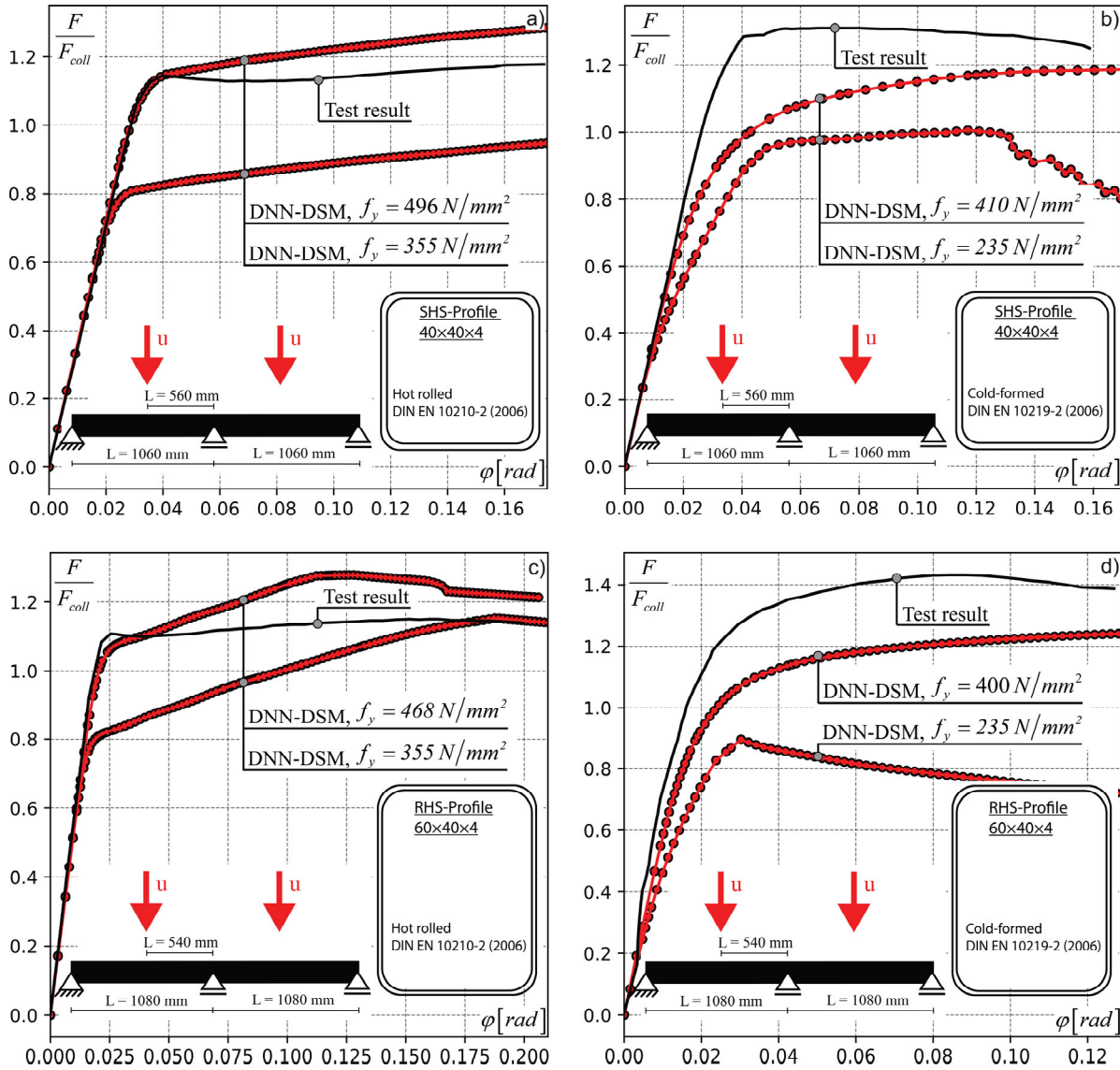


Figure 8-34: Comparison between test results from five-point bending tests by Gardner et al. [195] and DNN-DSM predictions for selected cross-sections

All comparisons between test results and DNN-DSM predictions lead to similar conclusions. The normalized load end-rotation curves lie almost on top of each other in the elastic range and shift apart with increasing nonlinearity, however, they are still comparable in terms of their overall course. As in the case of three and four point bending tests described before, DNN predictions were made based on the nominal yield strength $f_{y,nom}$ and the experimental value $f_{y,exp}$, being one of the DNN model features. In all considered cases, the nominal yield strength lead to a more conservative behaviour with lower expected forces. On the other hand, predictions based on the experimentally derived yield strength $f_{y,exp}$ lead to closer, but mostly slightly too optimistic results compared with tests, see Figure 8-34 a) and c). An evaluation of the post-buckling behaviour is in most

cases not directly possible, since the conducted test were terminated before reaching the post-buckling region or even the maximum force, see Figure 8-34 a). However, own DNN-DSM predictions tend to be too ductile, therefore overshoot in most cases the actual rotations. Table 8-12 shows the summarized results, comparing the maximum reached forces and corresponding member end-rotations between experimental results and DNN-DSM predictions.

Table 8-12: Comparison of the results from GMNIA simulations by Gardner et al. [195] and DNN-DSM

Profile	$f_{y,nom} \left[\frac{N}{mm^2} \right]$	$\frac{F_{max,DNN-DSM}}{F_{max,exp}}$	$\frac{\theta_{max,DNN-DSM}}{\theta_{max,exp}}$
	$f_{y,exp} \left[\frac{N}{mm^2} \right]$		
S355; SHS 40×40×3-HR	355	0.72	5.35
	504	0.87	3.70
S235; SHS 40×40×3-CF	235	0.68	1.42
	451	0.96	1.71
S355; SHS 40×40×4-HR	355	0.80	-
	496	1.09	-
S235; SHS 40×40×4-CF	235	0.77	1.78
	410	0.92	4.61
S355; RHS 60×40×4-HR	355	1.00	1.23
	468	1.12	0.84
S235; RHS 60×40×4-CF	235	0.63	0.31
	400	0.88	0.83

As described for the comparison of the three point bending tests (see Section 0), the general match of the exact course of deformations/rotations is not easy to obtain and depends on many factors, such as the cross-section geometry, imperfection shape and amplitude, the material model and the boundary conditions. Some of the factors mentioned have already been incorporated into the FE model selection and cannot be changed at this level of comparison. However, in the following two DNN-DSM models are used to investigate the influence of the boundary conditions and to explain the associated collapse mechanism. The middle support is modelled in two ways, as a pin support, which causes buckling in the two adjacent elements simultaneously (B1); and as two pin supports at both ends of one element placed directly in the middle (B2). Thus, local buckling is introduced in the middle element only.

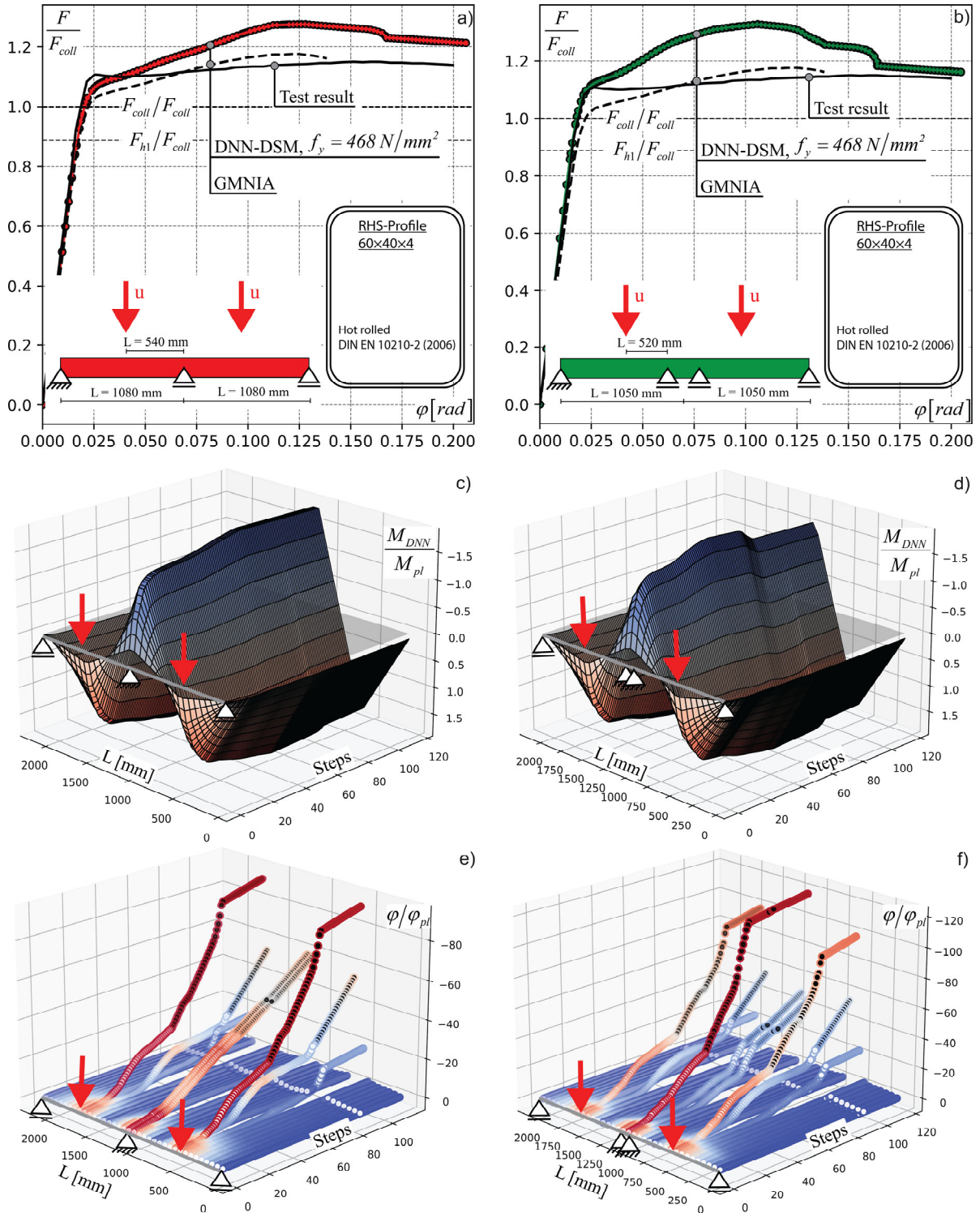


Figure 8-35: Comparison of the collapse mechanism based on different boundary conditions B1 and B2, a) and b) normalized force-rotation behaviour; c) and d) normalized moment distribution according to the calculated DNN-DSM steps; e) and f) normalized element rotation according to the calculated DNN-DSM steps

In [195], the observed plastic hinge mechanism was documented and described as follows. The first plastic hinge formed in the area of the middle support. The second and

third hinge, theoretically caused simultaneously, are formed directly at the points at load/displacement introduction. Figure 8-35 describes the collapse mechanism, predicted by using the two described boundary conditions B1 and B2 above. Figure 8-35 a) and b) show the experimental test result for a hot-rolled RHS60x40x4 profile, the boundary dependent DNN-DSM predictions and an additional independent GMNIA simulation, used by Fieber for his own model validation in [67]. The x-axis describes the member end rotation, the y-axis the forces normalized by the theoretical collapse load F_{call} . Horizontal lines show the points where the theoretical loads are reached during the formation of the first hinge F_{h1} , as well as the formation of a kinematic system, i.e., reaching the collapse load F_{call} . A slight difference can already be obtained from the boundary conditions B1 and B2 in Figure 8-35 a) and b).

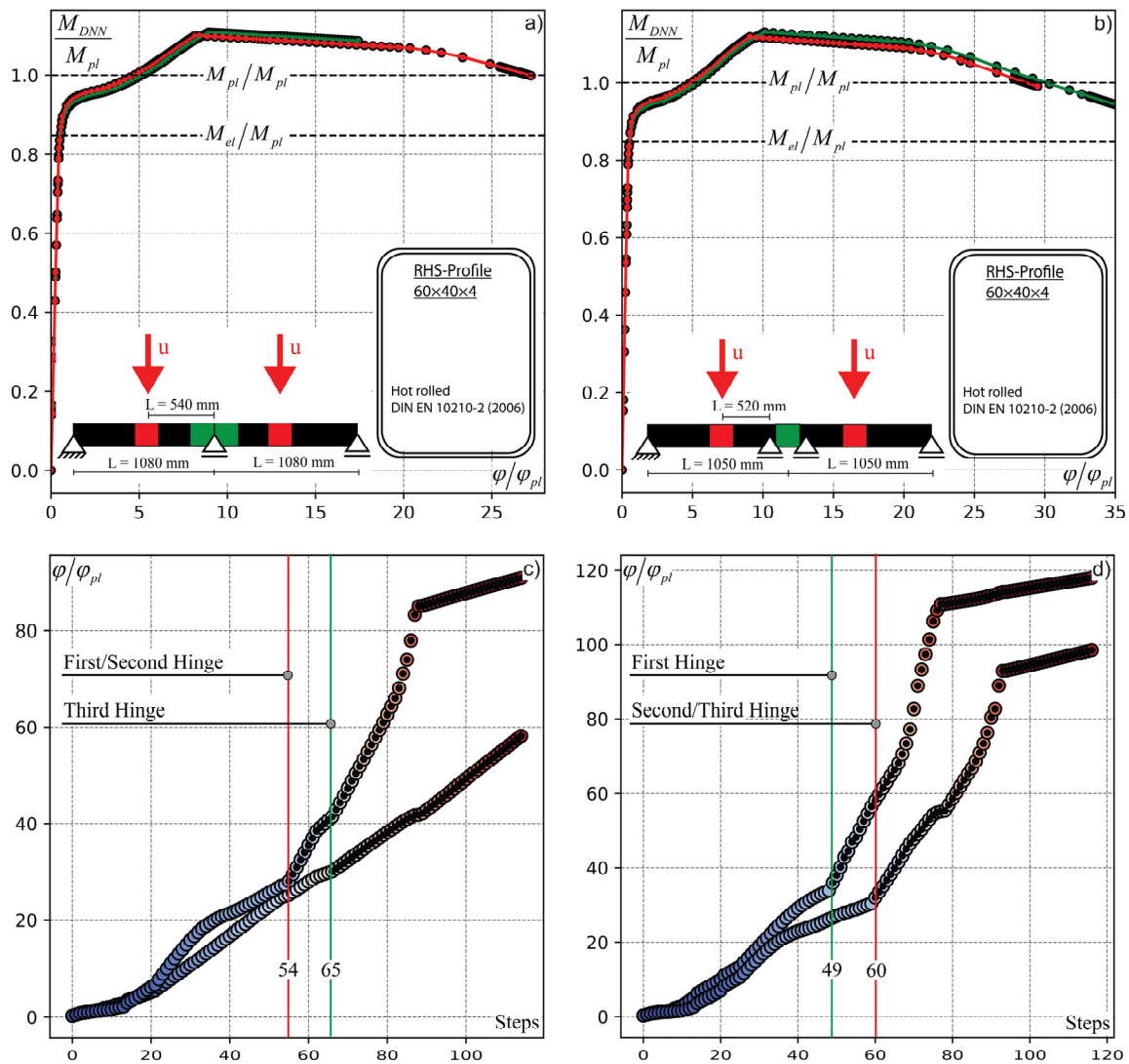


Figure 8-36: Comparison of the local element rotations in the area of the plastic hinges for boundary condition, a) and c) B1; b) and d) B2

The load-rotation curve shows a more ductile behaviour and reaches a lower maximum force in the case of boundary condition B1, compared to boundary condition B2. In both cases, the DNN-DSM predictions lie above the test result, as well as the corresponding GMNIA simulation. Figure 8-35 c) and d) illustrates the step dependent normalized moment distribution along the length of the member. Apparently, B2 behaves less ductile, with a stronger decrease of the moments after reaching the moment capacity. Figure 8-35 e) and f) show the normalized local element rotations, according to the predicted DNN-DSM step over the total length of the member.

It is evident that, for boundary condition B1, the first hinge formation occurs directly in the beam elements where the system deformations are initiated. Right after this load level, the two beam elements next to the middle support start to develop rotations above average values. A different behaviour is obtained for boundary condition B2. The first hinge forms in the middle beam element at the intermediate support, and only then the plastic hinges at the load application points. This load distribution behaviour is more in line with the observed mechanism from the experiments in [195].

The different load-rotation behaviour for boundary condition B1 and B2 is explained as follows. The black filled points in Figure 8-35 e) and f) symbolise three dimensional representation of the beam elements which are in post-buckling, according to a specific step in the progressive prediction process. The two beam elements in at the middle support (see Figure 8-35 e)) reach the moment, at which post-buckling occurs, slightly later than the elements in the area of load application. This is additionally illustrated in Figure 8-36 a) for condition B1 and b) for condition B2, showing the normalized moment-rotation curves directly at the locations of the formed hinges. The green curve represent the local rotation at the intermediate support and the red curve the rotations in the area of load introduction. Potentially higher absolute strains are reached for the elements in the area of load application than in the elements at the intermediate support (B1). The opposite is obtained for condition B2 in Figure 8-36 b), where the first hinge forms in the beam element at the intermediate support. The absolute local rotations are in comparison similar than for condition B1.

Figure 8-36 c) and d) is a broken down 2D side view representation of Figure 8-35 e) and f), showing the normalized strains corresponding to the calculated step in the elements that form the plastic hinges. This representation helps to understand the onset of post-buckling between the plastic hinges and their disproportional increase in rotations. For condition B1, the first two hinges appear at the load introduction, reaching after 54 steps post-buckling, while increasing rapidly in local rotation. The two elements at the intermediate support reach post-buckling after 65 steps, whereby the increase of the rotations remains almost linear. The moderate increase is reflected by larger end-rotations in the overall system behaviour. This assumption can be confirmed from the comparison with boundary condition B2, see Figure 8-36 d). The increase of the plastic hinge strains is similar in its shape, developing rapidly after reaching post-buckling at an earlier step. Compared to B1, where four main elements formed the plastic mechanism, in B2 mainly three elements are affected. This less amount leads to a slightly sharper drop in the post-buckling region of B2, see Figure 8-35 b).

8.5 Conclusions

The overall feasibility of the DNN-DSM approach was investigated and confirmed throughout Chapter 8 through verifications on the cross-sectional, as well as the member level. In a first step the overall DSM implementation was compared with the software Cubus, in order to confirm the structural behaviour in the elastic range. The verification of the cross-section capacity showed a high accuracy between the load bearing capacities resulted from Abaqus GMNIA simulations and DNN models. The overall prediction deviations lie around a maximum of 3%. Further, the comparison of the cross-section behaviour, i.e. the full load-deformation and moment-rotation curves from Abaqus GMNIA simulations with corresponding DNN-model predictions showed mainly a good agreement, although outliers were detected, where in some cases the overall behaviour was over-predicted by a maximum of around 15% leading to unsafe predictions. This uncertainties need to be investigated further and are part of ongoing investigations.

Further, the DNN-DSM approach was tested against numerical simulations (GMNIA) on isolated members, i.e. members in compression, members in compression with global imperfections and members in bending. The comparison for members subjected to pure

compression had the goal to investigate different DNN-DSM model approaches with varying imperfection amplitudes in the local beam elements along the member length. The general comparison of load-deformation curves showed a good agreement with corresponding GMNIA simulations. It was found that the stiffness drop in the post-buckling behaviour is mainly dependent on the formation of local buckling regions along the member, more specifically on its amount. If members fail explicitly in one local buckling area, the stiffness drop in the post-buckling range is significantly higher, since all residual deformations are concentrated in this plastic field. This sharp drop can be controlled according to the amount of local buckling areas, i.e. by forcing a simultaneous failure in all local beam elements, the post-buckling curve becomes much more pronounced and smoothens out. The DNN-DSM approach is capable to reproduce this behaviour by an explicit selection of local imperfection amplitudes in individual beam elements.

A comparison for members subjected to pure bending was done against three and four point bending considerations, using the results from shell based GMNIA simulations in Abaqus against recalculations from the DNN-DSM. Both approaches use the same non-linear material models for hot-rolled and cold-formed steel. In the case of three point bending two profiles, an SHS200×8 and SHS200×5 with the steel grade S355 were modelled with the same length of 1600mm in Abaqus and the DNN-DSM, using 77298 dofs and 18 dofs, respectively. On the other hand, models used for four point bending had a total length of 2700mm with a total amount of 146358 dofs in the Abaqus models and 20 dofs in the DNN-DSM models. Two cold-formed profiles, an RHS300×150×8 and RHS300×150×6 with the steel grade S355 were used for the comparison. Both load scenarios showed a very high accuracy with maximum deviations around 4% to 5% in the region of the reached maximum moments. However, this particular deviation can be drawn back on a local crushing effect directly in the load introduction area of the Abaqus FE models. This local behaviour can not directly be covered through the DNN-DSM approach, leading to higher capacities. Overall, the calculation time was halved compared to Abaqus GMNIA simulations, and can further be accelerated by a more economic implementation.

Subsequently, a validation against experimental results showed the potential of this data driven approach, although the overall comparison was mixed. For the case of pure compression, two test series from [195] and [2] were used. The recalculation with the DNN-DSM lead in all cases to similar load-deformation curves. Bigger deviations, which appeared mostly for the comparison with test series 2 [2] could be explained with own

shell based GMNIA simulations and are drawn back on differences in imperfection shapes and amplitudes; the real material model from experiments, which cannot be directly taken into account and therefore varies from the initially implemented material models. Further, only the yield strength appears as an input feature in the DNN models, currently without the possibility to adjust the ultimate strength. Additionally, a perfectly centric and equivalent load introduction along the specimen edges is assumed in the recalculation (in both, Abaqus GMNIA and DNN-DSM simulations) but cannot completely be fulfilled in the actual test. Similar conclusions were drawn for members in bending for three-, four- and five-point bending tests, to explain differences between recalculations and test results. However, comparisons of GMNIA simulations of four-point bending test from literature [163] with own DNN-DSM recalculations showed a very close match of the collected non-linear moment-rotation curves from tests and an even closed match with GMNIA simulations of the authors. One main shortcoming, that need to be tackled in further investigations, is the problem that redistributions are currently not captured correctly when beam elements are unloaded. The unloading path is exactly the same as for loading, meaning that plastic deformations are released or subtracted from the elements. This in particular leads to oscillating predictions in the post-buckling range, which occurred during the investigations on five-point bending tests.

9

Synthesis

Summary, Conclusions and Outlook

Outline of the chapter:

This chapter wraps up this thesis by providing a summary of the main steps towards the development of the presented DNN-DSM approach, followed by a set of conclusion regarding the made choices and obtained results. Shortcomings and subsequent optimizations are presented, together with a discussion of needed next steps towards a more robust and more widely-applicable approach.

9.1 Review of Objectives and Significance

Climate change and increasingly unreliable material procurement have refocused the efforts of structural engineering science on its core area: minimizing material consumption while achieving a high level of accuracy and reliability in the performance prediction of engineering structures, as used in buildings and civil infrastructures. Transformative progress in this domain requires novel, computationally and data-driven approaches to overcome current over-conservatism in design and significantly increase the environmental and economic sustainability of the construction industry.

With this in mind, the presented thesis set out to explore the potential of a new method for the simulation-based non-linear analysis and design of large-scale engineering structures, thereby focusing on lightweight steel structures as a particularly suitable application case: the method, termed “DNN-DSM” for “Deep Neural Network – Direct Stiffness Method”, attempts to integrate predictions by trained artificial neural networks of the non-linear behaviour of slender steel components in the standard, beam-theory DSM analysis method.

Whenever compressive stresses are present in thin-walled metallic components, local (cross-sectional) and global (member) instabilities determine the structural behaviour as the ultimate limit state is approached, thus leading to highly non-linear load-displacement characteristics that depend on the proneness of the section to develop buckling deformations at either lower or larger compressive strains. This nonlinearity, of geometric nature, cannot be easily captured by straightforward mechanical models alone: it generally requires either a highly localized (shell FEM) modelling of the buckling phenomenon, which typically is too onerous for a full-structure analysis, or significant simplifications and conservatism in structural analysis by beam models, followed by code-based verifications. The DNN-DSM approach thus aims at overcoming these difficulties by combining mechanics-based, beam-element type matrix-stiffness approaches (like the well-known and widely used Direct Stiffness Method – DSM for the analysis of bar-type structures, and more generally the finite element method – FEM) with data-driven models that make use of machine learning methods (such as Deep Neural Networks,

DNN). The latter are to be trained on large datasets of “synthetic structural tests” to predict the non-linear, coupled stress-displacement fields of structural components. As a result, a hybrid structural simulation technique is developed, in which a highly efficient beam-theoretical FEM element is modified and augmented by machine predictions of its non-linear tangent stiffness and load-deformation/moment-rotation paths. This in turn helps hugely increasing the accuracy of structural designs for steel structures, avoiding the significant over-conservatism produced by traditional structural design methods, while maintaining a level of computational efficiency suitable for industrial practice.

The present thesis is to be seen as an extended exploration of both the motivation and the feasibility of the described DNN-DSM approach. It takes the mechanically well-understood case of the local instability and non-linear behaviour of hollow section compression members and beams as an application example and develops the method up to the level of a demonstrator for this case. It makes use of recent experimental results from literature and ETH’s Chair of Steel and Composite Structure’s own work as a basis for the development of numerical (GMNIA) models, which in turn are used as the main source of data for the DNN training of non-linear stiffness matrix terms. The trained DNN stiffness predictors were then integrated in a standard, 2D DSM formulation and used to carry out validation simulations: by applying the developed method in the recalculation of stub column and beam tests, the potential and general feasibility of the method could be demonstrated, while the remaining difficulties and significant remaining work to bring the method to greater maturity and reliability, as well as to advance it to further application cases, was also made clear.

Further publications on current developments are on the way. All references, required data sets and python codes will be published at “SciML4StructEng_Repository” (<https://sciml4structeng.github.io/Repository/>), fostering the dissemination of data sets for structural engineering to allow the prototyping, development and benchmark testing of scientific machine and deep learning algorithms.

9.2 Main contributions and conclusions

This section summarizes the primary conclusions and contributions of the research carried out in this thesis, thereby indicating the relevant chapters and sections.

Overview of current design methods, Chapter 2: An overview of traditional design approaches in structural engineering was given, pointing out the current advanced analysis methods with background information on their development. A special attention is set on the AA-CSM (advanced analysis continuous strength method described in Section 2.5) developed by Fieber [67], generally an extension of the well-known CSM approach, making use of beam finite elements and CSM based strain limits. The method development included calibrated analytical formulas for calculating buckling half-wavelengths, used to average strains over a critical local length, e.g. to better account for system redistributions. The analytical length formulations were used for investigations in Section 5.3, for the assessment of local buckling lengths in own finite element shell based models.

Limitation of current design methods and novel approaches, Section 3.1, Section 3.2: An overview is given on the advantages and disadvantages of current advanced analysis methods. Apart from different method inherent limitations, all approaches have in common the use of overall strength/strain curves for the assessment of instability cases with buckling knock-down factors, which rely on the calculation of a relative slenderness linked to FE modelling and linear buckling analysis. The role of the slenderness determination is further evaluated exemplary, using three different finite element models to assess their impact on the CSM design procedure. This hypothetical example illustrates that the modelling approach can have a significant impact on the subsequent cross-section capacity, especially in slender regions. Despite current efforts to standardize design by finite element analysis, i.e. to provide appropriate modelling assumptions for practice, the modelling of cross-sections and structures will remain a major error-prone hurdle. Finally, machine learning and deep learning are introduced as a new approach in structural engineering. Some of the current trends in deep learning are presented and reference is made to related projects in the literature.

Formulation of the main research gaps, Section 3.3: *Data development form FEM simulations:* This point involves the core idea of using precise finite element models, which are calibrated against tests, and perform non-linear advanced analysis (GMNIA) for design purposes (design by analysis). Parametrized models are often used to make analytical inferences about the design formulation based on analytical expressions. However, the FE models herein are used in non-linear simulations to provide the necessary data sets for the training of DNN models, which forms the unique character of this data driven approach. *Representation of the inelastic buckling behaviour of thin-walled steel members through beam-element matrices:* The idea to use beam finite elements in advanced analysis is not necessarily new, as shown by Fieber [67], but involved inherent strain limit calculations as a break criterion in the design analysis. Also, limited to the area in the pre-buckling range, this method does not account for redistributions due to the stiffness losses in post-buckling. The proposed method is completely independent of reached strain limits, taking into account the whole load-deformation/moment-rotation behaviour through the prediction of incremental tangent stiffnesses and its incorporations in a DSM workflow. *Secondary knowledge gain on the behaviour of steel members:* This research gap tackles the idea to increase knowledge from present data with ML based method and expending those patterns to solution improvements.

Fundamental background on ML topics, Chapter 4: A brief introduction with selected theoretical background to machine and deep learning is presented. The main goal was to give the reader an overview some existing methods in the general content of machine learning. A gentle introduction to deep learning provides the necessary understanding for the methods used in Chapter 6 of this theses.

Benchmark modelling from the Hollosstab project, Section 5.1 and Section 5.2: This sections provide the evaluation of the finite element shell based models, used for the development of the data sets for Chapter 6. The experimental program, the performed non-linear shell finite element simulations and the subsequent calibrations towards parametrized numerical models were presented. This process provides the general assessment of finite element model assumptions, i.e., assumed cross-section geometry, FE model discretization, implementation of the non-linear material model.

Investigations on buckling half-wavelengths, Section 5.3: Investigations based on actual 3D surface scans of the specimens from the Hollosstab project were used in pre-developed procedures, to assess the FE model behaviour according to different imperfection shapes. This procedure involved Fourier series expansion, with the idea to decompose scanned imperfections by sine and cosine waves of different lengths and amplitudes, helping recognize the imperfections with the most influence on the buckling behaviour. Above all, a strong dependence of imperfections on the moment-rotation behaviour was obtained, although only a limited number of Fourier coefficients is needed to mimic the “real” behaviour. Additionally, use was made of 3D surface scans of specimens from the Hollosstab project, to assess and compare the measured buckling lengths from GMNIA simulations with buckling half-wavelength formulations from [67]. As a conclusion, the local buckling lengths, which are equal to the member lengths in the FE models, were set equal to the larger dimension of the profile height or the width, in each case for compression and bending.

Data pre-processing, Section 6.1: The general procedure from the FE simulation to data extraction was presented, explaining the automated workflow through several python scripts. This step was crucial for the general method development regarding the time management. Reading out the data manually would have taken far too long, as the 19462 Abaqus simulations, produces around 5.300.000 individual calculations steps, which had to be extracted. This procedure involved several attempts, since the parameters were changes throughout the development, leading to revised simulations.

Data post-processing, Section 6.2: A high focus was set on the topic of feature engineering. Investigations on data structure showed that the data density (relative distance between calculated increments) had a major influence on the prediction accuracy. The split of the data sets into pre- and post-buckling regions showed a big positive impact on the predictions. Further potential toward dimensionality reduction performing PCA considerations was identified. Important features, using Random Forest Regressor [187] and XGBoost Regressor [183], were identified and used for DNN model predictions. The overarching goal was to reduce the dimensionality and speed up the learning process.

Investigations on DNN model optimization, Section 6.3: Hyperparameter tuning was performed involving 193 different training runs with a set of changing parameters. Ultimately, a DNN model was presented, being relatively small with only 4 hidden layers and the amount of required neurons in each layer between 9 and 27. The model accuracy for the prediction of load dependent tangent stiffnesses was estimated between $r^2 = 0.96$ and $r^2 = 0.99$. The overall accuracy for the predicted cross-section accuracy was around $r^2 = 0.99$.

DNN-DSM implementation, Chapter 7: First, background information on the general procedure of the DSM (direct stiffness method) is given. The DNN-DSM approach is further implemented for the case of compression and bending separately, describing the incremental workflow throughout the predictions for the pre- and post-buckling range. At this stage of implementation, the two load cases are predicted independently and their mutual influence is accounted for in the sense of a DNN prediction. However, to simplify this limitation and still being able to account for interaction effects, an N-M interaction formulation was implemented based on Liew and Gardner [108]. To account for Th.2.Ord. effects, the geometrical stiffness term was added to the method using the Taylor series approximation.

Method validation against experimental results and simulations, Chapter 8: The general DSM implementation was first validated against existing software. The results showed a very good agreement with the software Cubus [297] with maximum deviations around 0.3%. Theory of second order effects were evaluated in the elastic range and show a good agreement with analytic considerations.

Subsequently, the model validation is carried out by comparing the non-linear DNN-DSM load-deformation predictions with numerical analyses using shell-element models, with otherwise similar assumptions regarding (nominal) material and imperfection definitions. Finally, the DNN-DSM predictions are compared against physical test results from the literature or the Hollosstab test series, with the aim of assessing the capability of the method to make predictions in parameter ranges that are outside of the immediate training range. The results confirm the viability and potential of the DNN-DSM approach, while also highlighting the need for further developments before maturity of the method is reached.

9.3 Outlook on Further Research Topics

The presented thesis introduces a novel data driven method to account for non-linear effects in thin-walled structures, while using classic, 4 or 6 DOF beam element analysis. Its potential versus traditional and advanced FEM-based design methods was demonstrated in this thesis, but will have to be developed in further studies. Areas of future research are presented in the followings.

- i. **Exploration of further deep learning models/architectures:** The proposed DNN models are capable of predicting the non-linear incremental tangent stiffness with a high accuracy. However, the used feed forward network architecture has the disadvantage that the predictions are simply made on the absolute deformation/rotation, without the information of previously predicted steps. This can lead to unreliable predictions in areas with very small incremental steps, typically around the areas of the maximum load bearing capacity and the post-buckling region. During the evaluation process of Chapter 8, oscillation in the predictions was observed in some cases. An example of such prediction is illustrated in see Figure 9-1 a). Such prediction inconsistencies could be solved by using recurrent neural network structures [298], ranging from Long Short Term Memory (LSTM) [299] to Gated Recurrent Unit (GRU) Networks [300]. This strategy is currently in the development and will be presented in future publications.
- ii. **Prediction sensitivity:** Prediction sensitivity was evaluated exemplarily for one profile in Section 8.2.3, by varying different input parameters, which appeared to be suitable in the framework of this thesis. However, the same procedure should be repeated in a more parametrized manner, in order to evaluate the overall sensitivity and therefore the safety of the predictions.
- iii. **Solving prediction inconsistencies:** The above mentioned problem is also affiliated with a specific inconsistency in the prediction of the maximum forces/moment, shown in Figure 9-1 b) for one local element and equal rotation at both ends. The black dashed line shows the GMNIA simulation on which the DNN model was trained on, the red dotted line the corresponding prediction. The trig-

gering models, which initiate the switch between pre- and post-buckling are initially trained on the actual GMNIA results (dashed line). While predicting the rotation based tangent stiffness and back calculating the moment-rotation curve (red dotted line) it might happen, that the point is reached where post-buckling should start (green vertical line) but is not triggered because of moment being lower than the triggering threshold. Thus, the prediction are continued for the pre-buckling range until the limit value is reached (red vertical line). This might affect the overall behaviour, especially for compact cross-sections with pronounced plastic plateaus. The onset of post-buckling might be too late, therefore lead to a wrong non-linear behaviour.

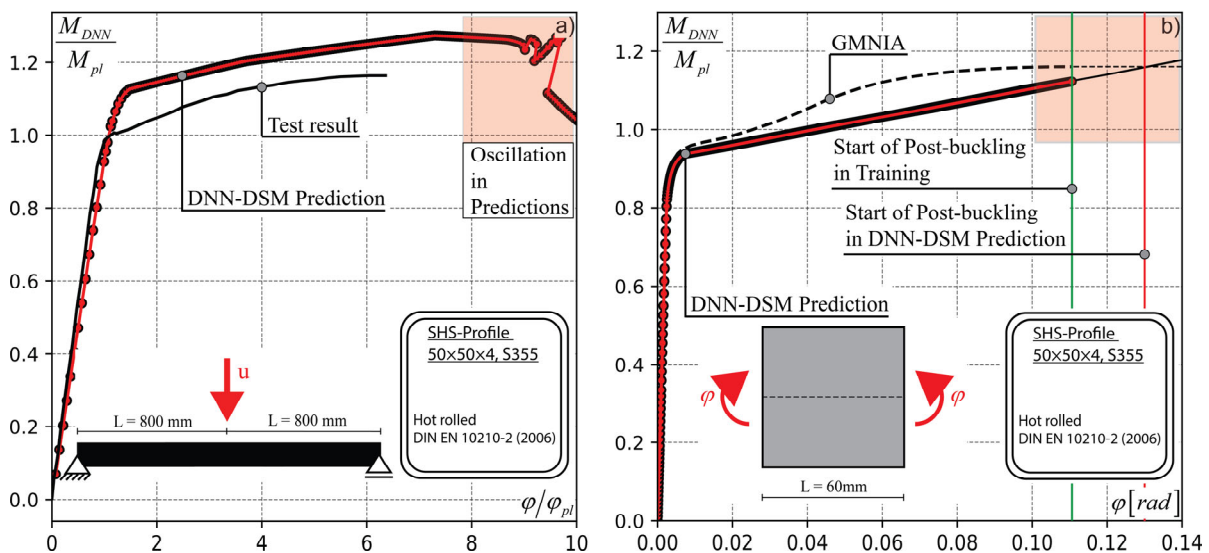


Figure 9-1: Mismatch problematic, a) oscillation in peak load area; b) mismatch of the load bearing capacity

- iv. **Inclusion of different section shapes:** One of the limitations of scope of this thesis is the exclusion of out of plane stability effects, such as lateral flexural and torsional buckling. This led to the current choice of SHS/RHS profiles as a suitable first validation object. However, future developments of the approach should incorporate open profiles, such as I-shaped, C-shaped or Z-shaped sections. It is believed that the method could be attractive both for general design of standard sections, but perhaps even more so for manufacturers and designers of highly thin-walled structures, i.e., customized cold-formed cross-sections e.g. in high-

bay warehouse structures, as customized analysis tools could be trained on specific, proprietary section types and design tools developed accordingly.

- v. **N-M interaction implementation:** For the purposes of load-displacement prediction, the load cases investigated are currently limited to pure compression or pure bending only. All cases in between are not considered, therefore need to be interpolated through interaction formulations. In the next steps, the data set will be expanded to combined load cases with additional GMNIA simulations, so that an interaction can be accounted for directly in the prediction process.
- vi. **Prediction of coupled non-linear stiffness terms:** The current limitation in the implementation of the DNN-DSM includes linear beam stiffness coupling terms. Ultimately, it is planned to make use of ML approaches such as Deep Neural Networks and its variants to predict the coupled, non-linear stiffness terms appearing in stiffness matrices when geometric as well as material nonlinearities appear. This task is graphically illustrated in Figure 9-2. The corresponding data development and feature engineering to be able to train a DNN for this prediction task is a key part of the research work plan and will require a high degree of engineering and computational effort. The results to be obtained from this task, specifically from the corresponding parameter sensitivity analysis and feature engineering, extend beyond the training of DNN and are expected to give deeper insight into the mechanics underlying elasto-plastic instabilities of steel sections.

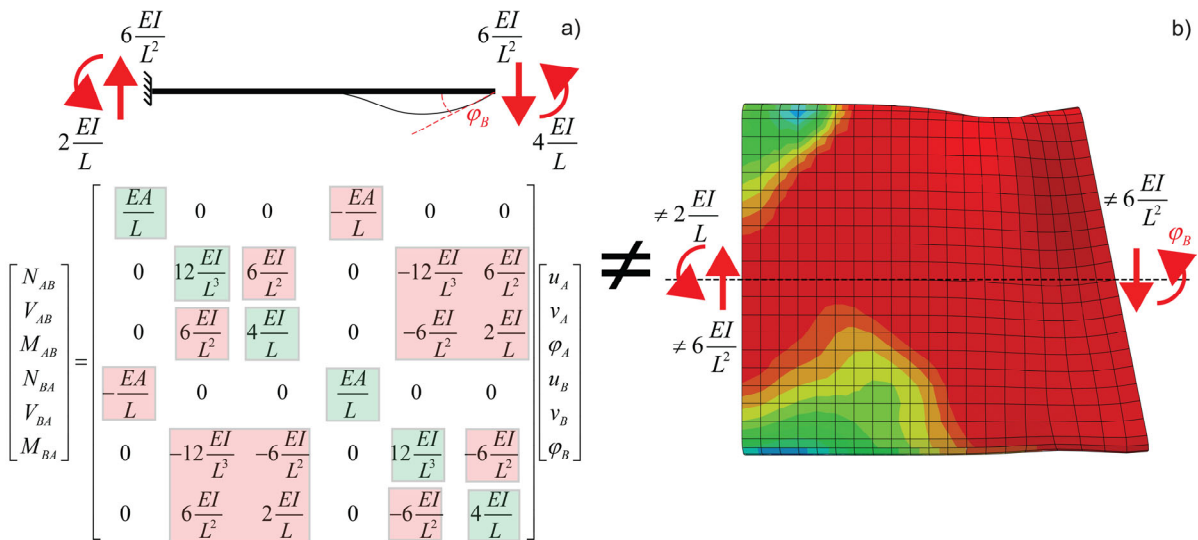


Figure 9-2: Illustration of the coupling terms for a beam element

- vii. **Software development:** The current code implementation level of the DNN-DSM is still in a preliminary state at the end of this thesis work. It generally lacks of a dynamic object oriented code basis and needs to be revised in terms of a better and computationally more economical performance. In the course of further method development, it is planned to extend this method to global imperfections for in and out of plane cases, therefore, enabling a 3D implementation and assessment. A possible schematic representation of a future software workflow is given in Figure 9-3.

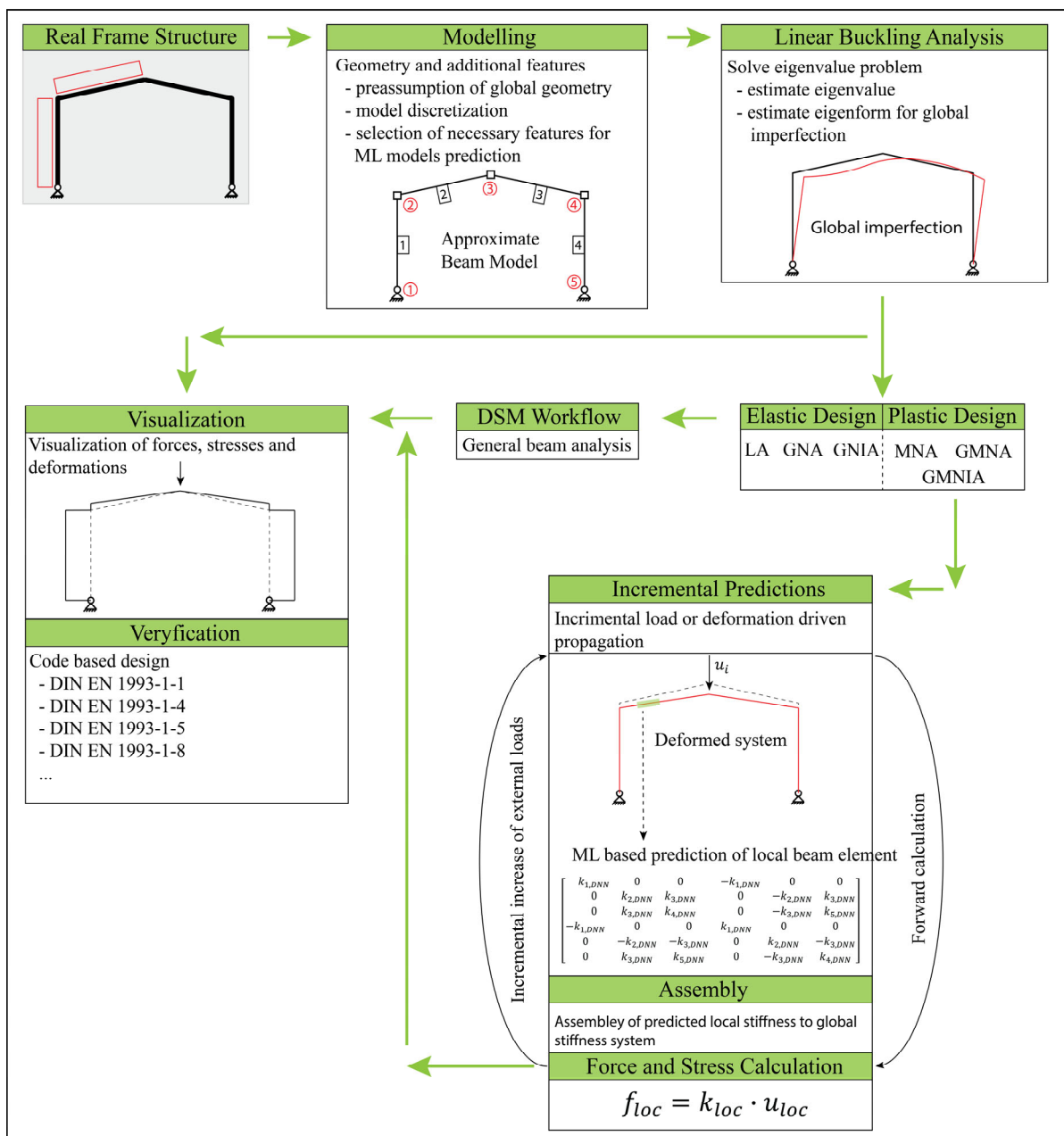


Figure 9-3: Schematic and simplified representation of the envisioned DNN-DSM Software workflow

- viii. **Validation of the DNN-DSM approach through numerical and large scale tests of a sample structure:** The implementation of the DNN-DSM is validated against test results from literature in this thesis. In these tests, only single beams or members were considered. It is of interest to validate the performance of larger models of full-scale structures (e.g. frames or trusses) experimentally. For example, taking inspiration from well-documented tests by Wilkinson & Hancock [301], a simple frame as shown in Figure 9-4 could be a suitable object of validation for the developed method; thereby, a frame structure made of high-strength steel hollow sections and locally reinforced to avoid failure in connections or other points of discontinuity (not covered by the new method) should be tested, in a minimum of two repetitions, for a minimum of two loading scenarios.

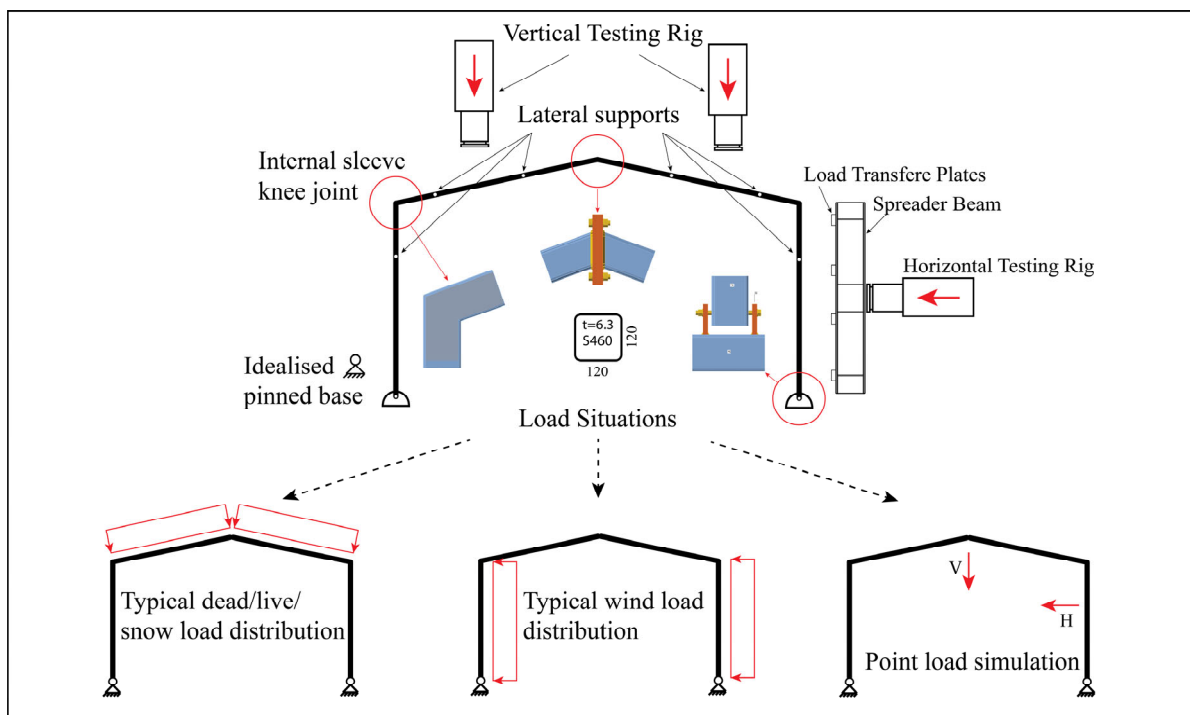


Figure 9-4: Schematic representation of a possible type of structure to be tested in full-scale validation tests, partially adopted from [301]

References

- [1] United Nations Environment Programme, '2022 Global Status Report for Buildings and Construction: Towards a Zero-emission, Efficient and Resilient Buildings and Construction Sector.', Nairobi, 2022.
- [2] A. Toffolon, 'Generalised slenderness-based resistance method for the strength prediction of hollow sections', Doctoral Thesis, Universität der Bundeswehr München, Germany, 2020.
- [3] M. A. Kraus and A. Taras, 'Physik-informierte Künstliche Intelligenz zur Berechnung und Bemessung im Stahlbau', *Stahlbau*, vol. 89, no. 10, pp. 824–832, Oct. 2020, doi: 10.1002/stab.202000074.
- [4] 'DIN EN 10210-2:2019-07, Warmgefertigte Hohlprofile für den Stahlbau_- Teil_2: Grenzabmaße, Maße und statische Werte; Deutsche Fassung EN_10210-2:2019', Beuth Verlag GmbH. doi: 10.31030/3058497.
- [5] 'DIN EN 10219-2:2019-07, Kaltgeformte geschweißte Hohlprofile für den Stahlbau_- Teil_2: Grenzabmaße, Maße und statische Werte; Deutsche Fassung EN_10219-2:2019', Beuth Verlag GmbH. doi: 10.31030/3058498.
- [6] X. Yun and L. Gardner, 'Stress-strain curves for hot-rolled steels', *J. Constr. Steel Res.*, vol. 133, pp. 36–46, Jun. 2017, doi: 10.1016/j.jcsr.2017.01.024.
- [7] L. Gardner and X. Yun, 'Description of stress-strain curves for cold-formed steels', *Constr. Build. Mater.*, vol. 189, pp. 527–538, Nov. 2018, doi: 10.1016/j.conbuildmat.2018.08.195.
- [8] J. A. Ewing, *The Strength of Materials*. Cambridge, 1899.
- [9] M. G. Lay, *Plastic Design in High Strength Steel: The Experimental Bases for Plastic Design; a Survey of the Literature*. Fritz Engineering Laboratory, Department of Civil Engineering, Lehigh University, 1963.
- [10] I. Lyse and H. J. Godfrey, 'Investigation of Web Buckling In Steel Beams', *Trans. Am. Soc. Civ. Eng.*, vol. 100, no. 1, pp. 675–695, Jan. 1935, doi: 10.1061/TACEAT.0004660.
- [11] F. Lab, 'Commentary on plastic design in steel: closure, ASCE Manual 41, 87 (ST8), p. 241, Reprint No. 191 and 178 (61-6) (61-18)'.
- [12] E. Meyer, 'Die Berechnung der Durchbiegung von Stäben deren Material dem Hook'schen Gesetze nicht folgt', *Z. Vereines Dtsch. Ingenieure*, vol. 52, no. 5, p. 167, 1908.
- [13] G. Kazinczy, 'Kísérletek befalazott tartókkal. (Experiments with clamped endbeams.)', *Betonszemle*, vol. 2, no. 6, pp. 101–104, 1914.
- [14] N. C. Kist, 'Die Zähigkeit des Materials als Grundlage für die Berechnung von Brücken, Hochbauten und ähnlichen Konstruktionen aus Flusseisen', *Eisenbau*, 1920.

- [15] M. Grüning, *Die Tragfähigkeit statisch unbestimmter Tragwerke aus Stahl bei beliebig häufig wiederholter Belastung*. Springer, 1926.
- [16] H. Maier-Leibnitz, 'Beitrag zur Frage der tatsächlichen Tragfähigkeit einfacher und durchlaufender Balkenträger aus Baustahl St 37 und Holz', *Bautech.*, vol. 6, no. 1, pp. 11–14, 1928.
- [17] H. Maier-Leibnitz, 'Versuche mit eingespannten und einfachen Balken von I-Form aus St. 37', *Bautechnik*, vol. 7, p. 313, 1929.
- [18] J. Fritsche, 'Die Tragfähigkeit von Balken aus Stahl mit Berücksichtigung des plastischen Verformungsvermögens', *Bauing.*, vol. 11, no. 49, pp. 851–855, 1930.
- [19] J. H. Schaim, 'Der durchlaufende Träger unter Berücksichtigung der Plastizität', *Stahlbau*, vol. 3, pp. 13–15, 1930.
- [20] K. Girkmann, *Bemessung von Rahmentragwerken unter Zugrundelegung eines ideal plastischen Stahles*. Hölder-Pichler-Tempsky in Komm., 1931.
- [21] J. F. Baker and J. W. Roderick, 'An Experimental Investigation of the Strength of Seven Portal Frame', *Trans. Inst. Weld.*, vol. 1, no. 4, 1938.
- [22] J. F. Baker and J. W. Roderick, 'Further Tests on Beams and Portals', *Trans. Inst. Weld.*, vol. 3, no. 2, 1940.
- [23] J. F. Baker, *the steel skeleton Volume 1 elastic behavior and design*, vol. 1. CUP Archive, 1960.
- [24] C. Massonnet, 'Die europäischen Empfehlungen (EKS) für die plastische Bemessung von Stahltragwerken', *Acier-Stahl-Steel*, vol. 32, pp. 146–156, 1976.
- [25] G. J. Jr. Driscoll *et al.*, 'Plastic design of multi-story frames', Fritz Engineering Laboratory, Lehigh University, Bethlehem, PA, 273.20, 1965.
- [26] T. V. Galambos, *Structural Members and Frames*. London, U.K.: Prentice-Hall Series in Structural Analysis and Design (W. J. Hall, editor), 1968.
- [27] T. J. Wilkinson, 'The Plastic Behaviour of Cold-Formed Rectangular Hollow Sections', Thesis, 1999. Accessed: Apr. 18, 2023. [Online]. Available: <https://ses.library.usyd.edu.au/handle/2123/843>
- [28] E. Saloumi, 'Development of a new design method to define the rotation capacity of steel hollow sections', Doctoral Thesis, Liège University, 2016.
- [29] 'Method of Finite Elements I – Structural Mechanics and Monitoring | ETH Zurich'. Accessed: Jun. 23, 2023. [Online]. Available: <https://chatzi.ibk.ethz.ch/education/method-of-finite-elements-i.html>
- [30] B. G. Neal, *The plastic methods of structural analysis*, 3. (S.I.) ed. London ; New York: Chapman and Hall, 1977.

- [31] G. C. Jr. Driscoll, 'Rotation capacity of a three span continuous beam', Fritz Engineering Laboratory, Lehigh University, Bethlehem, PA, Paper 1721, 1957.
- [32] G. C. Jr. Driscoll, 'Rotation capacity requirements for beams and portal frames', Doctoral Thesis, Lehigh University, 1958.
- [33] T. V. Galambos, 'Deformation and energy absorption capacity of steel structures in the inelastic range', Center for Cold-Formed Steel Structures Library, 180, 1968.
- [34] P. F. Adams, M. G. Lay, and T. V. Galambos, 'Experiments on High-Strength Steel Members', WRC Bulletin No. 110, Nov. 1965.
- [35] G. C. Lee and T. V. Galambos, 'Post-buckling strength of wide-flange beams', *J. Eng. Mech. Div.*, vol. 88, no. 1, pp. 59–75, 1962.
- [36] J. Prasad and T. V. Galambos, 'The influence of adjacent spans on the rotation capacity of beams, August 1963', 1963.
- [37] J. A. Yura, T. V. Galambos, and M. K. Ravindra, 'The bending resistance of steel beams', *J. Struct. Div.*, vol. 104, no. 9, pp. 1355–1370, 1978.
- [38] Eurocode 3 Editorial Group, 'The b/t Ratios Controlling the Applicability of Analysis Models in Eurocode 3', Aachen University, Germany, Background Documentation to Chapter 5 of Eurocode 3 Document 5.02, 1989.
- [39] R. M. Korol and J. Hudoba, 'Plastic behavior of hollow structural sections', *J. Struct. Div.*, vol. 98, no. 5, pp. 1007–1023, 1972.
- [40] S. W. Hasan and G. J. Hancock, 'Plastic bending tests of cold-formed rectangular hollow sections', *Steel Constr.*, vol. 23, no. 4, 1989.
- [41] X. L. Zhao and G. J. Hancock, 'Tests to determine plate slenderness limits for cold-formed rectangular hollow sections of grade C450', *Steel Constr.*, vol. 25, no. 4, pp. 2–16, 1991.
- [42] U. Kuhlmann, 'Definition of flange slenderness limits on the basis of rotation capacity values', *J. Constr. Steel Res.*, vol. 14, no. 1, pp. 21–40, 1989.
- [43] N. Stranghöner, G. Sedlacek, and P. Boeraeve, 'Rotation requirement and rotation capacity of rectangular, square and circular hollow section beams', in *Tubular Structures VI*, Grundy, Holgate & Wong (eds), 1994, pp. 143–150.
- [44] A. F. Lukey and P. F. Adams, 'Rotation capacity of beams under moment gradient', *J. Struct. Div.*, vol. 95, no. 6, pp. 1173–1188, 1969.
- [45] J. M. Ricles, R. Sause, and P. S. Green, 'High-strength steel: implications of material and geometric characteristics on inelastic flexural behavior', *Eng. Struct.*, vol. 20, no. 4–6, pp. 323–335, 1998.
- [46] P. Boeraeve, B. Lognard, J. Janss, J. C. Gerardy, and J. B. Schleich, 'Elasto-plastic behaviour of steel frame works', *J. Constr. Steel Res.*, vol. 27, no. 1–3, pp. 3–21, 1993.

- [47] A. R. Kemp, 'Interaction of plastic local and lateral buckling', *J. Struct. Eng.*, vol. 111, no. 10, pp. 2181–2196, 1985.
- [48] 'DIN EN 1993-1-1:2020-08, Eurocode_3: Bemessung und Konstruktion von Stahlbauten_- Teil_1-1: Allgemeine Bemessungsregeln und Regeln für den Hochbau; Deutsche und Englische Fassung prEN_1993-1-1:2020', Beuth Verlag GmbH. doi: 10.31030/3161839.
- [49] G. H. Bryan, 'On the Stability of a Plane Plate under Thrusts in its own Plane, with Applications to the "Buckling" of the Sides of a Ship', *Proc. Lond. Math. Soc.*, vol. 1, no. 1, pp. 54–67, 1890.
- [50] 'DIN EN 1993-1-5:2019-10, Eurocode_3_- Bemessung und Konstruktion von Stahlbauten_- Teil_1-5: Plattenförmige Bauteile; Deutsche Fassung EN_1993-1-5:2006_+ AC:2009_+ A1:2017_+ A2:2019', Beuth Verlag GmbH. doi: 10.31030/3085071.
- [51] G. Winter, 'Stress distribution in and equivalent width of flanges of wide, thin-wall steel beams', 1940.
- [52] S. Lindner, 'Schmidt (Hrsg.): Beuth-Kommentare: Erläuterungen zu DIN 18800, Teil 1 bis 4, 2', *Aufl Berl.*, 1994.
- [53] G. Haaijerl and B. Thürlimann, 'On Inelastic Buckling in Steel', *J. Eng. Mech. Div.*, vol. 84, no. 2, Apr. 1958, doi: 10.1061/JMCEA3.0000058.
- [54] G. Haaijer and B. Thürlimann, 'Inelastic Buckling in Steel', *Trans. Am. Soc. Civ. Eng.*, vol. 125, no. 1, pp. 308–338, Jan. 1960, doi: 10.1061/TACEAT.0007814.
- [55] M. G. Lay, 'Flange Local Buckling in Wide-Flange Shapes', *J. Struct. Div.*, vol. 91, no. 6, pp. 95–116, Dec. 1965, doi: 10.1061/JSDEAG.0001371.
- [56] B. Kato, 'Buckling strength of plates in the plastic range', in *International Association of Bridge and Structural Engineering*, 1965, pp. 127–141.
- [57] G. L. Kulak and M. L. Perlynn, 'Web slenderness limits for compact beam-columns', 1974.
- [58] N. M. Holtz and G. L. Kulak, 'Web slenderness limits for non-compact beams', 1975.
- [59] J. Nseir, 'Development of a new design method for the cross-section capacity of steel hollow sections', Doctoral Thesis, Liège University, 2015. [Online]. Available: <https://orbi.uliege.be/handle/2268/183084>
- [60] AISC, 'Specification for structural steel buildings', *ANSI/AISC*, vol. 360–16, 2016.
- [61] 'DIN EN 1993-1-1:2010-12, Eurocode_3: Bemessung und Konstruktion von Stahlbauten_- Teil_1-1: Allgemeine Bemessungsregeln und Regeln für den Hochbau; Deutsche Fassung EN_1993-1-1:2005_+ AC:2009', Beuth Verlag GmbH. doi: 10.31030/1723947.
- [62] DIN 18800-2: 2008-11, 'Stahlbauten; Teil 2: Stabilitätsfälle–Knicken von Stäben und Stabwerken'.

- [63] 'BS 5950-Structural use of steelwork in building', BSI British Standards. doi: 10.3403/BS5950.
- [64] C. S. Association, 'CAN/CSA-S16. 1 Limit States Design of Steel Structures', *Mississauga Ont.*, 2001.
- [65] 'Standards Australia International', Standards Australia, Reconfirmed 2016, May 1998.
- [66] M. Kettler, 'Elastic-plastic cross-sectional resistance of semi-compact H-and hollow sections', Doctoral Thesis, Graz University of Technology, 2008.
- [67] A. C. Fieber, 'Structural steel design using advanced analysis with strain limits', Doctoral Thesis, Imperial College London, 2019.
- [68] J. R. Liew, D. W. White, and W. F. Chen, 'Beam-column design in steel frameworks—Insights on current methods and trends', *J. Constr. Steel Res.*, vol. 18, no. 4, pp. 269–308, 1991.
- [69] S. L. Chan, Y. P. Liu, and Z. H. Zhou, 'Limitation of effective length method and codified second-order analysis and design', *Steel Compos. Struct. Int. J.*, vol. 5, no. 3, pp. 181–192, 2005.
- [70] W. F. Chen, 'Advanced analysis for structural steel building design', *Front. Archit. Civ. Eng. China*, vol. 2, pp. 189–196, 2008.
- [71] S. L. Chan, Y. P. Liu, and S. W. Liu, 'Structural design in the post-effective length era', *Procedia Eng.*, vol. 14, pp. 1005–1012, 2011.
- [72] 'Eurocode 3: Design of Steel Structures–Part 1-14: Design Assisted by Finite Element Analysis', Comité Européen de Normalisation (CEN) Brussels, 2020.
- [73] A. Rusch and J. Lindner, 'Überprüfung der grenz (b/t)-Werte für das Verfahren Elastisch-Plastisch', *Stahlbau*, vol. 70, no. 11, pp. 857–868, Nov. 2001, doi: 10.1002/stab.200102840.
- [74] A. Toffolon and A. Taras, 'Proposal of a design curve for the overall resistance of cold formed RHS and SHS members', *ce/papers*, vol. 3, no. 3–4, pp. 517–522, Sep. 2019, doi: 10.1002/cepa.1093.
- [75] A. Taras and A. Müller, *IDEA StatiCa Member, WP1-1: Comparison of the Buckling Resistance of SHS and RHS Profiles [online]. Chair of Steel and Composite Structures, ETH Zurich.* 2021.
- [76] A. Müller, M. Vild, and A. Taras, 'Decision tree for local + global imperfection combinations in double-symmetric prismatic members – Practical recommendations in the framework of advanced analysis', *Steel Constr.*, vol. 16, no. 1, pp. 2–15, Feb. 2023, doi: 10.1002/stco.202200041.
- [77] J. Lindner, A. Just, and U. Kuhlmann, 'Bow imperfections for flexural buckling according to Eurocode 3 part 1-1', presented at the SDSS, Timisoara, 2016, pp. 525–532.

- [78] J. Lindner, U. Kuhlmann, and A. Just, 'Verification of flexural buckling according to Eurocode 3 part 1-1 using bow imperfections', *Steel Constr.*, vol. 9, no. 4, pp. 349–362, 2016.
- [79] J. Lindner, 'Additional investigations concerning initial bow imperfections for flexural buckling according to Eurocode 3 Part 1-1', *ce/papers*, vol. 1, no. 5–6, pp. 35–42, 2017.
- [80] J. Lindner, 'Repräsentative Vorkrümmungen e_0 für das Biegeknicken–Ergänzende Untersuchungen', *Stahlbau*, vol. 86, no. 8, pp. 707–715, 2017.
- [81] F. Walport, 'Design of steel and stainless steel structures by advanced inelastic analysis', Doctoral Thesis, Imperial College London, 2019.
- [82] A. Taras and A. Müller, *IDEA StatiCa Member, WP1-2: Comparison of the Buckling Resistance of I-shaped crosssections [online]. Chair of Steel and Composite Structures, ETH Zurich*. 2021.
- [83] 'DIN EN 1993-1-6:2023-03, Eurocode_3: Bemessung und Konstruktion von Stahlbauten_- Teil_1-6: Festigkeit und Stabilität von Schalen; Deutsche und Englische Fassung prEN_1993-1-6:2023', Beuth Verlag GmbH. doi: 10.31030/3411682.
- [84] I. Vayas, J. Ermopoulos, and G. Ioannidis, *Design of Steel Structures to Eurocodes*. in Springer Tracts in Civil Engineering. Cham: Springer International Publishing, 2019. doi: 10.1007/978-3-319-95474-5.
- [85] B. W. Schafer, 'Review: The Direct Strength Method of cold-formed steel member design', in *Stability and Ductility of Steel Structures*, Lisbon, Portugal, 2006, p. 17. [Online]. Available: https://www.sefindia.org/forum/files/direct_strength_method_105.pdf
- [86] B. W. Schafer, 'Advances in the direct strength method of thin-walled steel design', in *Proceedings of the Eighth International Conference on Thin-walled Structures. Lisbon, Portugal*, 2018.
- [87] B. W. Schafer, 'Advances in the Direct Strength Method of cold-formed steel design', *Thin-Walled Struct.*, vol. 140, pp. 533–541, 2019.
- [88] B. W. Schafer and S. Adany, 'Buckling analysis of cold-formed steel members using CUFSM: conventional and constrained finite strip methods', in *Eighteenth international specialty conference on cold-formed steel structures*, Citeseer, 2006, pp. 39–54.
- [89] Z. Li and B. W. Schafer, 'Buckling analysis of cold-formed steel members with general boundary conditions using CUFSM conventional and constrained finite strip methods', 2010.
- [90] N. Silvestre, 'Generalised Beam Theory: new formulations, numerical implementation and applications', *Port. Ph Thesis Tech. Univ Lisbon*, 2005.
- [91] B. W. Schafer, 'Distortional Buckling of Cold-Formed Steel Columns', American Iron and Steel Institute, Research Report RP00-1, 2000. [Online]. Available:

<https://buildusingsteel.org/wp-content/uploads/2020/12/CFSD-Report-RP00-1.pdf>

- [92] B. W. Schafer, 'Local, distortional, and Euler buckling of thin-walled columns', *J. Struct. Eng.*, vol. 128, no. 3, pp. 289–299, 2002.
- [93] G. J. Hancock, Y. B. Kwon, and E. S. Bernard, 'Strength design curves for thin-walled sections undergoing distortional buckling', *J. Constr. Steel Res.*, vol. 31, no. 2–3, pp. 169–186, 1994.
- [94] G. J. Hancock, C. A. Rogers, and R. M. Schuster, 'Comparison of the distortional buckling method for flexural members with tests', in *Proceedings of the thirteenth international specialty conference on cold-formed steel structures*, 1996, pp. 125–140.
- [95] B. W. Schafer, 'Review: The Direct Strength Method of cold-formed steel member design', *J. Constr. Steel Res.*, vol. 64, no. 7–8, pp. 766–778, Jul. 2008, doi: 10.1016/j.jcsr.2008.01.022.
- [96] L. Gardner, 'The continuous strength method', *Proc. Inst. Civ. Eng. - Struct. Build.*, vol. 161, no. 3, pp. 127–133, Jun. 2008, doi: 10.1680/stbu.2008.161.3.127.
- [97] 'DIN EN 1993-1-4:2023-03, Eurocode 3_- Bemessung und Konstruktion von Stahlbauten_- Teil 1-4: Tragwerke aus nichtrostenden Stählen; Deutsche und Englische Fassung prEN_1993-1-4:2023', Beuth Verlag GmbH. doi: 10.31030/3406959.
- [98] S. Afshan and L. Gardner, 'The continuous strength method for structural stainless steel design', *Thin-Walled Struct.*, vol. 68, pp. 42–49, 2013.
- [99] L. Gardner, 'A new approach to structural stainless steel design', 2002.
- [100] L. Gardner and D. A. Nethercot, 'Structural stainless steel design: a new approach', *Struct. Eng.*, vol. 82, pp. 21–30, 2004.
- [101] L. Gardner and D. A. Nethercot, 'Experiments on stainless steel hollow sections—Part 1: Material and cross-sectional behaviour', *J. Constr. Steel Res.*, vol. 60, no. 9, pp. 1291–1318, 2004.
- [102] L. Gardner and D. A. Nethercot, 'Experiments on stainless steel hollow sections—Part 2: Member behaviour of columns and beams', *J. Constr. Steel Res.*, vol. 60, no. 9, pp. 1319–1332, 2004.
- [103] L. Gardner and M. Ashraf, 'Structural design for non-linear metallic materials', *Eng. Struct.*, vol. 28, no. 6, pp. 926–934, 2006.
- [104] M. Ashraf, L. Gardner, and D. A. Nethercot, 'Compression strength of stainless steel cross-sections', *J. Constr. Steel Res.*, vol. 62, no. 1–2, pp. 105–115, 2006.
- [105] M. Ashraf, L. Gardner, and D. A. Nethercot, 'Structural stainless steel design: Resistance based on deformation capacity', *J. Struct. Eng.*, vol. 134, no. 3, pp. 402–411, 2008.

- [106] C. Buchanan, L. Gardner, and A. Liew, 'The continuous strength method for the design of circular hollow sections', *J. Constr. Steel Res.*, vol. 118, pp. 207–216, 2016.
- [107] M. Ashraf and B. Young, 'Design formulations for non-welded and welded aluminium columns using Continuous Strength Method', *Eng. Struct.*, vol. 33, no. 12, pp. 3197–3207, 2011.
- [108] A. Liew and L. Gardner, 'Ultimate capacity of structural steel cross-sections under compression, bending and combined loading', in *Structures*, Elsevier, 2015, pp. 2–11.
- [109] O. Zhao, S. Afshan, and L. Gardner, 'Structural response and continuous strength method design of slender stainless steel cross-sections', *Eng. Struct.*, vol. 140, pp. 14–25, 2017.
- [110] O. Zhao and L. Gardner, 'The continuous strength method for the design of mono-symmetric and asymmetric stainless steel cross-sections in bending', *J. Constr. Steel Res.*, vol. 150, pp. 141–152, 2018.
- [111] X. Yun, L. Gardner, and N. Boissonnade, 'Ultimate capacity of I-sections under combined loading–Part 1: Experiments and FE model validation', *J. Constr. Steel Res.*, vol. 147, pp. 408–421, 2018.
- [112] X. Yun, L. Gardner, and N. Boissonnade, 'Ultimate capacity of I-sections under combined loading–Part 2: Parametric studies and CSM design', *J. Constr. Steel Res.*, vol. 148, pp. 265–274, 2018.
- [113] 'AISC. Design guide 27: Structural stainless steel.' American Institute of Steel Construction, 2013.
- [114] 'SCI. Design manual for structural stainless steel', The Steel Construction Institute (SCI), 4th Edition, 2017.
- [115] S. Ahmed, M. Ashraf, and M. Anwar-Us-Saadat, 'The Continuous Strength Method for slender stainless steel cross-sections', *Thin-Walled Struct.*, vol. 107, pp. 362–376, Oct. 2016, doi: 10.1016/j.tws.2016.06.023.
- [116] L. Gardner, F. Wang, and A. Liew, 'Influence of strain hardening on the behavior and design of steel structures', *Int. J. Struct. Stab. Dyn.*, vol. 11, no. 05, pp. 855–875, Oct. 2011, doi: 10.1142/S0219455411004373.
- [117] H. Kuwamura, 'Local Buckling of Thin-Walled Stainless Steel Members', *Steel Struct.*, vol. 3, pp. 191–201, 2003.
- [118] N. Saliba and L. Gardner, 'Cross-section stability of lean duplex stainless steel welded I-sections', *J. Constr. Steel Res.*, vol. 80, pp. 1–14, Jan. 2013, doi: 10.1016/j.jcsr.2012.09.007.
- [119] A. Talja and P. Salmi, *Design of stainless steel RHS beams, columns and beam-columns*. in Tiedotteita / Valtion Teknillinen Tutkimuskeskus, no. 1619. Espoo: Technical Research Centre of Finland, 1995.

- [120] L. Gardner, A. Talja, and N. R. Baddoo, 'Structural design of high-strength austenitic stainless steel', *Thin-Walled Struct.*, vol. 44, no. 5, pp. 517–528, May 2006, doi: 10.1016/j.tws.2006.04.014.
- [121] M. Theofanous and L. Gardner, 'Testing and numerical modelling of lean duplex stainless steel hollow section columns', *Eng. Struct.*, vol. 31, no. 12, pp. 3047–3058, Dec. 2009, doi: 10.1016/j.engstruct.2009.08.004.
- [122] S. Afshan and L. Gardner, 'Experimental Study of Cold-Formed Ferritic Stainless Steel Hollow Sections', *J. Struct. Eng.*, vol. 139, no. 5, pp. 717–728, May 2013, doi: 10.1061/(ASCE)ST.1943-541X.0000580.
- [123] ECSC, 'ECSC project - development of the use of stainless steel in construction.', The Steel Construction Institute, UK, Work Package 6 (WP6), 2000.
- [124] ECSC, 'ECSC project - development of the use of stainless steel in construction', The Steel Construction Institute, UK, Work Package 2 (WP2), 2000.
- [125] K. J. R. Rasmussen and G. J. Hancock, 'Design of Cold-Formed Stainless Steel Tubular Members. I: Columns', *J. Struct. Eng.*, vol. 119, no. 8, pp. 2349–2367, Aug. 1993.
- [126] K. J. R. Rasmussen and G. J. Hancock, 'Design of Cold-Formed Stainless Steel Tubular Members. II: Beams', *J. Struct. Eng.*, vol. 119, no. 8, pp. 2368–2386, Aug. 1993, doi: 10.1061/(ASCE)0733-9445(1993)119:8(2368).
- [127] H. X. Yuan, Y. Q. Wang, Y. J. Shi, and L. Gardner, 'Stub column tests on stainless steel built-up sections', *Thin-Walled Struct.*, vol. 83, pp. 103–114, Oct. 2014, doi: 10.1016/j.tws.2014.01.007.
- [128] F. Zhou and B. Young, 'Tests of cold-formed stainless steel tubular flexural members', *Thin-Walled Struct.*, vol. 43, no. 9, pp. 1325–1337, 2005.
- [129] X. Yun, L. Gardner, and N. Boissonnade, 'The continuous strength method for the design of hot-rolled steel cross-sections', *Eng. Struct.*, vol. 157, pp. 179–191, Feb. 2018, doi: 10.1016/j.engstruct.2017.12.009.
- [130] L. Gardner, X. Yun, L. Macorini, and M. Kucukler, 'Hot-Rolled Steel and Steel-Concrete Composite Design Incorporating Strain Hardening', *Structures*, vol. 9, pp. 21–28, Feb. 2017, doi: 10.1016/j.istruc.2016.08.005.
- [131] 'DIN EN 1993-1-5:2022-03, Eurocode_3_- Bemessung und Konstruktion von Stahlbauten_- Teil_1-5: Plattenförmige Bauteile; Deutsche und Englische Fassung prEN_1993-1-5:2022', Beuth Verlag GmbH. doi: 10.31030/3304046.
- [132] M.-N. Su, B. Young, and L. Gardner, 'Testing and design of aluminum alloy cross sections in compression', *J. Struct. Eng.*, vol. 140, no. 9, p. 04014047, 2014.
- [133] M.-N. Su, B. Young, and L. Gardner, 'The continuous strength method for the design of aluminium alloy structural elements', *Eng. Struct.*, vol. 122, pp. 338–348, 2016.
- [134] J. F. Huang, 'Stress-strain models for carbon steels', MSc thesis, Department of Civil and Environmental Engineering, University of ..., 2010.

- [135] A. S. J. Foster, L. Gardner, and Y. Wang, 'Practical strain-hardening material properties for use in deformation-based structural steel design', *Thin-Walled Struct.*, vol. 92, pp. 115–129, 2015.
- [136] A. J. Sadowski, J. M. Rotter, T. Reinke, and T. Ummenhofer, 'Statistical analysis of the material properties of selected structural carbon steels', *Struct. Saf.*, vol. 53, pp. 26–35, 2015.
- [137] A. Foster, 'Stability and design of steel beams in the strain-hardening range', Doctoral Thesis, Imperial College London, 2013. Accessed: May 10, 2023. [Online]. Available: <http://spiral.imperial.ac.uk/handle/10044/1/24117>
- [138] M. Bruneau, C.-M. Uang, and R. Sabelli, *Ductile design of steel structures*, 2nd ed. New York, NY: McGraw-Hill Education, 2011. [Online]. Available: <https://www.accessengineeringlibrary.com/content/book/9780071623957>
- [139] W. Ramberg and W. R. Osgood, 'Description of stress-strain curves by three parameters', 1943.
- [140] K. J. R. Rasmussen, 'Full-range stress–strain curves for stainless steel alloys', *J. Constr. Steel Res.*, vol. 59, no. 1, pp. 47–61, Jan. 2003, doi: 10.1016/S0143-974X(02)00018-4.
- [141] W. M. Quach, J. G. Teng, and K. F. Chung, 'Three-Stage Full-Range Stress-Strain Model for Stainless Steels', *J. Struct. Eng.*, vol. 134, no. 9, pp. 1518–1527, Sep. 2008, doi: 10.1061/(ASCE)0733-9445(2008)134:9(1518).
- [142] I. Arrayago, E. Real, and L. Gardner, 'Description of stress–strain curves for stainless steel alloys', *Mater. Des.*, vol. 87, pp. 540–552, Dec. 2015, doi: 10.1016/j.matdes.2015.08.001.
- [143] E. Mirambell and E. Real, 'On the calculation of deflections in structural stainless steel beams: an experimental and numerical investigation', *J. Constr. Steel Res.*, vol. 54, no. 1, pp. 109–133, 2000.
- [144] W. M. Quach and J. F. Huang, 'Stress-strain models for light gauge steels', *Procedia Eng.*, vol. 14, pp. 288–296, 2011.
- [145] B. Rossi, 'Mechanical properties, residual stresses and structural behavior of thin-walled stainless steel profiles', Doctoral Thesis, Liège University, Belgium, 2009.
- [146] *Abaqus. Analysis user's guide*. Providence RI, USA: Simulia Corp, 2016.
- [147] R. Schardt, *Verallgemeinerte Technische Biegetheorie: Lineare Probleme*. Springer-Verlag, 2013.
- [148] M. Seif and B. Schafer, 'Elastic buckling finite strip analysis of the AISC sections database and proposed local plate buckling coefficients', in *Structures Congress 2009: Don't Mess with Structural Engineers: Expanding Our Role*, 2009, pp. 1–10.
- [149] M. Seif and B. W. Schafer, 'Local buckling of structural steel shapes', *J. Constr. Steel Res.*, vol. 66, no. 10, pp. 1232–1247, 2010.

- [150] A. Fieber, L. Gardner, and L. Macorini, 'Formulae for determining elastic local buckling half-wavelengths of structural steel cross-sections', *J. Constr. Steel Res.*, vol. 159, pp. 493–506, 2019.
- [151] L. Gardner, A. Fieber, and L. Macorini, 'Formulae for calculating elastic local buckling stresses of full structural cross-sections', in *Structures*, Elsevier, 2019, pp. 2–20.
- [152] A. Liew, 'Design of structural steel elements with the Continuous Strength Method', Imperial College London, 2014.
- [153] X. Yun, 'Material modelling and design of hot-rolled and cold-formed steel structures', 2018.
- [154] A. Fieber, L. Gardner, and L. Macorini, 'Advanced analysis with strain limits for the design of steel structures', in *Proceedings of the Ninth International Conference on Advances in Steel Structures (ICASS 2018), Hong Kong, China*, 2018, pp. 5–7.
- [155] A. Fieber, L. Gardner, and L. Macorini, 'Design of steel structures using advanced analysis and strain limits', in *Proceedings of the Eighth International Conference on Thin-Walled Structures (ICTWS 2018), Lisbon, Portugal*, 2018, pp. 24–27.
- [156] A. Fieber, L. Gardner, and L. Macorini, 'Design of structural steel members by advanced inelastic analysis with strain limits', *Eng. Struct.*, vol. 199, p. 109624, 2019.
- [157] M. G. Lay and T. V. Galambos, *The inelastic behaviour of beams under moment gradient*. Lehigh University Institute of Research, 1964.
- [158] M. G. Lay, *Some studies of flange local buckling in wide-flange shapes*. Lehigh University Institute of Research, 1964.
- [159] N. Boissonnade, J. Nseir, and E. Saloumi, 'The overall interaction concept: an alternative approach to the stability and resistance of steel sections and members', in *Proceedings of the Annual Stability Conference, Structural Stability Research Council*, 2013, pp. 16–20.
- [160] N. Boissonnade, M. Hayeck, E. Saloumi, and J. Nseir, 'An Overall Interaction Concept for an alternative approach to steel members design', *J. Constr. Steel Res.*, vol. 135, pp. 199–212, 2017.
- [161] A. Taras *et al.*, 'Overall-Slenderness Based Direct Design for Strength and Stability of Innovative Hollow Sections (HOLLOSSTAB, RFCS Grant No. 2015-709892).', Munich, Final Report, 2019.
- [162] A. Toffolon, X. Meng, A. Taras, and L. Gardner, 'The generalized slenderness-based resistance method for the design of SHS and RHS', *Steel Constr.*, vol. 12, no. 4, pp. 327–341, 2019.
- [163] J. Wang, S. Afshan, M. Gkantou, M. Theofanous, C. Baniotopoulos, and L. Gardner, 'Flexural behaviour of hot-finished high strength steel square and rectangular hollow sections', *J. Constr. Steel Res.*, vol. 121, pp. 97–109, Jun. 2016, doi: 10.1016/j.jcsr.2016.01.017.

- [164] G. C. Driscoll Jr and L. S. Beedle, 'The plastic behavior of structural members and frames, *Welding Journal*, 36 (6), p. 275-s (1957), Reprint No. 115 (57-4)', 1957.
- [165] M. G. Lay, 'The Experimental Bases for Plastic Design-A Survey of the Literature', 1963.
- [166] V. Gioncu and D. Petcu, 'Available rotation capacity of wide-flange beams and beam-columns Part 2. Experimental and numerical tests', *J. Constr. Steel Res.*, vol. 43, no. 1-3, pp. 219-244, 1997.
- [167] A. Lechner, 'Plastic Capacity of Semi-Compact Cross-Sections', *Inst. Steel Struct. Shell Struct. Graz Univ. Technol. PhD Thesis*, 2005.
- [168] A. Taras, 'Contribution to the Development of Consistent Stability Design Rules for Steel Members', Doctoral Thesis, Graz University of Technology, 2010.
- [169] R. Kindmann and M. Kraus, 'FE-Berechnungen mit Fließzonen für Tragfähigkeitsnachweise nach DIN EN 1993-1-1: Vereinfachte Berechnungsmethode für stabilitätsgefährdete Bauteile', *Stahlbau*, vol. 88, no. 4, pp. 354-362, Apr. 2019, doi: 10.1002/stab.201900003.
- [170] Y. LeCun, L. Bottou, Y. Bengio, and P. Haffner, 'Gradient-based learning applied to document recognition', *Proc. IEEE*, vol. 86, no. 11, pp. 2278-2324, 1998.
- [171] W. Wang, Y. Yang, X. Wang, W. Wang, and J. Li, 'Development of convolutional neural network and its application in image classification: a survey', *Opt. Eng.*, vol. 58, no. 4, pp. 040901-040901, 2019.
- [172] A. Khan, A. Sohail, U. Zahoor, and A. S. Qureshi, 'A survey of the recent architectures of deep convolutional neural networks', *Artif. Intell. Rev.*, vol. 53, pp. 5455-5516, 2020.
- [173] L. Alzubaidi *et al.*, 'Review of deep learning: Concepts, CNN architectures, challenges, applications, future directions', *J. Big Data*, vol. 8, pp. 1-74, 2021.
- [174] B. E. Boser, 'A training algorithm for optimal margin classifiers', *Proc. 5th Annu. ACM Workshop Comput. Learn. Theory*, p. 144, 1992.
- [175] C. Cortes and V. Vapnik, 'Support-vector networks', *Mach. Learn.*, vol. 20, no. 3, pp. 273-297, Sep. 1995, doi: 10.1007/BF00994018.
- [176] V. N. Vapnik, *The Nature of Statistical Learning Theory*. New York, NY: Springer New York, 2000. doi: 10.1007/978-1-4757-3264-1.
- [177] A. Ben-Hur, D. Horn, H. T. Siegelmann, and V. Vapnik, 'Support vector clustering', *J. Mach. Learn. Res.*, vol. 2, no. Dec, pp. 125-137, 2001.
- [178] A. Tharwat, 'Parameter investigation of support vector machine classifier with kernel functions', *Knowl. Inf. Syst.*, vol. 61, pp. 1269-1302, 2019.

- [179] Y. Freund and R. E. Schapire, 'Experiments with a new boosting algorithm', presented at the Proceedings of the 13th International Conference on International Conference on Machine Learning, 1996, pp. 148–156.
- [180] Y. Freund and R. E. Schapire, 'A Decision-Theoretic Generalization of On-Line Learning and an Application to Boosting', *J. Comput. Syst. Sci.*, vol. 55, no. 1, pp. 119–139, Aug. 1997, doi: 10.1006/jcss.1997.1504.
- [181] R. E. Schapire, 'A brief introduction to boosting', presented at the Proceedings of the 16th International Joint Conference on Artificial intelligence, 1999, pp. 1401–1406.
- [182] J. H. Friedman, 'Greedy function approximation: A gradient boosting machine', *Ann. Stat.*, no. Vol. 29, No. 5, pp. 1189–1232, 2001.
- [183] T. Chen and C. Guestrin, 'XGBoost: A scalable tree boosting system', presented at the Proceedings of the 22nd ACM SIGKDD International Conference on Knowledge Discovery and Data Mining, 2016, pp. 785–794.
- [184] G. Ke *et al.*, 'LightGBM: a highly efficient gradient boosting decision tree', presented at the Proceedings of the 31st International Conference on Neural Information Processing Systems, 2017, pp. 3149–3157.
- [185] L. Prokhorenkova, G. Gusev, A. Vorobev, A. V. Dorogush, and A. Gulin, 'CatBoost: unbiased boosting with categorical features', presented at the Proceedings of the 32nd International Conference on Neural Information Processing Systems, 2018, pp. 6639–6649.
- [186] C. Bentéjac, A. Csörgő, and G. Martínez-Muñoz, 'A comparative analysis of gradient boosting algorithms', *Artif. Intell. Rev.*, vol. 54, no. 3, pp. 1937–1967, Mar. 2021, doi: 10.1007/s10462-020-09896-5.
- [187] L. Breiman, 'Random forests', *Mach. Learn.*, vol. 45, pp. 5–32, 2001.
- [188] H.-T. Thai, 'Machine learning for structural engineering: A state-of-the-art review', in *Structures*, Elsevier, 2022, pp. 448–491.
- [189] R. Bischof and M. Kraus, 'Multi-objective loss balancing for physics-informed deep learning', *ArXiv Prepr. ArXiv211009813*, 2021.
- [190] M. Raissi, P. Perdikaris, and G. E. Karniadakis, 'Machine learning of linear differential equations using Gaussian processes', *J. Comput. Phys.*, vol. 348, pp. 683–693, Nov. 2017, doi: 10.1016/j.jcp.2017.07.050.
- [191] M. Raissi, P. Perdikaris, and G. E. Karniadakis, 'Physics-informed neural networks: A deep learning framework for solving forward and inverse problems involving non-linear partial differential equations', *J. Comput. Phys.*, vol. 378, pp. 686–707, Feb. 2019, doi: 10.1016/j.jcp.2018.10.045.
- [192] J. Sirignano and K. Spiliopoulos, 'DGM: A deep learning algorithm for solving partial differential equations', *J. Comput. Phys.*, vol. 375, pp. 1339–1364, Dec. 2018, doi: 10.1016/j.jcp.2018.08.029.

- [193] K. Yang and G. E. Karniadakis, 'Physics-informed machine learning for predictive turbulence modeling: A priori and a posteriori studies', *J. Computa-Tional Phys.*, vol. 401, 2020.
- [194] M. D'Aniello, E. M. Güneyisi, R. Landolfo, and K. Mermerdaş, 'Analytical prediction of available rotation capacity of cold-formed rectangular and square hollow section beams', *Thin-Walled Struct.*, vol. 77, pp. 141–152, 2014.
- [195] L. Gardner, N. Saari, and F. Wang, 'Comparative experimental study of hot-rolled and cold-formed rectangular hollow sections', *Thin-Walled Struct.*, vol. 48, no. 7, pp. 495–507, Jul. 2010, doi: 10.1016/j.tws.2010.02.003.
- [196] R. Landolfo, M. D'Aniello, M. Brescia, and S. Tortorelli, 'Rotation capacity and classification criteria of steel beams', *Dev. Innov. Approaches Des. Steel-concrete Struct. Syst. Line*, vol. 5, pp. 2005–2008, 2011.
- [197] E. M. Güneyisi, M. D'Aniello, R. Landolfo, and K. Mermerdaş, 'Prediction of the flexural overstrength factor for steel beams using artificial neural network', *Steel Compos. Struct.*, vol. 17, no. 3, pp. 215–236, 2014.
- [198] M. D'Aniello, E. M. Güneyisi, R. Landolfo, and K. Mermerdaş, 'Predictive models of the flexural overstrength factor for steel thin-walled circular hollow section beams', *Thin-Walled Struct.*, vol. 94, pp. 67–78, Sep. 2015, doi: 10.1016/j.tws.2015.03.020.
- [199] J. J. Climenhaga, 'Local buckling in composite beams', Doctoral Thesis, University of Cambridge, 1971.
- [200] M. A. Grubb and P. S. Carskaddan, 'Autostress design of highway bridges, phase 3: initial moment-rotation tests', *AISI Proj.*, vol. 188, pp. 019–4, 1979.
- [201] M. A. Grubb and P. S. Carskaddan, 'Autostress design of highway bridges, phase 3: moment-rotation requirements', *AISI Proj.*, vol. 188, pp. 018–1, 1981.
- [202] C. G. Schilling, 'Moment-rotation tests of steel bridge girders', *J. Struct. Eng.*, vol. 114, no. 1, pp. 134–149, 1988.
- [203] C. G. Schilling, 'Moment-Rotation tests of steel Girders with Ultracompact Flanges', *Struct. Stab. Res. Counc.*, vol. Annual Technical Session, no. April 10-11, 1990.
- [204] A. Wargsjö, 'Plastisk rotationskapacitet hos svetsade stålbalkar', Doctoral Thesis, Luleå tekniska universitet, 1991.
- [205] W. Dahl, P. Langenberg, G. Sedlacek, and R. Spangemacher, 'Elastisch-plastisches Verhalten von Stahlkonstruktionen- Anforderungen und Werkstoffkennwerte', *EUR(Luxembourg)*, 1993.
- [206] T. Suzuki, T. Ogawa, and K. Ikarashi, 'A study on local buckling behavior of hybrid beams', *Thin-Walled Struct.*, vol. 19, no. 2–4, pp. 337–351, 1994.
- [207] M. D'Aniello, R. Landolfo, V. Piluso, and G. Rizzano, 'Ultimate behavior of steel beams under non-uniform bending', *J. Constr. Steel Res.*, vol. 78, pp. 144–158, 2012.

- [208] G. Sedlacek, W. Dahl, N. Stranghöner, B. Kalinowski, J. Rondal, and P. H. Boeraeve, 'Investigation of the rotation behaviour of hollow section beams', *EUR(Luxembourg)*, 1995.
- [209] M. Elchalakani, X. L. Zhao, and R. Grzebieta, 'Bending tests to determine slenderness limits for cold-formed circular hollow sections', *J. Constr. Steel Res.*, vol. 58, no. 11, pp. 1407–1430, 2002.
- [210] M. Elchalakani, X. L. Zhao, and R. H. Grzebieta, 'Plastic slenderness limits for cold-formed circular hollow sections', *Aust. J. Struct. Eng.*, vol. 3, no. 3, pp. 127–141, 2002.
- [211] H. Jiao and X.-L. Zhao, 'Section slenderness limits of very high strength circular steel tubes in bending', *Thin-Walled Struct.*, vol. 42, no. 9, pp. 1257–1271, 2004.
- [212] M. Elchalakani, X.-L. Zhao, and R. Grzebieta, 'Cyclic bending tests to determine fully ductile section slenderness limits for cold-formed circular hollow sections', *J. Struct. Eng.*, vol. 130, no. 7, pp. 1001–1010, 2004.
- [213] G. Kiyamaz, 'Strength and stability criteria for thin-walled stainless steel circular hollow section members under bending', *Thin-Walled Struct.*, vol. 43, no. 10, pp. 1534–1549, 2005.
- [214] M. Elchalakani, X.-L. Zhao, and R. Grzebieta, 'Variable amplitude cyclic pure bending tests to determine fully ductile section slenderness limits for cold-formed CHS', *Eng. Struct.*, vol. 28, no. 9, pp. 1223–1235, 2006.
- [215] J. Haedir, M. R. Bambach, X.-L. Zhao, and R. H. Grzebieta, 'Strength of circular hollow sections (CHS) tubular beams externally reinforced by carbon FRP sheets in pure bending', *Thin-Walled Struct.*, vol. 47, no. 10, pp. 1136–1147, 2009.
- [216] L. Guo, S. Yang, and H. Jiao, 'Behavior of thin-walled circular hollow section tubes subjected to bending', *Thin-Walled Struct.*, vol. 73, pp. 281–289, 2013.
- [217] E. T. Fonseca, M. M. Vellasco, M. A. C. Pacheco, P. C. D. S. Vellasco, and S. A. De Andrade, 'A neural network system for patch load prediction', *J. Intell. Robot. Syst.*, vol. 31, pp. 185–200, 2001.
- [218] E. T. Fonseca, P. C. da S. Vellasco, S. A. de Andrade, and M. M. Vellasco, 'A patch load parametric analysis using neural networks', *J. Constr. Steel Res.*, vol. 59, no. 2, pp. 251–267, 2003.
- [219] E. T. Fonseca, P. da S. Vellasco, S. A. L. De Andrade, and M. Vellasco, 'Neural network evaluation of steel beam patch load capacity', *Adv. Eng. Softw.*, vol. 34, no. 11–12, pp. 763–772, 2003.
- [220] E. T. Fonseca, P. da S. Vellasco, M. M. Vellasco, and S. A. de Andrade, 'A neuro-fuzzy evaluation of steel beams patch load behaviour', *Adv. Eng. Softw.*, vol. 39, no. 7, pp. 558–572, 2008.
- [221] S. S. Sakla, 'Neural network modeling of the load-carrying capacity of eccentrically-loaded single-angle struts', *J. Constr. Steel Res.*, vol. 60, no. 7, pp. 965–987, 2004.

- [222] A. Djerrad, F. Fan, X. Zhi, and Q. Wu, 'Artificial neural networks (ANN) based compressive strength prediction of afrp strengthened steel tube', *Int. J. Steel Struct.*, vol. 20, pp. 156–174, 2020.
- [223] Y. Xu, M. Zhang, and B. Zheng, 'Design of cold-formed stainless steel circular hollow section columns using machine learning methods', in *Structures*, Elsevier, 2021, pp. 2755–2770.
- [224] Y. Xu, B. Zheng, and M. Zhang, 'Capacity prediction of cold-formed stainless steel tubular columns using machine learning methods', *J. Constr. Steel Res.*, vol. 182, p. 106682, 2021.
- [225] Y. Pu and E. Mesbahi, 'Application of artificial neural networks to evaluation of ultimate strength of steel panels', *Eng. Struct.*, vol. 28, no. 8, pp. 1190–1196, 2006.
- [226] M. Sonmez and M. A. Komur, 'Using FEM and artificial networks to predict on elastic buckling load of perforated rectangular plates under linearly varying in-plane normal load', *Struct. Eng. Mech.*, vol. 34, no. 2, pp. 159–174, 2010.
- [227] Z. Sadovský and C. G. Soares, 'Artificial neural network model of the strength of thin rectangular plates with weld induced initial imperfections', *Reliab. Eng. Syst. Saf.*, vol. 96, no. 6, pp. 713–717, 2011.
- [228] Z. Sun *et al.*, 'Prediction of compression buckling load and buckling mode of hat-stiffened panels using artificial neural network', *Eng. Struct.*, vol. 242, p. 112275, 2021.
- [229] P. Mandal, 'Artificial neural network prediction of buckling load of thin cylindrical shells under axial compression', *Eng. Struct.*, vol. 152, pp. 843–855, 2017.
- [230] I. H. Guzelbey, A. Cevik, and A. Erklig, 'Prediction of web crippling strength of cold-formed steel sheetings using neural networks', *J. Constr. Steel Res.*, vol. 62, no. 10, pp. 962–973, 2006.
- [231] Z. Fang, K. Roy, Q. Ma, A. Uzzaman, and J. B. Lim, 'Application of deep learning method in web crippling strength prediction of cold-formed stainless steel channel sections under end-two-flange loading', in *Structures*, Elsevier, 2021, pp. 2903–2942.
- [232] Z. Fang, K. Roy, B. Chen, C.-W. Sham, I. Hajirasouliha, and J. B. Lim, 'Deep learning-based procedure for structural design of cold-formed steel channel sections with edge-stiffened and un-stiffened holes under axial compression', *Thin-Walled Struct.*, vol. 166, p. 108076, 2021.
- [233] Z. Fang, K. Roy, J. Mares, C.-W. Sham, B. Chen, and J. B. Lim, 'Deep learning-based axial capacity prediction for cold-formed steel channel sections using Deep Belief Network', in *Structures*, Elsevier, 2021, pp. 2792–2802.
- [234] S. Gholizadeh, A. Pirmoz, and R. Attarnejad, 'Assessment of load carrying capacity of castellated steel beams by neural networks', *J. Constr. Steel Res.*, vol. 67, no. 5, pp. 770–779, 2011.

- [235] A. Kaveh, A. Dadras Eslamlou, S. M. Javadi, and N. Geran Malek, 'Machine learning regression approaches for predicting the ultimate buckling load of variable-stiffness composite cylinders', *Acta Mech.*, vol. 232, pp. 921–931, 2021.
- [236] M. Pala, 'A new formulation for distortional buckling stress in cold-formed steel members', *J. Constr. Steel Res.*, vol. 62, no. 7, pp. 716–722, 2006.
- [237] M. Pala and N. Caglar, 'A parametric study for distortional buckling stress on cold-formed steel using a neural network', *J. Constr. Steel Res.*, vol. 63, no. 5, pp. 686–691, 2007.
- [238] J. L. R. Dias and N. Silvestre, 'A neural network based closed-form solution for the distortional buckling of elliptical tubes', *Eng. Struct.*, vol. 33, no. 6, pp. 2015–2024, 2011.
- [239] S. Tohidi and Y. Sharifi, 'Neural networks for inelastic distortional buckling capacity assessment of steel I-beams', *Thin-Walled Struct.*, vol. 94, pp. 359–371, 2015.
- [240] M. Hosseinpour, Y. Sharifi, and H. Sharifi, 'Neural network application for distortional buckling capacity assessment of castellated steel beams', in *Structures*, Elsevier, 2020, pp. 1174–1183.
- [241] A. Mukherjee, J. M. Deshpande, and J. Anmala, 'Prediction of buckling load of columns using artificial neural networks', *J. Struct. Eng.*, vol. 122, no. 11, pp. 1385–1387, 1996.
- [242] M. R. Sheidaii and R. Bahraminejad, 'Evaluation of compression member buckling and post-buckling behavior using artificial neural network', *J. Constr. Steel Res.*, vol. 70, pp. 71–77, 2012.
- [243] M. Kumar and N. Yadav, 'Buckling analysis of a beam–column using multilayer perceptron neural network technique', *J. Frankl. Inst.*, vol. 350, no. 10, pp. 3188–3204, 2013.
- [244] T.-H. Nguyen, N.-L. Tran, and D.-D. Nguyen, 'Prediction of critical buckling load of web tapered I-section steel columns using artificial neural networks', *Int. J. Steel Struct.*, vol. 21, no. 4, pp. 1159–1181, 2021.
- [245] M. Abambres, K. Rajana, K. D. Tsavdaridis, and T. P. Ribeiro, 'Neural Network-based formula for the buckling load prediction of I-section cellular steel beams', *Computers*, vol. 8, no. 1, p. 2, 2018.
- [246] Y. Sharifi, A. Moghbeli, M. Hosseinpour, and H. Sharifi, 'Neural networks for lateral torsional buckling strength assessment of cellular steel I-beams', *Adv. Struct. Eng.*, vol. 22, no. 9, pp. 2192–2202, 2019.
- [247] F. P. V. Ferreira, R. Shamass, V. Limbachiya, K. D. Tsavdaridis, and C. H. Martins, 'Lateral–torsional buckling resistance prediction model for steel cellular beams generated by Artificial Neural Networks (ANN)', *Thin-Walled Struct.*, vol. 170, p. 108592, 2022.

- [248] M. Shahin and M. Elchalakani, 'Neural networks for modelling ultimate pure bending of steel circular tubes', *J. Constr. Steel Res.*, vol. 64, no. 6, pp. 624–633, 2008.
- [249] G. M. Kotsovou, A. Ahmad, D. M. Cotsovos, and N. D. Lagaros, 'Reappraisal of methods for calculating flexural capacity of reinforced concrete members', *Proc. Inst. Civ. Eng.-Struct. Build.*, vol. 173, no. 4, pp. 279–290, 2020.
- [250] M. Z. Naser, 'An engineer's guide to eXplainable Artificial Intelligence and Interpretable Machine Learning: Navigating causality, forced goodness, and the false perception of inference', *Autom. Constr.*, vol. 129, p. 103821, 2021.
- [251] A. N. Hanoon, A. W. Al Zand, and Z. M. Yaseen, 'Designing new hybrid artificial intelligence model for CFST beam flexural performance prediction', *Eng. Comput.*, vol. 38, no. 4, pp. 3109–3135, 2022.
- [252] H. Basarir, M. Elchalakani, and A. Karrech, 'The prediction of ultimate pure bending moment of concrete-filled steel tubes by adaptive neuro-fuzzy inference system (ANFIS)', *Neural Comput. Appl.*, vol. 31, pp. 1239–1252, 2019.
- [253] M. Koçer, M. Öztürk, and M. H. Arslan, 'Determination of moment, shear and ductility capacities of spiral columns using an artificial neural network', *J. Build. Eng.*, vol. 26, p. 100878, 2019.
- [254] H. Naderpour and M. Mirrashid, 'Proposed soft computing models for moment capacity prediction of reinforced concrete columns', *Soft Comput.*, vol. 24, no. 15, pp. 11715–11729, 2020.
- [255] M. Congro, V. M. de Alencar Monteiro, A. L. Brandão, B. F. dos Santos, D. Roehl, and F. de Andrade Silva, 'Prediction of the residual flexural strength of fiber reinforced concrete using artificial neural networks', *Constr. Build. Mater.*, vol. 303, p. 124502, 2021.
- [256] S. Gopinath and A. Kumar, 'Artificial Neural Network–Based Numerical Model to Predict Flexural Capacity of Masonry Panels Strengthened with Textile Reinforced Mortar', *J. Compos. Constr.*, vol. 25, no. 1, p. 06020004, 2021.
- [257] C.-W. Tang, 'Using radial basis function neural networks to model torsional strength of reinforced concrete beams', *Comput. Concr.*, vol. 3, no. 5, pp. 335–355, Oct. 2006, doi: 10.12989/CAC.2006.3.5.335.
- [258] M. H. Arslan, 'Predicting of torsional strength of RC beams by using different artificial neural network algorithms and building codes', *Adv. Eng. Softw.*, vol. 41, no. 7–8, pp. 946–955, Jul. 2010, doi: 10.1016/j.advengsoft.2010.05.009.
- [259] H. C. Huang, 'Using a Hybrid Neural Network to Predict the Torsional Strength of Reinforced Concrete Beams', *Adv. Mater. Res.*, vol. 538–541, pp. 2749–2753, Jun. 2012, doi: 10.4028/www.scientific.net/AMR.538-541.2749.
- [260] M. H. Ilkhani, H. Naderpour, and A. Kheyroddin, 'A proposed novel approach for torsional strength prediction of RC beams', *J. Build. Eng.*, vol. 25, p. 100810, Sep. 2019, doi: 10.1016/j.job.2019.100810.

- [261] M. Haroon, S. Koo, D. Shin, and C. Kim, 'Torsional Behavior Evaluation of Reinforced Concrete Beams Using Artificial Neural Network', *Appl. Sci.*, vol. 11, no. 10, p. 4465, May 2021, doi: 10.3390/app11104465.
- [262] E. Alpaydin, 'Maschinelles Lernen', in *Maschinelles Lernen*, De Gruyter Oldenbourg, 2022.
- [263] J. Frochte, *Maschinelles Lernen: Grundlagen und Algorithmen in Python*. Carl Hanser Verlag GmbH Co KG, 2020.
- [264] S. Rao, 'Die Vorteile von KI im Bauwesen', Die Vorteile von KI im Bauwesen. [Online]. Available: <https://mep.trimble.com/de/resources/mep-blogs/ki>
- [265] L. Wuttke, 'Erratum zu: Praxisleitfaden für Künstliche Intelligenz in Marketing und Vertrieb', in *Praxisleitfaden für Künstliche Intelligenz in Marketing und Vertrieb*, Wiesbaden: Springer Fachmedien Wiesbaden, 2022, pp. E1–E1. doi: 10.1007/978-3-658-35626-2_7.
- [266] H. Adeli and C. Yeh, 'Perceptron learning in engineering design', *Comput. Civ. Infrastruct. Eng.*, vol. 4, no. 4, pp. 247–256, 1989.
- [267] W. S. McCulloch and W. Pitts, 'A logical calculus of the ideas immanent in nervous activity', *Bull. Math. Biophys.*, vol. 5, pp. 115–133, 1943.
- [268] D. Hebb, 'The organization of behavior', *N. Y.*, 1949.
- [269] M. Minsky and S. A. Papert, *Perceptrons, Reissue of the 1988 Expanded Edition with a new foreword by Léon Bottou: An Introduction to Computational Geometry*. MIT press, 2017.
- [270] A. Taras, A. Toffolon, I. Niko, L. Gardner, X. Meng, and N. Silvestre, 'Cross-sectional resistance and local buckling of RHS & SHS (HOLLOSSTAB, RFCS Grant No. 2015-709892).', Munich, Deliverable 4.2, 2019.
- [271] X. Meng, A. Toffolon, L. Gardner, and A. Taras, 'The generalised slenderness-based resistance method for the design of CHS and EHS', *Steel Constr.*, vol. 12, no. 4, pp. 342–353, 2019.
- [272] A. Toffolon, A. Müller, I. Niko, and A. Taras, 'Experimental and numerical analysis of the local and interactive buckling behaviour of hollow sections', *ce/papers*, vol. 3, no. 3–4, pp. 877–882, Sep. 2019, doi: 10.1002/cepa.1148.
- [273] *Zeiss Colin 3D*. Germany: Carl Zeiss Optotechnik GmbH.
- [274] 3D Systems, *Geomagic Design X*.
- [275] D. Girardeau-Montaut, *CloudCompare*. 2016.
- [276] A. Müller, B. Hausmann, and A. Taras, 'Study on the Influence of Imperfections and Strain Hardening on the Buckling Strength of Spiral-Welded Aluminum Circular Hollow Sections', presented at the Eighth International Conference on Thin-Walled Structures - ICTWS 2018, Lisbon, Portugal, Jul. 2018, p. 19.

- [277] A. Müller, T. Töpperwien, and A. Taras, 'Imperfection Evaluation Methods of Large Scale Spiral-welded Tubes based on Experimental Tests and Progressive Reverse Engineering Procedures', in *Proceedings of the 17th International Symposium on Tubular Structures(ISTS17)*, Research Publishing Services, 2019, pp. 488–495. doi: 10.3850/978-981-11-0745-0_098-cd.
- [278] L. E. McAnallen, D. A. Padilla-Llano, X. Zhao, C. D. Moen, B. W. Schafer, and M. R. Eatherton, 'Initial geometric imperfection measurement and characterization of cold-formed steel C-section structural members with 3D non-contact measurement techniques', *Proc. Struct. Stab. Res. Council.*, pp. 25–28, 2014.
- [279] A. J. Sadowski, S. H. Van Es, T. Reinke, J. M. Rotter, A. N. Gresnigt, and T. Ummenhofer, 'Harmonic analysis of measured initial geometric imperfections in large spiral welded carbon steel tubes', *Eng. Struct.*, vol. 85, pp. 234–248, 2015.
- [280] W. E. Ayrton and J. Perry, 'On struts', *The engineer*, vol. 62, no. 464–465, pp. 513–515, 1886.
- [281] A. Müller, M. Vild, and A. Taras, 'On the Choice of Eigenmode Shapes for Interactive Cases of Local and Global Buckling of RHS/SHS and I-Shaped Sections', *ce/papers*, vol. 5, no. 4, pp. 957–966, Sep. 2022, doi: 10.1002/cepa.1840.
- [282] R. Bjorhovde, 'Deterministic and probabilistic approaches to the strength of steel columns', Doctoral Thesis, Lehigh University, 1972.
- [283] R. D. Ziemian, *Guide to stability design criteria for metal structures*. John Wiley & Sons, 2010.
- [284] A. Toffolon and A. Taras, 'Development of an OIC-Type local buckling design approach for cold-formed unstiffened and groove-stiffened hollow sections', *Thin-Walled Struct.*, vol. 144, p. 106266, 2019.
- [285] A. Müller and A. Taras, 'Preliminary study on the impact of initial imperfections on the post-buckling rotation of square hollow sections in uniform bending', *ce/papers*, vol. 3, no. 3–4, pp. 835–840, Sep. 2019, doi: 10.1002/cepa.1167.
- [286] A. Müller and A. Taras, 'Study on the influence of measured geometric shape deviations on the deformation capacity and post buckling behavior of hollow sections loaded in compression and bending', in *Proceedings of the Annual Stability Conference Structural Stability Research Council*, Atlanta, Georgia, 2020, p. 17.
- [287] 'DIN EN 1993-1-3:2022-03, Eurocode_3_- Bemessung und Konstruktion von Stahlbauten_- Teil_1-3: Allgemeine Regeln_- Ergänzende Regeln für kaltgeformte Bauteile und Bleche; Deutsche und Englische Fassung prEN_1993-1-3:2022', Beuth Verlag GmbH. doi: 10.31030/3304044.
- [288] 'DIN EN 1993-1-12:2010-12, Eurocode_3: Bemessung und Konstruktion von Stahlbauten_- Teil_1-12: Zusätzliche Regeln zur Erweiterung von EN_1993 auf Stahlgüten bis_S700; Deutsche Fassung EN_1993-1-12:2007_+ AC:2009', Beuth Verlag GmbH. doi: 10.31030/1722663.

- [289] A. Müller, A. Taras, and M. A. Kraus, 'Scientific Machine and Deep Learning Investigations of the Local Buckling Behaviour of Hollow Sections', *ce/papers*, vol. 5, no. 4, pp. 1034–1042, Sep. 2022, doi: 10.1002/cepa.1848.
- [290] A. Müller and A. Taras, 'Prediction of the local buckling strength and load-displacement behaviour of SHS and RHS members using Deep Neural Networks (DNN)–Introduction to the Deep Neural Network Direct Stiffness Method (DNN-DSM)', *Steel Constr.*, vol. 15, no. S1, pp. 78–90, 2022.
- [291] A. Müller and A. Taras, 'Prediction of the load-displacement and local buckling behavior of hollow structural sections using Deep Neural Networks (DNN)', in *Proceedings of the Annual Stability Conference Structural Stability Research Council*, Denver, Colorado, 2022, p. 19.
- [292] A. Müller and A. Taras, 'Prediction of the deformation and local buckling behavior of structural systems using the deep neural network direct stiffness method (DNN-DSM)', in *Proceedings of the Annual Stability Conference Structural Stability Research Council*, Charlotte, North Carolina, 2023, p. 18. [Online]. Available: https://cloud.aisc.org/SSRC/2023/Muller_et_al_SSRC_2023.pdf
- [293] D. P. Kingma and J. Ba, 'Adam: A method for stochastic optimization', *ArXiv Prepr. ArXiv14126980*, 2014.
- [294] S. Ruder, 'An overview of gradient descent optimization algorithms', *ArXiv Prepr. ArXiv160904747*, 2016.
- [295] M. J. Turner, *The direct stiffness method of structural analysis*. Boeing Airplane Company, 1959.
- [296] R. Kindmann and M. Kraus, *Finite-Elemente-Methoden im Stahlbau*. John Wiley & Sons, 2020.
- [297] *Statik-8*. Switzerland: Cubus AG, Zürich.
- [298] Y. Bengio, I. J. Goodfellow, and A. Courville, 'Deep learning'An MIT Press book in preparation', *Draft Chapters Available At*, 2015.
- [299] S. Hochreiter and J. Schmidhuber, 'Long Short-Term Memory', *Neural Comput.*, vol. 9, no. 8, pp. 1735–1780, Nov. 1997, doi: 10.1162/neco.1997.9.8.1735.
- [300] J. Chung, C. Gulcehre, K. Cho, and Y. Bengio, 'Empirical evaluation of gated recurrent neural networks on sequence modeling', *ArXiv Prepr. ArXiv14123555*, 2014.
- [301] T. Wilkinson and G. J. Hancock, 'Tests of knee joints in cold-formed rectangular hollow sections', *Res. Rep.-Univ. Syd. Dep. Civ. Eng. R*, 1998.